

Clemson University

**TigerPrints**

---

All Dissertations

Dissertations

---

8-2023

## Multiscale Modeling and Gaussian Process Regression for Applications in Composite Materials

Joshua Arp  
jarp@clemson.edu

Follow this and additional works at: [https://tigerprints.clemson.edu/all\\_dissertations](https://tigerprints.clemson.edu/all_dissertations)



Part of the [Chemical Engineering Commons](#), [Engineering Science and Materials Commons](#), [Materials Science and Engineering Commons](#), and the [Mechanical Engineering Commons](#)

---

### Recommended Citation

Arp, Joshua, "Multiscale Modeling and Gaussian Process Regression for Applications in Composite Materials" (2023). *All Dissertations*. 3369.

[https://tigerprints.clemson.edu/all\\_dissertations/3369](https://tigerprints.clemson.edu/all_dissertations/3369)

This Dissertation is brought to you for free and open access by the Dissertations at TigerPrints. It has been accepted for inclusion in All Dissertations by an authorized administrator of TigerPrints. For more information, please contact [kokeefe@clemson.edu](mailto:kokeefe@clemson.edu).

MULTISCALE MODELING AND GAUSSIAN PROCESS REGRESSION FOR  
APPLICATIONS IN COMPOSITE MATERIALS

---

A Dissertation  
Presented to  
the Graduate School of  
Clemson University

---

In Partial Fulfillment  
of the Requirements for the Degree  
Doctor of Philosophy  
Chemical & Biomolecular Engineering

---

by  
Joshua Caleb Arp  
August 2023

---

Accepted by:  
Dr. Christopher L. Kitchens, Advisor and Committee Co-chair  
Dr. David A. Bruce, Committee Chair  
Dr. Amod A. Ogale, Committee Member  
Dr. Srikanth Pilla, Committee Member

## ABSTRACT

An ongoing challenge in advanced materials design is the development of accurate multiscale models that consider uncertainty while establishing a link between knowledge or information about constituent materials to overall composite properties. Successful models can accurately predict composite properties, reducing the high financial and labor costs associated with experimental determination and accelerating material innovation. Whereas early pioneers in micromechanics developed simplistic theoretical models to map these relationships, modern advances in computer technology have enabled detailed simulators capable of accurately predicting complex and multiscale phenomena.

This work advances domain knowledge via two means: firstly, through the development of high-fidelity, physics-based finite element (FE) models of composite microstructures that incorporate uncertainty in predictions, and secondly, through the development of a novel inverse analysis framework that enables the discovery of unknown or obscure constituent properties using literature data and Gaussian process (GP) surrogate models trained on FE model predictions. This work presents a generalizable approach to modeling a diverse array of composite subtypes, from a simple particulate system to a complex commercial composite.

The inverse analysis framework was demonstrated for a thermoplastic composite reinforced by spherical fillers with unknown interphase properties. The framework leverages computer model simulations with easily obtainable macroscale elastic property

measurements to infer interphase properties that are otherwise challenging to measure. The interphase modulus and thickness were determined for six different thermoplastic composites; four were reinforced by micron-scale particles and two with nano-scale particles.

An alginate fiber embedded with a helically symmetric arrangement of cellulose nanocrystals (CNCs) was investigated using multiscale FE analysis to quantify microstructural uncertainty and the subsequent effect on macroscopic behavior. The macroscale uniaxial tensile simulation revealed that the microstructure induces internal stresses sufficient to rotate or twist the fiber about its axis. The reduction in axial elastic modulus for increases in CNC spiral angle was quantified in a sensitivity analysis using a GP surrogate modeling approach.

A predictive model using GP regression was employed to investigate the link between input features and the mechanical properties of fiberglass-reinforced magnesium oxychloride (MOC) cement boards produced from a commercial process. The model evaluated the effect of formulation, crystalline phase compositions, and process control parameters on various mechanical performance metrics.



## DEDICATION

This dissertation is dedicated to my beloved family.

First and foremost, I extend my heartfelt gratitude to my beloved wife, Taylor, whose unwavering love, support, and selflessness have been the cornerstone of my journey. She has not only provided for me but also put her own aspirations on hold to enable me to complete my dreams. I am profoundly grateful for the sacrifices she has made. My parents, Dean and Anne, have provided unconditional love, support, and guidance throughout my life. They have truly set an example of selfless service and generosity towards others. Any achievements I have enjoyed were undoubtedly influenced by their nurturing and wise counsel. My cherished second set of parents, Bert and Debbie, have been a constant source of love, support, laughter, and generosity. They never hesitate to go the extra mile for me. I will always be indebted to their kindness. My dear brother-in-law and sister, Myers and Emily, have always cheered me on in my work and have generously granted my wife and me much-needed breaks. Their kindness and thoughtfulness have made us feel like royalty, and we are truly grateful for their presence in our lives.

I would like to express my gratitude to my former roommates and fellow ChemE's, Nick and Josh, for the incredible moments we shared in Clemson – from recruitment to the exciting lake trips and those late-night Cook-Out runs while towing the boat. I will always cherish the bond we formed during that time. Thank you both for making those experiences truly unforgettable.

## ACKNOWLEDGMENTS

I would like to express my deepest gratitude to my Ph.D. advisor, Dr. Christopher L. Kitchens, for his support, guidance, and mentorship as a doctoral student in his research group.

I would also like to thank Dr. Sez Atamturktur, Dr. Andrew Brown, and Dr. Joseph Geddes III for their interdisciplinary collaboration, which exposed me to new research areas. Their guidance and advice was extremely helpful during my doctoral program.

I would like to acknowledge the support by fellowships through Department of Education GAANN award P200A150310 and the National Science Foundation award NSF #1633608.

## TABLE OF CONTENTS

	Page
TITLE PAGE .....	i
ABSTRACT.....	ii
DEDICATION .....	iv
ACKNOWLEDGMENTS .....	v
LIST OF TABLES.....	ix
LIST OF FIGURES .....	x
 CHAPTER	
I. INTRODUCTION AND BACKGROUND .....	1
1.1 Introduction.....	1
1.2 Theoretical Background.....	3
1.2.1 Composite Materials .....	3
1.2.2 Mechanics of Composites .....	5
1.2.3 Analytical and Semi-Analytical Models.....	13
1.2.4 Finite Element-Based Homogenization of Composite Materials ..	18
1.2.5 Gaussian Process Models.....	27
1.2.6 Bayesian Inference.....	28
1.3 Dissertation Outline .....	29
II. INFERRING EFFECTIVE INTERPHASE PROPERTIES IN COMPOSITES BY INVERSE ANALYSIS .....	31
2.1 Abstract.....	31
2.2 Introduction.....	32
2.3 Background Perspectives .....	38
2.4 Methods.....	43
2.4.1 Finite Element-Based Homogenization .....	43
2.4.2 Bayesian Inference of Interphase Parameters .....	56
2.5 Results and Discussion .....	68
2.5.1 Inferred Interphase Parameters .....	68

## Table of Contents (Continued)

	Page
2.5.2 Comparison with Experimental Data.....	72
2.6 Conclusion .....	73
 III. MULTISCALE FINITE ELEMENT ANALYSIS OF HELICALLY SYMMETRIC CELLULOSE NANOCRYSTAL-REINFORCED ALGINATE COMPOSITE FIBERS .....	75
3.1 Abstract.....	75
3.2 Introduction.....	76
3.2.1 CNC Alignment and Effects on Mechanical Properties .....	76
3.2.2 Motivation.....	79
3.3 Methods.....	80
3.3.1 Microscale FE Model.....	80
3.3.2 Mapping from Micro to Macroscale .....	81
3.3.3 Macroscale Fiber Model .....	83
3.4 Results and Discussion .....	83
3.4.1 Elastic Modulus Sensitivity to CNC Spiral Angle and Circumferential Position .....	84
3.4.2 Elastic Modulus Sensitivity to CNC Spiral Angle and Volume Fraction .....	86
3.4.3 Validation of the Microscale FE Model.....	87
3.4.4 Macroscale Fiber FE Model Results.....	87
3.5 Conclusions.....	89
 IV. GAUSSIAN PROCESS REGRESSION FOR PREDICTING MAGNESIUM OXYCHLORIDE CEMENT BOARD PERFORMANCE .....	91
4.1 Introduction.....	91
4.1.1 Background on Magnesium Oxychloride Cement Boards .....	91
4.1.2 Motivation.....	94
4.2 Methods.....	97
4.2.1 Board Production and Data Collection .....	98
4.2.2 Gaussian Process Regression.....	100
4.2.3 Cross-Validation Scheme.....	106
4.2.4 Validation Scheme .....	109
4.3 Results and Discussion .....	111

## Table of Contents (Continued)

	Page
4.3.1 Evaluating Model Performance via Cross-Validation .....	111
4.3.2 Model Sensitivity to Hyperparameter Tuning .....	118
4.3.3 Validation of the Model .....	120
4.3.4 Feature Analysis.....	123
4.4 Conclusion .....	133
V. CONCLUSIONS AND FUTURE DIRECTIONS.....	135
5.1 Future Work.....	135
5.2 Conclusion .....	138
APPENDICES .....	140
A: Appendix A.....	141
Appendix A. Figures .....	142
Appendix A. Discussion .....	150
B: Appendix B .....	152
The code to generate the macroscale fiber model with 20 ‘pie-slice’ subdivisions in ANSYS SpaceClaim.....	153
The code used to assign material properties to the appropriate section .....	164
C: Appendix C .....	169
The cumulative cross-validation metrics evaluated over the 500 shuffle-splits for the remaining kernel structures.....	170
Tables of the validation performance for each kernel evaluated .....	178
REFERENCES .....	180

## LIST OF TABLES

Table	Page
Table 2-1. Summary of various approaches used to measure or calculate properties of interphases.....	40
Table 2-2. Summary of experimental data from Vollenberg and Heikens <sup>79</sup> .....	46
Table 2-3. Lower and upper bounds sampled for each parameter. ....	48
Table 2-4. Sensitivity analysis of model features to data .....	57
Table 2-5. Estimated calibration parameters for the glass-polystyrene composite .....	66
Table 2-6. Comparison of the posterior estimates of the calibration parameters for purposes of cross-validation. <sup>††</sup> .....	67
Table 2-7. Inferred interphase modulus, thickness, slope, and intercept for the glass composites. <sup>††</sup> .....	69
Table 2-8. The inferred interphase modulus, thickness, slope, and intercept for the alumina composites. <sup>§§</sup> .....	69
Table 2-9. 95% Highest posterior density (HPD) credible interval for the posterior distribution of the slope parameter.....	72
Table 4-1. Comparison of cross-validation and validation performance for best-performing kernel .....	123

## LIST OF FIGURES

Figure	Page
Figure 1-1. Overview of research areas, showing the three subdisciplines (Model Development, Experimental Data, and Design of Experiments) that are integrated to produce a deeper understanding of composite material performance and characterization. ....	2
Figure 1-2. Schematic of asymptotic expansion homogenization of material properties. At the local scale $y$ , the heterogeneous material has a rapidly varying and periodic field of an arbitrary characteristic property $\varphi$ . This material can be represented at the global scale $x$ by an effective material with constant or slowly varying fields. The ratio of the length of a unit vector at the local scale to that at the global scale is described by $y = x/\varepsilon$ , where $\varepsilon$ is a small parameter. ....	22
Figure 1-3. An example representative volume element (right), generated in Digimat-FE is shown as a representation for a spherical silica reinforced epoxy matrix. Micrograph (left) from Wang et al. <sup>54</sup> .....	24
Figure 1-4. Outline of the dissertation, highlighting the application areas and overlap of the methods employed throughout each application.....	29
Figure 2-1. Visual depiction of the framework presented in Chapter 2 highlighting the finite element model, Gaussian process surrogate model, and the Bayesian Inference results. ....	32
Figure 2-2. Roadmap of the proposed framework to infer the effective interphase thickness and modulus from experimental measurements of a composite's elastic modulus.....	36
Figure 2-3. Schematic of radial density variations within the effective interphase. Adapted from Odegard et al. <sup>71</sup> .....	39
Figure 2-4. Experimental data of the elastic modulus for glass beads in polystyrene from Vollenberg and Heikens <sup>17</sup> highlighting the effects of particle size on the elastic modulus and the inability to account for this effect with simple analytical models like the Mori-Tanaka and the Voigt and Reuss Bounds. ....	42
Figure 2-5. Example RVEs of particulate composites reinforced with spherical particles containing an interphase undergoing periodic, a) uniaxial and b) shear	

deformations. The colored contours represent the Equivalent (von-mises) stress. The particles within the RVE are uniformly sized; however, their appearances may vary due to the irregularities resulting from the cutting process at the RVE boundary. ....	50
Figure 2-6. Mesh refinement study showing the convergence of the calculated elastic modulus as the number of elements is increased (reduced mesh size), compared to the increases in solve time. The dashed red line indicates the selected, optimal mesh size. ....	54
Figure 2-7. Statistical convergence of effective elastic moduli as the size of the RVE is expanded. Each data point is calculated as an average modulus of three randomly filled RVEs. Error bars indicate the standard deviation due to randomly drawn RVEs. The dashed red line indicates the selected, optimal number of inclusions in the RVE.....	55
Figure 2-8. Cross-validation of the GP using four random permutations of training and testing subsets. Linear fits of each split are plotted as solid lines. Slopes close to unity with y-intercepts of zero indicate a good ability of the GP to predict the true finite element observations. ....	59
Figure 2-9. One-dimensional slices from fully trained GP across the (a) filler volume fraction, (b) interphase modulus at zero thickness, (c) interphase modulus at non-zero thickness, (d) relative thickness of interphase. Results validate expected physical behavior is predicted. Values in the legend represent the fixed, constant values assigned to the variables. ....	61
Figure 2-10. Two-dimensional slices at various fixed volume fractions, illustrating the effects of the two calibration parameters on the overall effective elastic modulus. The heat map indicates the confidence intervals estimated from the posterior distribution at a given set of inputs. ....	62
Figure 2-11. Approximate posterior distributions of the interphase modulus and absolute thickness for each particle size for the glass-polystyrene composite. ....	65
Figure 2-12. Approximate posterior distributions for the slope and intercept parameters for absolute thickness as a function of particle size for the glass-polystyrene composite. ....	65
Figure 2-13. The Gaussian process discrepancy functions as a function of volume fraction with 95% confidence bands.....	67



Figure 2-14. Comparison of the calibrated and experimental results for the glass-polystyrene composite. Continuous curves are from the GP, sliced across the filler volume fraction with fixed values of the calibrated interphase thickness and modulus. The markers indicate experimental measurements. ....	73
Figure 3-1. Representation of the preparation of CNCs via acid hydrolysis. ....	77
Figure 3-2. Schematic representation idealizing the helical morphology of the CNC calcium alginate fiber. Figure taken from Urena-Benavides and Kitchens <sup>59</sup> .....	78
Figure 3-3. Definition of theta and phi, which characterize the fixed alignment vector of the inclusions. ....	80
Figure 3-4. Material properties assigned to the matrix and filler, along with the bounds specified by the design of experiments. ....	81
Figure 3-5. Mapping of the microscale RVE to the global macroscale fiber model. ....	82
Figure 3-6. Example microscale RVE of perfectly aligned CNCs in the fiber direction undergoing one of six loading conditions (uniaxial loading in the z-direction) used to evaluate the effective or homogenized elastic stiffness matrix. The colored contours represent the accumulation of von-Mises stress as the RVE is loaded. The three plots on the left side show the matrix and filler for a single RVE at the beginning, middle, and end of the loading while those on the right have the matrix material hidden from view. ....	84
Figure 3-7. Gaussian process surrogate predictions for the elastic modulus in the z-direction ( $E_z$ ) as a function of the CNC spiral angle and circumferential position, $\theta$ and $\varphi$ , respectively. The volume fraction of filler was fixed at 0.25. Curves represent the GP posterior mean, shaded regions represent 95% confidence intervals, and the markers represent the underlying training data from the micro-level RVE. ....	85
Figure 3-8. Gaussian process surrogate predictions for the elastic modulus in the z-direction ( $E_z$ ) as a function of the CNC spiral angle and volume fraction, $\theta$ and $V_f$ , respectively. The circumferential position, $\varphi$ , was fixed at zero degrees. The surface plot represents the GP posterior mean, the heat map represents 95% confidence intervals, and the markers represent the underlying training data (shown for all values of $\varphi = 0 - 360^\circ$ ) from the micro-level RVE. ....	86
Figure 3-9. Validation of the FE model by comparing the $E_z$ from analytically computed rotations of a stiffness tensor (at a fixed $V_f$ ) to the $E_z$ predicted at equivalent	

values of $\theta$ and $\varphi$ by the finite element model. Similar values and trends indicate good agreement.....	87
Figure 3-10. The macroscale fiber model undergoing uniaxial loading in the z-direction mapped with helical symmetry of the stiffness tensor which was calculated from the microscale FE model. The colored contours represent the accumulation of von-mises stress as the RVE is loaded. The three plots show matrix and filler stresses that accumulate during the beginning, middle, and end of the loading..	88
Figure 4-1. Model input features, output targets, and a summary of the various compound kernel combinations evaluated.....	104
Figure 4-2. Flowchart of the methodology used for cross-validation.....	107
Figure 4-3. Flowchart of the methodology used for model validation. ....	110
Figure 4-4. The first three shuffle-split iterations of cross-validation where the true value is plotted against the predicted value. The $y = x$ line denotes a perfect prediction. Each row of graphs contains one iteration corresponding to one random configuration of test-train data. Each column of graphs corresponds to an output variable, from left to right: flexural strength, modulus of elasticity, brittleness index, lateral nail resistance, specific flexural strength, specific lateral nail resistance, and the specific lateral nail resistance normalized by thickness. Error bars denote 95% confidence intervals about the mean. ....	112
Figure 4-5. The cross-validation performance metrics for the sum + product kernel defined as $k = kSE - ARDcat + kSE - ARDnum + kSE - ARDcat * kSE - ARDnum$ calculated as a cumulative average at each iteration.....	114
Figure 4-6. Cross-validation performance of flexural (and specific) strength for each kernel averaged over 500 shuffle-split iterations arranged from left to right by decreasing $R^2$ . ....	116
Figure 4-7. Cross-validation performance of modulus of elasticity and brittleness index for each kernel averaged over 500 shuffle-split iterations arranged from left to right by decreasing $R^2$ .....	116
Figure 4-8. Cross-validation performance of lateral nail resistance, specific lateral nail resistance, and specific lateral nail resistance / thickness for each kernel averaged over 500 shuffle-split iterations arranged from left to right by decreasing $R^2$ . ..	117

Figure 4-9. Automatic relevance determination (ARD) plots for the most complex kernel evaluated. The relevance of each input dimension is proportional to the inverse of its characteristic length scale. The ARD plot is given as an example and corresponds to the kernel trained on the Specific Lateral Nail Resistance / Thickness. ....	119
Figure 4-10. Validation performance of flexural (and specific) strength for each kernel averaged over 10 shuffle-split iterations arranged from left to right by decreasing $R^2$ .....	121
Figure 4-11. Validation performance of modulus of elasticity and brittleness index for each kernel averaged over 10 shuffle-split iterations arranged from left to right by decreasing $R^2$ . ....	121
Figure 4-12. Validation performance of lateral nail resistance, specific lateral nail resistance, and specific lateral nail resistance / thickness for each kernel averaged over 10 shuffle-split iterations arranged from left to right by decreasing $R^2$ . ....	122
Figure 4-13. One-dimensional slices of Flexural Strength for Formula A (top) and Formula B (bottom). Fixed parameters are held at median values. ....	125
Figure 4-14. One-dimensional slices of Spc. Flexural Strength for Formula A (top) and Formula B (bottom). Fixed parameters are held at median values. ....	126
Figure 4-15. One-dimensional slices of Modulus for Formula A (top) and Formula B (bottom). Fixed parameters are held at median values. ....	127
Figure 4-16. One-dimensional slices of Brittleness Index for Formula A (top) and Formula B (bottom). Fixed parameters are held at median values. ....	128
Figure 4-17. One-dimensional slices of Lateral Nail Resistance for Formula A (top) and Formula B (bottom). Fixed parameters are held at median values. ....	129
Figure 4-18. One-dimensional slices of Spc. Lateral Nail Resistance for Formula A (top) and Formula B (bottom). Fixed parameters are held at median values. ....	130
Figure 4-19. One-dimensional slices of Spc. Lateral Nail Resistance/Thickness for Formula A (top) and Formula B (bottom). Fixed parameters are held at median values. ....	131
Figure 5-1. Illustration of the Pareto front, for a multi-objective optimization problem. ....	137

# CHAPTER 1

## INTRODUCTION AND BACKGROUND

### 1.1 Introduction

*Broader Motivation - An Integrated Approach to Material Innovation and Engineering Design*

Recent initiatives have identified emerging disciplines, such as Integrated Computational Materials Engineering (ICME), which advocate for a promising paradigm where “computational materials science tools [are integrated] into a holistic system that can accelerate materials development, transform the engineering design optimization process, and unify design and manufacturing.”<sup>1</sup> A significant component of ICME requires the quantification of uncertainty introduced at each level of the developed predictive models and simulations. Similar goals are echoed in the Materials Genome Initiative, with the objective “to accelerate the discovery, design, development, and deployment of new materials, at a fraction of the cost, by harnessing the power of data and computational tools in concert with experiment.”<sup>2</sup> These objectives undergird the motivation of this dissertation.

While realizing such objectives is in its infancy and will require ongoing multi-disciplinary research, this dissertation develops methods in pursuit of these goals. This work systematically explores how advanced numerical techniques and computational tools can be utilized in combination with experimental data to unravel the complex relationships in composite materials and structures across different length scales. Figure

1-1 depicts the subdomains this research encompasses to address the ongoing challenges.

The presented work expands on traditional modeling approaches by developing high-fidelity, physics-based, and data-driven multiscale models for composite materials to include uncertainty quantification while significantly reducing the financial and labor costs associated with experimentally determining composite properties. The results demonstrate an improved framework for accelerating the design and development of high-performance composite materials.

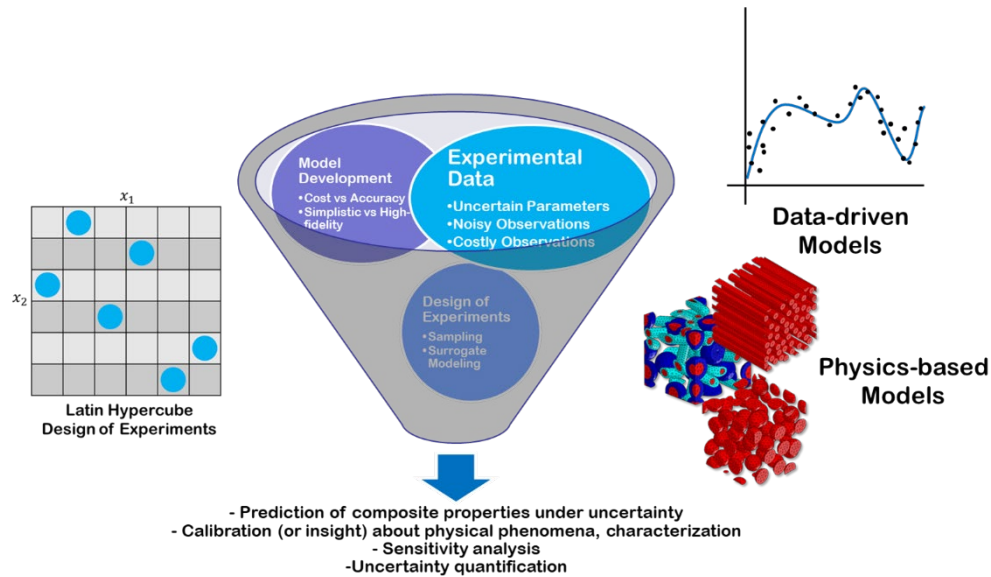


Figure 1-1. Overview of research areas, showing the three subdisciplines (Model Development, Experimental Data, and Design of Experiments) that are integrated to produce a deeper understanding of composite material performance and characterization.

## **1.2 Theoretical Background**

### ***1.2.1 Composite Materials***

Composite materials are a subclass of engineered materials that combine the properties of two or more different constituents to produce enhanced functional attributes. The constituents usually consist of a matrix phase and a filler or reinforcement phase(s), each giving the composite system unique mechanical, electrical, thermal, or chemical properties. The choice of constituent materials and their arrangement within the matrix are crucial in tailoring the final properties of composites.

The advancement of composite materials is recognized for its transformative potential across a broad spectrum of industries. The inherent advantages come from the ability to craft materials with unique properties derived from combinations of constituent materials. Such a task is achieved by strategically selecting and integrating the constituent phases of the composite. However, the final performance of a composite material is more complex than an additive composition of the constituent phase properties. A comprehensive understanding of the behavior of composite materials necessitates bridging the gap between multiple length scales spanning from the atomic to the micro and macro scales.

#### ***Shortcomings of Traditional Modeling Approaches***

Historically, micromechanics has been the primary field for predicting how individual phases interact to influence a composite's overall properties. Early pioneers relied on simplistic theoretical models that, while providing foundational knowledge, fell

short of accurately predicting composite behavior under complex and realistic conditions. Matrix and filler properties are typically known with a high degree of certainty and can often be measured experimentally. Initiatives to organize these properties into large databases are underway.<sup>3-6</sup> However, the combination of these properties and their contributions to the overall composite properties is not straightforward. Furthermore, the presence of a three-dimensional interphase, which can form at the two-dimensional interface between the constituent phases, significantly complicates matters.<sup>7-16</sup>

The interphase mediates load transfer and stress distribution between the filler and the matrix, a mechanism that distinguishes composites from homogeneous materials.<sup>17</sup> Interphase properties, such as the layer thickness and stiffness, are largely unknown, difficult to predict *a priori*, and introduce additional complexities and variations in mechanical behavior that simplistic models cannot adequately capture. As a result, predicting composite performance necessitates a consideration of the interphase properties and subsequent interactions with the adjacent phases. Sophisticated modeling techniques and experimental methodologies are required to account for these intricate interfacial effects. The investigation of interphase-related phenomena remains an active and challenging area of research.

Classical predictive models provide point estimates of composite properties based on knowledge of subcomponent attributes. These models often fail to incorporate uncertainty in the subcomponent attributes and uncertainty about how these attributes combine to result in a new material with unique properties. If interphase formation is

present, additional uncertainty is introduced into model predictions. Quantifying these uncertainties is crucial for optimizing the performance of composite materials and providing safe estimates about performance in the final engineered structure. The rise of high-performance computing and numerical methods has presented an opportunity to go beyond these traditional models, culminating in the development of detailed simulators capable of predicting complex and multiscale phenomena.

### ***1.2.2 Mechanics of Composites***

This section reviews the fundamental principles in continuum mechanics relevant to this work.

#### *1.2.2.1 Strain, Stress, and Equilibrium Criteria*

##### *Strain*

Strain is a measure of deformation representing the displacement between particles in a material body. Two types of strain are defined for small deformations: normal and shear. The normal strain measures the change in length of a small line element, and can be defined mathematically as the change in length divided by the original length. In the limit, as the change in length approaches zero, the strain is given by:

$$\epsilon = \lim_{\Delta l \rightarrow 0} \frac{\Delta l}{l} \quad (1)$$

For a three-dimensional problem with  $u$ ,  $v$ , and  $w$  as the displacements in the  $x$ ,  $y$ , and  $z$  directions, the normal strains can be defined as:



$$\begin{aligned}
\epsilon_{xx} &= \frac{\partial u}{\partial x} \\
\epsilon_{yy} &= \frac{\partial v}{\partial y} \\
\epsilon_{zz} &= \frac{\partial w}{\partial z}
\end{aligned} \tag{2}$$

The shear strain measures the change in angle between initially perpendicular line elements of a material body. By taking into account strain symmetries in three dimensions, the engineering shear strains can be computed as follows:

$$\begin{aligned}
\gamma_{xy} &= \frac{\partial u}{\partial y} + \frac{\partial v}{\partial x} = \gamma_{yx} \\
\gamma_{yz} &= \frac{\partial v}{\partial z} + \frac{\partial w}{\partial y} = \gamma_{zy} \\
\gamma_{zx} &= \frac{\partial w}{\partial x} + \frac{\partial u}{\partial z} = \gamma_{xz}
\end{aligned}$$

### *Stress*

Stress measures the internal forces in a material and is defined as the force exerted per unit area within materials. If  $\sigma$  represents the stress,  $F$  the force, and  $A$  the area over which the force is applied, the stress is given by:

$$\sigma = \frac{F}{A} \tag{3}$$

Stress, like strain, is a second-order tensor in three-dimensional space and can thus be specified with nine components where  $i, j = 1, 2, 3$  correspond to  $(1 \rightarrow x, 2 \rightarrow y, 3 \rightarrow z)$ . It is often represented in matrix form as:

$$\sigma_{ij} = \begin{bmatrix} \sigma_{11} & \sigma_{12} & \sigma_{13} \\ \sigma_{21} & \sigma_{22} & \sigma_{23} \\ \sigma_{31} & \sigma_{32} & \sigma_{33} \end{bmatrix} \quad (4)$$

The diagonal components are normal stresses (forces per unit area acting perpendicular to the faces of the element), and the off-diagonal terms are shear stresses (forces per unit area acting parallel to the faces).

#### *Equilibrium Conditions*

For a three-dimensional differential material element to be in equilibrium, the sum of all the forces in each orthogonal direction must equal zero ( $F = ma$ , where  $a = 0$ ). If  $B_i$  represents the body forces in the  $i$ -th direction acting on the volume of the body (gravity, electric, and magnetic fields), the equilibrium conditions can be expressed as:

$$\begin{aligned} \frac{\partial \sigma_{xx}}{\partial x} + \frac{\partial \sigma_{xy}}{\partial y} + \frac{\partial \sigma_{xz}}{\partial z} + B_x &= 0 \\ \frac{\partial \sigma_{yx}}{\partial x} + \frac{\partial \sigma_{yy}}{\partial y} + \frac{\partial \sigma_{yz}}{\partial z} + B_y &= 0 \\ \frac{\partial \sigma_{zx}}{\partial x} + \frac{\partial \sigma_{zy}}{\partial y} + \frac{\partial \sigma_{zz}}{\partial z} + B_z &= 0 \end{aligned} \quad (5)$$

#### *1.2.2.2 Linear Constitutive Relationships*

Hooke's Law is just one of many constitutive relationships used to describe solid-state mechanical behavior. While this is a fundamental relationship for linearly elastic materials within their elastic limit, it may not accurately represent the behavior of more complex materials. In material mechanics, linear behavior refers to the property of a

material to exhibit a linear relationship between the applied force (or stress) and the resulting deformation (or strain). When a material displays linear behavior (typically at small strains), Hooke's Law becomes applicable, and the deformation produced in the material is directly proportional to the applied force within its elastic limit. Other constitutive relationships address different material properties and deformation scenarios. Non-linear elasticity models, for example, are used to describe the behavior of materials that exhibit non-linear elastic behavior, whereas plasticity models describe the behavior of materials under plastic deformation. Viscoelastic materials necessitate specialized constitutive relationships that consider both elastic and viscous behavior. As a result, the constitutive relationship chosen depends on the specific material, its properties, and the range of loading conditions it will encounter during applications.

In linear elasticity theory, Hooke's law describes a constitutive relationship that maps strain fields in a pure material,  $\epsilon$ , to stress fields,  $\sigma$ . Hooke's law in a three-dimensional space can be expressed in index notation as  $\sigma_{ij} = C_{ijkl}\epsilon_{ij}$ . The stiffness tensor,  $C_{ijkl}$ , is a fourth-rank tensor whose elements describe the proportional changes to a (bounded and self-equilibrated) material stress field for a respective strain field. In continuum mechanics, the second-rank Cauchy stress and strain tensors completely define a material's stress and strain states and can be expressed as a matrix. Due to stress and strain symmetries that exist in an orthonormal coordinate system ( $e_1, e_2, e_3$ ) corresponding to (1→x, 2→y, 3→z), the matrices are commonly reduced in rank to column-vectors using Voigt notation.<sup>18</sup>

$$\sigma_{ij} = \begin{bmatrix} \sigma_{11} & \sigma_{12} & \sigma_{13} \\ \sigma_{21} & \sigma_{22} & \sigma_{23} \\ \sigma_{31} & \sigma_{32} & \sigma_{33} \end{bmatrix} \xrightarrow{Voigt} [\sigma] = \begin{bmatrix} \sigma_{11} \\ \sigma_{22} \\ \sigma_{33} \\ \sigma_{23} \\ \sigma_{13} \\ \sigma_{12} \end{bmatrix} = \begin{bmatrix} \sigma_1 \\ \sigma_2 \\ \sigma_3 \\ \sigma_4 \\ \sigma_5 \\ \sigma_6 \end{bmatrix} \quad \epsilon_{ij} = \begin{bmatrix} \epsilon_{11} & \epsilon_{12} & \epsilon_{13} \\ \epsilon_{21} & \epsilon_{22} & \epsilon_{23} \\ \epsilon_{31} & \epsilon_{32} & \epsilon_{33} \end{bmatrix} \xrightarrow{Voigt} [\epsilon] = \begin{bmatrix} \epsilon_{11} \\ \epsilon_{22} \\ \epsilon_{33} \\ 2\epsilon_{23} \\ 2\epsilon_{13} \\ 2\epsilon_{12} \end{bmatrix} = \begin{bmatrix} \epsilon_1 \\ \epsilon_2 \\ \epsilon_3 \\ \epsilon_4 \\ \epsilon_5 \\ \epsilon_6 \end{bmatrix} \quad (6)$$

Thus, the generalized Hooke's law can be expressed in matrix form as:

$$\begin{bmatrix} \sigma_1 \\ \sigma_2 \\ \sigma_3 \\ \sigma_4 \\ \sigma_5 \\ \sigma_6 \end{bmatrix} = \begin{bmatrix} C_{11} & C_{12} & C_{13} & C_{14} & C_{15} & C_{16} \\ C_{21} & C_{22} & C_{23} & C_{24} & C_{25} & C_{26} \\ C_{31} & C_{32} & C_{33} & C_{34} & C_{35} & C_{36} \\ C_{41} & C_{42} & C_{43} & C_{44} & C_{45} & C_{46} \\ C_{51} & C_{52} & C_{53} & C_{54} & C_{55} & C_{56} \\ C_{61} & C_{62} & C_{63} & C_{64} & C_{65} & C_{66} \end{bmatrix} \begin{bmatrix} \epsilon_1 \\ \epsilon_2 \\ \epsilon_3 \\ \epsilon_4 \\ \epsilon_5 \\ \epsilon_6 \end{bmatrix} \quad (7)$$

where the elements,  $C_{ij}$ , represent the 'elastic constants' of an infinitesimally small, homogeneous material volume. Note - The factor of two in front of the shear strain components (where  $i \neq j$ ) indicates  $2\epsilon_{ij} = \gamma_{ij}$ , where  $\gamma_{ij}$  represents the engineering shear strains and  $\epsilon_{ij}$  represents the tensor shear strains. Caution and consistency must be used when interfacing with various software environments that define  $\epsilon$  differently. For example, ANSYS Mechanical APDL uses  $\epsilon$  (output as EPEL) to represent the *engineering* shear strains for the simplicity of output.<sup>19</sup> The same care must be taken to ensure the relative ordering of the shear stresses with strains is consistent,  $[\sigma_{yz} \rightarrow \sigma_{xz} \rightarrow \sigma_{xy}]$  with  $[\epsilon_{yz} \rightarrow \epsilon_{xz} \rightarrow \epsilon_{xy}]$ , as well as the ordering of  $\sigma$  and  $\epsilon$  with the reported structure of the stiffness matrix.

The inverse relationship of Hooke's law describes strains resulting from a stress state with proportionality defined by the compliance tensor,  $S_{ijkl}$ . The inverse of the

stiffness matrix is the compliance matrix, with  $[S] = [C]^{-1}$ . Similarly, the constitutive relationship is represented in matrix form.

$$\begin{bmatrix} \epsilon_1 \\ \epsilon_2 \\ \epsilon_3 \\ \epsilon_4 \\ \epsilon_5 \\ \epsilon_6 \end{bmatrix} = \begin{bmatrix} S_{11} & S_{12} & S_{13} & S_{14} & S_{15} & S_{16} \\ S_{21} & S_{22} & S_{23} & S_{24} & S_{25} & S_{26} \\ S_{31} & S_{32} & S_{33} & S_{34} & S_{35} & S_{36} \\ S_{41} & S_{42} & S_{43} & S_{44} & S_{45} & S_{46} \\ S_{51} & S_{52} & S_{53} & S_{54} & S_{55} & S_{56} \\ S_{61} & S_{62} & S_{63} & S_{64} & S_{65} & S_{66} \end{bmatrix} \begin{bmatrix} \sigma_1 \\ \sigma_2 \\ \sigma_3 \\ \sigma_4 \\ \sigma_5 \\ \sigma_6 \end{bmatrix} \quad (8)$$

### 1.2.2.3 Stiffness Tensor Symmetries

The stiffness tensor of a Hookean material has 81 independent elements; however, stress and strain symmetries reduce this number to 36 unique entries. Major symmetries from the strain energy function reduce the compliance,  $S_{ijkl}$ , and stiffness matrices to 21 independent elastic constants and requires that  $C_{ij} = C_{ji}$  and  $S_{ij} = S_{ji}$ . A material with these symmetries and physical properties that vary depending on the measurement axes is called an anisotropic material. Further reductions in the number of independent constants can be made if the material exhibits planes of symmetry. For a generally anisotropic material:

$$\begin{aligned}
C_{ijkl} &= \begin{bmatrix} C_{11} & C_{12} & C_{13} & C_{14} & C_{15} & C_{16} \\ & C_{22} & C_{23} & C_{24} & C_{25} & C_{26} \\ & & C_{33} & C_{34} & C_{35} & C_{36} \\ & & & C_{44} & C_{45} & C_{46} \\ & sym. & & & C_{55} & C_{56} \\ & & & & & C_{66} \end{bmatrix} \\
S_{ijkl} &= \begin{bmatrix} S_{11} & S_{12} & S_{13} & S_{14} & S_{15} & S_{16} \\ & S_{22} & S_{23} & S_{24} & S_{25} & S_{26} \\ & & S_{33} & S_{34} & S_{35} & S_{36} \\ & & & S_{44} & S_{45} & S_{46} \\ & sym. & & & S_{55} & S_{56} \\ & & & & & S_{66} \end{bmatrix}
\end{aligned} \tag{9}$$

Orthotropic materials have three planes of symmetry perpendicular to each other. These planes are defined by the principal material axes:  $x$ ,  $y$ , and  $z$ . Along these planes, the material properties remain the same, and this leads to specific relationships between the material constants, resulting in nine independent elastic constants. In orthotropic materials, there is no coupling between the normal stresses ( $\sigma_1, \sigma_2, \sigma_3$ ) and the shear strains ( $\epsilon_4, \epsilon_5, \epsilon_6$ ). Hooke's Law in compliance form for an orthotropic material, expressed in terms of meaningful engineering constants, is:

$$\begin{bmatrix} \epsilon_1 \\ \epsilon_2 \\ \epsilon_3 \\ \epsilon_4 \\ \epsilon_5 \\ \epsilon_6 \end{bmatrix} = \begin{bmatrix} \frac{1}{E_1} & -\frac{\nu_{21}}{E_2} & -\frac{\nu_{31}}{E_3} & 0 & 0 & 0 \\ -\frac{\nu_{12}}{E_1} & \frac{1}{E_2} & -\frac{\nu_{32}}{E_3} & 0 & 0 & 0 \\ -\frac{\nu_{13}}{E_1} & -\frac{\nu_{23}}{E_2} & \frac{1}{E_3} & 0 & 0 & 0 \\ 0 & 0 & 0 & \frac{1}{2G_{23}} & 0 & 0 \\ 0 & 0 & 0 & 0 & \frac{1}{2G_{13}} & 0 \\ 0 & 0 & 0 & 0 & 0 & \frac{1}{2G_{12}} \end{bmatrix} \begin{bmatrix} \sigma_1 \\ \sigma_2 \\ \sigma_3 \\ \sigma_4 \\ \sigma_5 \\ \sigma_6 \end{bmatrix} \tag{10}$$

where  $(E_1, E_2, E_3)$  are the Young's or elastic moduli in the  $x$ ,  $y$ , and  $z$  directions, respectively, and  $(\nu_{12}, \nu_{13}, \nu_{21}, \nu_{23}, \nu_{31}, \nu_{32})$  are the Poisson's ratios.  $(G_{23}, G_{13}, G_{12})$  are the shear moduli.

An isotropic material possesses an infinite number of planes of symmetry, which means it exhibits the same properties and behavior in all directions. A material with these symmetries can be expressed in terms of just two independent elastic components, and the corresponding form of Hooke's law is:

$$\begin{bmatrix} \varepsilon_1 \\ \varepsilon_2 \\ \varepsilon_3 \\ \varepsilon_4 \\ \varepsilon_5 \\ \varepsilon_6 \end{bmatrix} = \begin{bmatrix} \frac{1}{E} & -\frac{\nu}{E} & -\frac{\nu}{E} & 0 & 0 & 0 \\ -\frac{\nu}{E} & \frac{1}{E} & -\frac{\nu}{E} & 0 & 0 & 0 \\ -\frac{\nu}{E} & -\frac{\nu}{E} & \frac{1}{E} & 0 & 0 & 0 \\ 0 & 0 & 0 & \frac{1}{2G} & 0 & 0 \\ 0 & 0 & 0 & 0 & \frac{1}{2G} & 0 \\ 0 & 0 & 0 & 0 & 0 & \frac{1}{2G} \end{bmatrix} \begin{bmatrix} \sigma_1 \\ \sigma_2 \\ \sigma_3 \\ \sigma_4 \\ \sigma_5 \\ \sigma_6 \end{bmatrix} \quad (11)$$

where the shear modulus is expressed in terms of the elastic modulus and Poisson's ratio with  $G = \frac{E}{2(1+\nu)}$ .

#### 1.2.2.4 Hooke's Law in Expanded - Algebraic Form

The components of stress can be calculated as linear combinations of the components of strain by expanding Hooke's law, in matrix notation, into a system of linear equations:

$$\begin{aligned} \sigma_{11} &= C_{11}\varepsilon_{11} + C_{12}\varepsilon_{22} + C_{13}\varepsilon_{33} + 2C_{14}\varepsilon_{23} + 2C_{15}\varepsilon_{13} + 2C_{16}\varepsilon_{12} \\ \sigma_{22} &= C_{21}\varepsilon_{11} + C_{22}\varepsilon_{22} + C_{23}\varepsilon_{33} + 2C_{24}\varepsilon_{23} + 2C_{25}\varepsilon_{13} + 2C_{26}\varepsilon_{12} \\ \sigma_{33} &= C_{31}\varepsilon_{11} + C_{32}\varepsilon_{22} + C_{33}\varepsilon_{33} + 2C_{34}\varepsilon_{23} + 2C_{35}\varepsilon_{13} + 2C_{36}\varepsilon_{12} \\ \sigma_{23} &= C_{41}\varepsilon_{11} + C_{42}\varepsilon_{22} + C_{43}\varepsilon_{33} + 2C_{44}\varepsilon_{23} + 2C_{45}\varepsilon_{13} + 2C_{46}\varepsilon_{12} \\ \sigma_{13} &= C_{51}\varepsilon_{11} + C_{52}\varepsilon_{22} + C_{53}\varepsilon_{33} + 2C_{54}\varepsilon_{23} + 2C_{55}\varepsilon_{13} + 2C_{56}\varepsilon_{12} \\ \sigma_{12} &= C_{61}\varepsilon_{11} + C_{62}\varepsilon_{22} + C_{63}\varepsilon_{33} + 2C_{64}\varepsilon_{23} + 2C_{65}\varepsilon_{13} + 2C_{66}\varepsilon_{12} \end{aligned} \quad (12)$$

The six equations contain a total of 36 elastic constants. Of course, from the symmetry in Equation (7), the equations for an anisotropic material could be expressed in terms of 21 independent elastic constants, with  $C_{ij} = C_{ji}$ . The determination of a materials stiffness matrix is possible through tedious experimental deformations and simultaneous

measurements of stress. As the number of independent elastic constants grows, the number and complexity of the required experiments grow.

### ***1.2.3 Analytical and Semi-Analytical Models***

The effective properties of composite materials can be predicted by analytical and semi-analytical models. While these models have the advantage of computational efficiency, simplicity, and interpretability, they rely on oversimplified assumptions about the nature of the microstructure and thus are only applicable over narrow classes of composites. A non-exhaustive survey of several different models is presented below. For a more extensive resource, see Ortolano et al.<sup>20</sup>. The basic steps to analytically computing effective properties involve 1) developing a simplified model, 2) exploiting fundamental continuum mechanics principles, and 3) estimating the local fields with a heterogeneous material in terms of known boundary conditions.<sup>21</sup>

#### ***1.2.3.1 Voigt and Reuss Bounds***

The Voigt upper bound (also known as the Rule of Mixtures) assumes that the strain is uniform throughout the composite, referred to as an iso-strain condition.<sup>22</sup> This assumption corresponds to a perfectly bonded material where the different phases deform identically when the composite is loaded. The effective elastic modulus  $E_{\text{eff}}^V$  in Voigt's model is given by the volume fraction weighted sum of the individual phase moduli, represented as:

$$E_{\text{eff}}^V = \sum_i^n f_i E_i, \quad (13)$$



where  $f_i$  is the volume fraction and  $E_i$  is the modulus of the  $i$ -th phase. It is ideal for modeling the axial properties of unidirectional composites in which the fibers (the rigid phase) are long and continuous, and the matrix (the soft phase) deforms to match the strain in the fibers. The Voigt model tends to exaggerate the properties of composites with discontinuous or randomly oriented particulate phases.

The Reuss lower bound (also known as the Inverse Rule of Mixtures) assumes an iso-stress condition, where the stress is uniform throughout the composite.<sup>23</sup> In this model, the material phases are considered perfectly bonded, such that they all bear the same load. The effective modulus  $E_{\text{eff}}^R$  in Reuss's model is calculated using a simple harmonic mean as follows:

$$E_{\text{eff}}^R = \left( \sum_i^n \frac{f_i}{E_i} \right)^{-1}. \quad (14)$$

The Reuss model is commonly used to approximate the transverse properties of a unidirectional composite. In this case, the matrix, which is often continuous in the transverse direction, carries a significant portion of the load, and the bulk material behaves as if it were under the same stress as the matrix.

Despite their simplicity, these models serve as the foundation for more complex models of composite behavior and provide theoretical bounds of plausible values for effective composite properties.

### 1.2.3.2 Eshelby's Equivalent Inclusion Model

John D. Eshelby's solution of the elastic fields of an ellipsoidal inclusion embedded in an infinite medium provided the foundation for many micromechanical models and marked a pivotal development in the field.<sup>24</sup> The resulting model is generally referred to as Eshelby's equivalent inclusion model and was derived from the solutions to two problems. The model is based on several assumptions, including linear elasticity, isotropy, and the absence of inclusion-inclusion interactions, which limits the applications to dilute regimes.

Problem 1: Eshelby imagined an infinite material body with uniform isotropic elastic properties. A portion of the body (an inclusion) undergoes a transformation called an eigenstrain. An eigenstrain is defined as a strain that produces a change in size and/or shape, such that if the surrounding matrix material were absent, the resulting state would be that of a homogenous strain. The restraint of deformation by the surrounding matrix produces a stressed state inside the inclusion. Through a series of imaginary cutting, straining, and welding operations, and by assuming the shape of the inclusion is ellipsoidal, Eshelby found that the stress inside the inclusion was uniform. The uniform strain in the inclusion  $\epsilon_{ij}^*$  is related to the stress-free strain  $\epsilon_{kl}^{(0)}$  through Eshelby's tensor  $S_{ijkl}$ .<sup>20</sup>

$$\epsilon_{ij}^* = S_{ijkl} \epsilon_{kl}^{(0)} \quad (15)$$

Problem 2: Applying the concepts from Problem 1 to an inhomogeneity, where the ellipsoidal inclusion has elastic constants different from the matrix, Eshelby derived

closed-form solutions for the elastic stress and strain fields inside and outside the inclusion in terms of  $S_{ijkl}$ . Eshelby's tensor only depends on the matrix elastic properties and the relationship between the major and minor axis of the ellipsoid.<sup>20</sup> Analytical expressions for the components of Eshelby's tensor for simple geometries (sphere, elliptic cylinder, penny shape, flat ellipsoid, oblate spheroid, prolate spheroid) are provided in Mura.<sup>25</sup>

### 1.2.3.3 Mori-Tanaka Model

The Mori-Tanaka model is an analytical homogenization model used to estimate the effective properties of composite materials. The model is an extension of Eshelby's equivalent inclusion method with additional assumptions that account for the interaction between multiple inclusions. Benveniste<sup>26</sup> reformulated the model presented by Mori and Tanaka<sup>27</sup> to provide a direct approach to compute effective elastic moduli. The effective elastic properties, represented by the fourth-order stiffness tensor,  $\mathbf{C}$  are calculated by:<sup>28</sup>

$$\mathbf{C} = (\mathbf{V}_m \mathbf{C}_m + \mathbf{V}_f \mathbf{C}_f \mathbf{A})(\mathbf{V}_m \mathbf{I} + \mathbf{V}_f \langle \mathbf{A} \rangle)^{-1} \quad (16)$$

where  $\mathbf{I}$  is the fourth-order tensor identity tensor,  $\mathbf{C}_f$  and  $\mathbf{C}_m$  are the fourth-order stiffness tensors for the fiber and matrix materials, and the Eshelby strain-concentration tensor  $\mathbf{A}$  is given in terms of the Eshelby's tensor  $\mathbf{S}$ :

$$\mathbf{A} = [\mathbf{I} + \mathbf{S}(\mathbf{C}_m)^{-1}(\mathbf{C}_f - \mathbf{C}_m)]^{-1} \quad (17)$$

#### 1.2.3.4 The Kerner Equation

The Kerner equation provides a solution for the shear modulus  $G_c$  of a composite consisting of a suspension of grains.<sup>29</sup> The grains are assumed to be spherical, perfectly bonded to the matrix material, and distributed spatially at random. The model expresses the shear modulus in terms of the matrix shear modulus,  $G_m$ , particle and matrix volume fractions,  $V_p$  and  $V_p$  respectively, and the Poisson's ratio of the matrix  $\nu_m$ . If the shear modulus of the grain exceeds that of the matrix, the composite shear modulus can be approximated in the following manner.<sup>30</sup>

$$G_c = G_m \left( 1 + \frac{V_p}{V_m} \frac{15(1 - \nu_m)}{8 - 10\nu_m} \right) \quad (18)$$

#### 1.2.3.5 The Cox Shear Lag Model

The model proposed by Cox,<sup>31</sup> often known as the Cox shear lag model, assumes a microstructure of aligned discontinuous fibers, where the load is transferred from the matrix to the fiber by shear stress along the fiber surface. The fibers carry the tensile stresses and are not transmitted at the axial ends as normal stresses.<sup>30,32</sup> If the axial composite strain  $\epsilon_c$  is assumed to generate an average stress in the matrix with proportionality defined by the matrix modulus  $E_m$ , the longitudinal (fiber-aligned direction) composite elastic modulus for high aspect ratio fibers can be calculated as:

$$E_c = E_m(1 - V_f) + E_f V_f \left( 1 - \frac{\tanh z}{z} \right) \quad (19)$$

$$\text{where } z = \frac{l}{2r} \left( \frac{2G_m}{E_f \ln(R/r)} \right)^{1/2},$$

with  $l$  defining the length of the fibers,  $r$  the radius, and  $R$  half of the inter-fiber distance.

#### ***1.2.4 Finite Element-Based Homogenization of Composite Materials***

FE-based homogenization is an alternative numerical strategy for modeling and predicting composite effective properties and behavior.<sup>33–38</sup> FE methods are considerably more versatile in terms of composite geometries, number of phases, and types of constitutive models that can be simulated. This flexibility enables greater fidelity than analytical and semi-analytical micromechanical models while requiring significantly fewer computational resources than Molecular Dynamics (MD)-based methods.

Despite the computational capability provided by today's high-speed computers, analyzing boundary value problems involving materials with a large number of heterogeneities remains a difficult task. A practical solution to overcoming this barrier is to replace the heterogeneous composite with an equivalent material model in a process known as homogenization. Homogenization methods consider the development of constitutive laws that link physical quantities operating across different length scales.

The critical assumption is that the heterogeneous materials can be statistically classified as homogeneous (or as an ‘effective’ or ‘equivalent’ homogeneous material) at sufficiently large macroscopic length scales. For this assumption to hold, the macroscopic length scale of the composite engineered structure ( $\sim 10^0 - 10^2$  meters; i.e., wind turbine blade, automobile body, airplane wing) must be many orders of magnitude

larger than the characteristic length scale of the microstructure or heterogeneity inherent to the material ( $10^{-9} - 10^{-3}$  meters; i.e., matrix-filler interphase thickness, fiber diameter, lamina thickness).<sup>39,40</sup>

This section gives a brief introduction to the finite element method and reviews two different FE-based homogenization methods.

1. Asymptotic Expansion Homogenization Theory (Not to be confused with the broad terminology “homogenization,” which refers to the replacement of a heterogeneous composite with an equivalent material)
2. Standard Representative Volume Element Approach (The method used throughout this dissertation)

#### *1.2.4.1 Finite Element Analysis*

The finite element method (FEM) is a robust numerical method for solving complex engineering and physical science problems. It is a valuable tool for analyzing physical systems and effectively approximates elliptical partial differential equations over intricate geometries and domains. In 1956, Turner et al.<sup>41</sup> introduced one of the first applications of the finite element method in aeronautical engineering to model the wing skin using three-noded triangular elements.<sup>42</sup> Its applications have since expanded to include electromagnetics, fluid dynamics, and solid mechanics.

The concept underlying FEM is the subdivision of the domain of interest into a collection of smaller and simplified domains called finite elements. These elements are interconnected at nodes and collectively form a mesh over the original domain. The

system's constitutive behavior is approximated over these elements, resulting in a problem amenable to a computer solution. The precision of the FEM solution is highly dependent on the quality of the mesh and the suitability of the trial functions; therefore, verification and validation are essential components of any FEM analysis. Finite element analysis (FEA) is the application of FEM to a particular problem and includes the following general steps:<sup>33,34</sup>

1. Formulation of the Problem: The first step is mathematically formulating the physical problem. Typically, this entails identifying the domain of interest, defining the boundary and initial conditions, and formulating the governing differential equations.

2. Discretization: The continuous domain is subdivided into a finite number of smaller regions known as elements. The collection of these elements is called a mesh, and adjacent meshes intersect at nodes.

3. Trial (basis) Functions: A simple trial function within each element approximates the field variable (such as temperature in a heat transfer problem or displacement in a structural analysis problem). This function is typically a polynomial, and its form is determined by the field variable values at the element's nodes. The trial solution for the entire domain is the collection of these functions for all elements.

4. Formulating the System of Equations: A system of linear equations can be obtained by substituting the trial solution into the governing differential equation and applying the method of mean-weighted residuals (often the Galerkin method). Typically expressed in matrix form, this system is known as the global stiffness matrix equation.

5. Solve the System of Equations: The equations are then solved to determine the field variable's nodal values. For large models, iterative solvers like the Gauss-Seidel and the conjugate gradient methods are frequently employed.

6. Post-processing: Nodal solutions are used to compute field variables at any point within each element by interpolating with the element shape functions. Other quantities of interest, such as stresses in a structural problem, can then be computed from the field variable. Results are frequently represented graphically using contour plots, deformed shape plots, and vector fields.

#### *1.2.4.2 Asymptotic Expansion Homogenization Theory*

Asymptotic expansion homogenization (AEH) theories have been formalized and are rooted in applied mathematics.<sup>43</sup> The theory is not exclusive to predicting composite properties; it forms the basis of many scientific and engineering fields. Since materials are made up of atoms or molecules, the fundamental assumption of continuous media in mechanics and physics can be understood as homogenization. The mathematical theory of homogenization has applications in various fields that deal with finely heterogeneous media. The concept has been applied in heat transfer, fluid flow in porous media, and electromagnetism.<sup>40,44–46</sup>

As depicted in Figure 1-2, AEH is a method for representing effective material properties using a bifurcated analysis of a composite material at two distinct spatial scales: the microscopic or local scale ( $y$ ) where an arbitrary characteristic property  $\varphi$  varies rapidly and the macroscopic or global scale ( $x$ ) where the function varies slowly or



is constant.<sup>47</sup> The ratio of the length of a unit vector at the local scale to that at the global scale is described by  $y = x/\epsilon$ , where  $\epsilon$  is a small parameter. The quantity  $1/\epsilon$  is intuitively understood as a magnification factor that would scale characteristic inhomogeneity dimension to that of the engineered structure. The governing equations of the composite behavior are expanded in powers of the small parameter.

$$\phi(x) = \phi_0(x) + \epsilon\phi_1(x, x/\epsilon) + \epsilon^2\phi_2(x, x/\epsilon) + \dots$$

Hassani and Hinton<sup>48</sup> formulate the AEH method in a finite element framework and derive the elastic constants for an isotropic material with rectangular voids. Hollister and Kikuchi<sup>47</sup> compare finite element implementations of the AEH approach to the standard mechanics approach.

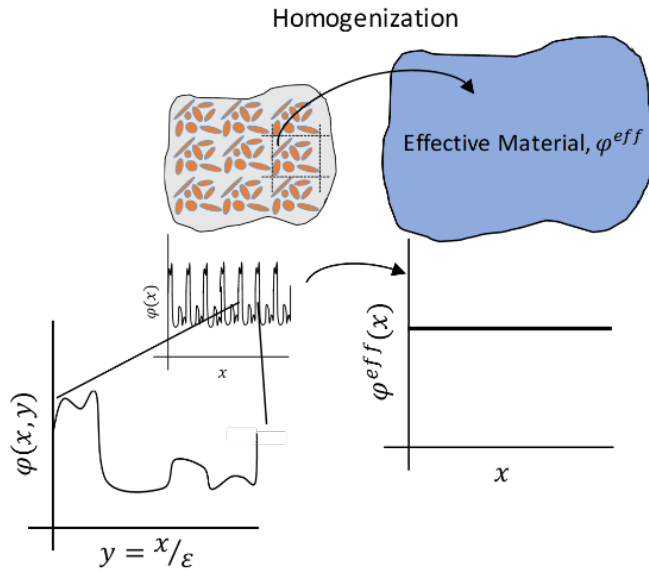


Figure 1-2. Schematic of asymptotic expansion homogenization of material properties. At the local scale  $y$ , the heterogeneous material has a rapidly varying and periodic field of an arbitrary characteristic property  $\phi$ . This material can be represented at the global scale  $x$  by an effective material with constant or slowly varying fields. The ratio of the length of a unit vector at the local scale to that at the global scale is described by  $y = x/\epsilon$ , where  $\epsilon$  is a small parameter.

#### *1.2.4.3 Standard Representative Volume Element Approach*

The FE-based homogenization approach developed and used throughout this dissertation involves the process of calculating and mapping effective material properties through a decoupled FE analysis of a composite at two spatial levels: local and global.<sup>47</sup> The methodology simulates the geometry of a statistical representative volume element (RVE) using Digimat-FE<sup>49</sup> and uses ANSYS Mechanical<sup>50</sup> to calculate stress distributions produced by the local-level microstructural features during virtual RVE displacement. The objective is to compute the volume averaged local stress and strain fields within the RVE to calculate the effective material properties, which are subsequently determined as the constitutive relationships between these stress and strain fields. By applying loads or deformations to the RVE, stress-strain responses can be calculated by solving well-known governing equations at the Gauss integration points of the finite elements.

A simulation at the global level would employ the use of a spatially homogenized material with the effective material properties determined from the local-level analysis. FE homogenization methods require the analysis of a periodic RVE that is large enough to capture the microstructural heterogeneities of a composite but small enough to function as a volume element of continuum mechanics.<sup>51</sup> Hill defines an RVE as “a sample that is structurally entirely typical of the whole mixture on average and contains a sufficient number of inclusions for the apparent overall moduli to be effectively independent of the surface values of traction and displacement, as long as these values are macroscopically

uniform.”<sup>52,53</sup> An example RVE, generated in Digimat-FE is shown in Figure 1-3 for a spherical silica reinforced epoxy matrix.<sup>54</sup>

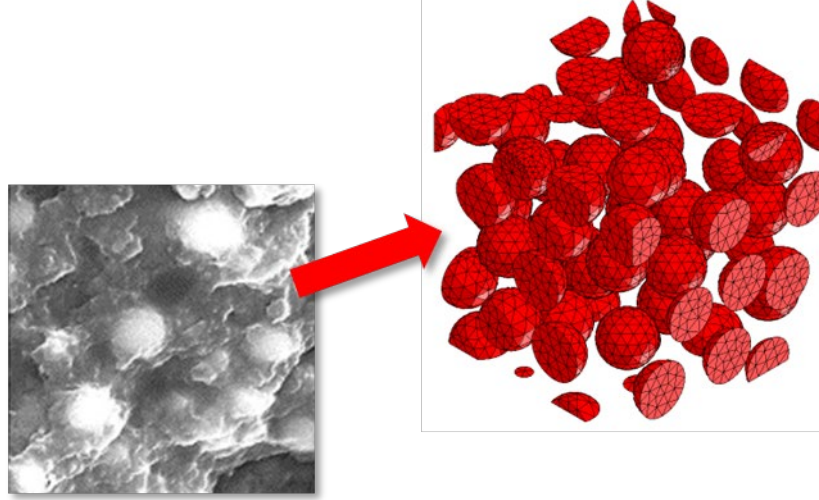


Figure 1-3. An example representative volume element (right), generated in Digimat-FE is shown as a representation for a spherical silica reinforced epoxy matrix. Micrograph (left) from Wang et al.<sup>54</sup>

### *Loading Conditions*

Six independent loading conditions (LCs) are defined for each RVE. These are prescribed to generate three periodic, uniaxial strains in the three principal directions and three shearing modes.<sup>55</sup> The applied strain value ( $< 5\%$ ) is arbitrarily small since the constituent materials are defined as linearly elastic.

### *Calculation of the Effective Elastic Modulus:*

The complete effective material stiffness matrix,  $C_{eff}$ , is obtained by applying linear elastic constitutive relationships and solving the system of linear equations below. An application of Hooke’s law at the microscopic level<sup>47</sup>, in conjunction with strain energy equivalence principles<sup>56</sup>, allows a mapping of the volume-averaged RVE strain

field,  $\bar{\varepsilon}_{6x6}$ , to that of the stress field,  $\bar{\sigma}_{6x6}$ , with proportionality defined by  $C_{eff}$ , a 36-element stiffness matrix. The volume-averaged fields of the microscopically heterogeneous RVE are calculated from equations below.

$$\bar{\varepsilon}_{ij} = \frac{1}{V_{RVE}} \int_{V_{RVE}} \varepsilon_{ij}(x, y, z) dV_{RVE} \quad (20)$$

$$\bar{\sigma}_{ij} = \frac{1}{V_{RVE}} \int_{V_{RVE}} \sigma_{ij}(x, y, z) dV_{RVE} \quad (21)$$

These averaged fields give the (macroscopically) uniform stress and strain states that an equivalent or effective homogenous medium would develop under identical loading. Thus, the elastic properties of the effective material are related to the RVE fields and can be expressed in matrix form as follows.

$$[ \bar{\sigma}_{6x6} ] = [ C_{eff} ] [ \bar{\varepsilon}_{6x6} ] \quad (22)$$

Each column of  $\bar{\varepsilon}_{6x6}$  and  $\bar{\sigma}_{6x6}$  is obtained by computing equations (20) and (21) using ANSYS Parametric Design Language (APDL) macros, adapted from Barbero,<sup>33</sup> for each of the six loading conditions. The matrices were constructed as shown below:

$$\bar{\varepsilon}_{6 \times 6} = \begin{bmatrix} \varepsilon_{xx}^{LC1} & \varepsilon_{xx}^{LC2} & \dots & \dots & \dots & \varepsilon_{xx}^{LC6} \\ \varepsilon_{yy}^{LC1} & \varepsilon_{yy}^{LC2} & \dots & \dots & \dots & \varepsilon_{yy}^{LC6} \\ \varepsilon_{zz}^{LC1} & \vdots & \vdots & \vdots & \vdots & \vdots \\ \varepsilon_{xy}^{LC1} & \vdots & \vdots & \vdots & \vdots & \vdots \\ \varepsilon_{xz}^{LC1} & \vdots & \vdots & \vdots & \vdots & \vdots \\ \varepsilon_{yz}^{LC1} & \varepsilon_{yz}^{LC2} & \dots & \dots & \dots & \varepsilon_{yz}^{LC6} \end{bmatrix} \quad (23)$$

$$\bar{\sigma}_{6 \times 6} = \begin{bmatrix} \sigma_{xx}^{LC1} & \sigma_{xx}^{LC2} & \dots & \dots & \dots & \sigma_{xx}^{LC6} \\ \sigma_{yy}^{LC1} & \sigma_{yy}^{LC2} & \dots & \dots & \dots & \sigma_{yy}^{LC6} \\ \sigma_{zz}^{LC1} & \vdots & \vdots & \vdots & \vdots & \vdots \\ \sigma_{xy}^{LC1} & \vdots & \vdots & \vdots & \vdots & \vdots \\ \sigma_{xz}^{LC1} & \vdots & \vdots & \vdots & \vdots & \vdots \\ \sigma_{yz}^{LC1} & \sigma_{yz}^{LC2} & \dots & \dots & \dots & \sigma_{yz}^{LC6} \end{bmatrix} \quad (24)$$

Equation (22) results in a system of 36 linear equations that are solved for the unknown components of  $C_{eff}$ . The effective compliance matrix,  $S_{eff}$ , is then calculated as the inverse of the stiffness matrix.

$$S_{eff} = C_{eff}^{-1} \quad (25)$$

If the effective compliance matrix is assumed to be generally orthotropic ( $S_{eff} \approx S_{ortho}$ ), one can deduce meaningful engineering constants. The assumption is much less stringent than treatment as an isotropic material and preserves directionally dependent material elasticity in three orthogonal directions. The compliance matrix takes the following form for an orthotropic material with three planes of symmetry.

$$S_{ortho} = \begin{bmatrix} \frac{1}{E_x} & -\frac{\nu_{yx}}{E_y} & -\frac{\nu_{zx}}{E_z} & 0 & 0 & 0 \\ -\frac{\nu_{xy}}{E_x} & \frac{1}{E_y} & -\frac{\nu_{zy}}{E_z} & 0 & 0 & 0 \\ -\frac{\nu_{xz}}{E_x} & -\frac{\nu_{yz}}{E_y} & \frac{1}{E_z} & 0 & 0 & 0 \\ 0 & 0 & 0 & \frac{1}{2G_{xy}} & 0 & 0 \\ 0 & 0 & 0 & 0 & \frac{1}{2G_{xz}} & 0 \\ 0 & 0 & 0 & 0 & 0 & \frac{1}{2G_{yz}} \end{bmatrix} \quad (26)$$

The elastic and shear moduli,  $E_i$  and  $G_{ij}$  respectively, are calculated from Equation (26), as well as the Poisson's ratios,  $\nu_{ij}$ .

### 1.2.5 Gaussian Process Models

Gaussian process (GP) models have attracted widespread interest as a versatile supervised machine learning technique due to their robust predictive performance and their ability to quantify uncertainty in predictions for a range of input parameter types. As a stochastic model, GPs can be viewed as distributions over functions and are utilized in numerous applications, including regression, classification, and optimization. GPs are often used as a surrogate model to approximate computationally demanding computer models at a reduced computational expense.<sup>57–60</sup>

A GP specifies a prior distribution over functions, which can be converted into a posterior distribution after observing data and updating the prior using Bayes theorem. A Gaussian process is completely specified by its mean function and covariance function

(kernel). The mean function is typically taken as zero (though it does not have to be), and the covariance function is chosen to reflect the assumptions about the function we are modeling. The mathematical formulation of GPs in the context of GP regression is given in Chapter 4, Section 4.2.2.

### ***1.2.6 Bayesian Inference***

Bayesian inference is a statistical inference approach that uses Bayes' theorem to update a hypothesis' probability estimate when new data or information becomes available. The cornerstone of Bayesian inference is Bayes' theorem, which can be formulated as:<sup>61</sup>

$$P(H|E) = \frac{P(E|H) \cdot P(H)}{P(E)}, \quad (27)$$

where:

- $P(H|E)$  is known as the posterior and represents the probability of hypothesis H being true given the evidence E
- $P(E|H)$  is the likelihood of observing evidence E, given that hypothesis H is true
- $P(H)$  is known as the prior and represents the probability of hypothesis H being true before considering any evidence
- $P(E)$  is the probability of observing evidence E, regardless of any specific hypothesis.

### 1.3 Dissertation Outline

The methods developed herein rely on experimental data, finite element (FE) analysis, Bayesian inference, and Gaussian process machine learning models to maximize insight into physical phenomena. This work expands our understanding of the structure-property relationships in heterogeneous media, focusing on quantifying and propagating uncertainty about constituent properties throughout model predictions.

This dissertation presents a generalized approach to modeling different composite subtypes and is demonstrated for a range of composites, from simple particulate systems to complex commercial composites. An outline of the dissertation is given in Figure 1-4 and highlights the overlapping methods utilized in each application area.

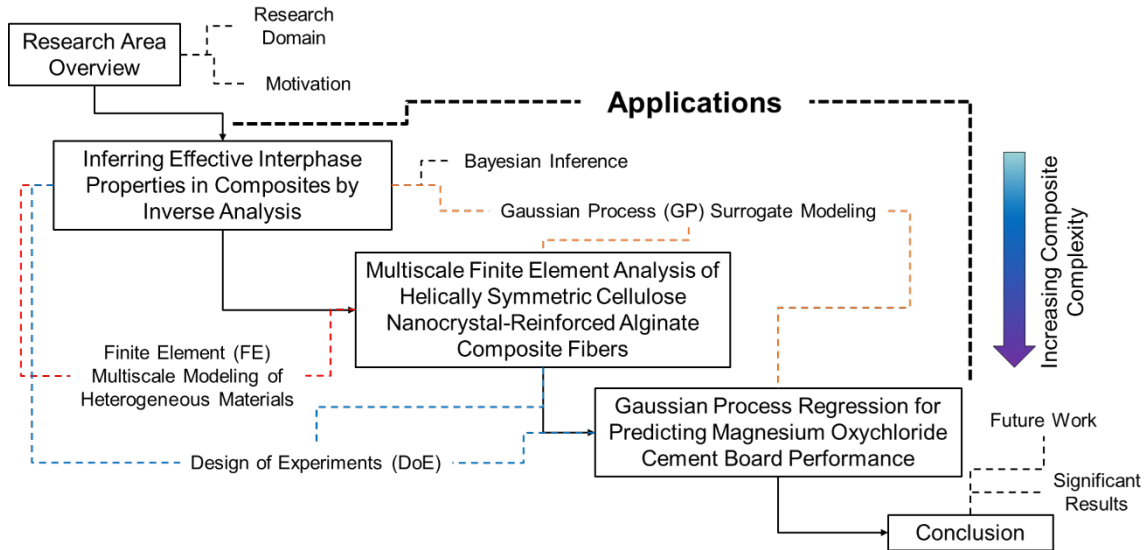


Figure 1-4. Outline of the dissertation, highlighting the application areas and overlap of the methods employed throughout each application.



Chapter 2 introduces a robust framework for the modeling and characterization of a composites' interphase. The framework couples FE analysis with Bayesian inference while leveraging easily obtainable measurements of a composite's bulk elastic properties to infer information about the interphase, which is difficult to determine experimentally.

Chapter 3 explores a multiscale model of anisotropic cellulose nanocrystals (CNCs) embedded in an alginate fiber to understand the effect of CNC alignment on the overall mechanical response of the composite. The model covers two length scales: the microscale, where CNC alignment is captured using a representative volume element (RVE), and the macroscale, where the long-range ordering of RVEs in a helical pattern around the alginate fiber axis is simulated in a macroscopic fiber model.

Chapter 4 presents the application of Gaussian process regression in predicting the mechanical properties of a commercial composite: fiberglass-reinforced magnesium oxychloride (MOC) cement boards. The model assesses the effects of formulation, crystalline phase compositions, and process control parameters on the composite's mechanical performance.

## CHAPTER 2

### INFERRING EFFECTIVE INTERPHASE PROPERTIES IN COMPOSITES BY INVERSE ANALYSIS

#### 2.1 Abstract

Composite materials consist of a matrix reinforced by one or more fillers, each having unique material properties. Coated and uncoated fillers possess an interphase region between the matrix and filler with distinct but poorly known physio-chemical properties. Determination of the physical properties of this region is essential for the modeling and design of composite materials, especially when considering nanoscale reinforced systems where the interphase may comprise a significant volume fraction of the overall composite. Direct measurements of the interphase properties are challenging, and most experimental methods involve abrasive techniques that alter local mechanical properties or suffer from experimental bias.

This study proposes a comprehensive framework to numerically model the interphase effects and infer the key mechanical properties of the interphase region from experimental measurements of the composite elastic modulus, a macroscale property that can be readily measured. This framework, depicted in Figure 2-1, is demonstrated for a matrix reinforced by randomly distributed spherical particles using finite element (FE) analysis but is generalizable to any mechanical composite system.

Representative volume elements are analyzed under periodic strains, and the resulting stresses are used to determine the effective stiffness (or modulus) of the

simulated composite. Gaussian process regression is used to generate computationally efficient surrogate models that approximate the FE model output. The surrogate models are then explored through statistical inverse analysis to infer the interphase thickness and modulus that best match macroscale experimental data of six different composite systems. This work presents the obtained results from calibrated FE analysis as an alternative for the mechanical characterization of interphase regions. The calibrated results show good agreement with the experimental measurements of the composite modulus and account for particle size-dependent elastic behavior. Furthermore, the relationship between filler particle size and the interphase thickness and modulus is explored.

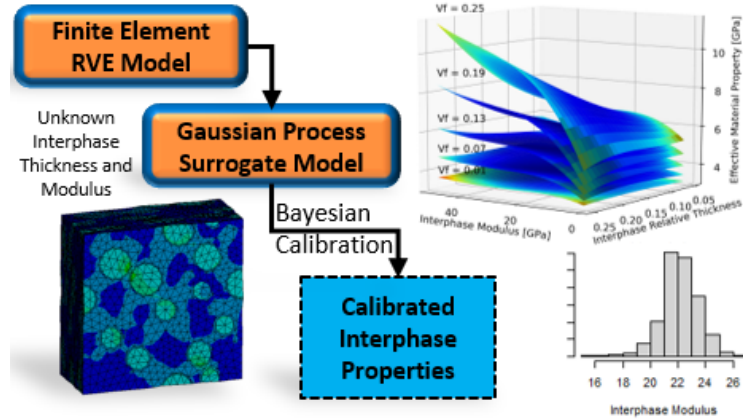


Figure 2-1. Visual depiction of the framework presented in Chapter 2 highlighting the finite element model, Gaussian process surrogate model, and the Bayesian Inference results.

## 2.2 Introduction

A composite can be defined as a material consisting of two or more physically and chemically distinct constituent materials that, when combined, yield overall properties different than each constituent. Composite materials have been widely adopted for engineering products owing to their tunable characteristics.<sup>62–65</sup> While pure

materials may exhibit a few desirable properties, they often lack in others or fail to meet essential constraints, limiting their applicability in engineered designs.

The simplest composite material consists of a matrix reinforced by a filler. Changing the volumetric ratio of these two constituents, among many other parameters, such as the aspect ratio and orientation of the filler, provides a highly tunable system capable of addressing the increasing demands of modern engineered designs. More recently, incorporating nanometer-sized fillers has enabled a higher degree of tunability and expanded the performance space of traditional filled systems.<sup>7,66,67</sup> The distinguishing advantage nanoparticles provide when compared to traditional macroparticles, is related to the increased interfacial phenomena of the constituents. Interfacial phenomena can be broadly classified into two categories: sizing- or coating-induced phenomena and matrix-perturbed phenomena.

A sizing or coating is an intentional layer applied to a filler during manufacturing to improve compatibility or binding between the dissimilar filler and matrix materials. These coatings aid in processability and filler-matrix interfacial adhesion, facilitating load transfer from matrix to filler. The overall properties of composites containing coated fillers can depend on the filler size as it affects the surface-area-to-volume ratio of the filler. This effect is often pronounced for nanoparticles with a significant free surface area, leading to a higher interphase volume fraction of the coating.

On the other hand, matrix-perturbed phenomena arise when a filler's presence induces a localized perturbation in the matrix properties near the interface, creating a

region with properties significantly different from the bulk matrix. When the presence of an interface confines polymer chains, they take on different free energies (due to an entropic change from restricted chain conformations) when compared to polymer chains in the bulk matrix phase. The resulting interfacial conformation depends on several factors, such as the radius of gyration for neighboring matrix molecules, filler-matrix interaction energies, filler-filler particle distances, cohesive interactions within the bulk polymer, and the filler size, curvature, and roughness, among others.<sup>8,68–70</sup>

A filler embedded in a polymer matrix can also induce polymer crystallization well into the bulk matrix.<sup>9</sup> Transcrystallization is an example where the surface of a filler provides a sufficient density of heterogeneous nucleation sites to induce crystallization perpendicular to the filler surface. The density of nucleating sites at the interface laterally confines the crystallization resulting in a columnar (in the case of a fiber) crystalline layer that grows radially from the fiber surface.<sup>71</sup> The formation of transcrystalline layers is difficult to predict a priori as it depends on many factors related to the nature of the filler-matrix pair and processing conditions. These factors include polymer tacticity, filler-matrix epitaxy, filler surface roughness, filler-matrix thermal coefficient mismatch, and the composition and surface energy of the filler surface.<sup>71</sup> The altered morphology leads to interfacial regions exhibiting mechanical, thermal, optical, or electrical properties that differ from the bulk matrix.

The perturbed interfacial regions are more accurately described by non-continuum mechanisms<sup>66</sup> but are commonly simplified as an “effective interphase” of a finite

thickness with homogenous or gradually varying properties.<sup>10–13,72–76</sup> Thus, a two-phase composite system dominated by interfacial phenomena can be modeled as a three-phase system consisting of a matrix, filler, and an interphase layer. If the mechanical properties of the interphase are weaker than those of the matrix phase, a coating or sizing agent might be employed. An important distinction between sizing- or coating-induced phenomena and matrix-perturbed phenomena is that the former describes an interphase consisting of an intentionally added coating, while the latter describes the creation of a “pseudo” layer of matrix material. Both classes of phenomena can be modeled as an effective interphase, and both may lead to filler size-dependent material properties.

Filler size-dependent properties can originate from changes in the interphase volume fraction. For example, reducing a filler particle’s size that is coated with an interphase of constant thickness might result in the domination of composition by the interphase (Appendix A, Figure A-1). The domination of interphase regions can lead to dramatically different overall composite material properties; thus, it is important to accurately account for the properties of the interphase when developing accurate micromechanical models. The issue then lies in determining the actual volume fraction (or thickness) of the interphase in addition to the physical properties.

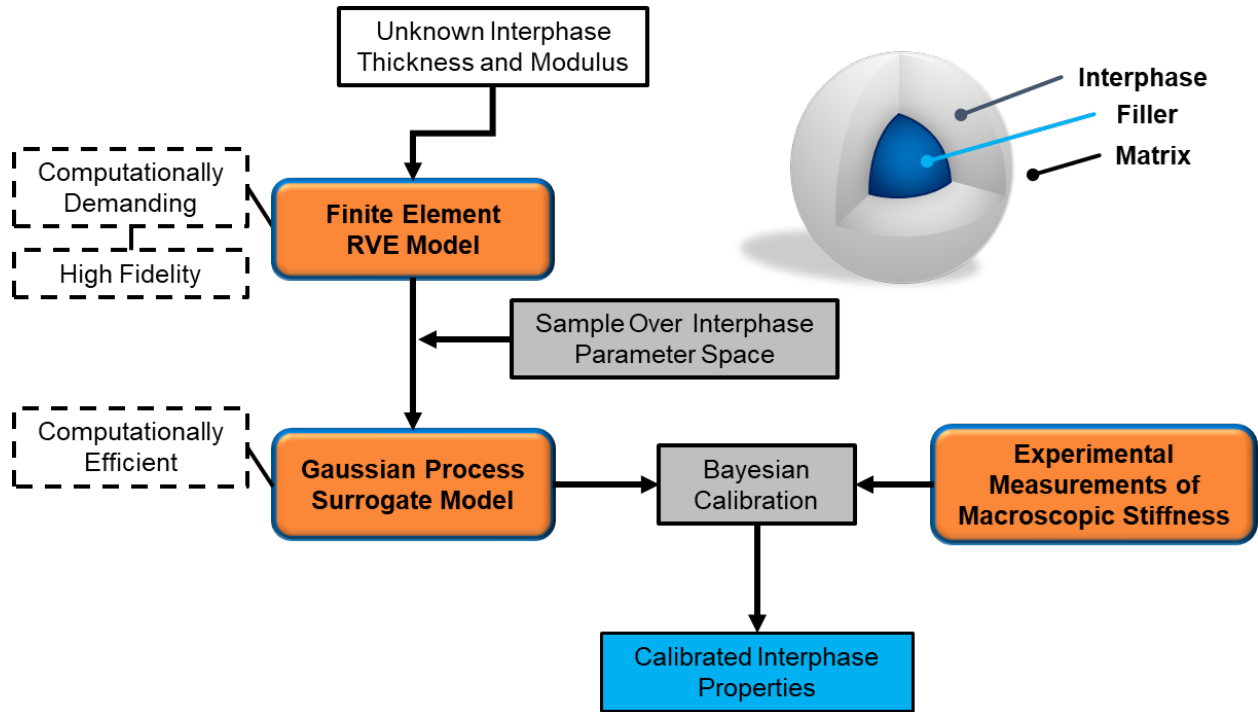


Figure 2-2. Roadmap of the proposed framework to infer the effective interphase thickness and modulus from experimental measurements of a composite's elastic modulus.

This work proposes a comprehensive inverse analysis framework to infer interphase properties from easily obtained macro-level experimental measurements of the composite elastic modulus by leveraging high-fidelity computer model simulations. The approach utilizes a Gaussian process (GP) as a surrogate model to capture the relationships between the inputs and outputs of the computationally demanding model realizations at a reduced cost. Using GP emulators avoids constraints on the functional form, allowing the training data to decide the emulator response surface. Additionally, GP emulators readily offer statistical approximations about the uncertainty in predictions. The framework presented in this work determines the values of the

interphase thickness and modulus that give the closest agreement to experimental measurements of the elastic modulus of a composite material, a property that can be readily measured experimentally. The framework, shown in Figure 2-2, involves (1) developing finite element (FE)-based computer models of a periodic microstructure reinforced by spherical particles with an interphase region, (2) computing the effective elastic properties of the representative volume element (RVE) over a large material parameter space, (3) training a GP surrogate model on the FE observations, (4) interrogating the surrogate model to seek the optimal calibration parameter values (i.e., interphase thickness and modulus) and (5) quantifying uncertainty in the model predictions with the calibrated values. Herein, the proposed framework is demonstrated for a matrix reinforced by randomly distributed spherical particles but is generalizable to any composite system.

#### *Framework Generalizability*

The proposed framework is designed to characterize interphases' effective behaviors in thermoset and thermoplastic composites. While these two types of polymers give rise to different interphase characteristics, the framework's statistical RVE approach is flexible enough to accommodate both scenarios. Previous studies have demonstrated the modeling of heterogeneous interphases as homogeneous "effective" interphases, which can capture the effective contribution of the interphase to macroscopic mechanics.<sup>10–13,72–76</sup> This framework does not aim to simulate heterogeneous interphases directly but instead utilizes their mechanical contributions to infer the effective interphase



properties. The framework can be applied to various composite systems, including both thermoset and thermoplastic matrices, as well as particulate and fiber reinforcements, as long as an RVE can be simulated and macroscopic elastic properties can be obtained over a range of filler sizes and volume fractions. Herein, the proposed framework is demonstrated for thermoplastic matrices reinforced by randomly distributed spherical particles but is generalizable to any composite system for which 1) a statistical RVE can be simulated and 2) macroscopic elastic properties can be obtained over a range of filler sizes and volume fractions.

### **2.3 Background Perspectives**

Attempts to experimentally measure interphase properties are challenging, especially for the case of matrix-induced phenomena. Atomic force microscopy and nanoindentation have been used to probe this region and correlate changes in load-displacement curves with that of the matrix, filler, and interphase regions.<sup>11,12</sup> Kim et al.<sup>12</sup> compared three interphase characterization techniques: nanoindentation, nanoscratch, and thermal capacity jump measurements and found that nanoindentation tests produced significant variations between specimens and were not sensitive enough to distinguish the effects between various silane coupling agents in a glass fiber/polymer resin composite. Agreeable trends were found between heat capacity-based and nanoscratch measurements, although the former predicted larger values of the interphase thickness. While these experimental techniques can be insightful, they require significant

assumptions, can be confounded by sample preparation, include measurement bias, and are limited to certain classes of materials and properties to be measured.

An alternative approach to determining interphase properties involves rigorous computational methods.<sup>8,72,74</sup> Odegard et al.<sup>72</sup> used coarse-grained molecular dynamics (MD) simulations to calculate radially varying density profiles in interphase regions. They show how spontaneous molecular rearrangements of polymer around a filler particle can result in significant mechanical property perturbations from the bulk

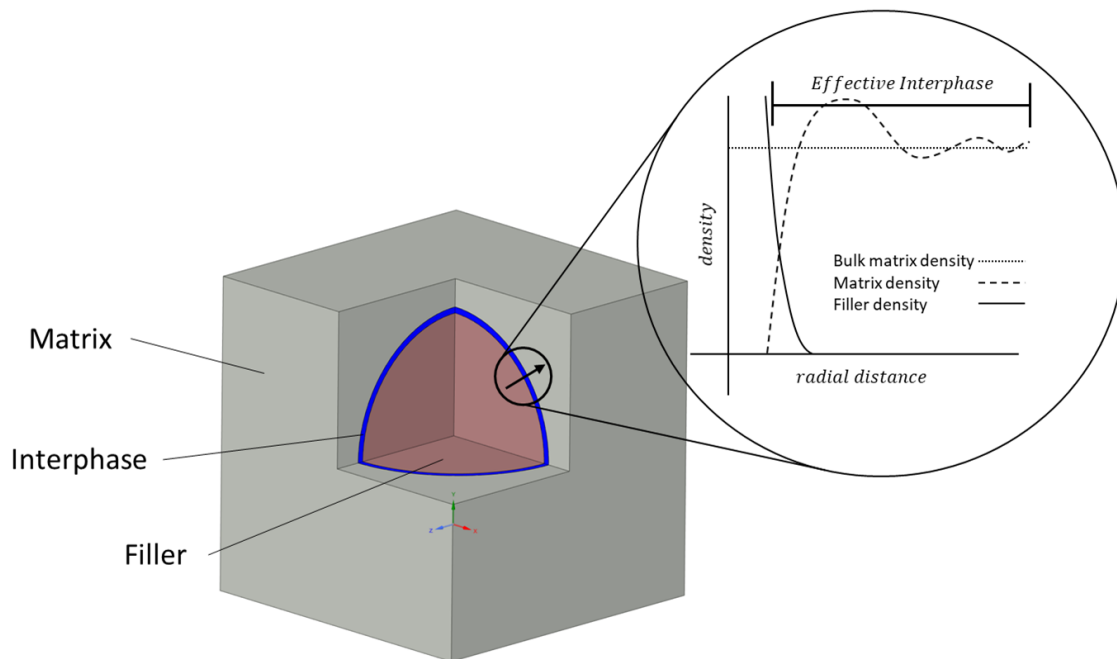


Figure 2-3. Schematic of radial density variations within the effective interphase. Adapted from Odegard et al.<sup>71</sup>

polymer. Figure 2-3 shows an idealization of the radial density variations that are characterized as an effective interphase. While this region is discrete and non-homogenous, an equivalent-continuum model of an interphase layer was used to account

for these discrete effects. The interphase thickness and elastic modulus were determined directly from the MD simulations.

The experimental and rigorous MD simulation-based methods for determining interphase properties become costly when evaluating a wide range of matrix and filler properties, geometric configurations, processing conditions, and other tailoring methods used to fine-tune heterogeneous materials. A summary of various experimental and MD simulation studies to measure or calculate interphase properties can be found in Table 2-1

Table 2-1. Summary of various approaches used to measure or calculate properties of interphases.

Reference	Material System	Method	Interphase Thickness	Interphase Modulus	Particle/Fiber Size
<sup>8</sup> Ghanbari et al.	Silica nanoparticle / polystyrene	MD Simulation	~ 2 nm	-	4-nm nanoparticle
<sup>72</sup> Odegard et al.	Silica nanoparticle / polyimide	MD Simulation	12 Å	2.4 GPa	15-Å nanoparticle
<sup>74</sup> Yu et al.	Alumina / epoxy	MD Simulation	~ 6 Å	3-10 GPa	6-10 Å, spherical particles
<sup>77</sup> Khodadadi et al.	Carbon nanotubes (CNTs) / epoxy	MD Simulation	2.25 Å	-	Cylindrical Diameter: 5.42 Å Length: 164.8 Å
	Carbon nano diamond particles (CNPs) / epoxy		2.35 Å	-	Sphere Radius: 11 Å
<sup>15</sup> Williams et al.	Carbon fiber / epoxy	Tensioned-fiber method	0.7 µm	0.825 GPa	7-nm fiber
<sup>78</sup> Munz et al.	Carbon fiber / polyphenylenesulfide (PPS)	Scanning force microscopy (SFM) with sinusoidal displacement modulation (DM)	20 – 80 nm	-	~ 15-µm fiber

12 Kim et al.	Glass fiber / polymer resin (with various silane coupling agents)	Nanoindentation	1 μm	Gradient 4.3 – 80 GPa	9 μm fiber
		Nanoscratch	0.8 - 1.5 μm	-	
		Thermal capacity jump measurement	1.3 – 1.6 μm	-	
11 Bedi et al.	Stainless steel (SS) wire, brass wire, carbon fiber (CF) / epoxy (with and without carbon nanotube (CNT) sizing)	Nanoindentation	Without CNTs: 2 – 8 μm	CF: Gradient 3.5 GPa – 60 GPa	SS wire: 500-μm  Brass wire: 160 and 250-μm  CF: 7-μm
			With CNTs: 5 - 10 μm	SS: Gradient 3.5 – 8 GPa	
		SEM-EDS	Without CNTs: 0.25 μm – 7 μm	-	
			With CNTs: 0.6 – 21 μm		
79 Vollenberg and Heikens	Glass and alumina spheres / polymer	Series model fit from measurements of elastic modulus	Assumed 3 μm	100-μm Glass: 1.7 GPa 0.035-μm Alumina: 6 GPa	Glass beads: 4, 30, 100-μm  Alumina spheres: 0.035, 0.4-μm

Analytical, semi-analytical, and empirical micromechanical models are widely used as an alternative to the resource-intensive experimental and MD simulation-based approaches. Analytical models, such as Mori-Tanaka<sup>27</sup>, approximate overall composite properties using assumed stress/strain relationships between the filler and matrix, usually derived as extensions to Eshelby's equivalent-inclusion concept.<sup>24</sup> The computational efficiency of explicit and closed-form solutions comes at the expense of idealized representations of the heterogeneous media. These micromechanical models are

fundamentally simplistic and are, thus, limited in the features they can describe. In some cases, they predict behavior that violates the established symmetries of the stiffness and compliance tensors.<sup>80</sup> Figure 2-4 presents data from

Vollenberg and Heikens<sup>79</sup> and illustrates the disparity of three analytical models,

Mori-Tanaka and the Voigt and Reuss models. These models are a function of inclusion volume fraction and not particle size despite clear experimental particle size-dependent

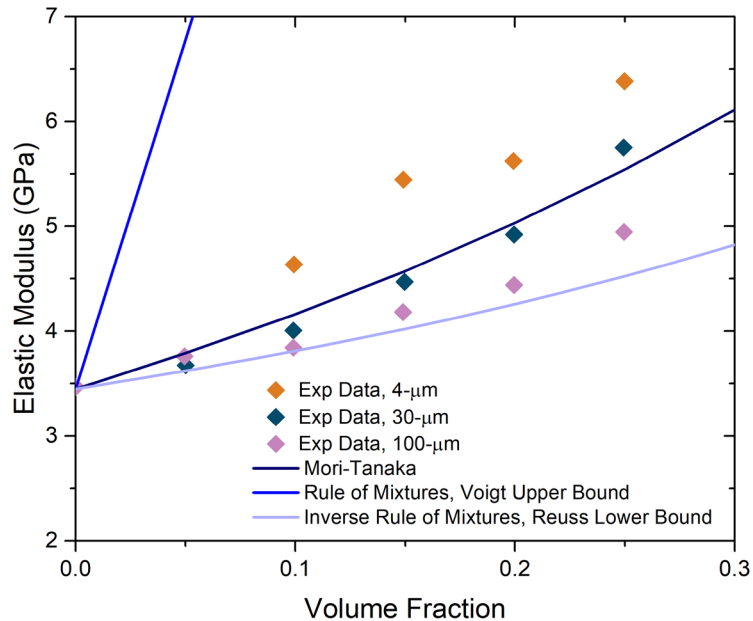


Figure 2-4. Experimental data of the elastic modulus for glass beads in polystyrene from Vollenberg and Heikens<sup>17</sup> highlighting the effects of particle size on the elastic modulus and the inability to account for this effect with simple analytical models like the Mori-Tanaka and the Voigt and Reuss Bounds.  
 $E_m = 3.45 \text{ GPa}$   $E_f = 70 \text{ GPa}$   $v_m = 0.34$   $v_f = 0.22$

properties. The significant size dependency not captured by the two-phase Mori-Tanaka model suggests the presence of an interphase layer.

FE analysis is an alternative numerical approach to modeling the properties and performance of composite systems.<sup>51,77,81–83</sup> FE methods have much greater flexibility in the composite geometries, number of phases, and classes of constitutive models that can be simulated and have been used to model a composite's interphase.<sup>83</sup> These capabilities promote higher fidelity than the analytical and semi-analytical micromechanical models while having computational demands that are significantly lower than MD simulation-based computational approaches. FE approaches to predicting effective composite properties offer a balanced tradeoff between micromechanical accuracy and geometric flexibility, enabling the accurate representation of composite materials with feasible demands on computational resources.

## **2.4 Methods**

### ***2.4.1 Finite Element-Based Homogenization***

The homogenization approach used in the proposed framework is the process by which effective material properties are calculated through a decoupled analysis of a composite at two spatial levels: local and global (Appendix A, Figure A-2).<sup>47</sup> FE-based homogenization methods simulate local-level microstructural features, tying local stress and strain fields within the RVE to the average stress and strain of the RVE. The effective material properties are calculated as the constitutive relationships between these stress and strain fields. A simulation at the global level would employ the use of a

spatially homogenized material with the effective material properties determined from the local-level analysis. FE homogenization methods require the analysis of a periodic RVE that is large enough to capture the microstructural heterogeneities of a composite but small enough to function as a volume element of continuum mechanics.<sup>51</sup> By applying loads or deformations to the RVE, stress-strain responses can be calculated by solving well-known governing equations at the Gauss integration points of the finite elements.

This study uses FE homogenization to determine the effective material properties of particulate composites reinforced with spherical glass particles containing an interphase layer. The FE model developed herein contains eight input parameters: interphase modulus, interphase Poisson's ratio, interphase relative thickness, matrix modulus, matrix Poisson's ratio, filler modulus, filler Poisson's ratio, and filler volume fraction. The output from the FE model is the effective elastic properties, as calculated in Section 2.4.1.2. For this system, we categorize the inputs into those known with a low degree of uncertainty and others with a high degree of uncertainty. The matrix modulus, matrix Poisson's ratio, filler modulus, filler Poisson's ratios, and volume fraction are known with a high degree of certainty and are considered fixed. The interphase Poisson's ratio is assumed to be equivalent to the matrix. The interphase modulus and interphase (relative) thickness have a high degree of uncertainty and are ideal candidates to be inferred from the experimental data.

#### *2.4.1.1 Exploration of Model Parameter Space via Design of Experiments*

In forward propagation of model input uncertainties, the design of computer experiments guides how the parameter space will be explored through computer model realizations.<sup>84</sup> The design of experiments was influenced by the structure of the data from physical experiments and is explained briefly.

##### *Experimental Data for Calibration:*

The physical experimental data came from the work of Vollenberg and Heikens<sup>79</sup> for six different composites (summarized in Table 2-2), each consisting of a different combination of filler and matrix, with a five percent experimental error for each observation.<sup>79</sup> In each experimental data set, separate experiments measured the change in Young's, or elastic modulus, against filler volume fraction,  $V_f$ , for different particle sizes, as shown in Figure 2-4. The matrix modulus,  $E_m$ , filler modulus,  $E_f$ , matrix Poisson's ratio,  $\nu_m$ , and filler Poisson's ratio,  $\nu_f$ , were fixed in each experiment. The filler volume fraction and particle size are independent control variables manipulated during experiments for a given material.



Table 2-2. Summary of experimental data from Vollenberg and Heikens<sup>79</sup>

Composite	Abbreviation	$E_m$ [GPa]	$E_f$ [GPa]	$\nu_m$	$\nu_f$	$V_f$	Particle Sizes [ $\mu\text{m}$ ]
Glass-Polystyrene	G-PS	3.45	70	0.34	0.22	0-0.25	4, 30, 100
Glass-Polycarbonate	G-PC	2.15	70	0.38	0.22	0-0.25	4, 30, 100
Glass-Styrene-acrylonitrile	G-SAN	3.80	70	0.33	0.22	0-0.15	4, 30, 100
Glass-Polypropylene	G-PP	1.56	70	0.42	0.22	0-0.25	4, 30, 100
Alumina-PS	A-PS	3.45	200	0.34	0.22	0-0.15	0.035, 0.4
Alumina-SAN	A-SAN	3.80	200	0.33	0.22	0-0.15	0.035, 0.4

#### *Modeling of the Interphase Layer:*

The interphase layer was modeled as a distinct region of the matrix influenced by the filler particle. The interphase Poisson's ratio was assumed to be equal to that of the matrix.<sup>82</sup> Each composite was assumed to have a different interphase thickness and modulus with freedom to vary with particle size. The interphase thickness was sampled as a relative quantity equal to the ratio of the simulated interphase thickness to the simulated particle radius. It is important to note that FE RVEs are agnostic to length scales, and the specified dimensions are relative entities within the simulation domain. Since the size of the RVE was defined as 40 inclusions (See Section 2.4.1.3), increasing the volume fraction of the filler entails enlarging the simulated particle relative diameter. Defining the interphase thickness as a relative thickness enabled an equivalent interphase volume fraction (i.e., a function of the simulated particle size and interphase thickness) to be simulated at various volume fractions.

### *Sampling of the Relevant Parameter Space:*

A design of experiments approach was used to efficiently select inputs for the FE model over a large parameter space for each composite, enabling input-output data to condition a GP surrogate model. By training separate GPs for each composite, the eight-parameter FE model could be represented by a three-parameter GP with a reduced set of inputs: volume fraction, interphase modulus, and interphase relative thickness. The parameter type and upper and lower bounds for the FE model inputs are summarized in Table 2-3. Within these bounds, a Latin hypercube sampling (LHS)<sup>85</sup> scheme (n=228) explored the parameter space due to its desirable space-filling properties. Because the interphase stiffness was unknown, the sampled bounds represent plausible values between 0.01 GPa and 50 GPa, reflecting a spectrum of possible interphase stiffnesses, from highly deformable to highly rigid.<sup>4</sup> The bounds for relative thickness were chosen out of consideration for FE computational expense and geometric limitations. At small relative interphase thicknesses ( $<0.05$ ), extremely fine meshing is required to represent the thin layer accurately, and computational demand becomes prohibitive. Geometric restrictions also limit the interphase thickness (interphase thickness  $\leq 0.25$  at volume fractions of  $\sim 0.25$ ) due to interphase placement collisions with other filler particles.

Table 2-3. Lower and upper bounds sampled for each parameter.

Predictor	Input Type	Symbol	Lower Bound	Upper Bound
Matrix Modulus	Control	$E_m$	Fixed, from Exp Data	Fixed, from Exp Data
Filler Modulus	Control	$E_f$	Fixed, from Exp Data	Fixed, from Exp Data
Matrix Poisson's Ratio	Control	$\nu_m$	Fixed, from Exp Data	Fixed, from Exp Data
Filler Poisson's Ratio	Control	$\nu_f$	Fixed, from Exp Data	Fixed, from Exp Data
Filler Volume Fraction	Control	$V_f$	$0^\dagger$ , 0.05	0.25
Interphase Poisson's Ratio	Control	$\nu_i$	Fixed, = $\nu_m$	Fixed, = $\nu_m$
Interphase Modulus	Calibration	$E_i$	0.01 GPa	50 GPa
Interphase Relative Thickness	Calibration	$rel_{thick}$	$0^\#$ , 0.05	0.25

<sup>#</sup>Special case lower bound

In addition to the LHS, it was determined that two special cases with a lower parameter bound of zero were required. A zero-filler volume fraction lower bound was obtained by setting the overall modulus directly equal to the fixed matrix modulus and sampling the two calibration parameters via LHS (n=70). A lower bound of zero interphase relative thickness was sampled by generating 2-phase RVEs (Figure S3) consisting of only matrix and filler, where the volume fraction and interphase modulus were sampled via LHS (n=75).

#### *Batch Sequential Surrogate Model Improvement:*

When training a surrogate model on the FE outputs, the initial number of samples used in the design of experiments may be too small to accurately represent the underlying computer model in unsampled areas of the parameter space. The maturity of a surrogate

model is typically evaluated through cross-validation. We adopted a batch-wise strategy<sup>86</sup> to expand the initial design until the desired cross-validation performance was obtained. After training the surrogate model on the initial sample of FE observations, the design space was probed, selecting batches ( $n=15$ ) of parameter values that resulted in the maximum variance, as estimated by the surrogate model. New FE observations were then collected at the parameter values, and the process was repeated until satisfactory cross-validation was obtained (Section 2.4.2.2).

#### *2.4.1.2 Homogenization using Representative Volume Elements*

Digimat-FE<sup>49</sup> was used to generate three-dimensional, cubical RVEs of composite microstructures with randomly distributed spherical inclusions. In this case, the characteristic RVE consisted of a matrix reinforced by equal-sized, randomly distributed, non-intersecting spherical particles. The interphase was modeled as a concentric spherical coating of constant thickness surrounding each filler particle. Interphases were permitted to overlap but not other filler particles (i.e., permissible inter-particle distance  $\geq$  interphase thickness). The matrix, filler, and interphase were treated as linearly elastic, isotropic materials with perfectly bonded interfaces. Geometric periodicity was enforced, requiring filler and interphase intersections at the RVE boundaries to be cleaved and continued so that they enter the RVE from the opposite parallel surface. The geometric RVE (Parasolid) was exported from Digimat to ANSYS-Static Structural, Release 19.0.<sup>50</sup>

The transfer of ANSYS Workbench scripts from Digimat-FE was automated to import the geometric model, assign meshing controls and material parameters, enforce

periodic boundary conditions, apply loading conditions (LCs), and insert post-processing macros. Ten-node quadratic tetrahedral elements (SOLID187) were assigned to three-dimensional RVE components. Eight-node contact elements (CONTA174) were used to represent bonded contact between intersecting three-dimensional target surfaces (TARGE170). Examples of the meshed RVEs and loading modes are shown in Figure 2-5.

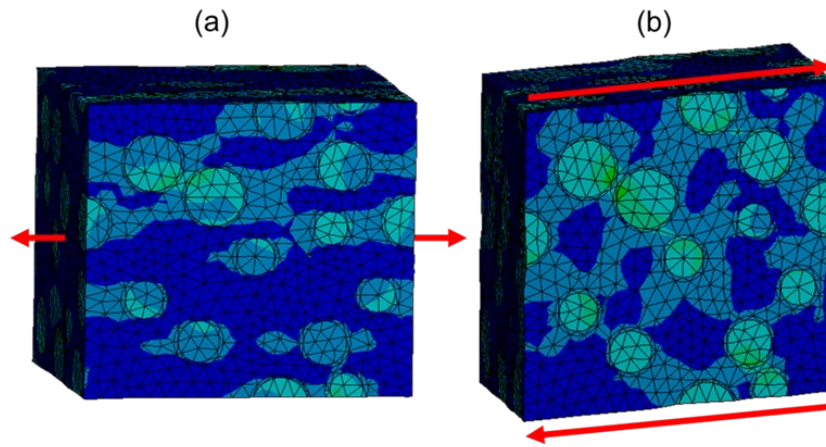


Figure 2-5. Example RVEs of particulate composites reinforced with spherical particles containing an interphase undergoing periodic, a) uniaxial and b) shear deformations. The colored contours represent the Equivalent (von-mises) stress. The particles within the RVE are uniformly sized; however, their appearances may vary due to the irregularities resulting from the cutting process at the RVE boundary.

Six independent LCs were defined for each RVE. These were prescribed to generate three periodic, uniaxial strains in the three principal directions and three shearing modes.<sup>55</sup> The applied strain value ( $< 5\%$ ) was arbitrarily small since the simulation material was defined as linearly elastic. The stiffness and compliance matrices are reduced to two independent components for a truly isotropic material with infinite planes of symmetry. These constants could be determined by applying only one

LC.<sup>87,88</sup> Using one LC reduces the overall computational budget, but directionally-dependent material properties are not predicted. It is important to note that the randomly positioned inclusion microstructures are not perfectly isotropic. The presented method below utilizes a general approach, where the six loading scenarios are used to calculate the complete stiffness matrix. This is useful to determine the degree to which the RVE represents a truly isotropic material. Furthermore, this method would be necessary for RVEs with non-isotropic microstructures like fiber-reinforced composites or particulate composites with clustering and other directionally dependent behavior.

*Calculation of the Effective Elastic Modulus:*

Herein, the complete effective material stiffness matrix,  $C_{eff}$ , was obtained by applying linear elastic constitutive relationships and solving the system of linear equations below (see Appendix A, AD-1). An application of Hooke's law at the microscopic level<sup>47</sup>, in conjunction with strain energy equivalence principles<sup>56</sup>, allows a mapping of the volume-averaged RVE strain field,  $\bar{\epsilon}_{6 \times 6}$ , to that of the stress field,  $\bar{\sigma}_{6 \times 6}$ , with proportionality defined by  $C_{eff}$ , a 36-element stiffness matrix. The volume-averaged fields of the microscopically heterogeneous RVE are calculated from equations (28) and (29).

$$\bar{\epsilon}_{ij} = \frac{1}{V_{RVE}} \int_{V_{RVE}} \epsilon_{ij}(x, y, z) dV_{RVE} \quad (28)$$

$$\bar{\sigma}_{ij} = \frac{1}{V_{RVE}} \int_{V_{RVE}} \sigma_{ij}(x, y, z) dV_{RVE} \quad (29)$$

These averaged fields give the (macroscopically) uniform stress and strain states that an equivalent or effective homogenous medium would develop under identical loading. Thus, the elastic properties of the effective material are related to the RVE fields and can be expressed in matrix form as follows.

$$[ \bar{\sigma}_{6 \times 6} ] = [ C_{eff} ] [ \bar{\varepsilon}_{6 \times 6} ] \quad (30)$$

Each column of  $\bar{\varepsilon}_{6 \times 6}$  and  $\bar{\sigma}_{6 \times 6}$  was obtained by computing equations (28) and (29) using ANSYS Parametric Design Language (APDL) macros, adapted from Barbero,<sup>33</sup> for each of the six loading conditions. The matrices were constructed as shown in equations (31) and (32).

$$\bar{\varepsilon}_{6 \times 6} = \begin{bmatrix} \varepsilon_{xx}^{LC1} & \varepsilon_{xx}^{LC2} & \dots & \dots & \dots & \varepsilon_{xx}^{LC6} \\ \varepsilon_{yy}^{LC1} & \varepsilon_{yy}^{LC2} & \dots & \dots & \dots & \varepsilon_{yy}^{LC6} \\ \varepsilon_{zz}^{LC1} & \vdots & \vdots & \vdots & \vdots & \vdots \\ \varepsilon_{xy}^{LC1} & \vdots & \vdots & \vdots & \vdots & \vdots \\ \varepsilon_{xz}^{LC1} & \vdots & \vdots & \vdots & \vdots & \vdots \\ \varepsilon_{yz}^{LC1} & \varepsilon_{yz}^{LC2} & \dots & \dots & \dots & \varepsilon_{yz}^{LC6} \end{bmatrix} \quad (31)$$

$$\bar{\sigma}_{6 \times 6} = \begin{bmatrix} \sigma_{xx}^{LC1} & \sigma_{xx}^{LC2} & \dots & \dots & \dots & \sigma_{xx}^{LC6} \\ \sigma_{yy}^{LC1} & \sigma_{yy}^{LC2} & \dots & \dots & \dots & \sigma_{yy}^{LC6} \\ \sigma_{zz}^{LC1} & \vdots & \vdots & \vdots & \vdots & \vdots \\ \sigma_{xy}^{LC1} & \vdots & \vdots & \vdots & \vdots & \vdots \\ \sigma_{xz}^{LC1} & \vdots & \vdots & \vdots & \vdots & \vdots \\ \sigma_{yz}^{LC1} & \sigma_{yz}^{LC2} & \dots & \dots & \dots & \sigma_{yz}^{LC6} \end{bmatrix} \quad (32)$$

Equation (30) results in a system of 36 linear equations that is solved for the unknown components of  $C_{eff}$ . The effective compliance matrix,  $S_{eff}$ , is then calculated as the inverse of the stiffness matrix.

$$S_{eff} = C_{eff}^{-1} \quad (33)$$

The effective compliance matrix was assumed to be generally orthotropic ( $S_{eff} \approx S_{ortho}$ ), enabling one to deduce meaningful engineering constants. This assumption is much less stringent than treatment as an isotropic material and preserves directionally dependent material elasticity in three orthogonal directions. For an orthotropic material with three planes of symmetry, the compliance matrix takes the following form.

$$S_{ortho} = \begin{bmatrix} \frac{1}{E_x} & -\frac{\nu_{yx}}{E_y} & -\frac{\nu_{zx}}{E_z} & 0 & 0 & 0 \\ -\frac{\nu_{xy}}{E_x} & \frac{1}{E_y} & -\frac{\nu_{zy}}{E_z} & 0 & 0 & 0 \\ -\frac{\nu_{xz}}{E_x} & -\frac{\nu_{yz}}{E_y} & \frac{1}{E_z} & 0 & 0 & 0 \\ 0 & 0 & 0 & \frac{1}{2G_{xy}} & 0 & 0 \\ 0 & 0 & 0 & 0 & \frac{1}{2G_{xz}} & 0 \\ 0 & 0 & 0 & 0 & 0 & \frac{1}{2G_{yz}} \end{bmatrix} \quad (34)$$

The elastic and shear moduli,  $E_i$  and  $G_{ij}$  respectively, were calculated from (34), as well as the Poisson's ratios,  $\nu_{ij}$ . Ideally, for an isotropic material, one would expect  $E_x = E_y = E_z$ . However, the FE model will inevitably deviate slightly from isotropy due



to non-symmetric RVEs and random particle placement. We report the numerical model prediction of the effective elastic modulus as the average of  $E_x$ ,  $E_y$ , and  $E_z$  with variability associated with the degree of non-isotropic behavior. These homogenized material properties were used for model calibration and validation against experimental data (Sections 2.4.2.3 and 2.5.2). We consider this average property of the computer model output on which we condition our GP.

#### *Mesh Refinement Study:*

The ANSYS Patch Conforming<sup>89</sup> meshing algorithm was used to mesh each RVE. A mesh refinement study<sup>90</sup> was performed to ensure an appropriate mesh size was used. A single RVE was simulated with iterative mesh size refinement to ensure convergence of the calculated elastic modulus. Mesh size was determined based on solve time,

numerical stability, and solution accuracy. The results in Figure 2-6 demonstrate the tradeoffs between the number of elements, solution accuracy, and solve time. The mesh size yielding the least number of elements (125683) and the shortest solve time in Figure

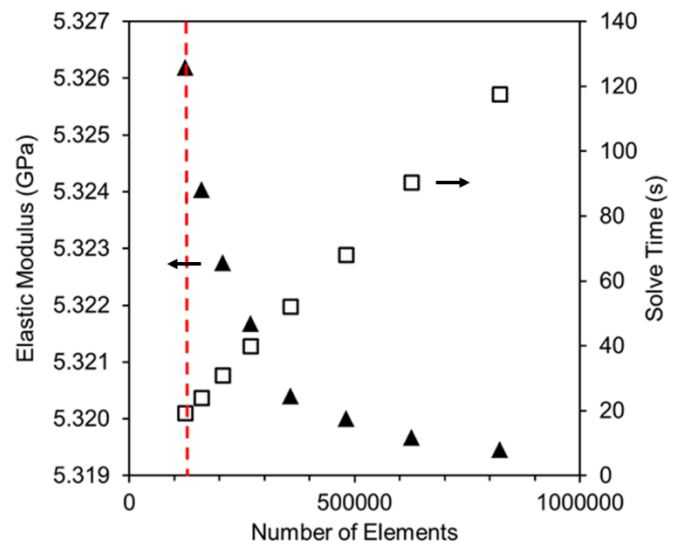


Figure 2-6. Mesh refinement study showing the convergence of the calculated elastic modulus as the number of elements is increased (reduced mesh size), compared to the increases in solve time. The dashed red line indicates the selected, optimal mesh size.

2-6 was chosen as it only creates an error of  $\sim 0.1\%$  from the calculated value at the highest level of refinement sampled.

#### 2.4.1.3 Determination of Representative Volume Element Size

We define the “size” of the RVE by the number of inclusions it contains. To determine a suitable RVE size, the number of randomly filled spherical particles with an interphase layer inside a cubical domain of arbitrary length was incrementally increased

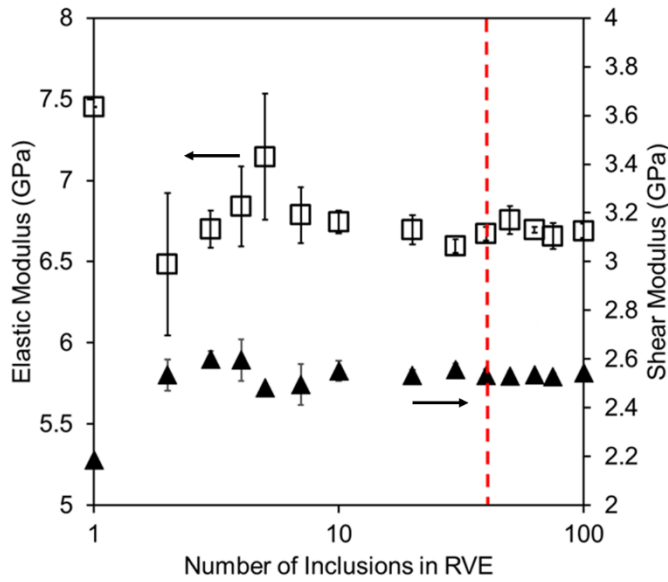


Figure 2-7. Statistical convergence of effective elastic moduli as the size of the RVE is expanded. Each data point is calculated as an average modulus of three randomly filled RVEs. Error bars indicate the standard deviation due to randomly drawn RVEs. The dashed red line indicates the selected, optimal number of inclusions in the RVE.

from 1 to 100 while holding the meshing density (Appendix A, AD-2), relative interphase thickness, and volume fraction constant. A typical epoxy matrix reinforced by silica spheres at a volume fraction of 25% was used as the representative composite material. The interphase relative thickness and elastic modulus were set to 0.1 and 15 GPa,

respectively, representing values in the mid-range of their corresponding parameter bounds.

For each RVE size, three separate RVEs were generated, each with a different random configuration of spherical fillers. The effective moduli for each RVE were

calculated in triplicate per Section 2.4.1.2 and averaged for each RVE size. A satisfactory statistical convergence of the effective material properties was used to select the appropriate RVE size. Figure 2-7 shows the convergence of the elastic and shear moduli as the RVE is expanded. The error bars indicate the standard deviation of the calculated moduli across triplicate RVE predictions. If we assume the effective properties for the largest RVE size represent the best statistical representation of a randomly filled system, then we can compare the accuracy of the solution at other sizes to this value. A size of 40 inclusions was selected as optimal, as RVEs with at least 40 inclusions yielded moduli statistically equivalent to the RVEs with 100 inclusions and had small deviations between random RVE realizations. Simulating a smaller number of inclusions permits larger mesh sizes and reduced computational expense but increases effective property variance due to random inclusion placement and error due to RVEs that poorly represent a randomly filled, isotropic composite.

## ***2.4.2 Bayesian Inference of Interphase Parameters***

### ***2.4.2.1 Gaussian Process Surrogate Model***

For this analysis, the Kennedy O'Hagan model<sup>84</sup> was employed, which is a two-stage model that first develops a Gaussian process (GP) surrogate model based upon training data, and then calibrates the necessary parameters, as well as a discrepancy function that represents the bias of the surrogate model to reality. The first step of performing the statistical analysis is to build a surrogate model that effectively predicts the output values based on a given set of inputs. GP models are chosen in this framework

as they are excellent interpolators and provide an effective means of uncertainty quantification.<sup>91</sup>

Prior to the training of the GP model, an ANOVA based sensitivity analysis was performed to determine which parameters are critical to include in the surrogate model. The results of sensitivity analysis in Table 2-4 for the G-PS composite suggest that none of the parameters should be removed from the model.

Table 2-4. Sensitivity analysis of model features to data

<b>Model Feature</b>	<b><math>R^2</math> (as a percentage) **</b>
Interphase Modulus	44.5
Interphase Relative Thickness	22.9
Filler Volume Fraction	32.6

\*\* Can be considered as a percentage contribution to the variation in the data.

The collection of FE simulations is then used to train the GP in which the parameters are selected, as detailed in Section 2.4.1.1. Each input and output is normalized to have a mean of zero and a standard deviation of one so that each parameter is represented equally. It is assumed that there is a small variation in successive simulations from identical control inputs, as discussed in Section 2.4.1.3, so the surrogate model should reflect a white noise component. This is used to describe the simulation more accurately and improve the conditioning of the posterior covariance matrix to avoid numerical inaccuracy.

Since it is reasonable to expect that the output has a smooth relationship with the inputs, a square exponential radial kernel is selected, as it produces infinitely differentiable realizations.<sup>84</sup> To allow each input to have an individualized effect on the

output, a product exponential kernel  $k(x, y) = \tau \exp\{-\sum_{i=1}^3 d_i |x_i - y_i|^2\}$  is selected rather than an isotropic radial exponential kernel. In the context of functional estimation, one can interpret  $\tau$  as a measure of the variation of the function, and each  $d_i$  can be interpreted as a measure of the smoothness of the output with respect to each input with values closer to zero, indicating a smoother relationship.

Estimation is performed through a Bayesian design, and posterior distributions are approximated via the Metropolis-Hastings algorithm.<sup>84</sup> Prior distributions for the smoothness parameters are selected to encourage the parameters to stay close to zero so that the resulting surface generated does not overfit the data and captures general trends.

#### *2.4.2.2 Cross-Validation of the Gaussian Process Surrogate Model*

Cross-validation of the GP is necessary to accurately evaluate the surrogate model's ability to model behavior outside of training data. A GP model with too few training observations will not fully capture the underlying computer model features and could be prone to overfitting. One can train the GP on a subset of the training data by using hold-out data and testing model accuracy on the held-out data. This cross-validation strategy will give a measure of conformity to the true FE solution in areas where observed data was withheld from the GP training. A random permutation hold-out method was used for cross-validation. In each random permutation, 10% of the FE observations were withheld for testing, and 90% were used for training. The hold-out method was repeated for a total of four splits.

The cross-validation results are shown in Figure 2-8. By plotting the true values, determined by the FE model, versus the GP predictions, we can observe the fidelity of the surrogate. The average slope and  $R^2$  from the four permutations were 1.02 and 0.989, respectively, with y-intercepts close to zero, indicating good agreement between the GP predictions and the withheld FE observations.

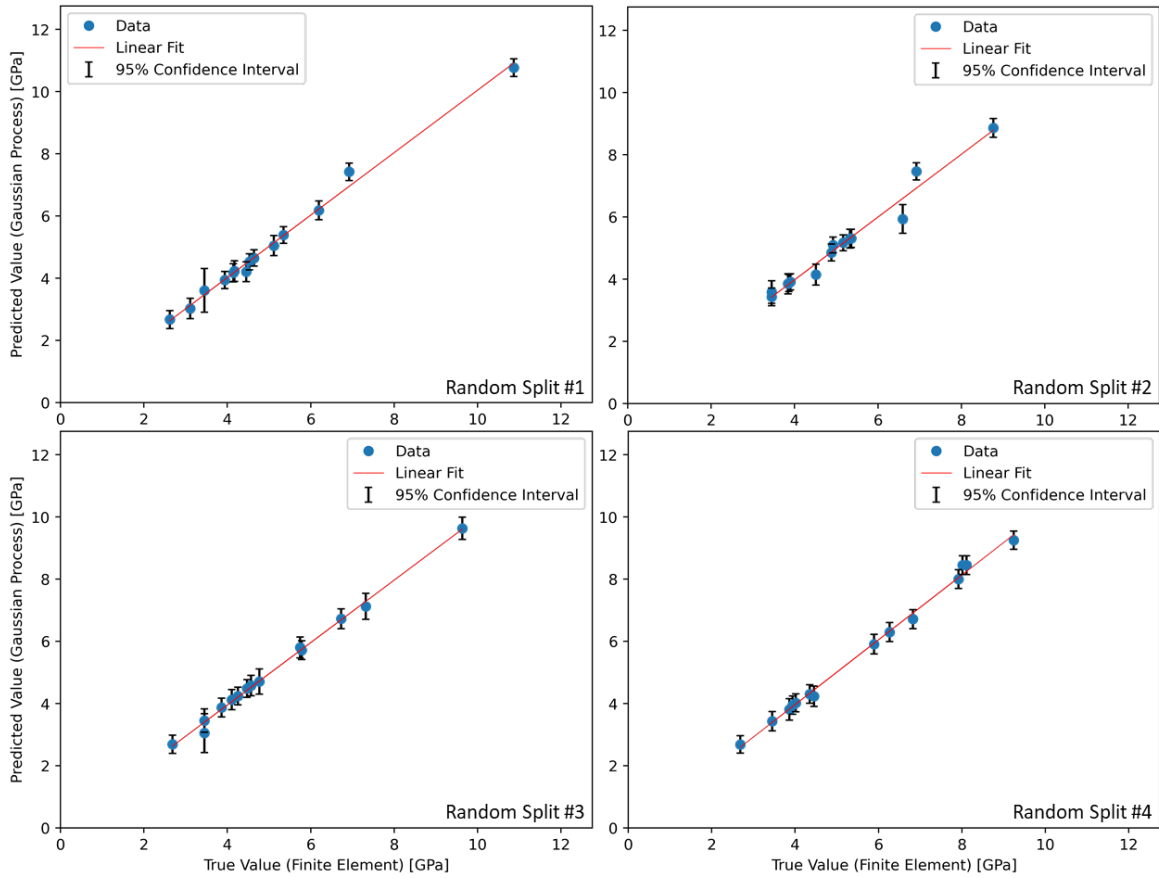


Figure 2-8. Cross-validation of the GP using four random permutations of training and testing subsets. Linear fits of each split are plotted as solid lines. Slopes close to unity with y-intercepts of zero indicate a good ability of the GP to predict the true finite element observations.

Predictions (or slices) drawn from the trained GP surrogate model (i.e., predictions across one dimension while holding the other parameters constant) are shown in Figure 2-9. The results confirm that the trained GP surrogate predictions align with the expected behavior as follows:

Figure 2-9a. As the filler volume fraction approaches zero, the surrogate model estimates an elastic modulus close to the matrix modulus. This is expected, as there should be no reinforcing effects from filler or interphase contributions when only the matrix is present.

Figure 2-9b. A constant elastic modulus is observed for a relative thickness of zero as the interphase modulus is varied. Variations in the interphase modulus should not affect the overall elastic modulus when the interphase is insignificant.

Figure 2-9c. Consistent with expected behavior, increasing the interphase modulus at non-zero volume fractions and interphase thicknesses increases overall modulus.

Figure 2-9d. As expected, increasing the interphase thickness (interphase volume fraction) increases the overall modulus when the interphase modulus is greater than that of the matrix modulus.

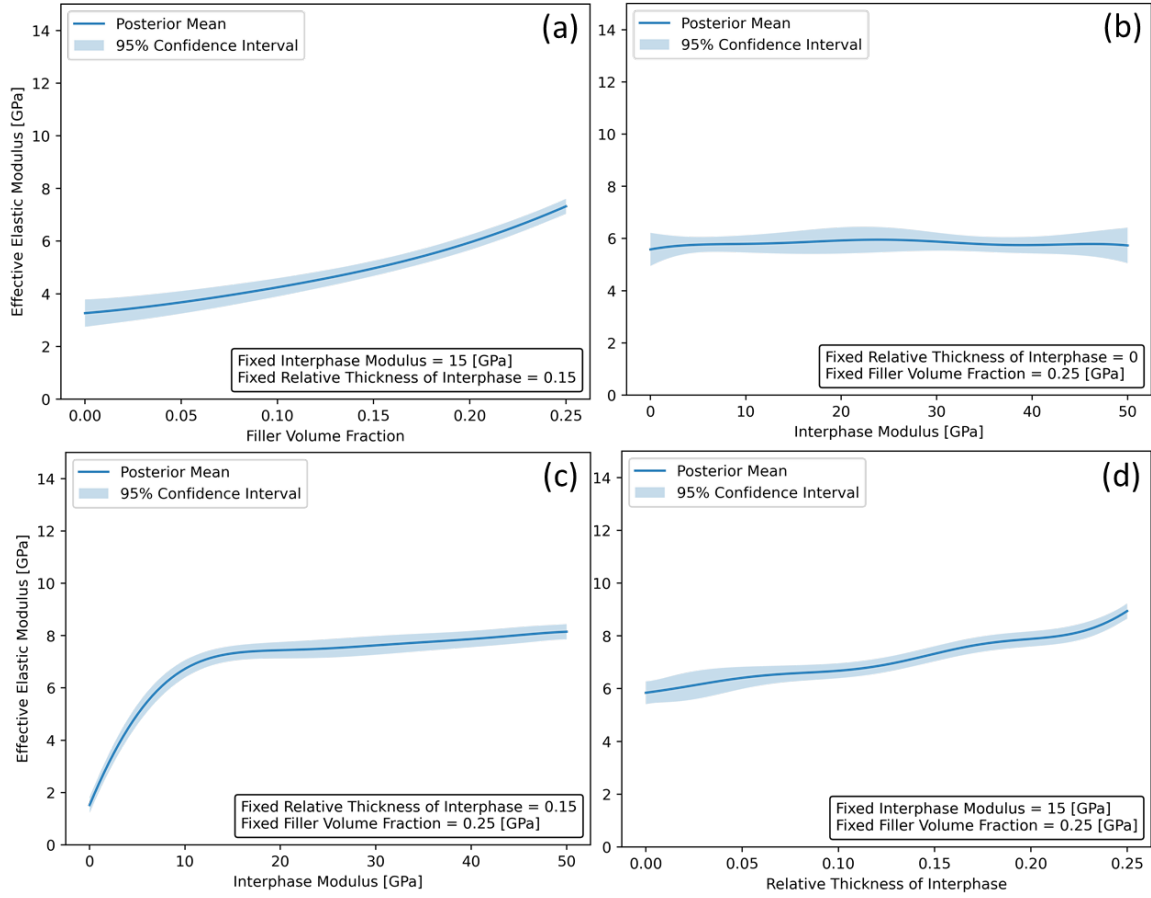


Figure 2-9. One-dimensional slices from fully trained GP across the (a) filler volume fraction, (b) interphase modulus at zero thickness, (c) interphase modulus at non-zero thickness, (d) relative thickness of interphase. Results validate expected physical behavior is predicted. Values in the legend represent the fixed, constant values assigned to the variables.

Figure 2-10 shows two-dimensional slices of the interphase calibration parameters while holding the volume fraction constant (additional angle in SI). When the interphase modulus is greater than that of the matrix modulus (3.45 GPa), any relative thickness increase increases the overall effective elastic modulus. This observation agrees with the expected behavior. Increasing the thickness when the interphase modulus is less than the matrix modulus results in a slight decrease in overall modulus because a higher modulus



matrix is replaced with a lower modulus interphase. The complex surfaces predicted in Figure 2-10 highlight the advantages of a non-parametric surrogate modeling approach. In addition, the stochastic nature of this approach permits the quantification of uncertainty, thereby driving statistical inference, which is discussed in the next section.

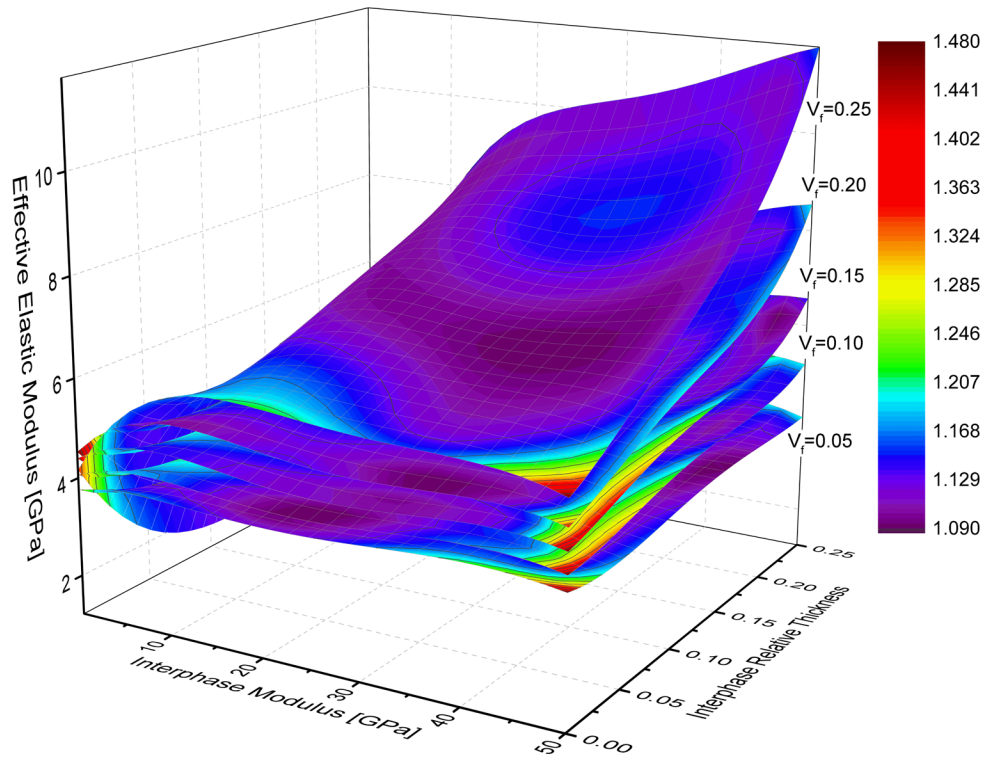


Figure 2-10. Two-dimensional slices at various fixed volume fractions, illustrating the effects of the two calibration parameters on the overall effective elastic modulus. The heat map indicates the confidence intervals estimated from the posterior distribution at a given set of inputs.

$$E_m = 3.45 \text{ GPa} \quad E_f = 70 \text{ GPa} \quad \nu_m = 0.34 \quad \nu_f = 0.22$$

#### 2.4.2.3 Bayesian Inference

The methodology is illustrated using the experimental data for the G-PS composite (See Appendix A for the results from the other five composites in Table 2-2). This experiment contains observations of Young's modulus for varying filler volume fractions and for particles of size 4, 30, and 100- $\mu\text{m}$ . In an elementary sense, one may think of Young's modulus as a weighted volume average of the filler, interphase, and matrix modulus. Therefore, as relative interphase thickness increases, the effect of interphase modulus becomes more pronounced, which indicates that the effects of relative interphase thickness and interphase modulus are reciprocal in describing elastic modulus. To avoid this confounding effect, considerations were made to limit the values which the parameters could take during calibration. For a given composite system under the same processing conditions, prior published research suggested that the interphase thickness remains relatively constant for similar particle sizes.<sup>74</sup>

To effectively constrain the parameters, the calibration parameters are defined as follows:

- $\theta_i$  the interphase modulus for particle size  $i$ . This value is sought for the particle sizes 4, 30, and 100- $\mu\text{m}$  particles (i.e.,  $\theta_4$ ,  $\theta_{30}$ ,  $\theta_{100}$ )
- $\rho_0$  and  $\rho_1$ , the variables that define the relationship between absolute thickness and particle radius as follows:

$$\text{Absolute Thickness} = \rho_0 + \rho_1 \times \text{Particle Radius}.$$

The benefit of this parameterization approach that focuses on absolute interphase thickness is the ability to evaluate particle size effects on the interphase thickness while reducing the number of parameters and mitigating the risks of overfitting (i.e., a two-parameter model for three particle sizes). It is important to note that this approach still considers the possibility that absolute thickness does not depend on particle size (in the case  $\rho_1 = 0$ ). This formulation provides a means of evaluating whether absolute thickness is a function of particle size for a given material system, which is described later in greater detail. Calibration parameters are assumed to follow a truncated normal distribution *a priori* with large variance to encourage exploration of the constrained domain.<sup>92</sup> The upper and lower bounds for each interphase modulus parameter coincide with those in Table 2-3. The bounds for  $\rho_0$  and  $\rho_1$  are set so that each resulting absolute thickness, when converted to relative thickness, remains in the bounds for relative thickness given in Table 2-3.

The model for calibration includes a discrepancy GP for each particle size, which is included to capture the model bias against experimental data. If one were to assume there is no experimental error in data collection, the discrepancy would capture the bias of the surrogate model to reality. However, as Vollenberg and Heikens<sup>79</sup> note, there is a 5% experimental error in data collection, implying that the discrepancy also captures the experimental error. The magnitude of the discrepancy also indicates how effective the FE simulation represents the experimental data. Histograms of the posterior distributions of the calibration parameters are shown in Figure 2-11 and Figure 2-12. The posterior

distributions of the absolute thickness for each particle size are available as functions of the posterior distributions of  $\rho_0$  and  $\rho_1$  and are additionally given in Figure 2-11.

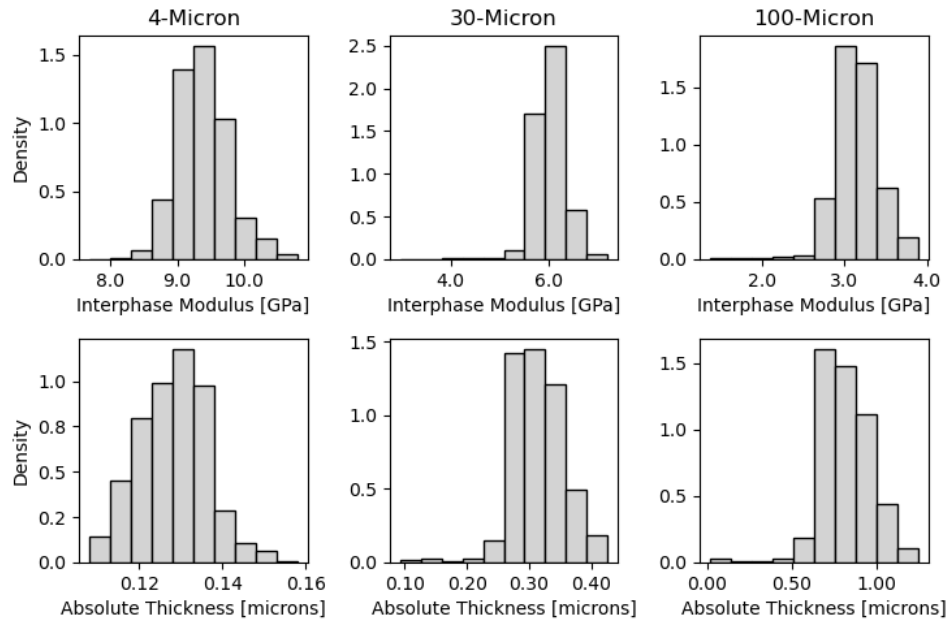


Figure 2-11. Approximate posterior distributions of the interphase modulus and absolute thickness for each particle size for the glass-polystyrene composite.

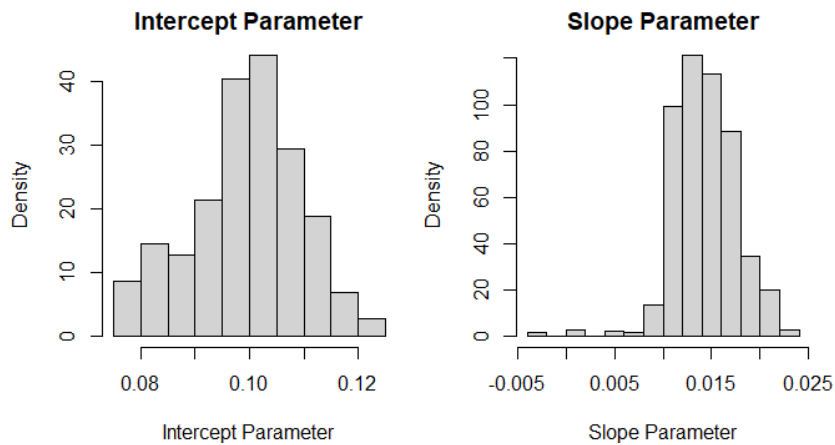


Figure 2-12. Approximate posterior distributions for the slope and intercept parameters for absolute thickness as a function of particle size for the glass-polystyrene composite.

As shown in Figure 2-12, the calibrated non-zero slope parameter suggests that the filler particle size influences the interphase thickness, but this notion will be formalized later. The posterior mode estimates for the parameters are summarized in Table 2-5.

Table 2-5. Estimated calibration parameters for the glass-polystyrene composite

Parameter	Estimate
$\theta_4$	9.3 GPa
$\theta_{30}$	6.1 GPa
$\theta_{100}$	3.1 GPa
$\rho_0$	0.10 $\mu\text{m}$
$\rho_1$	0.012

Recalling that the calibration parameters were estimated while forcing the discrepancy function to have a minimal effect, model bias is captured via Gaussian processes.<sup>84</sup> Shown below in Figure 2-13 are the plots of the discrepancy functions for each particle size. Recalling that the experimental error is around 5% and the experimental data is between 3-7 GPa, the corresponding absolute measurement error is between 0.2-0.4 GPa. Thus, observing the range of the discrepancy in the plots suggests that the calibrated model is performing reasonably well.

Cross-validation was performed to further observe the model's effectiveness by holding out a single observation from the experimental data for each particle size and recalibrating the augmented data set. As sample sizes were limited in the data set for each composite material, cross-validation was performed on the G-PP data, as it contained the most observations for each particle size.

Table 2-6 compares the calibrated parameters via holding out an observation with the calibration parameters under the whole data set. The differences in the calibration

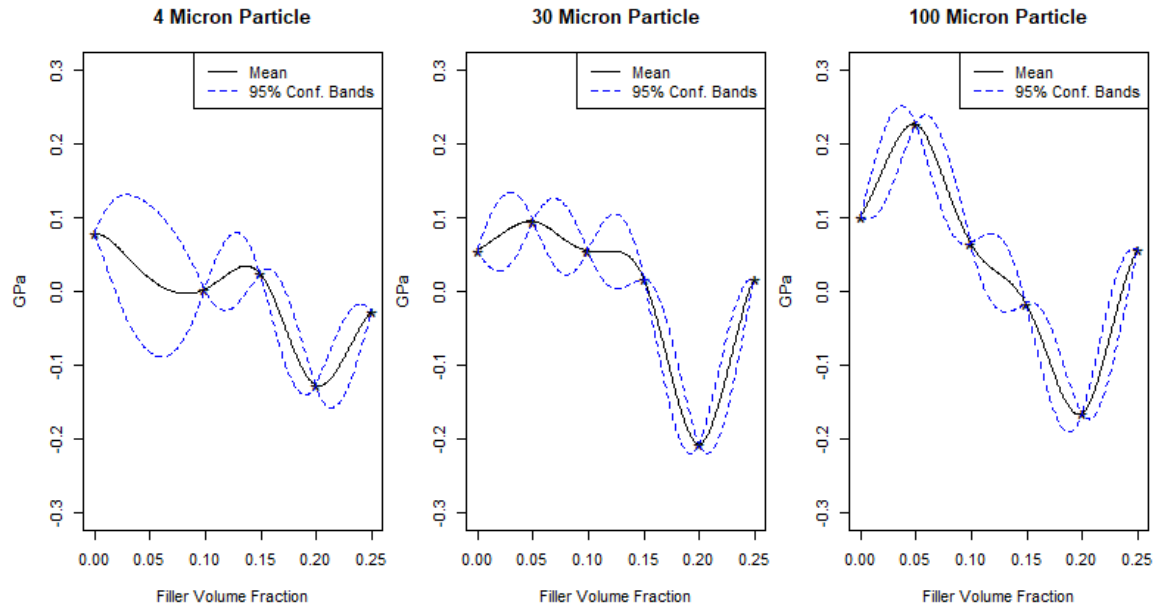


Figure 2-13. The Gaussian process discrepancy functions as a function of volume fraction with 95% confidence bands.

parameters are minimal with respect to their standard errors, which suggests that the model performs well.

Table 2-6. Comparison of the posterior estimates of the calibration parameters for purposes of cross-validation. <sup>††</sup>

	$E_{\text{int}}$ , 4- $\mu\text{m}$ [GPa]	$E_{\text{int}}$ , 30- $\mu\text{m}$ [GPa]	$E_{\text{int}}$ , 100- $\mu\text{m}$ [GPa]	Intercept	Slope	Abs. Thick., 4- $\mu\text{m}$ [ $\mu\text{m}$ ]	Abs. Thick., 30- $\mu\text{m}$ [ $\mu\text{m}$ ]	Abs. Thick., 100- $\mu\text{m}$ [ $\mu\text{m}$ ]
Holdout Data	12 (1.1)	4.6 (0.35)	1.6 (0.37)	0.094 (0.010)	0.015 (0.0022)	0.13 (0.0084)	0.32 (0.029)	0.84 (0.11)
Full Data	14 (1.11)	4.4 (0.319)	1.4 (1.8)	0.092 (0.0077)	0.013 (0.0022)	0.12 (0.0088)	0.30 (0.033)	0.76 (0.11)

<sup>††</sup> the reported values are the mode of the posterior distributions with standard deviations shown in parenthesis

The assumed linear relationship of interphase thickness as a function of particle size provides the ability to assess whether the absolute thickness depends on particle size. Results of some studies have suggested that particle size does not affect absolute thickness for similarly sized particles.<sup>74</sup> This would correspond to  $\rho_1 = 0$ . Thus, to evaluate the dependence of absolute thickness on particle size for a given material, it suffices to test the hypothesis that  $\rho_1 = 0$ . This can be achieved by constructing a  $(1 - \alpha) \times 100\%$  credible interval for the posterior distribution for a given level of certainty  $\alpha$ .

A 95% highest posterior density (HPD) credible interval for the posterior distribution for  $\rho_1$  for the G-PS composite is given by (0.0097,0.021), which does not contain zero. This suggests that particle size influences the interphase thickness of the G-PS system. The positive slope indicates that the interphase thickness increases as a function of the filler size.

## 2.5 Results and Discussion

### 2.5.1 Inferred Interphase Parameters

Recalling from Section 2.4.2.3, the intercept and slope calibration parameters,  $\rho_0$  and  $\rho_1$ , define the relationship between absolute thickness and particle radius where: *Absolute Thickness* =  $\rho_0 + \rho_1 \times \text{Particle Radius}$ . The inferred values (mode) of the interphase modulus and thickness, slope, and intercept parameters for each composite are shown in Table 2-7 for particles greater than 1 micron and Table 2-8 for particles less than 1 micron.

Table 2-7. Inferred interphase modulus, thickness, slope, and intercept for the glass composites. <sup>‡‡</sup>

Composite	E <sub>int</sub> , 4-μm [GPa]	E <sub>int</sub> , 30-μm [GPa]	E <sub>int</sub> , 100-μm [GPa]	Intercept	Slope	Abs. Thick., 4-μm [μm]	Abs. Thick., 30-μm [μm]	Abs. Thick., 100-μm [μm]
G-PS	9.3 (0.34)	6.1 (0.30)	3.1 (0.26)	0.10 (0.0097)	0.012 (0.0029)	0.13 (0.0079)	0.29 (0.039)	0.72 (0.13)
G-PC	20. (1.1)	22 (1.4)	17 (1.4)	0.24 (0.012)	-0.0041 (0.0020)	0.23 (0.011)	0.18 (0.029)	0.025 (0.098)
G-SAN	11 (1.7)	14 (1.3)	15 (1.8)	0.26 (0.020)	0.093 (0.012)	0.44 (0.0096)	1.7 (0.16)	4.9 (0.58)
G-PP	14 (1.1)	4.4 (0.32)	1.4 (1.8)	0.092 (0.0077)	0.013 (0.0022)	0.12 (0.0088)	0.30 (0.033)	0.76 (0.11)

<sup>‡‡</sup> the reported values are the mode of the posterior distributions with standard deviations shown in parenthesis.  $E_{PS} = 3.45$  GPa,  $E_{PC} = 2.15$  GPa,  $E_{SAN} = 3.80$  GPa,  $E_{PP} = 1.56$  GPa

Table 2-8. The inferred interphase modulus, thickness, slope, and intercept for the alumina composites. <sup>§§</sup>

Composite	E <sub>int</sub> , 0.035- μm [GPa]	E <sub>int</sub> , 0.4- μm [GPa]	Intercept	Slope	Abs. Thick., 0.035-μm [μm]	Abs. Thick., 0.4-μm [μm]
A-PS	24 (1.7)	21 (1.2)	0.00057 (8.4e-5)	0.26 (0.0016)	0.0051 (7.9e-5)	0.052 (0.00029)
A-SAN	40. (2.1)	40. (2.0)	-0.00013 (6.6e-5)	0.26 (0.0020)	0.0044 (5.9e-5)	0.052 (0.00037)

<sup>§§</sup> the reported values are the mode of the posterior distributions with standard deviations shown in parenthesis.  $E_{PS} = 3.45$  GPa,  $E_{SAN} = 3.80$

We can interpret whether the interphase interactions increase or decrease the overall composite stiffness by examining the relative magnitudes of the calibrated interphase moduli compared to the corresponding bulk matrix modulus. For the 100-μm G-PS composite, the interphase modulus was calibrated to be 3.1 GPa, compared to the



matrix modulus of 3.45 GPa, indicating that interfacial interactions reduced the stiffness of the matrix. This was also observed in the G-PP composite. Increases in polymer density generally result in increases in elastic properties.<sup>72,79,93,94</sup> Accordingly, possible explanations for the reduced interphase stiffness of the 100- $\mu\text{m}$  G-PS and G-PP composites could be reductions in the polymer density near the particle surface due to composite processing, entropically driven depletion zones<sup>69,95</sup> or some other phenomena. For the remaining composites and particle sizes studied, the effective interphase is predicted to have an increased modulus compared to the pure matrix, suggesting a region of increased polymer density compared to the pure matrix.

The calibrated interphase modulus for the PS and PP composites increased as the reinforcing particle size decreased to varying degrees depending on the polymer phase (Table 7). This trend was observed in MD simulations of an alumina/epoxy nanocomposite.<sup>74</sup> For the SAN and PC composites, the inferred interphase moduli do not exhibit the same particle size dependency, particularly when accounting for the standard deviation of the inferred parameter. Vollenberg and Heikens note that in the case of SAN and PC, a noticeable physical adhesion between the matrix and filler occurs, and due to the nonpolar nature of PS and PP, there is very poor adhesion between the matrix and filler. Based on this disparity, the inferred interphase moduli suggest that more favorable matrix filler compatibility will decrease particle size dependency. This is further supported by evidence where particle surface modification to enhance matrix compatibility decreases particle size dependency on the composite modulus.<sup>72,79</sup> Any

discrepancies in particle size effects on interphase properties are confounded by polymer processing methods, which likely influence the interphase properties and cannot be accounted for in this case.

Using the inferred slope and intercept for each composite, the interphase volume fraction can be approximated as a linear function of particle size and filler volume fraction by assuming monodisperse, spherical reinforcement with concentric interphase (plotted for each composite in Figure S10 of the SI). Although the calibrated interphase thickness typically increased with increasing particle size, for all composites except the A-SAN, the interphase volume fraction decreased with increasing particle size due to the differences in the number of particles at a given volume fraction. In other words, smaller particles are predicted to facilitate a larger volume fraction of interphase at a given filler volume fraction despite having a thinner interphase.

Theoretically, the inferred y-intercept parameters in Table 2-7 and Table 2-8 describe the interphase thickness as the reinforcing particle size reduces to zero. However, this mathematical description has little physical significance; (1) this value is extrapolated far from the particle sizes on which it was inferred, and (2) it is impossible to have a filler particle size of zero. The slope parameter is more insightful and explains how particle size influences interphase thickness. The highest posterior density (HPD) credible interval<sup>92</sup> for the posterior distributions of the slope parameters are in Table 2-9 for each composite system. For all except the G-PC composite, the slope parameter was positive. This indicates that increasing filler particle size for most composites increases

the inferred interphase thickness. For the G-PC composite, the interval contained zero, indicating that the particle size had no statistically significant effect on the interphase thickness.

Table 2-9. 95% Highest posterior density (HPD) credible interval for the posterior distribution of the slope parameter

<b>Composite</b>	<b>Slope Lower Credible Interval</b>	<b>Slope Upper Credible Interval</b>
G-PS	0.0097	0.021
G-PC	-0.0051	0.0017
G-SAN	0.051	0.12
G-PP	0.0086	0.017
A-PS	0.25	0.26
A-SAN	0.26	0.26

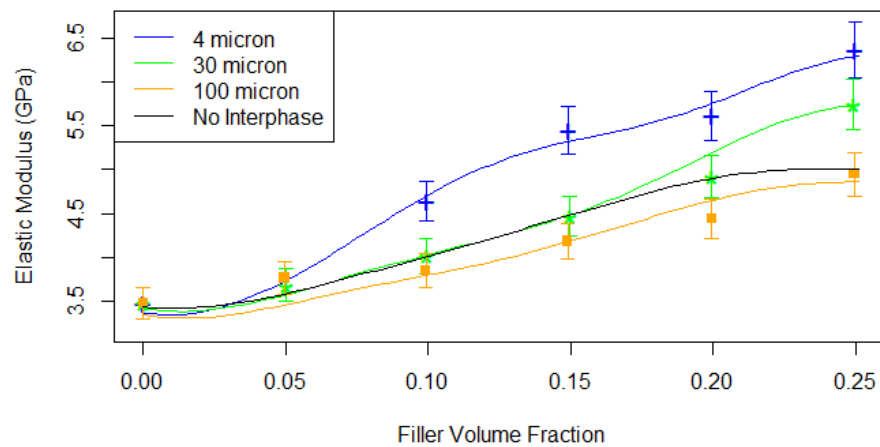
### ***2.5.2 Comparison with Experimental Data***

GP predictions of the effective elastic modulus at the inferred interphase thicknesses and interphase moduli for the G-PS composite are shown in Figure 2-14 as a slice across the relevant volume fractions. The results indicate good agreement within the experimental error ( $\sim 5\%$ ) of the data. The “No Interphase” slice is drawn from the GP by setting the relative thickness equal to zero. The inferred interphase modulus for the 100- $\mu\text{m}$  particle was 3.1 GPa, below the matrix modulus of 3.45 GPa for polystyrene. As explained in the previous section, we expect the “No Interphase” slice to lie above that of the reduced interphase modulus, 100- $\mu\text{m}$  curve. The surrogate model predictions in Figure 2-14 agree with this expectation.

The calibrated interphase parameters effectively capture the particle-size-dependent elastic behavior. It is important to recall that the FE observations used to

inform the GP in the “No Interphase” parameter space (relative thickness of zero) are generated from 2-phase RVE simulations of only matrix and filler. The interphase modulus is set at more-or-less arbitrary values within the sampled parameter bounds in this parameter space. It is possible that different fixed values of the interphase modulus could yield slightly different curves for the “No Interphase” slice, but the differences are expected to be small since this region of the parameter space was thoroughly sampled in

the  
of



design

Figure 2-14. Comparison of the calibrated and experimental results for the glass-polystyrene composite. Continuous curves are from the GP, sliced across the filler volume fraction with fixed values of the calibrated interphase thickness and modulus. The markers indicate experimental measurements.

experiments.

## 2.6 Conclusion

This work introduced a comprehensive framework to infer the effective moduli and thickness from readily obtained experimental measurements of a composite’s elastic modulus. The framework involved building FE-based micromechanical models of a

periodic RVE. A three-phase RVE consisting of a matrix, filler, and an interphase layer was simulated over a large parameter space to generate the relationship between the control/calibration parameters and the effective elastic modulus. After training a Gaussian process surrogate model on the FE model output, the GP model was calibrated against experimental data to infer the most likely interphase thickness and modulus values.

This framework was demonstrated for a polystyrene composite reinforced by randomly distributed spherical glass beads of 4, 30, and 100 microns. Results were also shown for five other composite systems. The effects of the reinforcing particle size on the inferred interphase thickness and modulus were explored. The inferred interphase parameters agree well with the experimental measurements of the composite elastic modulus and can account for the particle size-dependent elastic behavior observed in the composite systems. The proposed framework is generalizable and can be adapted to simulate any periodic composite microstructure.

## CHAPTER 3

### MULTISCALE FINITE ELEMENT ANALYSIS OF HELICALLY SYMMETRIC CELLULOSE NANOCRYSTAL-REINFORCED ALGINATE COMPOSITE FIBERS

#### **3.1 Abstract**

Cellulose nanocrystals (CNCs) incorporated into wet-spun calcium alginate fibers can result in the spiral alignment of CNCs about the alginate fiber axis. In this study, the effect of the CNC alignment on the mechanical behavior of the calcium alginate fiber composite is examined using finite element (FE) analysis at two different length scales, 1) at the “micro” level where the CNCs within a representative volume element (RVE) can be considered as cylindrical aligned with one another at a fixed angle off of the fiber axis, and 2) at the “macroscale” where the longer-range alignment of RVEs forms a helically symmetric spiral around the alginate fiber axis.

The stiffness of the RVE at the micro-level is evaluated using virtual periodic displacements to determine the resulting stresses and, thus, the effective stiffness tensor. The effective stiffness at each integration point within the global fiber model is specified by the sectorial division of the macroscale fiber model with regions of stiffness determined by analytically computed rotations of the effective stiffness tensor for a single micro-level RVE, such that the resulting rotations align with the mesoscale spiral symmetry.

The macroscale fiber model is loaded with virtual displacements to simulate loading in uniaxial tension, and the corresponding stress distributions generated in the fiber are calculated to model the effect of the CNC alignment on the macroscopic mechanical response of the fiber. The developed framework is generalizable to other composites with multiple scales of order. The results establish a structure-property link relating microstructural heterogeneity to macroscopic mechanical behavior, which is especially relevant for biomaterials, which usually have high degrees of uncertainty and heterogeneity.

## **3.2 Introduction**

### ***3.2.1 CNC Alignment and Effects on Mechanical Properties***

Alginate is a natural polymer isolated from brown seaweed that can be spun into calcium alginate fibers through a wet-spinning process.<sup>96</sup> The fibers are widely used in wound dressings, as they are non-toxic, provide excellent moisture management, and can act as a hemostatic agent due to ion-exchange processes with wound exudate.<sup>97–101</sup> To improve alginate fibers' relatively low mechanical properties, cellulose nanocrystals (CNCs) have been incorporated into the wet-spinning process.<sup>96,102</sup> CNCs are renewable, bio/environmentally friendly, and cost-effective reinforcement with high tensile strength (~10 GPa) and modulus (~140 GPa).<sup>96,102–107</sup> They are prepared via acid hydrolysis of the amorphous regions between crystalline cellulose blocks, as represented in Figure 3-1.<sup>108,109</sup>

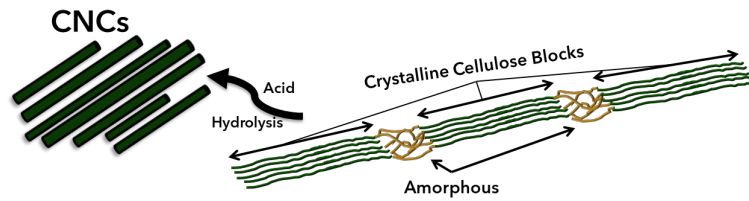


Figure 3-1. Representation of the preparation of CNCs via acid hydrolysis.

Urena-Benavides and Kitchens<sup>96</sup> observed spiral alignment of CNCs about the alginate fiber axis resulting from processing, as indicated by wide-angle x-ray diffraction (WAXD) measurements of the azimuthal peak width corresponding to the (2,0,0) reflection from the cellulose I $\beta$  crystal.<sup>102</sup> The alignment of the CNCs was found to depend upon the CNC loading and the apparent jet stretch of the fiber.<sup>96</sup> Higher loadings increased the tendency to form spiral configurations (oriented away from the fiber axis), while processing at a higher jet stretch tended to increase CNC alignment with the fiber axis. The CNC alignment about the fiber axis, idealized in Figure 3-2, resulted in a helical morphology that altered the composites' elastic modulus, tenacity, and toughness.



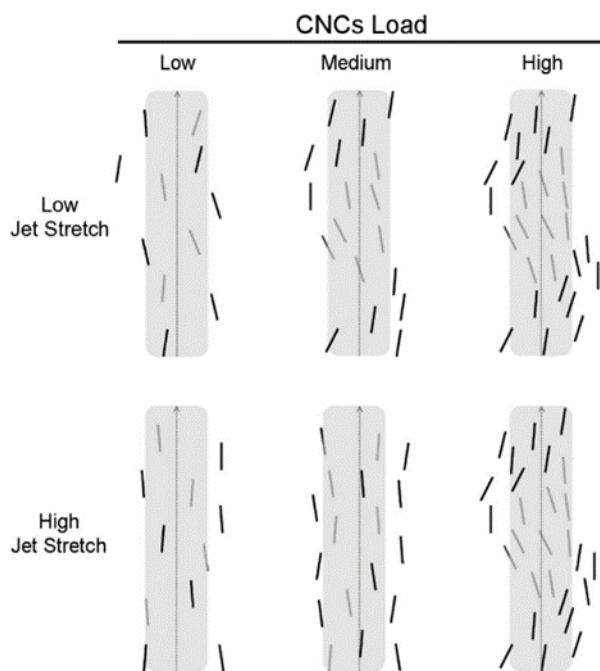


Figure 3-2. Schematic representation idealizing the helical morphology of the CNC calcium alginate fiber. Figure taken from Urena-Benavides and Kitchens<sup>59</sup>

Chen et al.<sup>110</sup> noted similar observations in a system of dry-spun cellulose acetate (CA) fibers reinforced by CNCs. Using 2D XRD, the alignment of the CNCs about the fiber axis was quantified with Herman's order parameter ( $S$ )<sup>102,111,112</sup> and was found to increase with CNC loading until a critical loading of  $\sim 30$  wt %. As expected, the mechanical properties correlated strongly with CNC alignment with the fiber axis until the critical loading. The failure mechanism at concentrations beyond the critical loading was attributed to stress concentrations from defects such as CNC agglomeration, fiber porosity, and irregular fiber diameter and cross-sectional shape. Increased shear during the spinning process increased CNC alignment with the fiber axis.

### **3.2.2 Motivation**

The spiral alignment of CNCs around the alginate fiber axis can significantly influence the composite's overall performance. This work establishes a model to understand and quantify the impact of CNC alignment by using finite element (FE) analysis at both the micro and macroscales. The proposed methodology offers notable advantages compared to traditional methods like the Mori-Tanaka<sup>27</sup> model. The micro-level analysis involves the direct simulation of a representative volume element (RVE) which captures geometric features such as the alignment of the CNCs, agglomeration effects due to inclusion placement, and stress concentrations near filler-filler interfaces and filler boundaries. The effect of polydisperse CNCs is captured by allowing the size of the simulated CNC to be sampled from a normal distribution about a mean size. The methodology also provides a means to quantify uncertainty about the spiral angle or volume fraction, which is assessed through a systematic search over a design space. Furthermore, RVE-based analyses are readily adaptable to simulate nonlinear material behavior and complex microstructures.

## **3.3 Methods**

### **3.3.1 Microscale FE Model**

Digimat-FE<sup>49</sup> was used to generate three-dimensional, rectangular RVEs of the composite microstructure by randomly distributing cylindrical inclusions representing the CNCs. The characteristic RVE consisted of an alginate matrix reinforced by forty non-intersecting cylindrical inclusions with a length drawn from a normal distribution

corresponding to a mean of 130 nm and a standard deviation of 63 nm.<sup>96,102,107,113</sup> The diameter was specified by maintaining an aspect ratio of 9.56. The orientation of the CNCs was defined as fixed, with angles theta and phi. As shown in Figure 3-3, theta characterized the deviation of the principal orientation vector of the inclusion from the fiber axis, while phi characterized the position or the rotation of the CNC about the fiber axis.

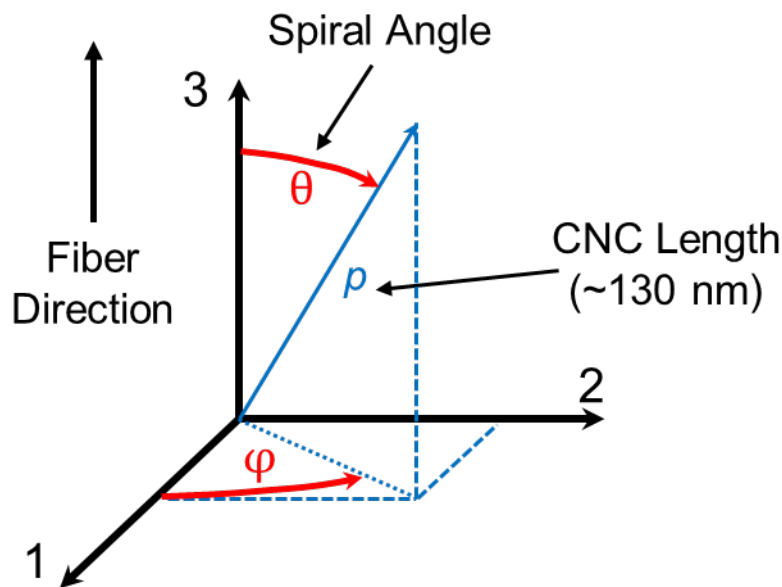


Figure 3-3. Definition of theta and phi, which characterize the fixed alignment vector of the inclusions.

The matrix and filler were treated as linearly elastic (small strain approximation) isotropic materials with perfectly bonded interfaces. Geometric periodicity was enforced, requiring filler intersections at the RVE boundaries to be cleaved and continued so that they enter the RVE from the opposite parallel surface. To analyze the effect of CNC alignment and loading on the overall elastic properties, a design of experiments (DoE)

was conducted in which the relevant micro-level parameter space was sampled using full factorial sampling. The homogenized effective elastic properties were determined over this design space as in Section 2.4.1, and a Gaussian process (GP) surrogate model was trained on the inputs and outputs of the FE micro-level model. The material properties<sup>96,102,107,113</sup> and sampled parameter space are summarized in Figure 3-4.

	<b>Predictor</b>	<b>Lower Bound</b>	<b>Upper Bound</b>
	Matrix Modulus	487 MPa	487 MPa
	Filler Modulus	143 GPa	143 GPa
	Matrix Poisson's Ratio	0.30	0.30
	Filler Poisson's Ratio	0.38	0.38
Parameter Space	Filler Volume Fraction	0.05	0.25
	CNC Spiral Angle, $\theta$	0°	16°
	CNC Position, $\varphi$	0°	360°

Figure 3-4. Material properties assigned to the matrix and filler, along with the bounds specified by the design of experiments.

### 3.3.2 Mapping from Micro to Macroscale

The multiscale analysis entails mapping the homogenized material properties to transition from the micro- to the macroscale. As illustrated in Figure 3-5, the global anisotropic stiffness matrix is expected to be a function of  $\theta$  and  $\varphi$ . Mapping was performed by computing the anisotropic effective stiffness tensor at the micro-level for one RVE for a given set of fixed parameters, rotating the fourth-order stiffness tensor using Euler rotations<sup>114–117</sup>, and mapping the rotated tensor to each Gauss integration point of the macroscopic fiber model. In practice, this was achieved in ANSYS<sup>50</sup> by partitioning the fiber into “pie slices” of  $d\varphi$  from zero to 360 degrees, where each slice is

assigned a unique material corresponding to its rotated anisotropic stiffness tensor. A total of 20 sectorial divisions were used. Too many divisions lead to small, irregular meshes at the boundaries where each material is joined in the center of the fiber (radius=0). Each unique material profile's generation, assignment of anisotropic stiffness matrix, and importation into ANSYS was automated via Python batch code to import the materials as "Engineering Data."

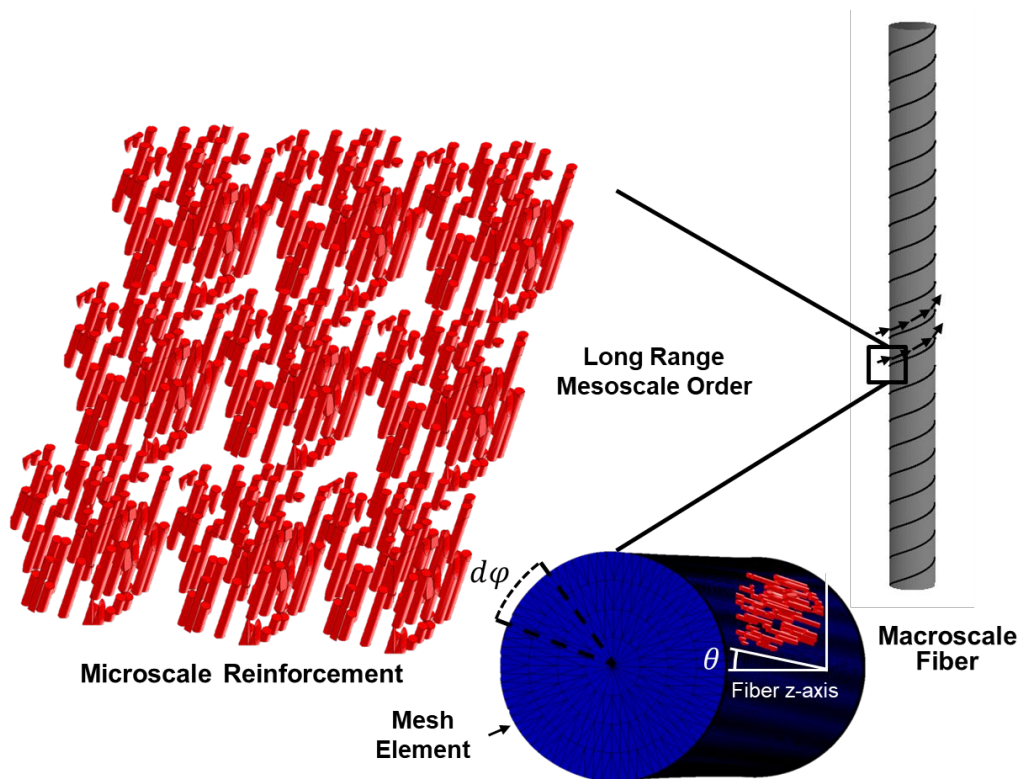


Figure 3-5. Mapping of the microscale RVE to the global macroscale fiber model.

### **3.3.3 Macroscale Fiber Model**

The macroscale FE model representing the CNC-reinforced alginate composite was simulated as a cylinder with a length of 30 mm and a diameter of 400 microns. The entire workflow was automated using ANSYS Workbench scripting, including; the generation of materials, assignment of stiffness matrix, drawing of the fiber geometry in SpaceClaim, assignment of materials corresponding to each partition to the appropriate body, and post-processing commands. The model was meshed using ten-node quadratic tetrahedral elements (SOLID187) assigned to three-dimensional RVE components. Eight-node contact elements (CONTA174) represented bonded contact between intersecting three-dimensional target surfaces (TARGE170). A sweep method was used, and the meshing was refined near the ends of the fiber where stress concentration was expected due to applied boundary conditions. A uniaxial tension test was simulated by constraining all nodal degrees of freedom of the negative z-direction surface nodes and displacing the nodes on the opposite parallel surface in the positive z-direction at 5% strain. All rotational and the x and y translational nodal displacements on the displaced surface were unconstrained to visualize the rotational effects of the helical CNC symmetry.

## **3.4 Results and Discussion**

An example microscale RVE of perfectly aligned CNCs in the fiber direction is shown in Figure 3-6, undergoing one of six loading conditions (uniaxial loading in the z-direction) used to evaluate the effective or homogenized elastic stiffness matrix. The

colored contours represent the accumulation of von-Mises stress as the RVE is loaded. The three plots on the left side show the matrix and filler for a single RVE at the beginning, middle, and end of the loading, while those on the right have the matrix material hidden from view.

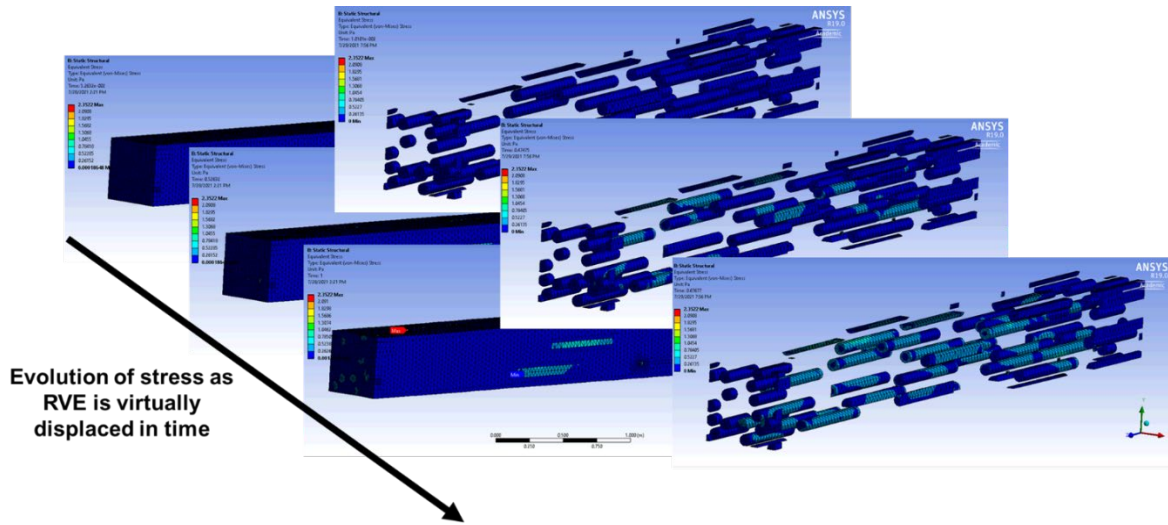


Figure 3-6. Example microscale RVE of perfectly aligned CNCs in the fiber direction undergoing one of six loading conditions (uniaxial loading in the z-direction) used to evaluate the effective or homogenized elastic stiffness matrix. The colored contours represent the accumulation of von-Mises stress as the RVE is loaded. The three plots on the left side show the matrix and filler for a single RVE at the beginning, middle, and end of the loading while those on the right have the matrix material hidden from view.

### 3.4.1 Elastic Modulus Sensitivity to CNC Spiral Angle and Circumferential Position

The sensitivity of the homogenized elastic modulus in the z-direction ( $E_z$ , aligned with the macroscale fiber axis) to the CNC spiral angle and circumferential position,  $\theta$  and  $\varphi$ , respectively, was assessed by the surrogate model trained on data from the micro-level FE model. Slices across the varied parameters,  $\theta$  and  $\varphi$ , were taken while fixing the filler volume fraction. The results are shown in Figure 3-7 for a fixed volume

fraction of filler  $V_f$ . The results indicate, as expected, a decrease in the axially aligned modulus when the CNCs are oriented away from the fiber direction by an increase in  $\theta$ . Furthermore, this modulus is insensitive to rotations about the circumference by an angle  $\varphi$ .

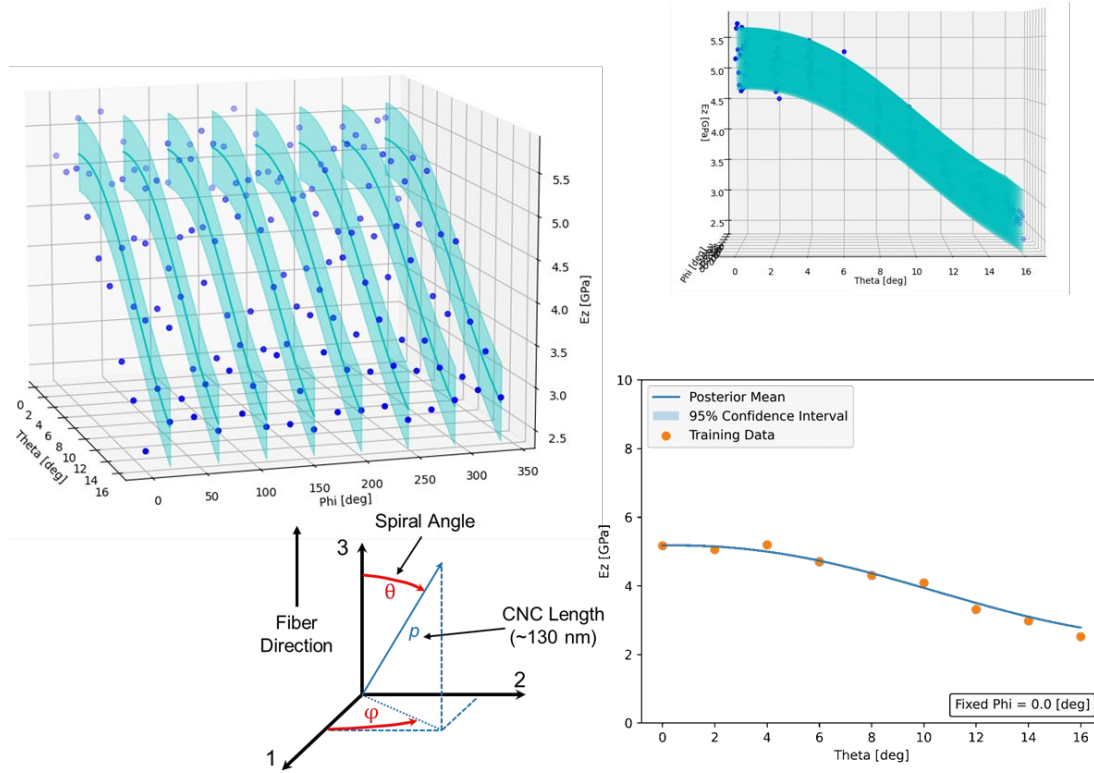


Figure 3-7. Gaussian process surrogate predictions for the elastic modulus in the z-direction ( $E_z$ ) as a function of the CNC spiral angle and circumferential position,  $\theta$  and  $\varphi$ , respectively. The volume fraction of filler was fixed at 0.25. Curves represent the GP posterior mean, shaded regions represent 95% confidence intervals, and the markers represent the underlying training data from the micro-level RVE.



### 3.4.2 Elastic Modulus Sensitivity to CNC Spiral Angle and Volume Fraction

The sensitivity of the  $E_z$  to the volume fraction was visualized in Figure 3-8 by taking parameter slices from the GP across the relevant domains of  $\theta$  and  $V_f$  while the circumferential position,  $\varphi$ , was fixed at zero degrees. As expected, increases in the volume fraction of CNCs increase the  $E_z$ . This effect is mitigated when the CNCs are oriented at large spiral angles away from the fiber direction.

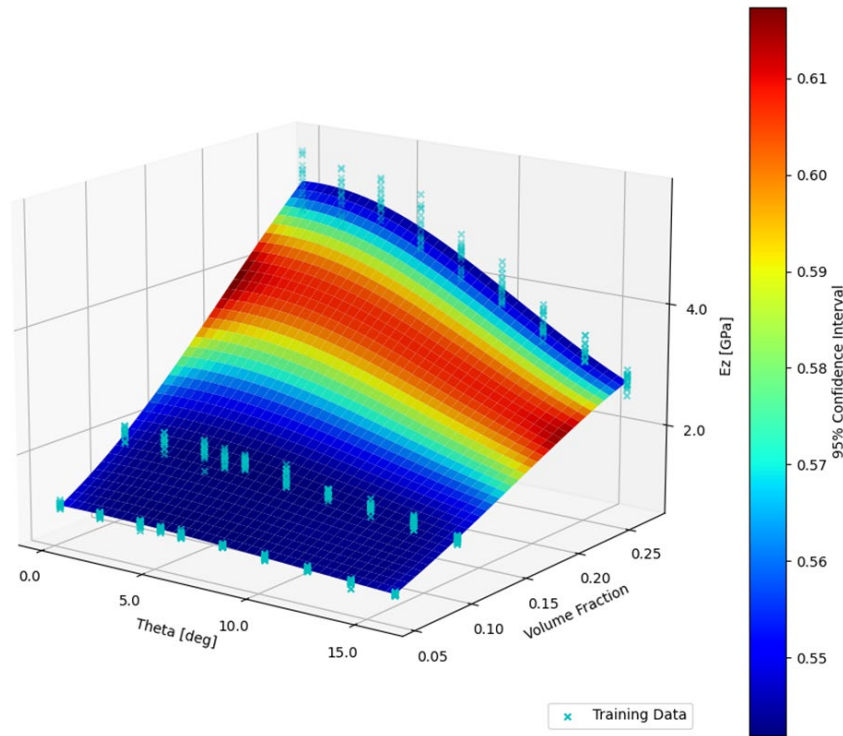


Figure 3-8. Gaussian process surrogate predictions for the elastic modulus in the z-direction ( $E_z$ ) as a function of the CNC spiral angle and volume fraction,  $\theta$  and  $V_f$ , respectively. The circumferential position,  $\varphi$ , was fixed at zero degrees. The surface plot represents the GP posterior mean, the heat map represents 95% confidence intervals, and the markers represent the underlying training data (shown for all values of  $\varphi = 0 - 360^\circ$ ) from the micro-level RVE.

### 3.4.3 Validation of the Microscale FE Model

The microscale FE model was validated by comparing the  $E_z$  determined by analytically computed rotations of a stiffness tensor (for the RVE corresponding to perfectly aligned CNCs in the fiber direction at a fixed  $V_f$ ) to the  $E_z$  predicted at equivalent values of  $\theta$  and  $\varphi$  by the finite element model. The results in Figure 3-9 indicate similar predicted values and trends and, thus, good agreement between the FE model predictions and analytical solution.

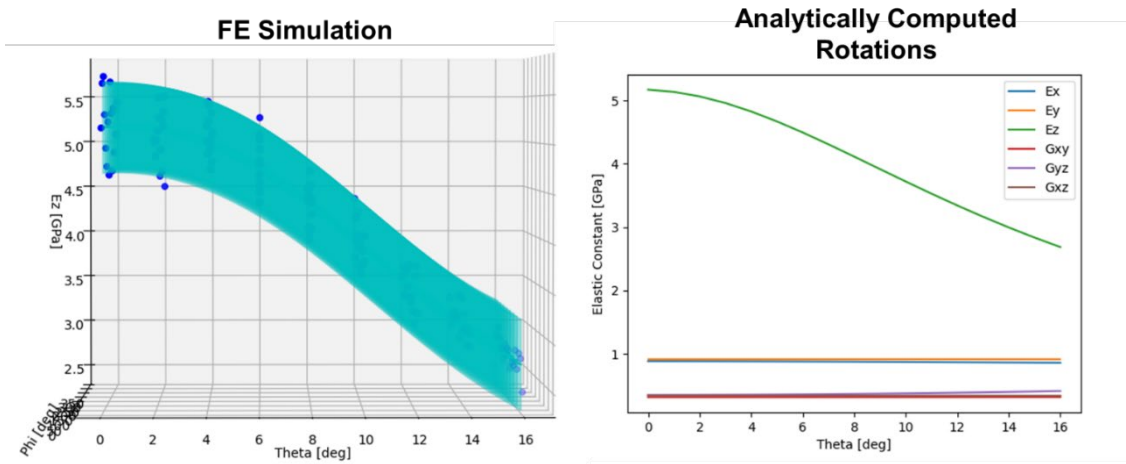


Figure 3-9. Validation of the FE model by comparing the  $E_z$  from analytically computed rotations of a stiffness tensor (at a fixed  $V_f$ ) to the  $E_z$  predicted at equivalent values of  $\theta$  and  $\varphi$  by the finite element model. Similar values and trends indicate good agreement.

### 3.4.4 Macroscale Fiber FE Model Results

The homogenized stiffness tensor calculated for a particular rotation of  $\theta$  and  $\varphi$  was mapped to the macroscale model representing the helically symmetric CNC-Alginate composite undergoing a virtual uniaxial fiber tension test. The evolution of von-Misses

stress and its subsequent effect on the rotation of the fiber about its axis is shown in Figure 3-10. The globally anisotropic nature of the mapped stiffness throughout the fiber induces a rotation about the fiber z-axis. This effect is entirely due to the microstructural order since nodal degrees of freedom (on the positive z surface) were only constrained in the positive z-direction.

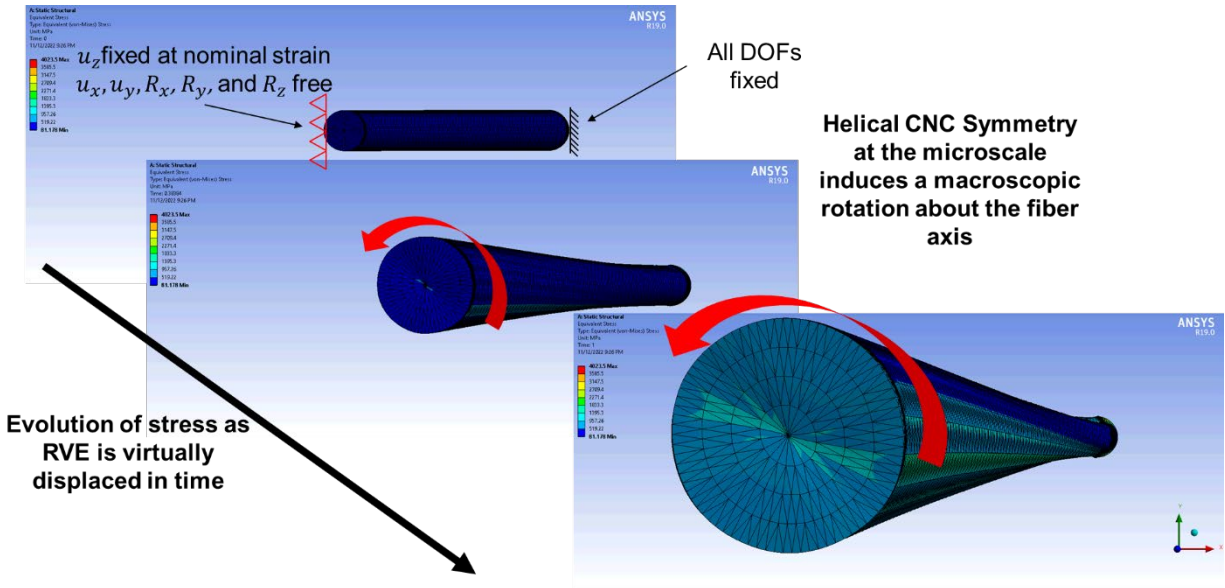


Figure 3-10. The macroscale fiber model undergoing uniaxial loading in the z-direction mapped with helical symmetry of the stiffness tensor which was calculated from the microscale FE model. The colored contours represent the accumulation of von-mises stress as the RVE is loaded. The three plots show matrix and filler stresses that accumulate during the beginning, middle, and end of the loading.

The twisting of the fiber matches the expected behavior for the prescribed loading conditions; however, in an actual uniaxial fiber tension test, mechanical grips at the fiber ends would constrain rotations about the z-axis, and instead, internal stresses would accumulate. The macroscopic fiber behavior confirms the transmission of the configurational information from the microscale to the macroscale.

It should be noted that the fixed support used to constrain the negative-z surface leads to an over-constraint of the surface. Over-constrained edge effects occur when a structure is over-restrained or fixed at its edges rigidly. In such cases, fixed supports restrict the material's natural lateral deformation and displacements, resulting in excess localized stress near the edges. The Poisson effect drives this effect and is quantified by the Poisson's ratio. The Poisson effect expresses the tendency of a material to contract or expand in directions perpendicular to loading. These over-constrained edge effects can drastically affect the structure's behavior and overall performance, causing lateral deviations from idealized behavior.

### 3.5 Conclusions

The impact of the helical alignment of cellulose nanocrystals (CNCs) on the macroscopic mechanical behavior of wet-spun calcium alginate fibers was studied in this chapter. Finite element (FE) analysis was performed on models at two separate length scales to map the micro-level configuration information to the macro-level. The effective stiffness of a representative volume element (RVE) was calculated at the microscale by considering the fixed alignment of CNCs at angles  $\theta$  and  $\varphi$  from the fiber axis. Longer-range RVE alignment was mapped to the macroscale by considering a helically symmetric spiral around the composite fiber axis.

The microscale model was validated based on analytical solutions for rotations of the RVE's effective stiffness tensor. The sensitivity of the effective elastic properties to the volume fraction of filler,  $\theta$ , and  $\varphi$  was evaluated using a Gaussian process surrogate

model. The homogenized effective stiffness tensors of the helically aligned CNCs induced a rotation in the macroscopic fiber model due to the symmetries of the generated stress that accumulated during uniaxial tension. The proposed methodology illustrates a robust approach to simulating multiscale phenomena and quantifying the effect of uncertain parameters on macroscopic mechanical behavior, a critical component for analyzing biomaterials with high degrees of uncertainty and heterogeneity.

## CHAPTER 4

### GAUSSIAN PROCESS REGRESSION FOR PREDICTING MAGNESIUM OXYCHLORIDE CEMENT BOARD PERFORMANCE

#### 4.1 Introduction

##### *4.1.1 Background on Magnesium Oxychloride Cement Boards*

The non-hydraulic cement magnesium oxychloride (MOC or Sorel cement), first reported by Sorel<sup>118</sup> in 1867, has reemerged as an alternative to conventional building materials such as plywood, gypsum, oriented strand board (OSB), and Portland cement board.<sup>119</sup> MOC is an attractive material owing to its rapid setting times, high specific flexural and compressive strengths<sup>120,121</sup>, good thermal, fire, and abrasion resistance, compatibility with diverse filler materials<sup>122</sup>, and acoustic dampening<sup>123</sup>. MOC is primarily used in construction as wall insulation panels, roofing elements, floor tile, and backer board.<sup>124</sup> Other applications include use as an abrasive agent in grinding wheels and as a reinforcing and binding agent in lightweight, high-strength rubberized concrete.<sup>125,126</sup> MOC has been explored as a potential resorbable orthopedic biomaterial for bone repair since it exhibits good biocompatibility and antibacterial characteristics.<sup>127–130</sup>

MOC is formed by mixing an aqueous solution of magnesium chloride with light-burnt magnesium oxide (magnesia) powder.<sup>131</sup> The reaction proceeds with the formation of a number of crystalline phases determined by molar ratios of the ternary  $\text{MgO} \cdot \text{MgCl}_2 \cdot \text{H}_2\text{O}$  mixture, curing temperature and humidity, and magnesia

reactivity.<sup>122,131</sup> Phases 3 and 5 are primarily responsible for the hardening and strength of the final cement, with the latter being the dominant and preferred phase regarding mechanical properties.<sup>121,131</sup> The curing process produces mechanically interlocking and interpenetrating needle-shaped crystals characterized as scroll-tubular whiskers that result in a space-filling, dense microstructure of low porosity.<sup>123,131,132</sup> The desired reaction to produce Phase 5 MOC competes with the formation of Phase 3 and brucite (Mg(OH)<sub>2</sub>). Excess water in the reaction mixture can favor the production of a mechanically loose brucite phase, while excess MgO can lead to reduced workability and incomplete hydration.<sup>121,133,134</sup> Excess MgCl<sub>2</sub> drives the formation of Phase 3 MOC and can lead to free chlorides in the cured cement.<sup>135</sup> As MOC ages in the presence of CO<sub>2</sub>, there is a potential for carbonation at the surface to form a semi-protective layer of chlorartinite, a crystalline phase that has been suggested to preserve the mechanical integrity of MOC in moist conditions.<sup>136–138</sup>



Commercial MOC boards for building applications commonly incorporate fillers like wood flour and perlite to reduce the material's cost and density, improve the paste's workability, and increase thermal insulation and acoustic dampening. Wood flour can reduce brittleness and increase toughness, improving the ability of the material to hold nails or screws without fracture.<sup>122,139</sup> Foaming and de-foaming agents may be added to

the mixture to modulate the board's workability and final porosity (density). Adding foaming agents increases the air entrainment in the mixture resulting in a lower board density at the expense of reducing the mechanical properties through a disruption in the interlocking MOC needles.<sup>140</sup> MOC can be reinforced for structural support with glass fibers due to its relatively low pH (pH ~ 10-11), providing an advantage over traditional Portland cement boards (pH ~ 12-13), where an alkaline attack on glass is possible.<sup>122,141,142</sup> Chemical additives, such as soluble phosphates, are used to improve the strength retention and water stability of MOC in moist environments.<sup>122,143</sup> Through the judicious selection and combination of these components, MOC cements offer an advanced, customizable composite material for building applications with tunable performance properties that balance durability, processability, and environmental resilience.

Despite the numerous advantages of MOC cement boards, several challenges have limited their widespread adoption as a construction material: uncertainty in formulations due to variability in raw material quality, availability, and prices; excess free chlorides can be corrosive on metallic building materials; MOC exposed to water is susceptible to degradation; and variations in mechanical properties due to compositional and phase changes over the life of the material. Understanding the factors that dictate the mechanical properties of MOC and the development of effective formulations and manufacturing processes is crucial to its broader adoption in the construction industry.



#### **4.1.2 Motivation**

The wide gamut of fillers and additives used in commercial-grade MOC boards results in complex mixtures with modified compatibility, workability, curing rate, and hydration dynamics. Each component introduces additional variability and uncertainty in the final composite's mechanical, chemical, and physical properties by further complicating the sensitive stoichiometric reactions, selectivity, and hydration mechanisms. The complicated nature of these multi-component mixtures results in a composite board with properties that are difficult to predict a priori. Furthermore, varying raw material purities and production controls confound the accurate quantification of the uncertainty in final board properties. It is, therefore, critical to understand how these factors influence MOC board performance to optimize their formulations and production processes.

Traditional approaches to understanding how constituent materials influence macroscopic composite mechanical properties rely on analytical or semi-analytical models, such as the Mori-Tanka<sup>27</sup> or Halpin-Tsai<sup>144</sup>. Mean field theories relate local stress and strain fields experienced by inclusions to averaged fields experienced at the macroscopic level. These are often based on or are extensions of Eshleby's<sup>24</sup> closed form solution for the elastic field generated in an ellipsoidal inclusion subjected to a homogenous strain. Models in these categories are advantageous in their computational tractability but are inherently simplistic and limited in scope. They can provide accurate predictions but are usually only valid for narrow classes of materials over an even

narrower range of properties. For example, the Mori-Tanka model, widely regarded as one of the most dependable analytical models, fails to estimate multi-phase and high-volume fraction composite properties adequately.<sup>145,146</sup>

Numerical techniques have been employed in the homogenization process to ascertain the macroscopic or effective properties of composite materials and offer more accurate and robust predictions than conventional methods.<sup>34–36,87,145–149</sup> Finite element based-methods can simulate complex filler-matrix combinations and geometries by directly simulating the composite microstructure or representative volume element (RVE). While advancements in computing technology have increased the feasible modeling space for numerical micromechanical approaches, high computational demands still limit RVE complexity. This limitation is pronounced for microstructures exhibiting hierarchical length scales of order. Many composites exhibit heterogeneity at multiple length scales, spanning the nano-, micro-, and macro-scale. In such a case, RVE homogenization must be performed at each length scale, increasing the computational complexity.<sup>37,77,145,145,150–154</sup>

In this work, we propose to use Gaussian process (GP) regression to learn the relationships between the input (features) and output (targets) to model the effects of process control parameters, formulation, and composition on multiple mechanical performance metrics for fiber-reinforced MOC boards. The primary benefit of this approach is in the flexibility and nature of the inputs the model needs to make predictions. Analytical, semi-analytical, and homogenization-based approaches require

knowledge about constituent material properties, which might not be known to a high degree of certainty in the case of the complex multi-component MOC composite. Properties that are known may vary due to heterogeneity in raw materials. The material and geometric microstructure of the numerous crystalline and amorphous phases would need to be measured with reasonable accuracy for these traditional micromechanical models to be implemented. Even with a thorough understanding of these properties, the fundamental assumptions behind the models would not adequately capture the intricate, heterogeneous bonding and stress distribution mechanisms present within the actual composite material. Given the complex nature of the MOC-filler system and the uncertain constituent properties, GP regression enables the performance of the final board to be inferred directly from the available data, avoiding the need for explicit microstructural modeling.

GP regression offers flexibility in modeling complex and non-linear relationships between input features and material properties.<sup>155,156</sup> Unlike analytical methods that rely on simplifying assumptions or closed-form equations, GPs capture intricate patterns and adapt to various data distributions without explicitly defining the underlying functional form.<sup>157</sup> GPs offer more interpretability than alternative machine-learning models, such as neural networks, through intuitive feature relevance determination and kernel analysis, which is important when working with medium-sized data sets.<sup>158–161</sup> Additionally, GPs provide probabilistic predictions with uncertainty estimates, enabling a more comprehensive understanding of the confidence in the predictions.

## 4.2 Methods

### *Methods Overview:*

In this study, a predictive model was developed using GP regression to learn the relationships between various input features on target variables representing the mechanical properties of fiberglass-reinforced MOC cement boards. The training data was obtained from the production and testing of MOC boards constructed under various process controls using two different formulations in which the filler material compositions were varied. The input variables include board thickness, density, free chloride percentage, 5-phase MOC percentage, amorphous percentage, reaction selectivity, fiberglass strength, and formulation type. The output variables included flexural strength, modulus of elasticity, brittleness index, lateral nail resistance, specific flexural strength, specific lateral nail resistance, and the specific lateral nail resistance normalized by thickness. The output targets were treated as independent, with a single GP (and its associated hyperparameters) being trained for each output.

Since the dataset contained mixed data types, the GP kernel structure was constructed as a combination of two squared-exponential kernels, one over a continuous numerical domain and the other over a categorical domain space. Different mathematical combinations of the two kernels were tested. Correlations among input variables and the resultant effects on the model outputs were assessed via automatic relevance determination (ARD). Hyperparameter selection was performed by optimization of the marginal likelihood, and cross-validation was used to compare the performance of the

different kernel structures. The cross-validation results were evaluated based on performance metrics to determine the most optimal kernel combination for a model output target. The final performance for each model was evaluated using held-out validation test datasets.

#### ***4.2.1 Board Production and Data Collection***

The complete collected dataset (n=80) came from the production and testing of fiberglass-reinforced MOC cement boards. The production of the fiberglass-reinforced MOC cement boards was conducted in accordance with US Patent US7867597B2<sup>140</sup> and US10696595B2<sup>162</sup>. Two different formulations of the boards were produced, Formula A and Formula B, where each formulation is distinguished by its unique weight fraction of filler materials. The cement boards were produced by mixing magnesium chloride with water to form a brine solution and then mixing the resultant solution with magnesium oxide, perlite, and a binding agent (e.g., wood flour) to form a wet ‘mud’ that was laid onto flat polymer sheets in layers with defined thickness. The paste was further reinforced by layering a polyester mesh and fiberglass scrim on the top and bottom of the screeded mud to form a reinforced MOC board of uniform and controlled thickness. The exact filler compositions are proprietary but were within the specified bounds in the referenced patents. Three different fiberglass scrims were sampled and are delineated by their tensile strengths (75, 105, and 150 lbs/in). The thickness and density (ASTM C1185-08<sup>163</sup>) of the samples were determined from fully cured test specimens. The free

chloride percentages were determined by assessing the water-soluble chloride content in accordance with ASTM C1218-20.<sup>164</sup>

The formulation and fiberglass inputs were treated as control parameters since these were directly manipulated to understand their effect on board performance. Several input features are not directly controlled through processing but vary due to controlled parameters. These are best described as derived parameters and include board thickness, density, free chloride percentage, 5-phase MOC percentage, amorphous percentage, and selectivity. For example, the measured board thickness might be a function of the process target board thickness as well as the formulation and other uncontrolled parameters (noise) that inevitably occur during processing. All other processing conditions, such as the curing temperature, humidity, and production speed, were controlled within equipment tolerances.

#### *4.2.1.1 Determination of MOC Board Composition via X-Ray Diffraction (XRD)*

The crystalline composition of each board was determined by quantitative X-ray diffraction (XRD) using the D2 PHASER (Bruker AXS) coupled with DIFFRAC.TOPAS (Bruker AXS) software.<sup>165</sup> The composition was analyzed by fitting diffractograms via Rietveld refinement<sup>166</sup> with crystalline profiles representing 5 Phase MOC, 3 Phase MOC, MgOH, chlorartinite, MgO, and hydromagnesite along with an amorphous profile to capture any amorphous phase from incomplete crystallization, side reactions or filler materials. Selectivity was computed as the ratio of 5 Phase MOC to the sum of phases from expected side reactions.

$$Selectivity = \frac{5 \text{ Phase MOC } \%}{(MgOH + Chlorartinite + 3 \text{ Phase MOC} + MgO + Hydromagnesite)\%} \quad (35)$$

#### 4.2.1.2 Board Performance Metrics

The mechanical performance of the boards was measured using a Shimadzu 10kN precision universal tester with appropriate fixtures to determine flexural strength (ASTM C1185-08<sup>163</sup>), modulus of elasticity (ASTM D1037-12<sup>167</sup>), brittleness index, and lateral nail resistance (ASTM D1037-12<sup>167</sup>). The brittleness index was calculated as the inverse of the failure strain from the 3-point break test. The specific mechanical properties were calculated by dividing by the sample density.

#### 4.2.2 Gaussian Process Regression

Gaussian process (GP) regression is a nonparametric, Bayesian approach to learning input-output mappings from empirical data. It is a supervised machine learning method that provides probabilistic predictions with greater model interpretability than conventional methods, such as neural networks. Interpretability is important in this specific application because it allows the relationship between each input feature and the corresponding influence on the output to be structured and quantitatively accessed. GP regression also outperforms neural networks when training datasets are smaller.<sup>168,169</sup>

The derivations and notations herein follow the function-space view, presented by Rasmussen and Williams<sup>170</sup>, which is equivalent to the weight-space view. A GP is formally defined as “...a collection of random variables, any finite number of which have

a joint Gaussian distribution.”<sup>170</sup> A GP is entirely specified by its mean function  $m(x)$  and covariance function (or kernel),  $k(x, x')$ . In this study, a single GP was trained for each target output variable. The Python library GPy<sup>171</sup> was used to handle the building and optimization of the GPs.

The collected training dataset  $\mathcal{D}$  (from section 4.2.1) for a single output target consisted of  $n$  observations,  $\mathcal{D} = \{(x_i, y_i) | i = 1, \dots, n\}$ , where each input  $x$  is represented as a  $D$ -dimensional vector over the input space  $\mathcal{X} \in \mathbb{R}^D$  corresponding to an output  $y$ . The task of the regression problem was to learn the real process  $f(x)$ , which mapped the inputs to the outputs, and then make predictions at a new input  $x_*$ . The mean function  $m(x)$  was defined as the expected value of our real process  $f(x)$  and was assumed to be zero.<sup>161,170</sup> The covariance function can be considered as a measure of similarity between input  $x$  and an alternate input  $x'$ . The GP was defined by its mean function and covariance of the outputs.

$$\begin{aligned} m(x) &= \mathbb{E}[f(x)] = 0 \\ k(x, x') &= \mathbb{E}[(f(x) - m(x))(f(x') - m(x')))] = \text{cov}[f(x), f(x')] \end{aligned} \tag{36}$$

Since the collected observations were assumed to be noisy, the real process was allowed to differ from the observations by additive independent, identically distributed (iid) Gaussian noise  $\varepsilon$  with variance  $\sigma_n^2$ . Thus, the GP regression problem took the form,

$$y = f(x) + \varepsilon, \text{ where } f \sim \mathcal{GP}(0, k(x, x')) \text{ and } \varepsilon \stackrel{\text{iid}}{\sim} \mathcal{N}(0, \sigma_n^2). \tag{37}$$

The covariance functions used in this study were combinations of the popular squared-exponential (SE) kernel,  $k_{SE}$ , and a SE-ARD (automatic relevance



determination<sup>172</sup>) kernel,  $k_{SE-ARD}$ , each defined over subdomains of the input space where the Gaussian noise can be absorbed into the kernel as the noise level parameter,  $\sigma_n^2$ ,

$$k_{SE}(x, x') = \sigma_f^2 \exp\left(-\frac{(x - x')^2}{2l^2}\right) + \sigma_n^2 \delta_{xx'},$$

$$k_{SE-ARD}(x, x') = \prod_{d=1}^D \sigma_d^2 \exp\left(-\frac{(x_d - x'_d)^2}{2l_d^2}\right) = \sigma_f^2 \exp\left(-\frac{1}{2} \sum_{d=1}^D \frac{(x_d - x'_d)^2}{l_d^2}\right) + \sigma_n^2 \delta_{xx'}. \quad (38)$$

The covariance functions are expressed in terms of hyperparameters  $\theta = (\sigma_f^2, \sigma_n^2, l_d, \dots, l_D)$ , representing the output or signal variance, the noise level parameter, and the characteristic lengthscales for each dimension  $d$ , respectively. The covariance functions in Equation (38) express the covariance between outputs as a function of the inputs (and hyperparameters). The selection of hyperparameters is discussed below (Section 4.2.2.3). Once the hyperparameters are chosen, the covariance matrix  $K(X, X)$  (or Gram matrix) can be evaluated from the input data for all pairs of inputs resulting in an  $n \times n$  matrix,

$$K(X, X) = \begin{bmatrix} k(x_1, x_1) & k(x_1, x_2) & \cdots & k(x_1, x_n) \\ k(x_2, x_1) & k(x_2, x_2) & \cdots & k(x_2, x_n) \\ \vdots & \vdots & \ddots & \vdots \\ k(x_n, x_1) & k(x_n, x_2) & \cdots & k(x_n, x_n) \end{bmatrix} \quad (39)$$

or with noise,  $K(X, X) + \sigma_n^2 I$ .

To make predictions  $f_*$  at a set of new query points,  $X_*$ , the joint distribution can be calculated from an augmented matrix containing the previous covariance matrix updated with the covariance between the training and new query points given by,

$$\begin{bmatrix} y \\ f_* \end{bmatrix} \sim \mathcal{N} \left( 0, \begin{bmatrix} K(X, X) + \sigma_n^2 I & K(X, X_*) \\ K(X_*, X) & K(X_*, X_*) \end{bmatrix} \right). \quad (40)$$

By conditioning the joint Gaussian prior distribution on the observations,  $f_*|X, y, X_* \sim \mathcal{N}(\bar{f}_*, \text{cov}(f_*))$ , the following predictive equations for the mean  $\bar{f}_*$  and covariance  $\text{cov}(f_*)$  can be derived, completely specifying the GP.

$$\begin{aligned} \text{prior} + \text{data} &\rightarrow \text{posterior} \\ \bar{f}_* &= K(X_*, X)[K(X, X) + \sigma_n^2 I]^{-1}y \\ \text{cov}(f_*) &= K(X_*, X_*) - K(X_*, X)[K(X, X) + \sigma_n^2 I]^{-1}K(X, X_*) \end{aligned} \quad (41)$$

#### 4.2.2.1 Data Preprocessing

The collected data set contained no missing values. The continuous (or numerical parameters) features were standardized by subtracting the mean and dividing the difference by the standard deviation. The input feature representing formulation was treated as a categorical feature by constructing two dummy variables using one-of-k binary encoding. This encoding adds ‘k’ additional input dimensions (one for each category) where the active dummy variable is specified by a one, and all other dummy variables are set equal to zero.

#### 4.2.2.2 Kernel Structure

The input space,  $\mathcal{X}$ , spanned a total of nine dimensions (including dummy variables) as determined by the prescribed formulations and the controlled or derived parameters. The input space was further divided into two subdomains: one over the numerical dimensions  $\mathcal{X}_{num} \in w$  and one over the categorical dimensions  $\mathcal{X}_{cat} \in u$ . A

valid compound kernel over  $\mathcal{X}$  can be obtained by the sum and product of kernels defined over the subdomains,  $\mathcal{X}_{num}$  and  $\mathcal{X}_{cat}$ .<sup>173</sup> Figure 4-1 details the model inputs, outputs, and various kernel structures tested. It was suspected that multiple local optima would exist when learning the optimal set of hyperparameter values, especially for the highest complexity compound kernel (sum + product, SE-ARD over both categorical and

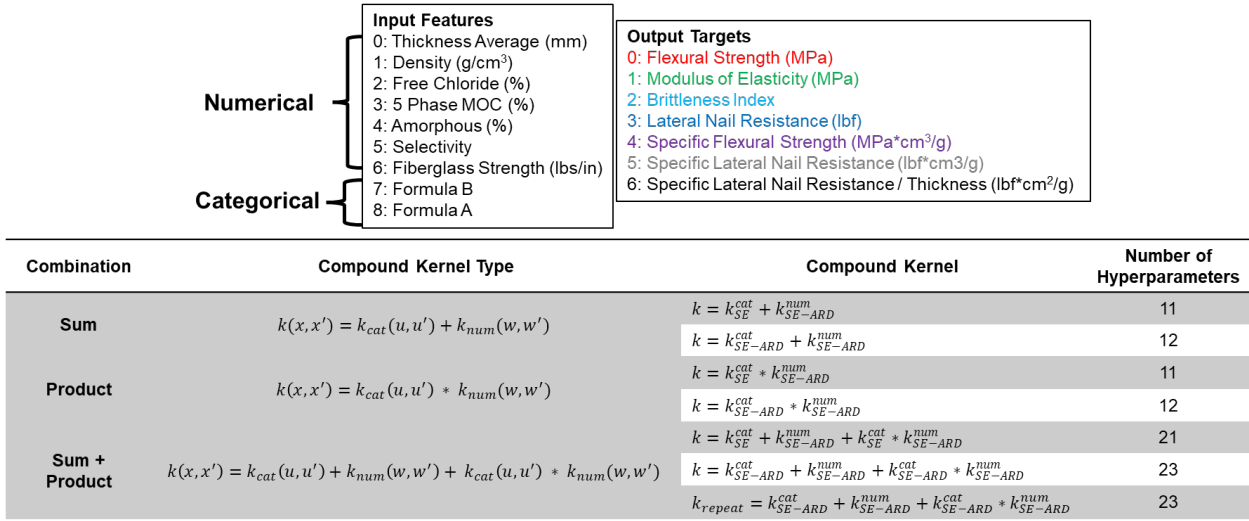


Figure 4-1. Model input features, output targets, and a summary of the various compound kernel combinations evaluated.

numerical domains), and the model behavior would be sensitive to the learning process.

The highest complexity compound kernel was repeated to evaluate the model robustness to hyperparameter learning, where a new set of hyperparameters was learned and compared with the previous set.

#### 4.2.2.3 Hyperparameter Optimization

Since the GP is a nonparametric model representing a real, unknown process, the appropriate set of hyperparameter values is unknown and must be learned or inferred from the data. The general process of choosing these values is referred to as hyperparameter optimization. Alternate nomenclature includes hyperparameter tuning, training, learning, or inferring. The optimal set is often chosen by maximizing the partial derivatives of the marginal likelihood with respect to the hyperparameters. Rasmussen and Williams<sup>170</sup> give the marginal likelihood as

$$\log p(y|X, \theta) = -\frac{1}{2} y^T K_y^{-1} y - \log |K_y| - \frac{n}{2} \log 2\pi \quad (42)$$

where  $K_f$  is the noise-free covariance matrix and  $K_y = K_f + \sigma_n^2 I$  is the covariance matrix accounting for noisy observations. The marginal likelihood in Equation (42) comprises three interpretable terms. The first term, which includes the targets,  $y$ , penalizes to encourage accurate predictions. The second term is a function of the inputs and covariance function and penalizes complex models (longer lengthscales favored), while the third is a normalization constant. The natural inclusion of a trade-off between the data-fit and complexity terms increases the resilience of this approach to overfitting.

Taking the partial derivative with respect to the hyperparameters yields

$$\frac{\partial}{\partial \theta_j} \log p(y|X, \theta) = \frac{1}{2} \text{tr} \left( (\alpha \alpha^T - K_y^{-1}) \frac{\partial K_y}{\partial \theta_j} \right) \text{ where } \alpha = K_y^{-1} y. \quad (43)$$

The set of optimal hyperparameters  $\theta$  was obtained by minimizing the negative log-likelihood via a scaled conjugate gradient (SCG) optimizer. Since the marginal likelihood may have multiple local minima, the initial guess for  $\theta$  was adjusted during a number of optimization restarts. One hundred restarts were used during cross-validation (Section 4.2.3), and ten restarts were used during validation (Section 4.2.4).

#### ***4.2.3 Cross-Validation Scheme***

Cross-validation was used to assess the performance and as a proxy for the generalization error for each kernel selection. A model's generalizability refers to its ability to perform well on completely unseen data, known as a test or validation dataset. Cross-validation is often used when access to a true validation dataset is unavailable, or the acquisition of additional data is expensive or unobtainable. Cross-validation includes the following general steps:

1. A full dataset is shuffled and partitioned into a training and testing set with the proportion defined by the practitioner (commonly 80:20 or 70:30, train-test split)
2. A predictive model is trained on the training set
3. Predictions are made using the inputs associated with the test set
4. Error and other performance metrics are calculated by comparing the predicted values with that of the test values (true values)
5. Steps 1-4 are repeated until satisfactory convergence of the performance metrics is obtained

The total number of observations in the collected dataset was small ( $n = 80$ ); therefore, a 90:10 train-test split was selected for cross-validation. The full dataset was used to estimate the hyperparameters by optimizing over one hundred random restarts of the initial guess. The estimated parameters were fixed for all successive shuffle-splits. The covariance matrix was calculated from the training dataset (90% of the full dataset), and the cross-validation performance was evaluated as a cumulative average of the performance metrics over the 500 shuffle-splits. A flowchart of the cross-validation methodology is shown in Figure 4-2.

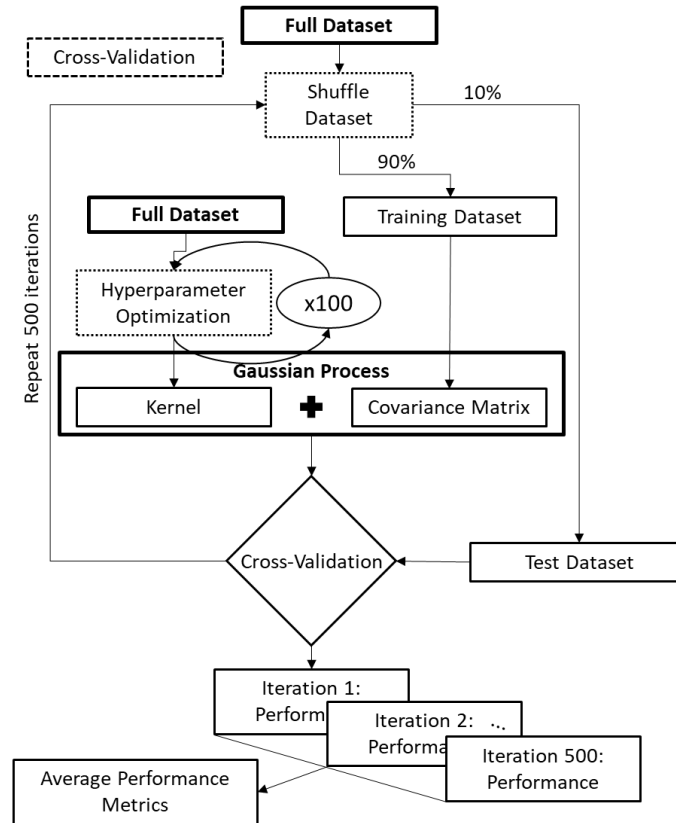


Figure 4-2. Flowchart of the methodology used for cross-validation.

### Model Performance Metrics

Each GP consisted of a particular kernel structure for a single target output. Once the hyperparameters for each GP have been selected, the model's performance can be assessed by comparing the predicted target outputs from the GP posterior mean to the true held-out target values. The following model performance metrics<sup>174</sup> (averaged over the number of shuffle-splits) were used to assess the fidelity of each kernel structure for each output:

- Slope:  $m$  of the linear regression line fit to a plot of the predicted values vs. true values where  $m = \frac{\sum_{i=1}^n ((x_i - \bar{x})(y_i - \bar{y}))}{\sum_{i=1}^n ((x_i - \bar{x})^2)}$  and a horizontal bar denotes the average value of that expression over the set of  $n$  samples for the independent  $x_i$  and dependent variables  $y_i$ . The slope is unitless, and a slope closer to unity *usually* indicates better performance (for the reason of “*usually*,” see references, <sup>175,176</sup>).
- Y-intercept:  $b$  of the linear regression line fit to a plot of the predicted value vs. true value where  $b = \bar{y} - m\bar{x}$ . An intercept closer to zero *usually* indicates better performance (for the reason of “*usually*” see references, <sup>175,176</sup>). The y-intercept takes on the units of the dependent variable.
- $R^2$ : or Coefficient of Determination where  $R^2 = 1 - \frac{\sum_1^n (y_p - y_e)^2}{\sum_1^n (y_e - \bar{y}_e)^2} = 1 - \frac{SSE}{\sum_1^n (y_e - \bar{y}_e)^2}$  and  $y_p$ ,  $y_e$ , and  $\bar{y}_e$  denote the predicted output, observed true value, and the average observed true value. SSE represents the sum of squared errors. An  $R^2$  value describes the proportion, from zero to unity, of the total variance

in the observed data that can be explained by the model, with higher values indicating that the model more accurately captures or explains the patterns and trends in the data.

- RMSE: or Root Mean Square Error where  $RMSE = \sqrt{\frac{\sum_1^n (y_p - y_e)^2}{n}}$ . It is interpreted as a measure of how much the predicted values deviate, on average, from the observed values; thus, a lower RMSE indicates better predictive performance. The RMSE is measured in the same units as the dependent variable and emphasizes larger errors (since the errors are squared first before taking the square root). This penalizes outliers more heavily than MAE. This metric is more useful when large errors are detrimental.
- MAE: or Mean Absolute Error where  $\frac{\sum_1^n |y_p - y_e|}{n}$ . MAE measures the average magnitude of the residuals (i.e., the differences between the observed and predicted values) without considering their direction. MAE is a more natural measure of average error than RMSE.<sup>177</sup>

#### ***4.2.4 Validation Scheme***

Model validation was performed by shuffling the full dataset and removing 10% to be withheld entirely from the training process as a validation dataset. Model training consisted of optimizing the hyperparameters (Section 4.2.2.3) on the 90% of data reserved as a training dataset over ten random restarts of the initial guess. The covariance matrix was also constructed from the 90% training dataset. Validation metrics were



computed by comparing the predicted values from the GP mean to the true values withheld in the independent test dataset. The validation performance was averaged over ten shuffle-splits, each time re-training a new set of hyperparameters. The performance metrics were those defined for cross-validation. A flowchart of the validation methodology is shown in Figure 4-3.

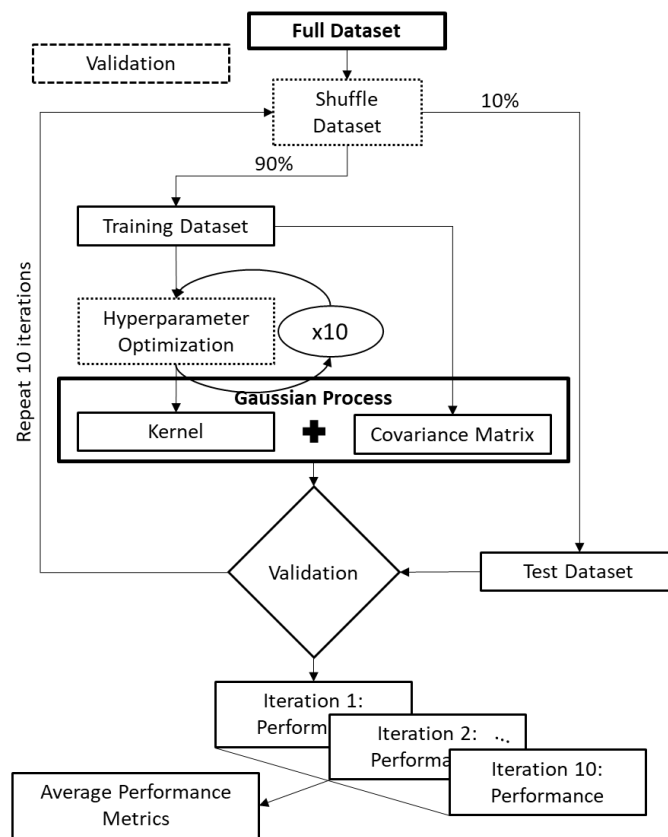


Figure 4-3. Flowchart of the methodology used for model validation.

## 4.3 Results and Discussion

### 4.3.1 Evaluating Model Performance via Cross-Validation

The first three shuffle-split iterations of cross-validation (for an example kernel,  $k = k_{SE-ARD}^{cat} * k_{SE-ARD}^{num}$ ), where the true value is plotted against the predicted value, is shown in Figure 4-4 as an example. Each row of graphs contains one iteration corresponding to one random configuration of test-train data. Each column of graphs corresponds to an output variable, from left to right: flexural strength, modulus of elasticity, brittleness index, lateral nail resistance, specific flexural strength, specific lateral nail resistance, and the specific lateral nail resistance normalized by thickness.

Visually one can assess the performance of a target variable for a given kernel by comparing the linear fit to the  $y = x$  line which denotes a perfect prediction. The third column of graphs corresponds to the evaluation of the Brittleness Index performance, which appears to perform the worst as evidenced by deviation from the perfect fit line and large 95% confidence intervals associated with the posterior mean predictions. While a qualitative performance measure can be assessed from these three iterations, a more accurate performance of the kernels is quantitatively measured by averaging the performance metrics over five hundred shuffle-split iterations.

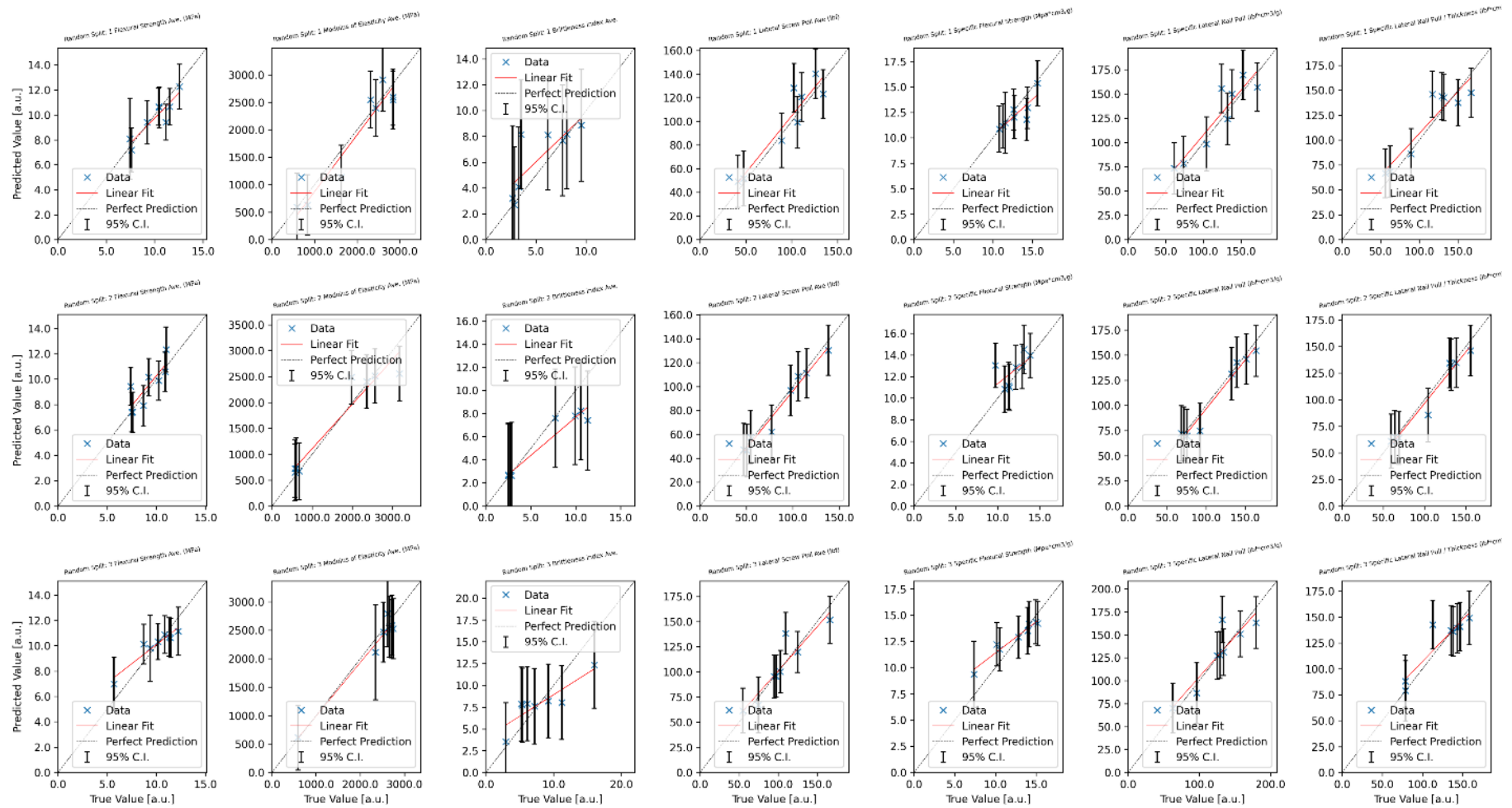


Figure 4-4. The first three shuffle-split iterations of cross-validation where the true value is plotted against the predicted value. The  $y = x$  line denotes a perfect prediction. Each row of graphs contains one iteration corresponding to one random configuration of test-train data. Each column of graphs corresponds to an output variable, from left to right: flexural strength, modulus of elasticity, brittleness index, lateral nail resistance, specific flexural strength, specific lateral nail resistance, and the specific lateral nail resistance normalized by thickness. Error bars denote 95% confidence intervals about the mean.

An important distinction must be made when discussing the ‘training’ of a GP as contrasted with other types of training in the machine learning literature. The training of a GP could be thought of as two distinct processes, one where 1) the hyperparameters are estimated from a training dataset and 2) the covariance or Gram matrix is calculated from a training dataset. These two components of ‘training’ are often performed on the same dataset; however, with a GP, this need not be. Within the context of cross-validation and validation, the Gram matrix will always be calculated from the training dataset alone because predicting values that the model has already ‘seen’ is trivial and not a useful metric. However, it is possible to learn the hyperparameters using the full dataset (rather than a subset, i.e., training dataset) while using the limited training dataset to compute the Gram matrix.

This study used the full dataset in cross-validation to estimate GP hyperparameters, an approach similar to ‘pre-training’ or ‘pre-optimization’ within the broader machine learning literature.<sup>178,179</sup> This is contrasted with the validation methodology, which optimizes for a new set of hyperparameters each iteration. Since the hyperparameters are not retrained each successive shuffle-split iteration, the computational cost is reduced, and the total number of shuffle-splits (500) can be large, resulting in a cumulative average performance metric that is robust to any specific configuration (or shuffle) of training data. This is demonstrated in Figure 4-5 for the most complex kernel, the sum + product kernel (ARD for both numerical and categorical

dimensions), where the cumulative average performance metrics approach a convergent value.

The results in Figure 4-5 demonstrate that a significant bias, as indicated by rapid oscillations, in the performance metrics exists when the total number of shuffle-split

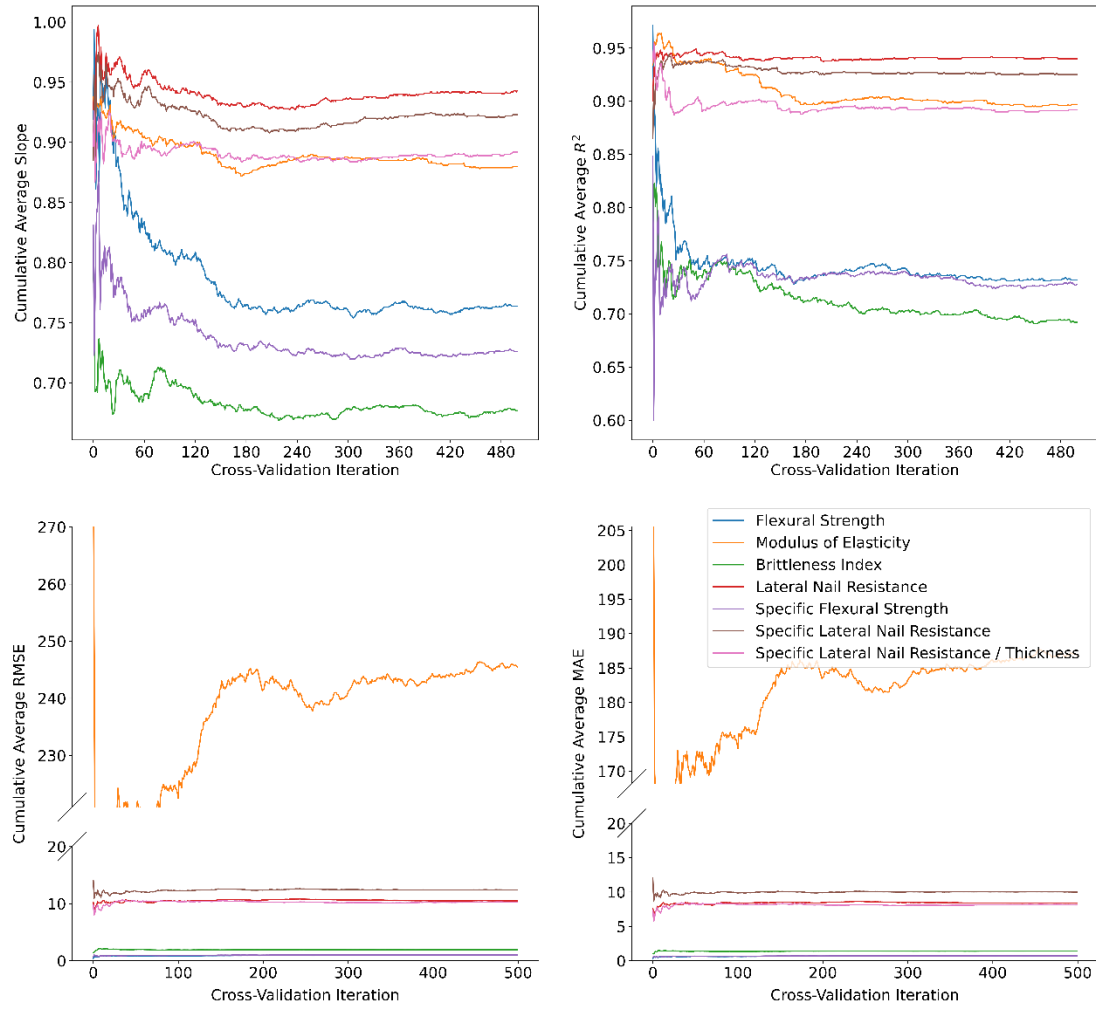


Figure 4-5. The cross-validation performance metrics for the sum + product kernel defined as  $k = k_{SE-ARD}^{cat} + k_{SE-ARD}^{num} + k_{SE-ARD}^{cat} * k_{SE-ARD}^{num}$  calculated as a cumulative average at each iteration.

iterations is small. This is expected as the configuration of the training-test split alters the domain on which the model is trained and the domain on which predictions are made. There is a significant variance in the model error estimates at a low number of iterations due to the configurational bias of the test-train split. This variance is induced by changes to the values the model must extrapolate and interpolate. A GP might perform well at interpolating within a trained input space but can usually only extrapolate accurately from its domain about the distance of one length scale hyperparameter away from its respective dimension.<sup>161,170,172</sup> The length scale hyperparameter of a squared-exponential kernel, estimated during optimization, encodes the average length over which a GP will decay back to its specified mean (in this study, zero). Therefore, the model error will increase if the prediction of held-out data requires extrapolation due to training on a subset (limited domain). Despite learning hyperparameters from the full dataset, interpolation performance is also affected by altering the covariance matrix at each iteration. The cumulative cross-validation metrics over the 500 shuffle-splits are given in Appendix C for the remaining kernel structures evaluated.

The final performance metric for cross-validation is taken as the cumulative average at iteration=500, and the performance for prediction of the flexural (and specific) strength for each kernel is summarized in Figure 4-6 (tabulated values are given in Appendix C). The performance associated with predicting the modulus of elasticity and brittleness index is shown in Figure 4-7 and Figure 4-8 for the lateral nail resistance, specific lateral nail resistance, and specific lateral nail resistance / thickness. The kernel

structures in these figures are arranged from left to right by decreasing  $R^2$  (the best-performing kernel on the left).

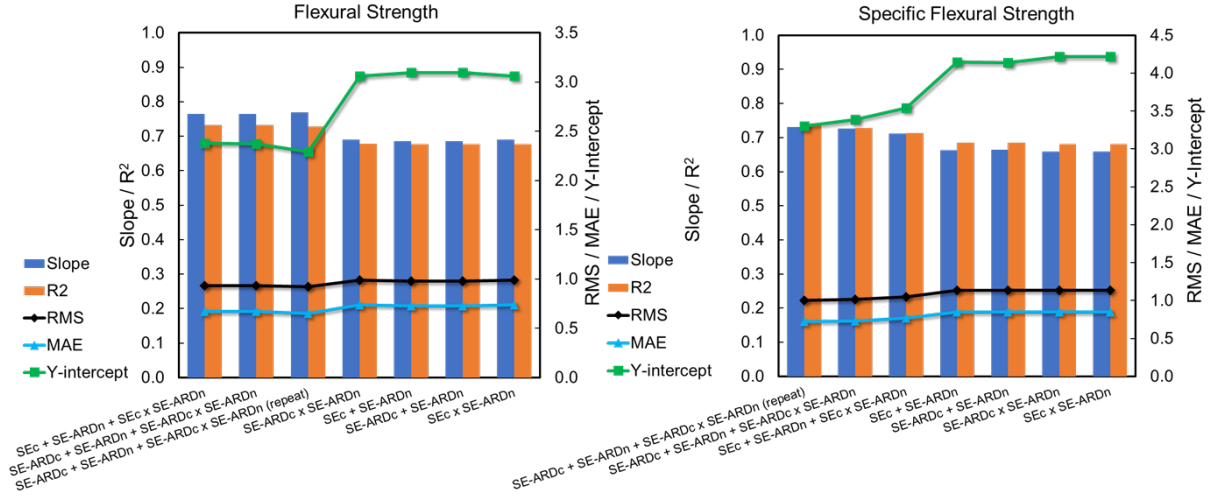


Figure 4-6. Cross-validation performance of flexural (and specific) strength for each kernel averaged over 500 shuffle-split iterations arranged from left to right by decreasing  $R^2$ .

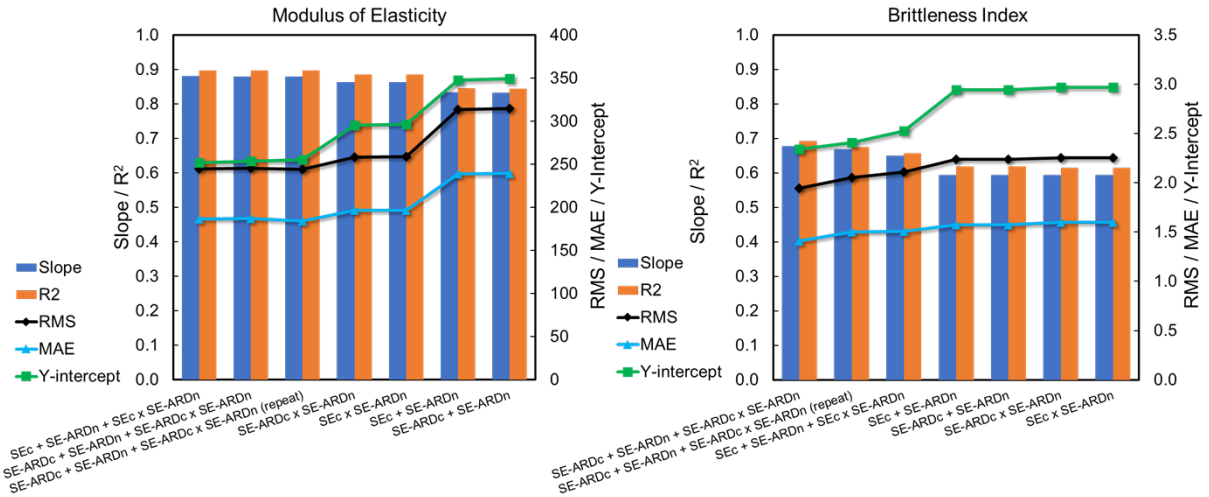


Figure 4-7. Cross-validation performance of modulus of elasticity and brittleness index for each kernel averaged over 500 shuffle-split iterations arranged from left to right by decreasing  $R^2$ .

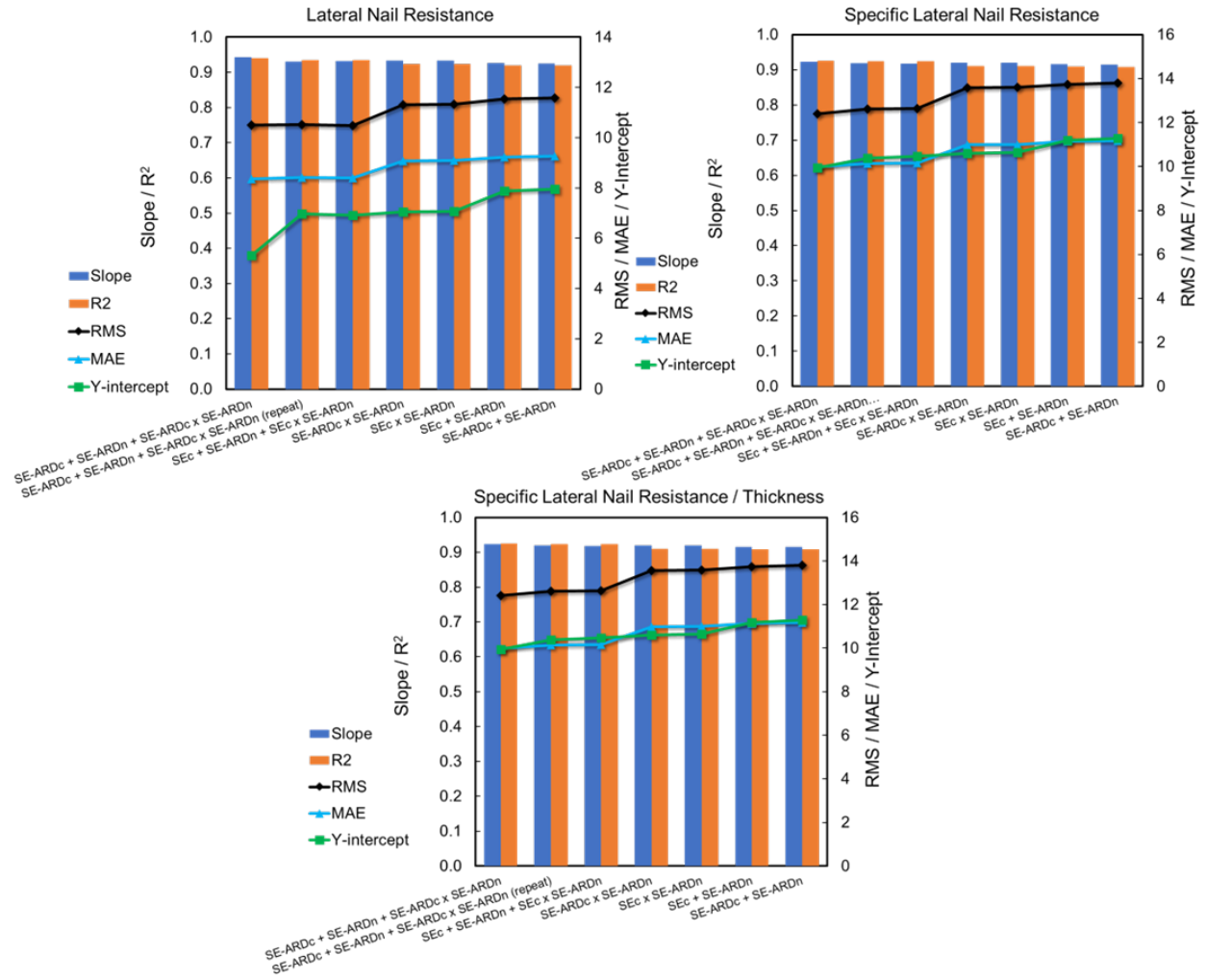


Figure 4-8. Cross-validation performance of lateral nail resistance, specific lateral nail resistance, and specific lateral nail resistance / thickness for each kernel averaged over 500 shuffle-split iterations arranged from left to right by decreasing  $R^2$ .

A few general trends can be observed from the figures. As expected, kernel performance for a given model output as measured by  $R^2$  corresponded almost perfectly with the ranking by the other metrics. In other words, increases in  $R^2$  almost always coincided with decreases in RMSE and MAE, slopes closer to unity, and y-intercepts closer to zero. Interestingly, the ranking of kernel performance by  $R^2$  was identical for



all forms of lateral nail resistance (including specific and normalized thickness). This might be expected since ‘specific’ and ‘specific normalized by thickness’ lateral nail resistance is a function of the density and thickness, both of which are included as inputs to the model; however, the same trend is not observed with flexural and specific flexural strength. Also notable, for all forms of lateral nail resistance, the y-intercept tended to be less than the RMSE or MAE, contrary to the trend established by the other outputs. For all outputs in general, the more complex kernel structures having more parameters (i.e., Sum + Product) tended to perform the best. By taking the best-performing kernel for each output as determined by  $R^2$ , the outputs can be compared to one another and ranked according to how easily they can be predicted from the data given the assumptions of the GP. From highest predictive capacity to least:

Lateral Nail Resistance → Specific Lateral Nail Resistance → Modulus of Elasticity →  
 Specific Lateral Nail Resistance / Thickness → Specific Flexural Strength → Flexural  
 Strength → Brittleness Index

#### ***4.3.2 Model Sensitivity to Hyperparameter Tuning***

Figure 4-9 compares the optimal set of length scale hyperparameters for the most complex kernel structure learned from the full dataset to a repeated instance of the same kernel structure. Both kernels were optimized over one hundred restarts of the initial

guess. The noted kernel consists of two SE-ARD kernels, one over the categorical domain and one over the numerical domain. It is defined as:

$$k = k_{SE-ARD}^{cat} + k_{SE-ARD}^{num} + k_{SE-ARD}^{cat} * k_{SE-ARD}^{num}$$

and contains 23 hyperparameters. The ARD kernel lets each input feature have its own characteristic length scale, the inverse of which serves as a proxy for the feature's value or relevance in the regression process. When the length scale becomes infinitely large, it implies no correlation between the latent function values along that dimension.<sup>170,172,180</sup> Therefore, the inverse of a large length scale can be thought of as a measure of its relevance to the prediction. This feature-specific length scale is computed automatically during model training, thus the phrase "Automatic Relevance Determination."

The interpretability of the model hyperparameters distinguishes GPs from the myriad of machine learning methods and assists the practitioner in feature selection, providing intuition about underlying data.<sup>181–183</sup> In Figure 4-9, the similar proportional

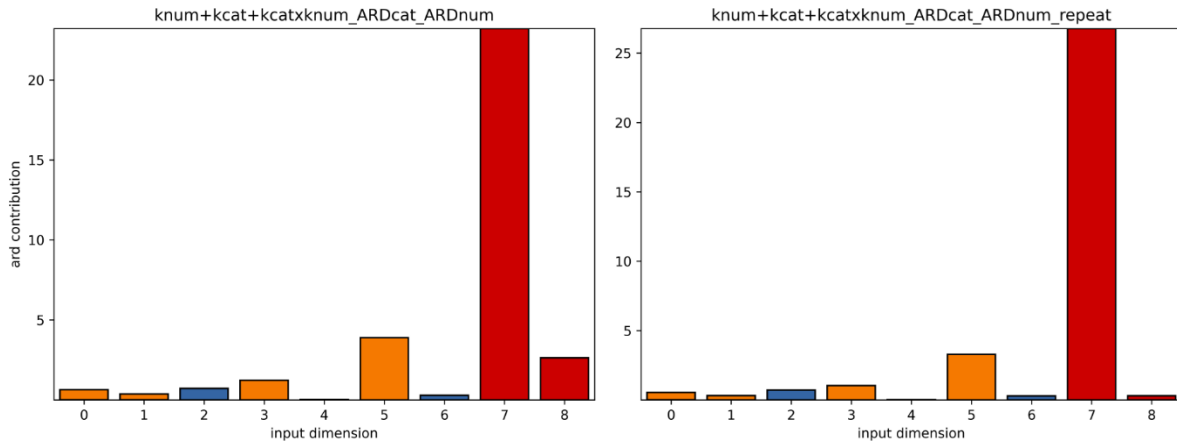


Figure 4-9. Automatic relevance determination (ARD) plots for the most complex kernel evaluated. The relevance of each input dimension is proportional to the inverse of its characteristic length scale. The ARD plot is given as an example and corresponds to the kernel trained on the Specific Lateral Nail Resistance / Thickness.

ARD contributions by each dimension (inverse of the lengthscale) for the repeated kernel demonstrate the robustness of the hyperparameter estimation under the specified optimization framework. It should be noted that this measures how robust the hyperparameter estimation is to the optimization for a given dataset, not how robust the estimation is to a changing dataset, as one would encounter in successive iterations of cross-validation.

#### ***4.3.3 Validation of Model***

In contrast to the methodology used for cross-validation, model validation was performed by holding out a true ‘unseen’ validation dataset where the hyperparameters are re-trained each successive test-train split using only the limited training dataset. The performance evaluated during validation gives a more accurate measurement of how well the model fitting procedure (including the hyperparameter tuning) generalizes to new data. Validation also measures how robust the model is to the hyperparameter estimation for a changing training dataset. Successive validation (shuffle-split) iterations yielding significantly different hyperparameter values indicate sensitivity to the training subset, and thus, a point estimate of the hyperparameters may not be accurate.

The validation performance metrics are summarized in Figure 4-11, Figure 4-10, and Figure 4-12 (tabulated values are given in Appendix C). The ranking of kernel structures with each output tended to be more disordered than in cross-validation. This was expected as the performance metrics were only averaged over ten shuffle-split iterations. Instead of ranking kernel structure performance within an output, the

validation results give an overall idea of how well the kernels perform, as a collective, on unseen data.

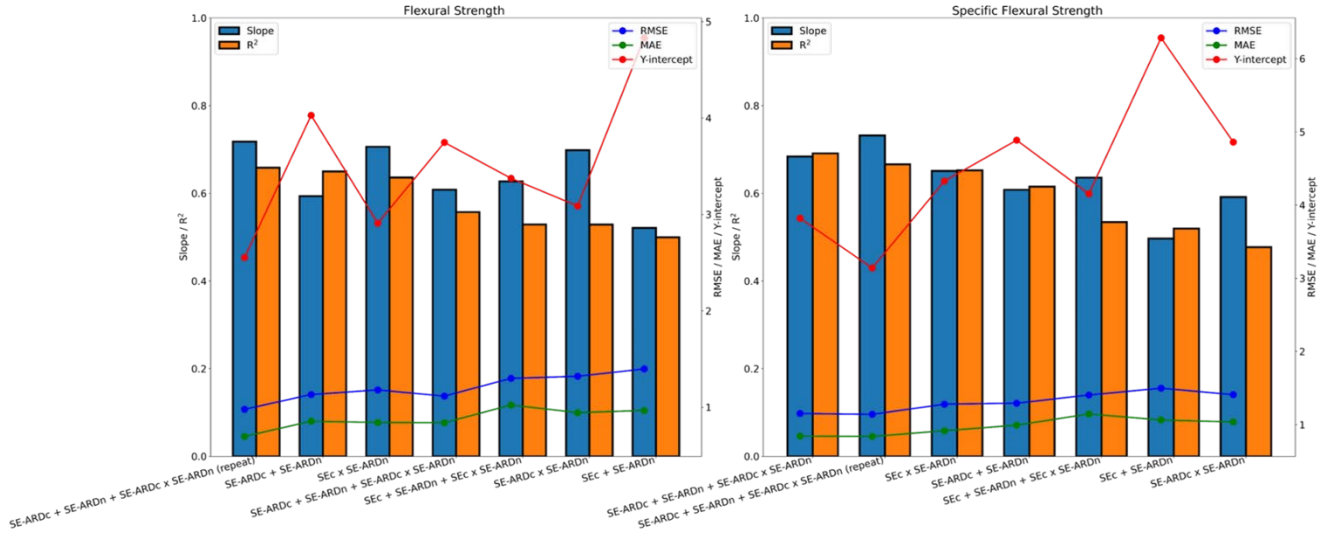


Figure 4-10. Validation performance of flexural (and specific) strength for each kernel averaged over 10 shuffle-split iterations arranged from left to right by decreasing  $R^2$ .

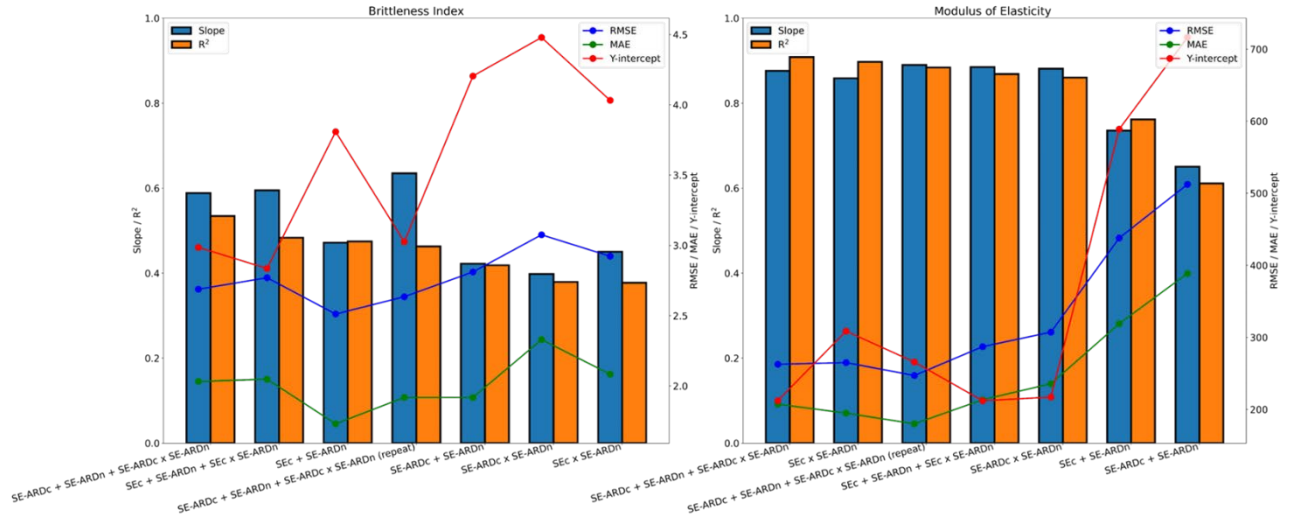


Figure 4-11. Validation performance of modulus of elasticity and brittleness index for each kernel averaged over 10 shuffle-split iterations arranged from left to right by decreasing  $R^2$ .

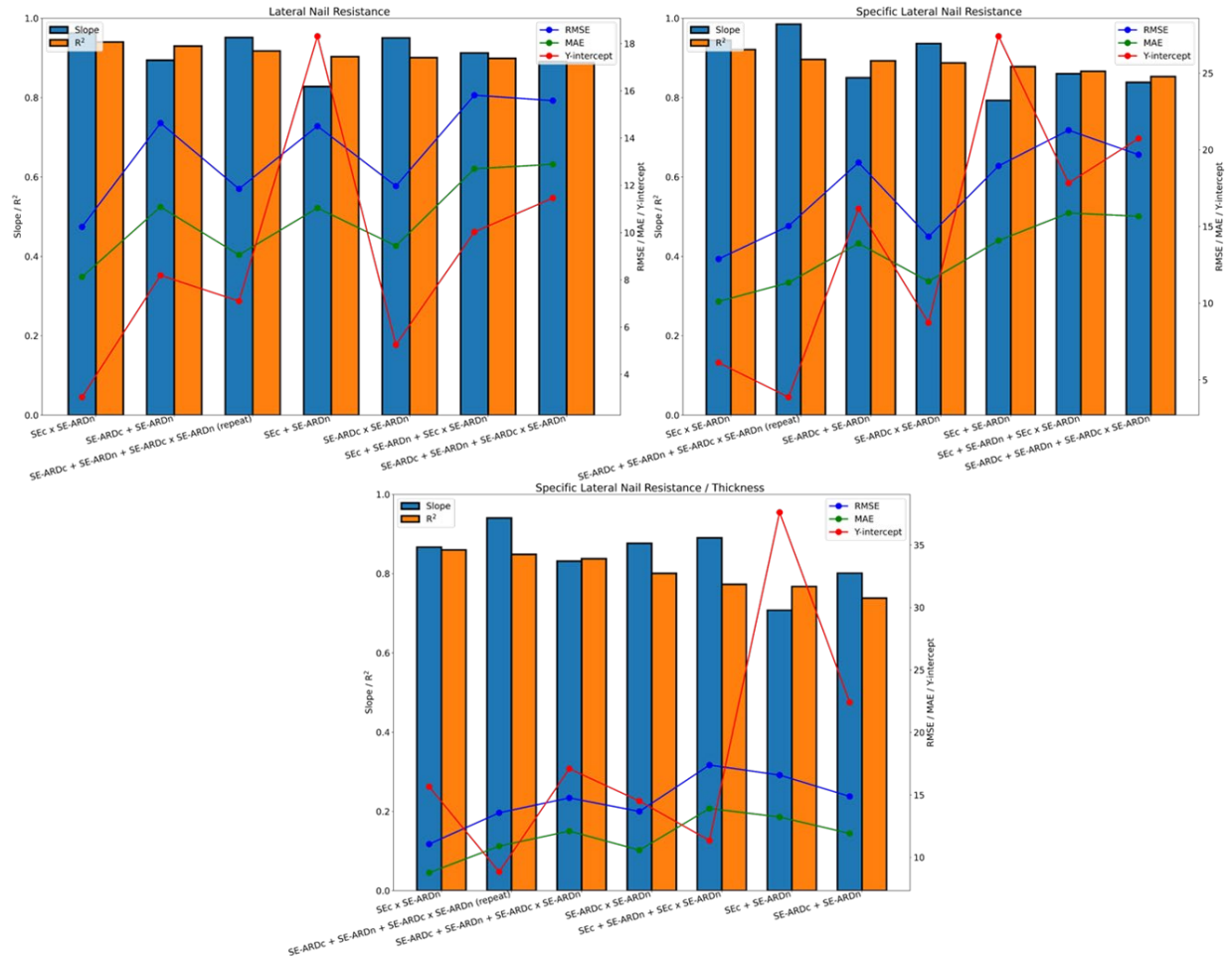


Figure 4-12. Validation performance of lateral nail resistance, specific lateral nail resistance, and specific lateral nail resistance / thickness for each kernel averaged over 10 shuffle-split iterations arranged from left to right by decreasing  $R^2$ .

The results indicate that the proposed kernels perform exceptionally well at predicting lateral nail resistance properties and the modulus of elasticity, reasonably well flexural strength properties, and the worst at the brittleness index. Table 4-1 compares

the cross-validation and validation performance for the best-performing kernel for each mechanical property.

Table 4-1. Comparison of cross-validation and validation performance for best-performing kernel

Output	R <sup>2</sup> Cross-validation	R <sup>2</sup> Validation
Lateral Nail Resistance	0.940	0.940
Specific Lateral Nail Resistance	0.925	0.921
Modulus of Elasticity	0.898	0.908
Specific Lateral Nail Resistance / Thickness	0.892	0.86
Specific Flexural Strength	0.735	0.691
Flexural Strength	0.732	0.659
Brittleness Index	0.692	0.535

#### 4.3.4 Feature Analysis

The sensitivity and importance of each input feature on each model output can be assessed by examining the ARD contributions, as shown in Figure 4-9, and by taking one-dimension slices from the fully trained GP across the relevant input parameter space while holding all other parameters constant. Because these parameters must be fixed, the most reasonable approach is to fix each at their respective median values.

Since the formulation is a categorical variable, it was fixed at either a one or zero for each set of parameter slices. The ‘slicing’ across the formulation is an abstract idea that can be intuitively understood as blending Formula A to Formula B for a given output giving an idea of the comparative magnitudes each formulation has for each output. Slicing across the formulations was performed by varying the one-of-k encoding representing Formula A [0→1] while simultaneously varying the encoding for B as [1→0]. In practice, predictions would always occur at a one or zero, as any other value is

a hypothetical construct. One-dimensional slices are shown in Figure 4-13 - Figure 4-19 for an example kernel  $k = k_{SE-ARD}^{cat} * k_{SE-ARD}^{num}$ . The underlying training data is plotted as markers colored according to their formulation (red for Formulation A and blue for Formulation B). The continuous curves represent the GP posterior mean and the shaded regions 95% confidence intervals about the mean.

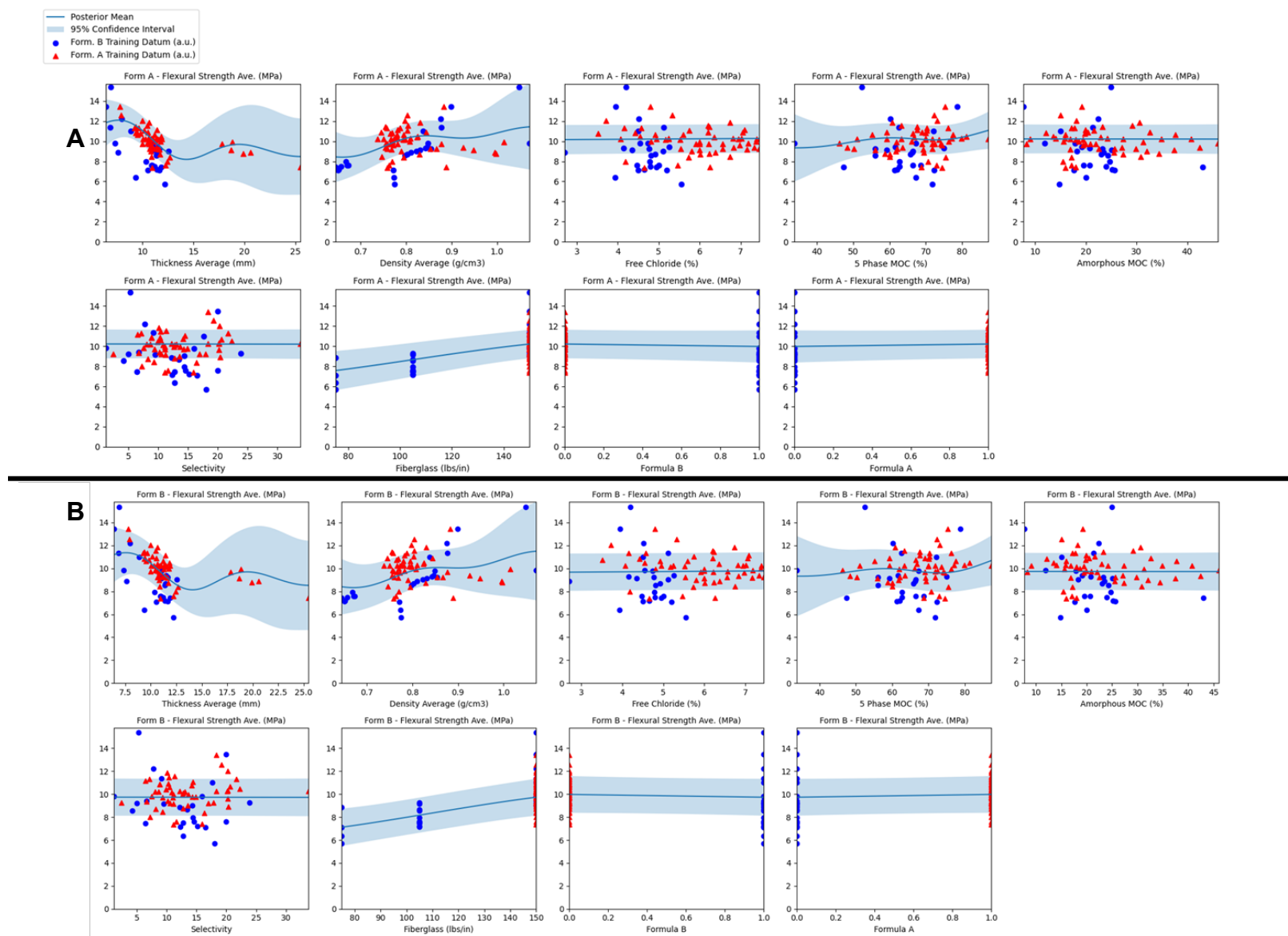


Figure 4-13. One-dimensional slices of Flexural Strength for Formula A (top) and Formula B (bottom). Fixed parameters are held at median values.



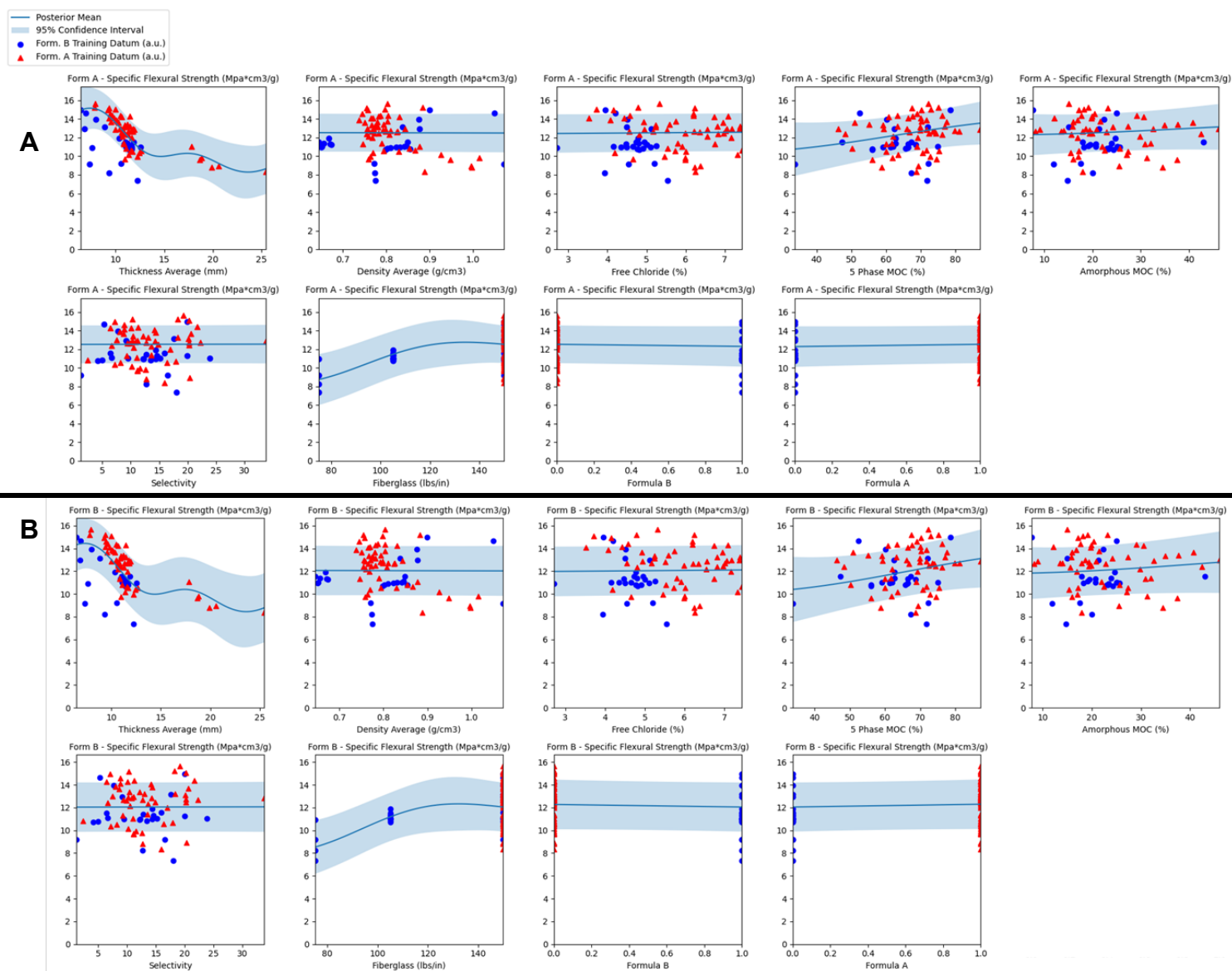


Figure 4-14. One-dimensional slices of Spc. Flexural Strength for Formula A (top) and Formula B (bottom). Fixed parameters are held at median values.

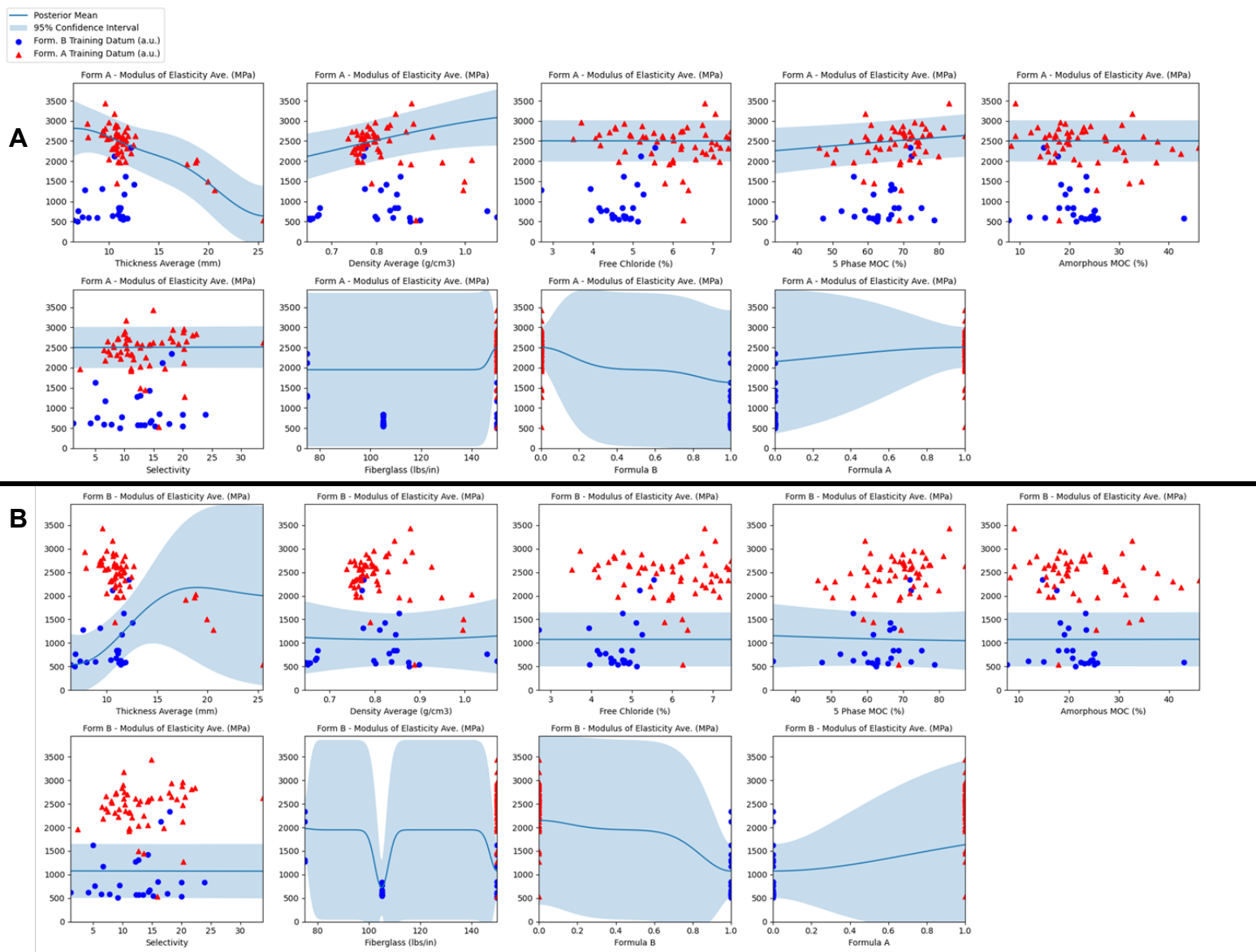


Figure 4-15. One-dimensional slices of Modulus for Formula A (top) and Formula B (bottom). Fixed parameters are held at median values.

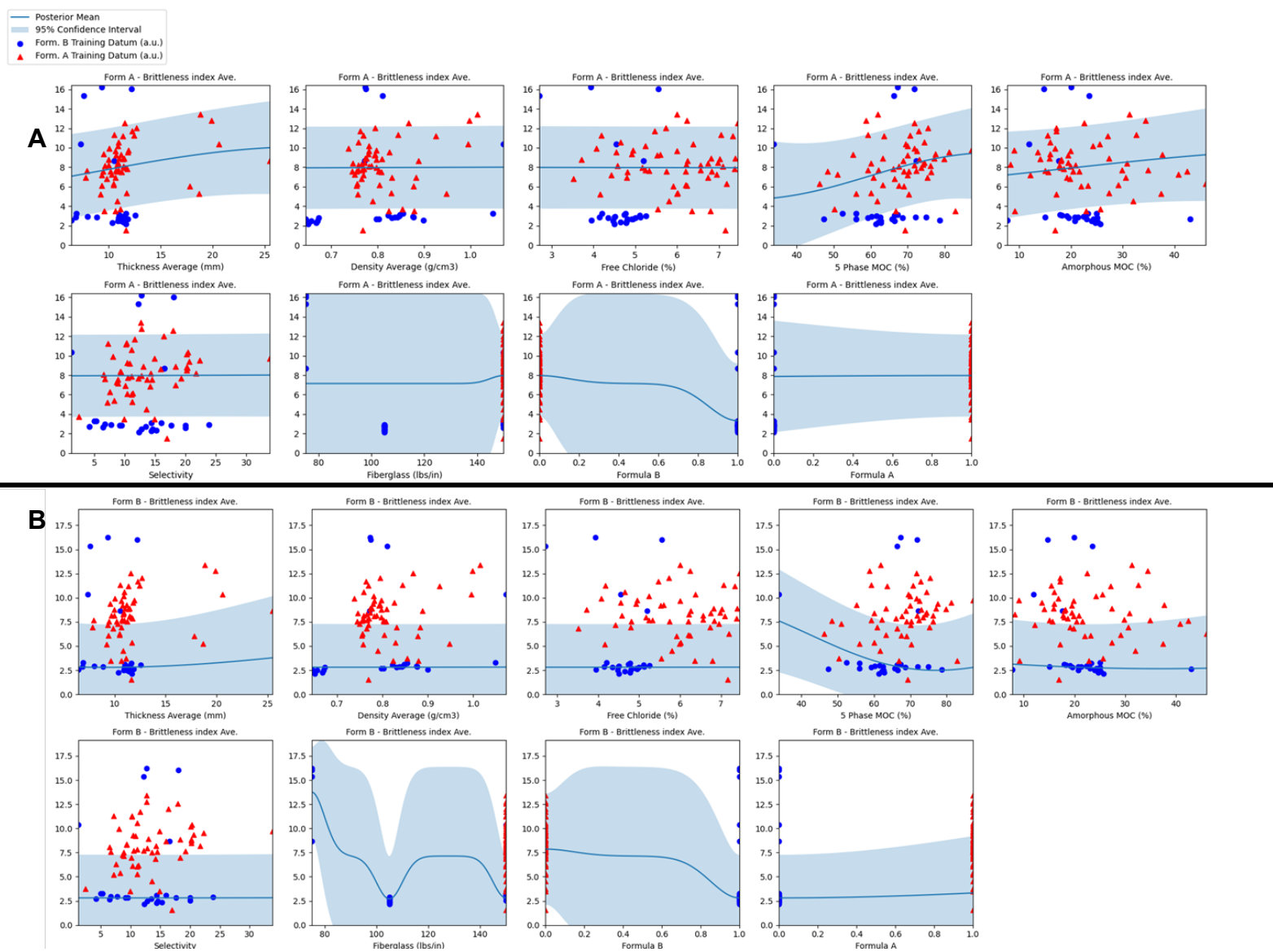


Figure 4-16. One-dimensional slices of Brittleness Index for Formula A (top) and Formula B (bottom). Fixed parameters are held at median values.

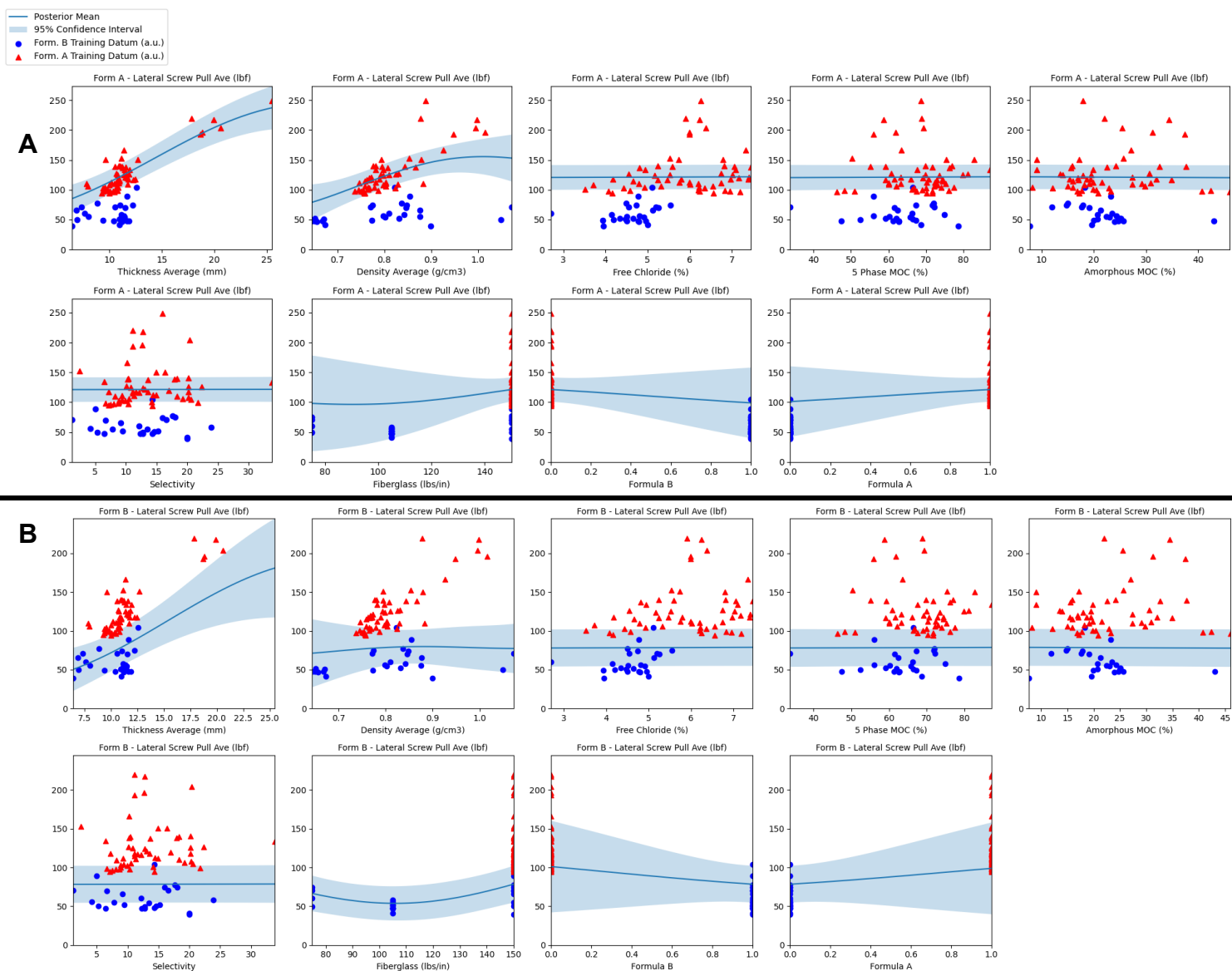


Figure 4-17. One-dimensional slices of Lateral Nail Resistance for Formula A (top) and Formula B (bottom). Fixed parameters are held at median values.

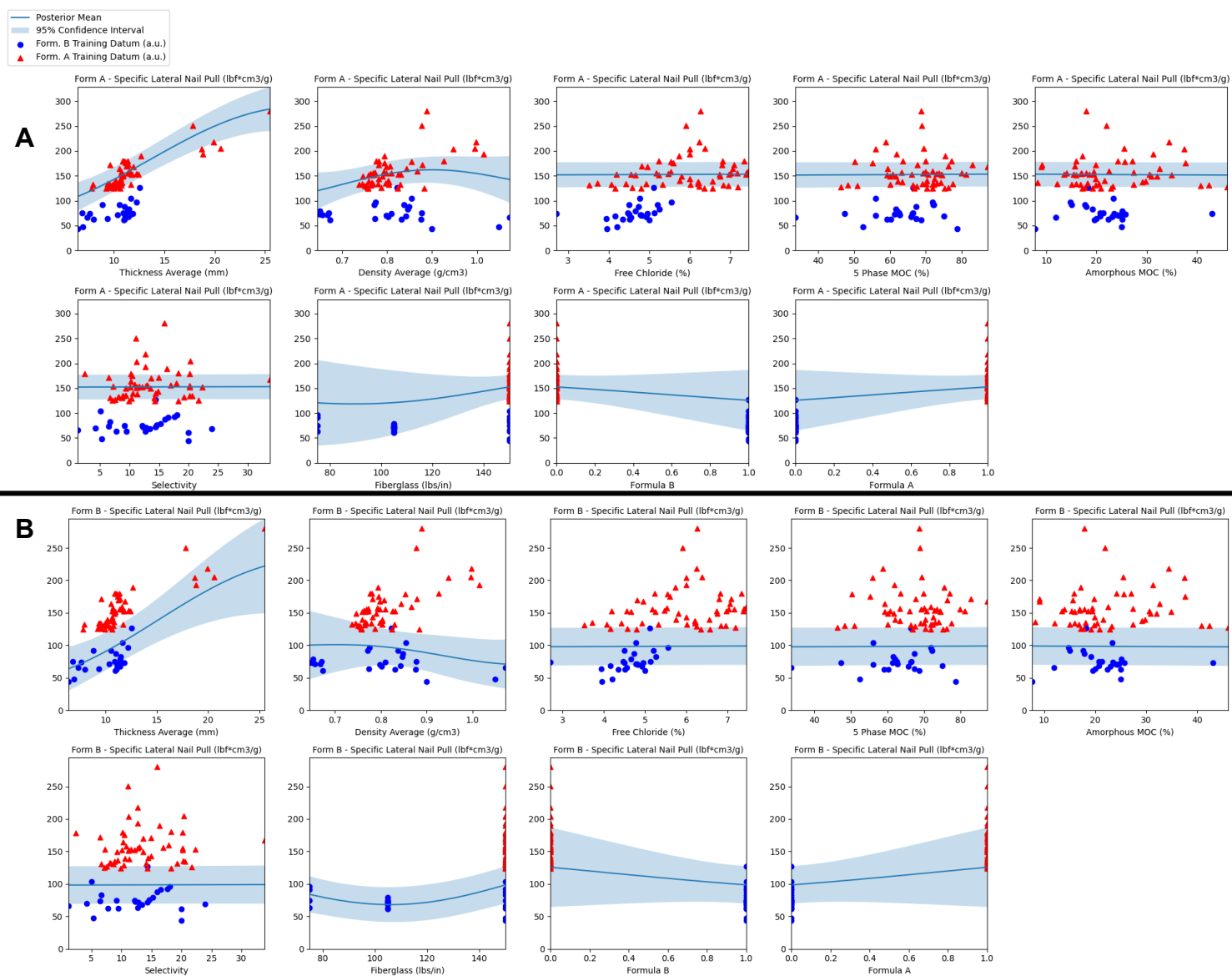


Figure 4-18. One-dimensional slices of Spc. Lateral Nail Resistance for Formula A (top) and Formula B (bottom). Fixed parameters are held at median values.

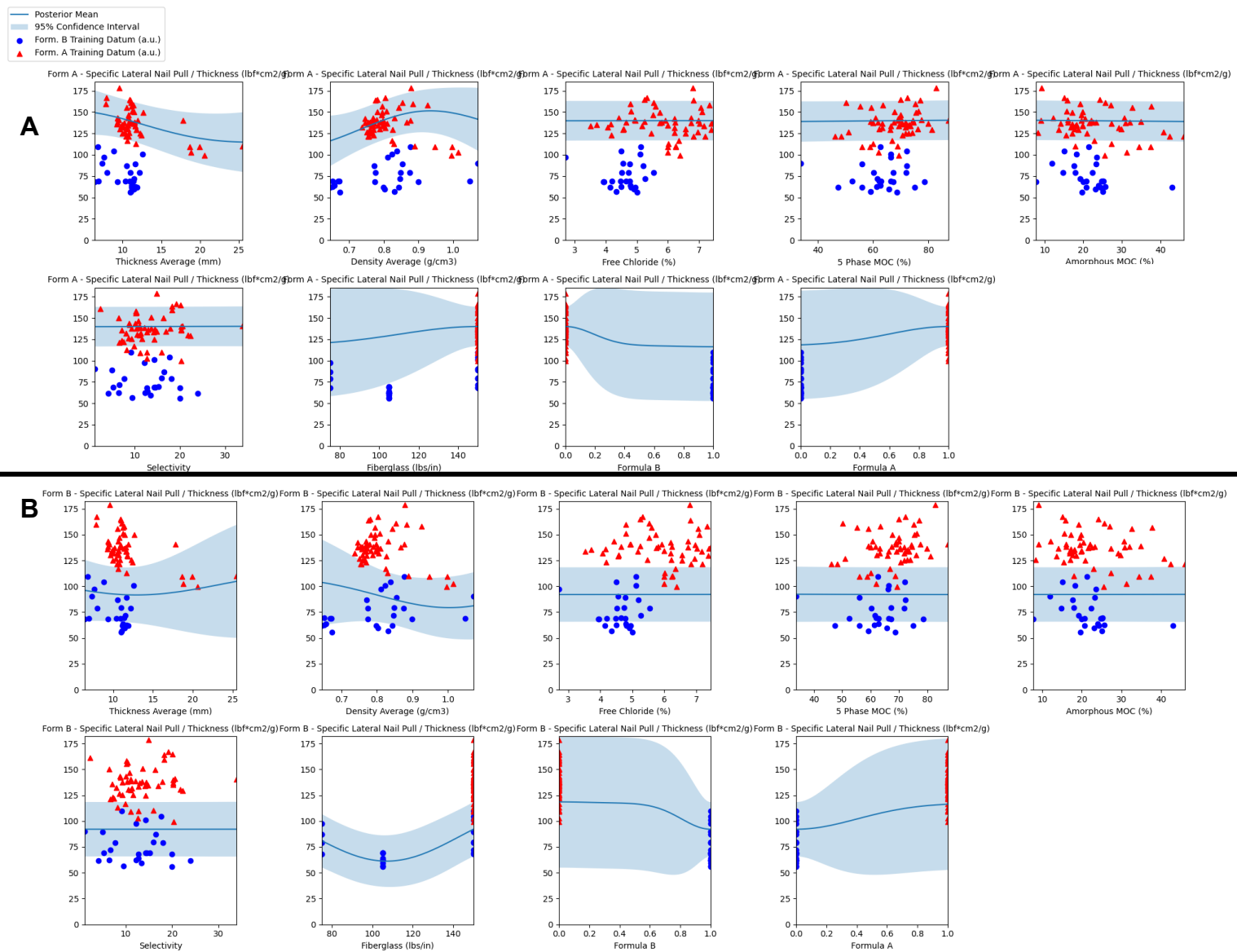


Figure 4-19. One-dimensional slices of Spc. Lateral Nail Resistance/Thickness for Formula A (top) and Formula B (bottom). Fixed parameters are held at median values.

Some notable observations are:

- Comparing the curves for Formula A vs. B with the underlying training data, it is observed that the model accurately separates the mean based on the active category.
- The GP intuitively quantifies uncertainty about unknown input domain areas with sparse training data.
- The GP intuitively quantifies the data's spread resulting from noisy observations.
- Increasing the fiber-glass reinforcement strength increased the composite flexural strength, as expected.
- Mechanical properties sensitive to thickness and density are accurately predicted to be insensitive when normalized by the respective thickness or density.
- All mechanical performance metrics were insensitive to free chloride percentage and selectivity (across the domains sampled by the training data).
- An increase in the 5-Phase MOC percentage generally improved all the mechanical performance metrics for both formulations except for the lateral nail resistance properties.
- The lateral nail resistance was highly correlated with thickness as expected. Thicker boards generally provide more material for the nails to distribute the

load, resulting in higher resistance to lateral forces. This effect was mitigated after normalizing by the thickness.

- The complex non-linear surfaces predicted by the model highlight the advantages of the nonparametric statistical model.

#### **4.4 Conclusion**

In this work, a predictive model was built using Gaussian Process (GP) regression to understand the relationships between various input features and the mechanical properties of fiberglass-reinforced MOC cement boards. The model was trained using data obtained from the production and testing of MOC boards with different process controls and formulations. The input variables included board thickness, density, free chloride percentage, MOC 5-phase percentage, amorphous percentage, reaction selectivity, fiberglass strength, and formulation type. The output variables consisted of flexural strength, modulus of elasticity, brittleness index, lateral nail resistance, specific flexural strength, specific lateral nail resistance, and specific lateral nail resistance normalized by thickness. Each output was modeled separately using a GP with its associated kernel and hyperparameters.

Different combinations of kernels were tested, and correlations among input variables were assessed using automatic relevance determination and visualization of one-dimensional slices across the input feature space. The test kernel structures consisted of additive and product combinations of squared-exponential kernels (and SE-ARD) over continuous numerical and categorical features. The most optimal kernel combination for



each model output was determined based on performance metrics from cross-validation, and the final performance of each model was evaluated using held-out validation test datasets.

Based on the validation results, the proposed kernels performed exceptionally well at predicting lateral nail resistance properties ( $R^2=0.940$ ) and the modulus of elasticity ( $R^2=0.908$ ), reasonably well flexural strength properties ( $R^2=0.691$ ), and the worst at the brittleness index ( $R^2=0.535$ ). The application of GP regression to predict the performance of fiber-reinforced MOC cement boards is an innovative approach that improves our understanding of the material and the factors that lead to enhanced performance and utility in the industry.

## CHAPTER 5

### CONCLUSIONS AND FUTURE DIRECTIONS

#### 5.1 Future Work

This research has provided significant strides in the development of comprehensive frameworks that predict the mechanical behavior of composite materials while quantifying and propagating uncertainty throughout predictions. Through the combination of computational methods, including finite element analysis and Gaussian process regression, it was shown that it is possible to infer the interphase properties of composite materials, model the effects of helically symmetric microstructures on macroscopic behavior, and develop accurate predictive models for complex composite systems. The nature of scientific exploration suggests that every answer opens new questions. Future research could expand upon the foundation built in this dissertation in several important directions:

1. Non-linear behavior: The applications of the research presented in this work only needed to assume linear elastic behavior, which usually approximates material behavior in small strain regimes. The FE-based framework is easily adaptable and particularly well suited for expansion to the non-linear regime of composite materials, which could enable the prediction and calibration for many other classes of composites and constitutive relationships.

2. Exploring other machine learning algorithms: The presented work has effectively utilized Gaussian process regression for surrogate modeling and predictions,

which is relevant to an engineer interested in model parameter interpretability. However, the rapidly evolving landscape of machine learning (ML) provides many other algorithms that may offer different or more precise insights into related tasks. Each ML method has its own advantages and requirements. Selecting the most suitable ML algorithm would depend on the specifics of the problem, including the nature and amount of data available, the complexity of the task, and the balance between prediction accuracy and model interpretability. Furthermore, a combination of multiple models, also known as ensemble methods or hybrid models, might provide better performance by leveraging the strengths of different ML techniques.

3. Optimization of MOC board formulation: A prospective line of research could revolve around perfecting the formulation of the MOC cement boards by employing Multi-Objective optimization techniques. These techniques aim to find the best trade-offs when dealing with conflicting objectives, and they are especially suited to problems where no single solution optimizes all objectives simultaneously. The optimization process could center on multiple objectives, namely maximizing performance attributes (such as mechanical strength, durability, and stability) while simultaneously minimizing cost, density, and even product variability. These goals often conflict: enhancing performance characteristics may necessitate more expensive materials or processes or increases in density. Conversely, minimizing costs or density may negatively impact performance. A detailed model of the relationships between MOC board formulation, its performance characteristics, cost, and density will be essential for this optimization. The

computational models developed in this research could provide valuable insights into these relationships.

The optimization procedure would likely require a suitable algorithm for Multi-Objective Optimization, such as Pareto-based evolutionary algorithms or swarm intelligence techniques, which can effectively navigate the trade-off surface to identify the Pareto-optimal solutions.<sup>184–188</sup> These represent the set of solutions for which no other solution exists that is better in all objectives, as shown in Figure 5-1, thus providing a range of optimal choices depending on the relative importance of the objectives. The result would enable informed decision-making in MOC board design and manufacturing process, improving product performance and cost-effectiveness.

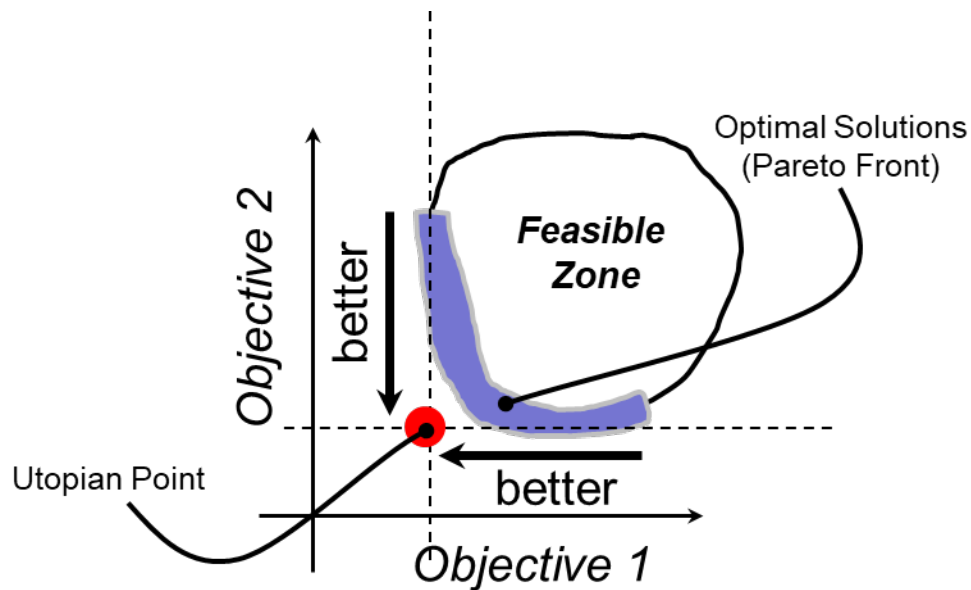


Figure 5-1. Illustration of the Pareto front, for a multi-objective optimization problem.

4. **Correlated Outputs:** The Gaussian process (GP) models developed in this work treated each output as independent, creating a distinct GP for every output. However, different output variables may exhibit correlations in many physical systems, including composite materials. For example, the strength and stiffness of a composite could be influenced by similar factors and thus could be correlated. Ignoring these correlations may lead to sub-optimal models and underutilized data.

A future direction could be to improve the GP models by considering correlations between different output variables. This could be accomplished by utilizing Multi-task GPs, a class of models that have been specifically developed to model and predict multiple outputs that are potentially correlated. Multi-task GPs extend the standard GP models by modeling the functions that represent each output and the cross-correlations between these functions. The correlation is typically expressed in terms of a covariance function (or kernel), much like in standard GPs, but now the covariance is a function of both the input and the output tasks. This allows the model to share information across tasks, improving the model's predictive performance, especially when some tasks have fewer observations than others.

## **5.2 Conclusion**

Each chapter in this dissertation focused on various aspects of multiscale composite material modeling, providing unique insights into the intricacies of the relationship between structure and properties. In Chapter 2, a novel framework was proposed to model the interphase effects and infer the key mechanical properties of the

interphase region from experimental measurements of the composite's bulk elastic modulus. The framework demonstrated the ability to match experimental data within experimental error and revealed insights into the relationship between filler particle size and interphase properties. Chapter 3 investigated the effect of CNC alignment in an alginate matrix on the composite's mechanical behavior. A multi-scale model was developed that captured the helical microstructural alignment of the CNCs and its effect on the macroscopic mechanical behavior of the composite. The results show the significant influence of microstructural heterogeneity on the macroscopic properties. Chapter 4 developed a predictive model using Gaussian process regression to understand the relationship between various input features and the mechanical properties of fiberglass-reinforced MOC cement boards. The model showed promising results in predicting multiple mechanical properties, providing a valuable framework for optimizing the production process.

The work presented in this dissertation significantly expands composite materials research, paving the way for more accurate predictions that consider uncertainty, rapid material discovery, and the optimization of engineered structures. Future research endeavors will further strengthen the impact of the reported work.

## APPENDICES

## APPENDIX A



## Appendix A. Figures

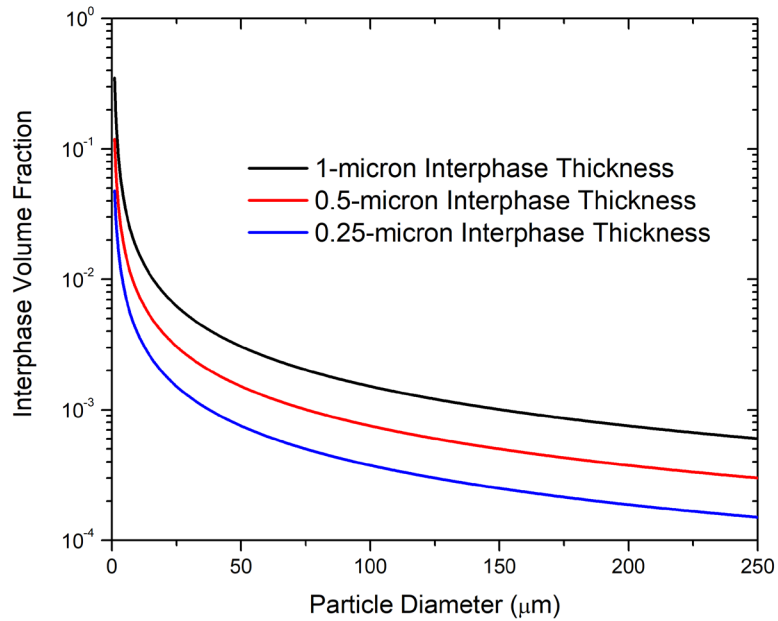


Figure A-1. Calculation of the interphase volume fraction for a composite with constant interphase thicknesses for spherical filler particles at a volume fraction of 0.05.

Comment: Figure A-1 demonstrates how the interphase volume fraction changes significantly with particle size for a fixed interphase thickness. Note that this interphase volume fraction can potentially exceed the 5 % vol. of filler used in this scenario. As the particle size is reduced, the interphase volume fraction starts to dominate the composite composition. This domination of interphase regions can lead to dramatically different overall composite material properties; thus, it is essential to accurately account for the properties of the interphase when developing accurate micromechanical models.

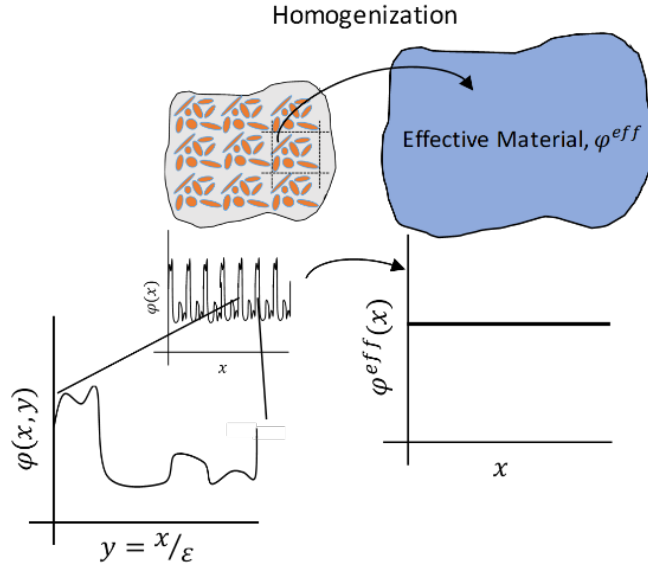


Figure A-2. Schematic of material homogenization. At the local scale, the heterogeneous material has a rapidly varying and periodic field of material properties. This material can be represented at the global scale by an effective material with constant fields.

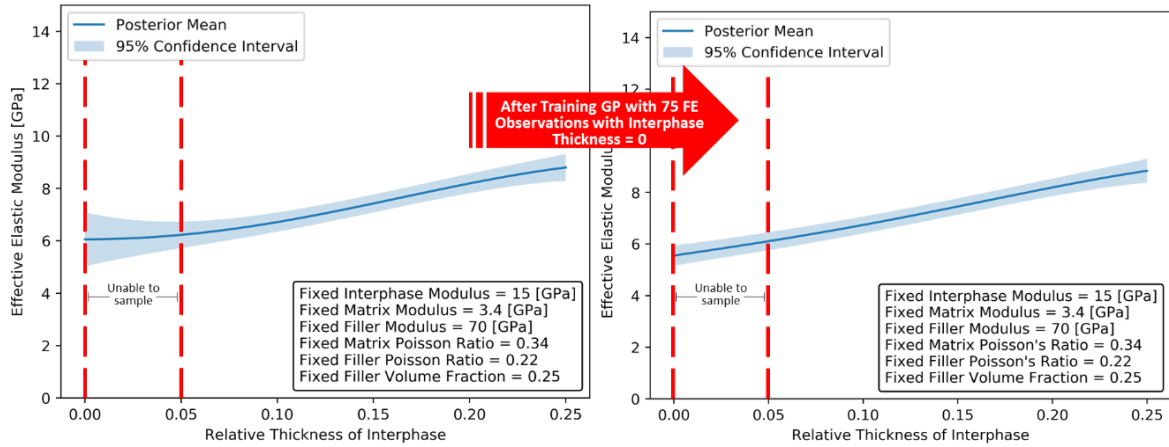


Figure A-3. Improvement of the GP by adding 75 additional FE observations when the interphase thickness was zero, i.e., only matrix and filler were included in the RVE.

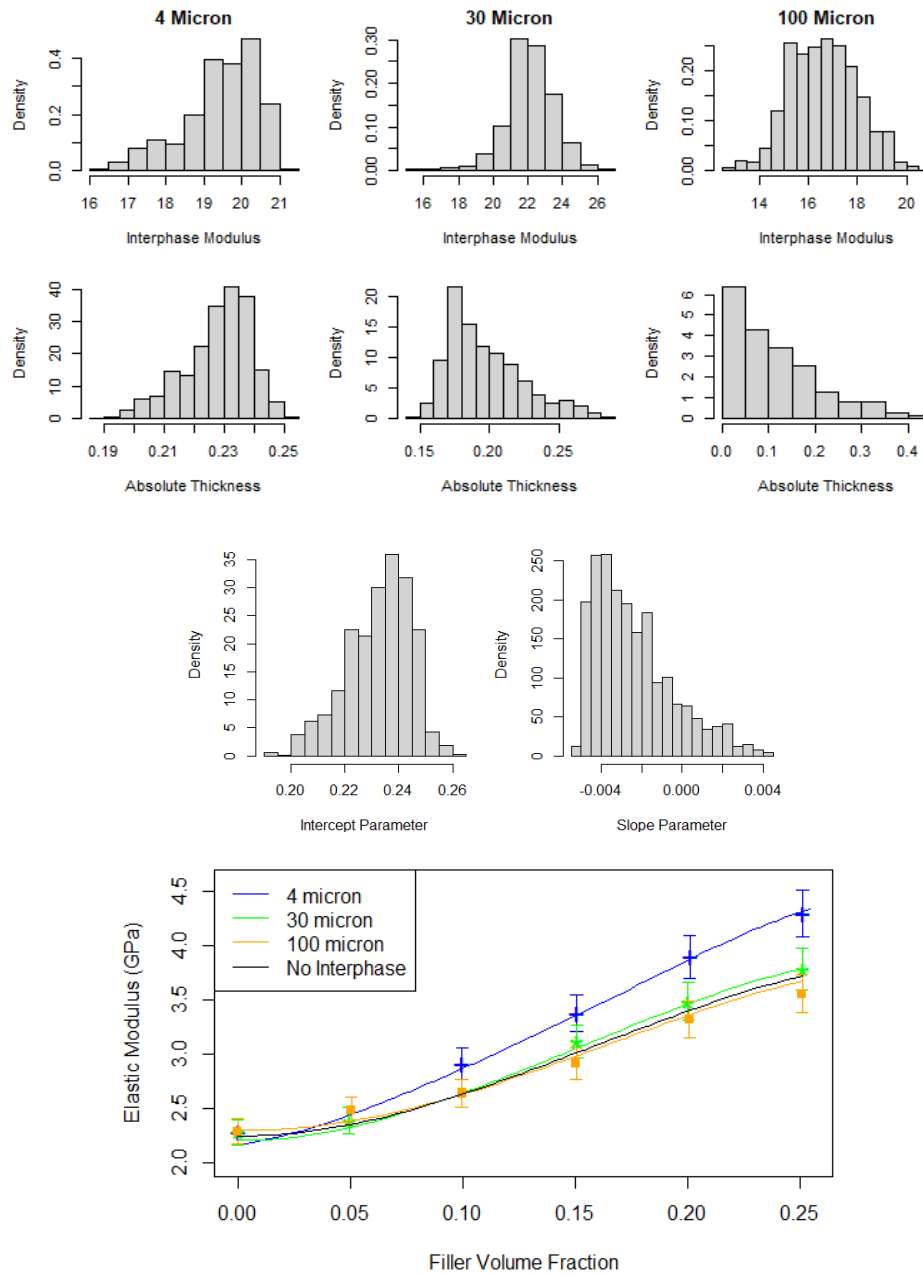


Figure A-4. The following are given for the glass-polycarbonate composite: a) approximate posterior distributions of the interphase modulus and absolute thickness for each particle size as indicated above, b) approximate posterior distributions for the slope and intercept parameters for absolute thickness as a function of particle size, and c) a comparison between the calibrated results and experimental results. Continuous curves are from the GP, sliced across the filler volume fraction with fixed values of the calibrated interphase thickness and modulus. The markers indicate experimental measurements. thickness and modulus.

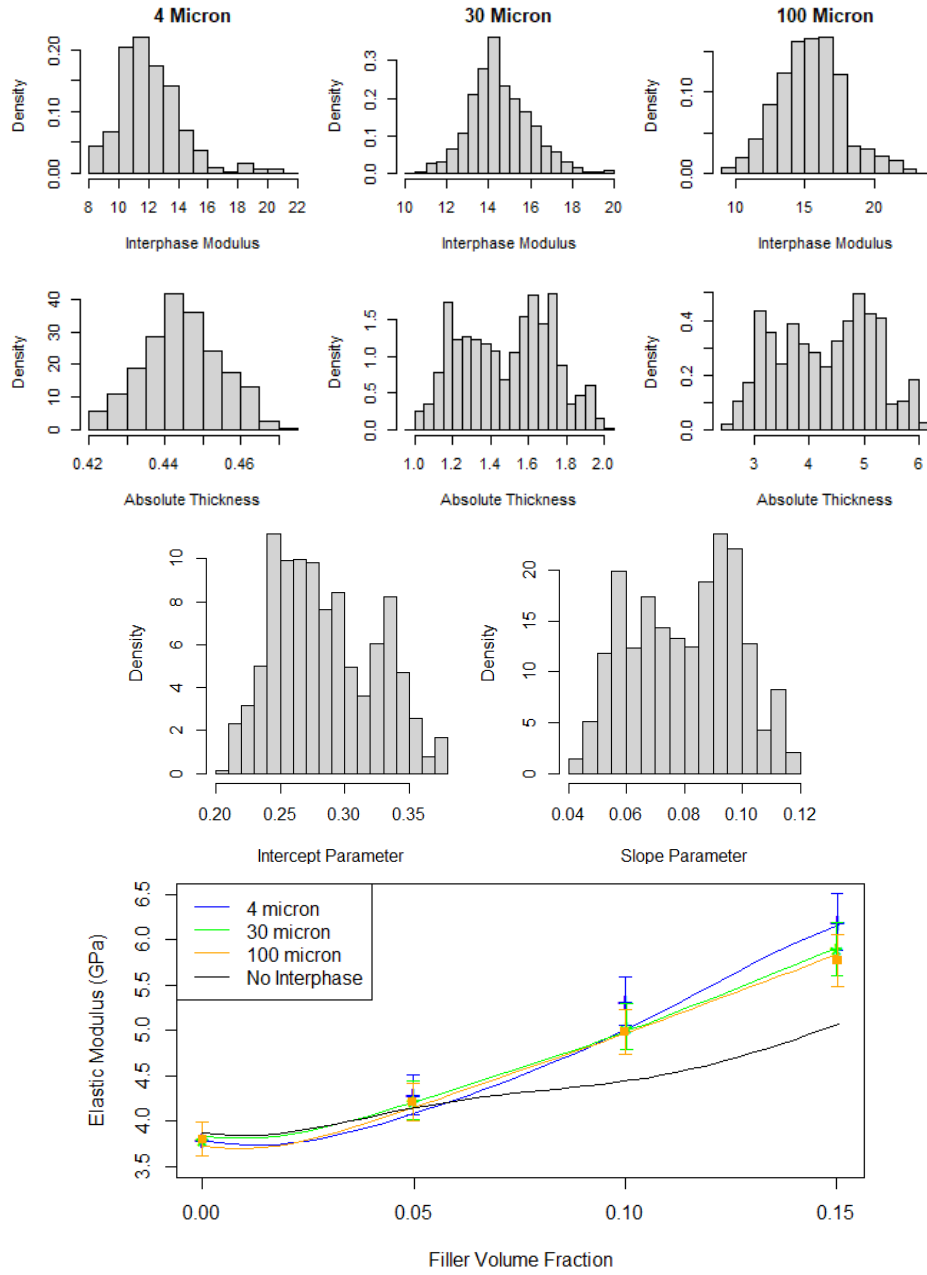


Figure A-5. The following are given for the glass-SAN composite: a) approximate posterior distributions of the interphase modulus and absolute thickness for each particle size as indicated above, b) approximate posterior distributions for the slope and intercept parameters for absolute thickness as a function of particle size, and c) a comparison between the calibrated results and experimental results. Continuous curves are from the GP, sliced across the filler volume fraction with fixed values of the calibrated interphase thickness and modulus. The markers indicate experimental measurements.

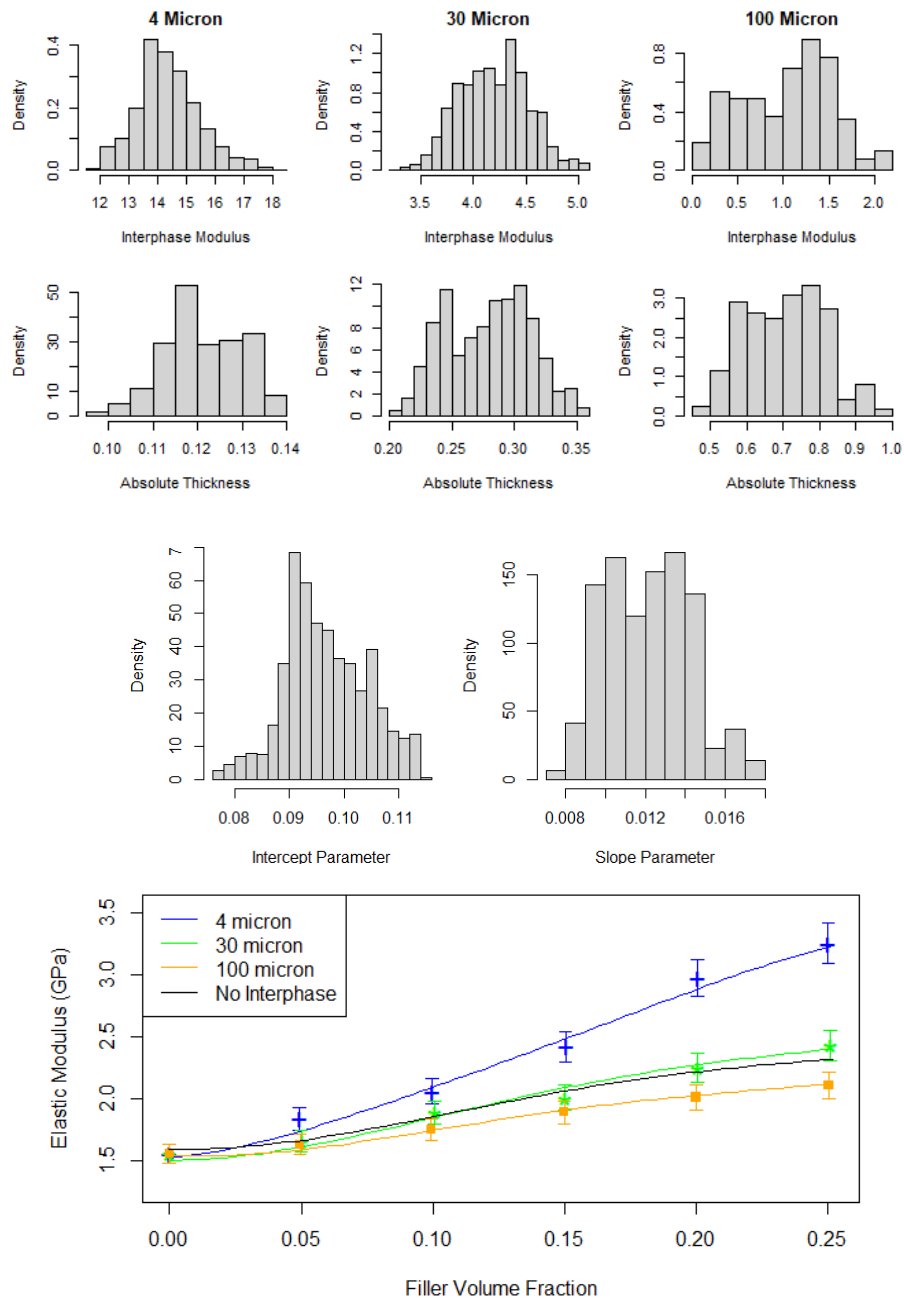


Figure A-6. The following are given for the glass-PP composite: a) approximate posterior distributions of the interphase modulus and absolute thickness for each particle size as indicated above, b) approximate posterior distributions for the slope and intercept parameters for absolute thickness as a function of particle size, and c) a comparison between the calibrated results and experimental results. Continuous curves are from the GP, sliced across the filler volume fraction with fixed values of the calibrated interphase thickness and modulus. The markers indicate experimental measurements.

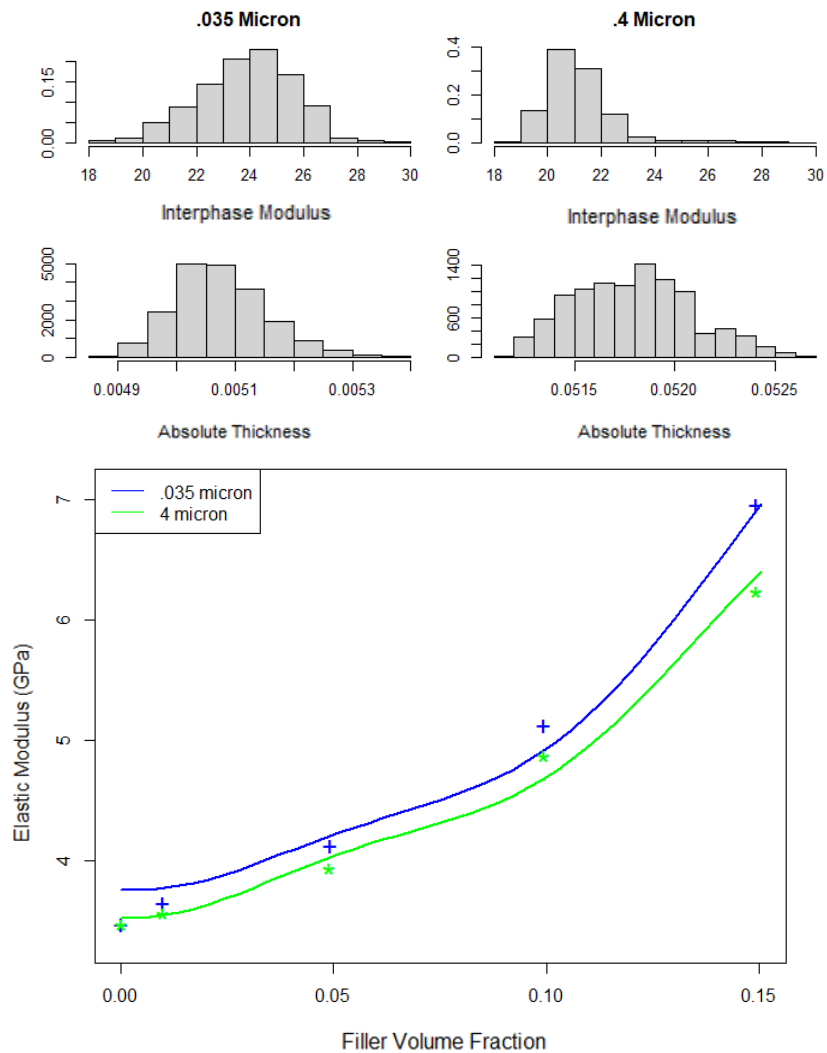


Figure A-7. The following are given for the alumina-polystyrene composite: a) approximate posterior distributions of the interphase modulus for each particle size, b) absolute thickness for each particle size, and c) a comparison between the calibrated results and experimental results. Continuous curves are from the GP, sliced across the filler volume fraction with fixed values of the calibrated interphase thickness and modulus. The markers indicate experimental measurements.

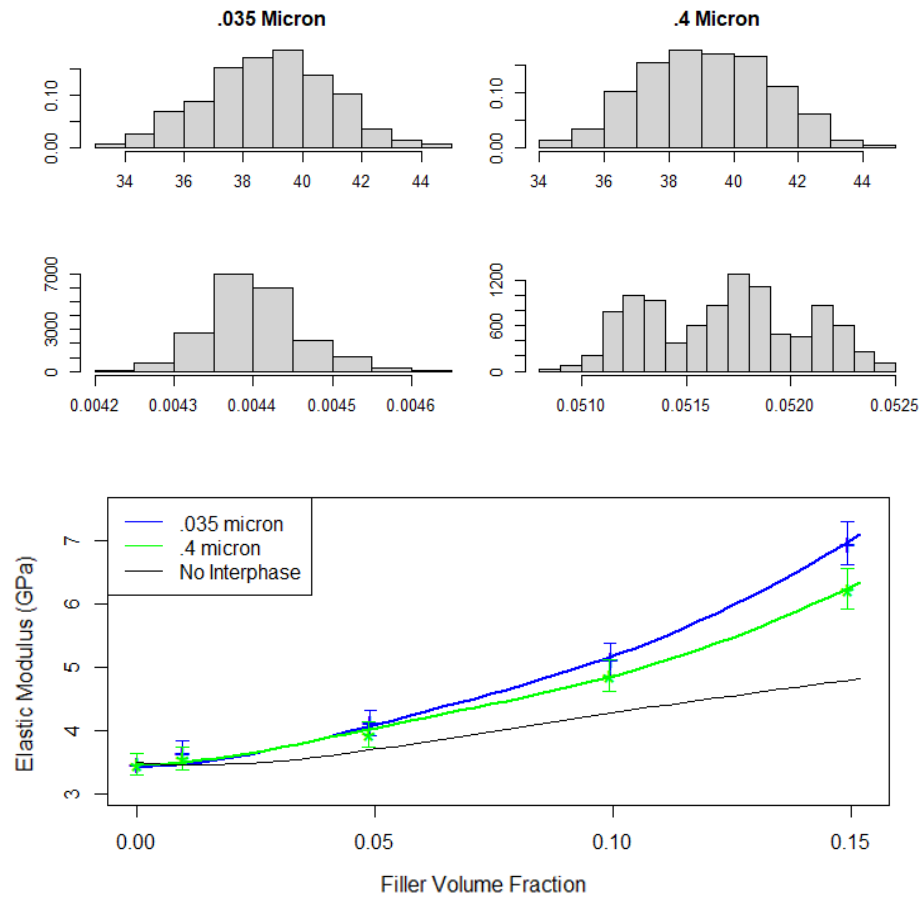


Figure A-8. The following are given for the alumina-SAN composite: a) approximate posterior distributions of the interphase modulus for each particle size, b) absolute thickness for each particle size, and c) a comparison between the calibrated results and experimental results. Continuous curves are from the GP, sliced across the filler volume fraction with fixed values of the calibrated interphase thickness and modulus. The markers indicate experimental measurements.

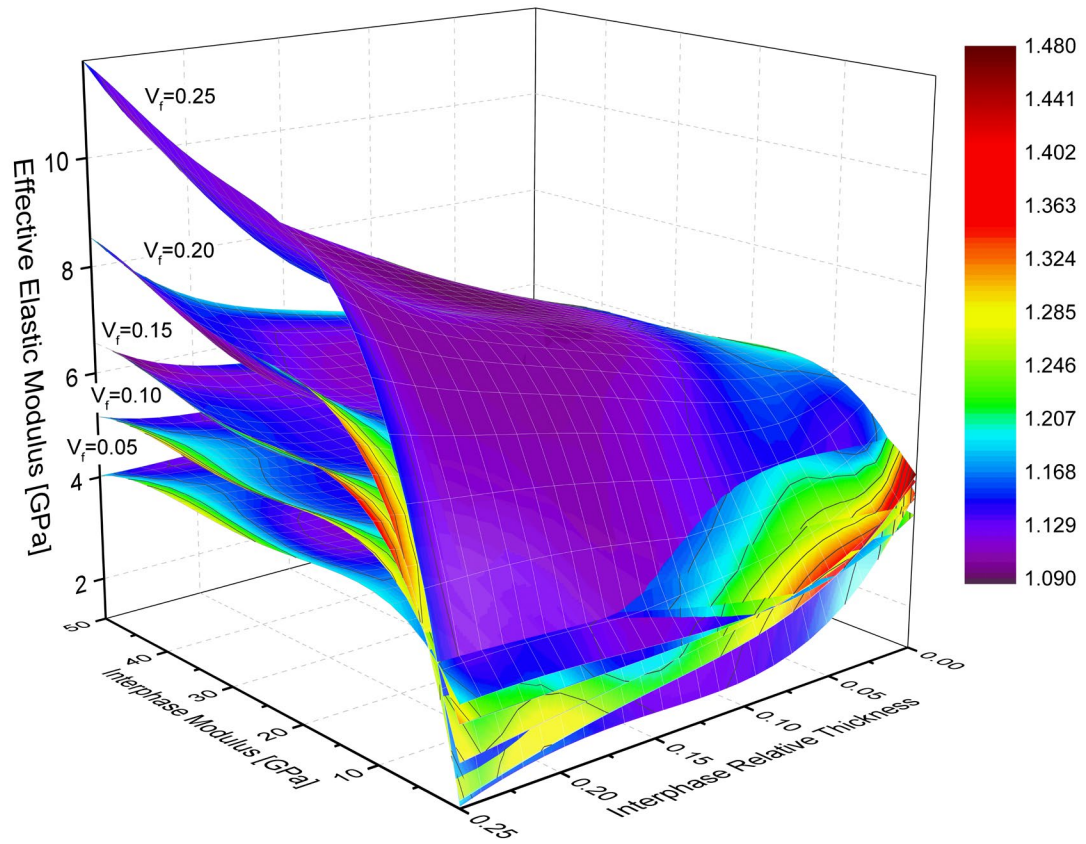


Figure A-9. Alternate angle of two-dimensional slices at various fixed volume fractions, illustrating the effects of the two calibration parameters on the overall effective elastic modulus. The heat map indicates the confidence intervals estimated from the posterior distribution at a given set of inputs.

$$E_m = 3.45 \text{ GPa } E_f = 70 \text{ GPa } \nu_m = 0.34 \nu_f = 0.22$$



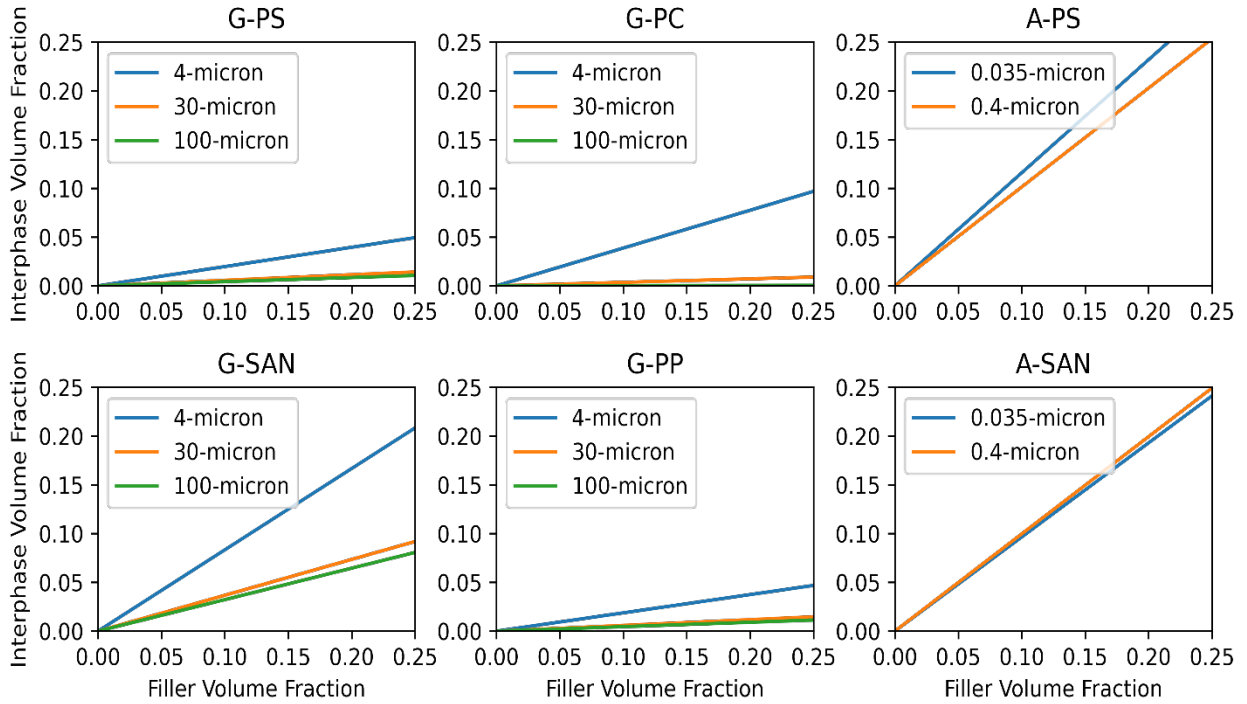


Figure A-10. Interphase volume fraction vs filler volume fraction plotted using the calibrated slope and intercept for each of the six composites.

## Appendix A. Discussion

### AD-1.

The stiffness tensor of a material obeying Hooke's law has 81 independent elements; however, stress and strain symmetries reduce this number to 36 unique entries. These entries can be represented in matrix notation.<sup>189</sup> Major symmetries from the strain energy function reduce the compliance,  $S$ , and stiffness matrices to 21 independent elastic constants and requires that  $C_{ij} = C_{ji}$  and  $S_{ij} = S_{ji}$ . A material with these symmetries and physical properties that vary depending on the axes of measurement is referred to as

an anisotropic material. Further reductions in the number of independent constants can be made if the material exhibits planes of symmetry.

AD-2.

The meshing density (number of elements per inclusion) was held approximately constant as the number of inclusions in the RVE was increased. This was achieved by scaling the mesh size by the simulated particle size.

## APPENDIX B

**The code to generate the macroscale fiber model with 20 ‘pie-slice’ subdivisions in ANSYS SpaceClaim.**

File name = ‘dissertation\_20\_pie\_slice\_geometry\_drawer.scsript’

```
# Python Script, API Version = V17
```

```
# Set Sketch Plane
```

```
selection = Selection.Create(CoordinateSystem1)
```

```
result = ViewHelper.SetSketchPlane(selection, Info1)
```

```
# EndBlock
```

```
# Sketch Point
```

```
point = Point2D.Create(MM(0), MM(0))
```

```
result = SketchPoint.Create(point)
```

```
# EndBlock
```

```
# Sketch Circle
```

```
origin = Point2D.Create(MM(0), MM(0))
```

```
result = SketchCircle.Create(origin, MM(0.2))
```

```
# EndBlock
```

```
# Rename 'Point' to 'Origin'
```

```
selection = Selection.Create(Curve1)
```

```
result = RenameObject.Execute(selection, "Origin")
```

```
# EndBlock
```

```
# Sketch Line
```

```
start = Point2D.Create(MM(1.22460635382238E-17), MM(0.2))
```

```
end = Point2D.Create(MM(0), MM(0))
```

```
result = SketchLine.Create(start, end)
```

```
# EndBlock
```

```
# Solidify Sketch
```

```
mode = InteractionMode.Solid
```

```
result = ViewHelper.SetViewMode(mode, Info2)
```

```
# EndBlock
```

```
# Extrude 20 Edges
```

```
selection = Selection.Create(Curve2, Curve3, Curve4, Curve5, Curve6, Curve7, Curve8,  
Curve9, Curve10, Curve11, Curve12, Curve13, Curve14, Curve15, Curve16, Curve17,  
Curve18, Curve19, Curve20, Curve21)
```

```

options = ExtrudeEdgeOptions()
options.PullSymmetric = False
options.Copy = False
options.ExtrudeType = ExtrudeType.None
result = ExtrudeEdges.Execute(selection, MM(30), options, Info3)
# EndBlock

# Extrude 20 Faces
selection = Selection.Create(Face1, Face2, Face3, Face4, Face5, Face6, Face7, Face8,
Face9, Face10, Face11, Face12, Face13, Face14, Face15, Face16, Face17, Face18,
Face19, Face20)
options = ExtrudeFaceOptions()
options.KeepMirror = True
options.KeepLayoutSurfaces = False
options.KeepCompositeFaceRelationships = True
options.PullSymmetric = False
options.OffsetMode = OffsetMode.IgnoreRelationships
options.Copy = False
options.ForceDoAsExtrude = False
options.ExtrudeType = ExtrudeType.Add
result = ExtrudeFaces.Execute(selection, MM(30), options, Info4)
# EndBlock

# Create Datum Plane
selection = Selection.Create(Face21)
result = DatumPlaneCreator.Create(selection, True, Info5)
# EndBlock

# Create Datum Plane
origin = Point.Create(MM(0.2), MM(0), MM(0))
zDir = Direction.DirX
result = DatumPlaneCreator.Create(origin, zDir, True, Info6)
# EndBlock

# Delete Objects
selection = Selection.Create(DatumPlane1)
result = Delete.Execute(selection)
# EndBlock

# Delete Objects
selection = Selection.Create(DatumPlane2)
result = Delete.Execute(selection)

```

# EndBlock

# Create Datum Plane

origin = Point.Create(MM(0.2), MM(0), MM(30))

zDir = Direction.DirY

result = DatumPlaneCreator.Create(origin, zDir, False, Info7)

# EndBlock

# Create Datum Plane

origin = Point.Create(MM(0.190211303259031), MM(-0.0618033988749895), MM(30))

zDir = Direction.Create(0.309016994374947, 0.951056516295154, 0)

result = DatumPlaneCreator.Create(origin, zDir, False, Info8)

# EndBlock

# Create Datum Plane

origin = Point.Create(MM(0.16180339887499), MM(-0.117557050458495), MM(30))

zDir = Direction.Create(0.587785252292473, 0.809016994374948, 0)

result = DatumPlaneCreator.Create(origin, zDir, False, Info9)

# EndBlock

# Create Datum Plane

origin = Point.Create(MM(0.117557050458495), MM(-0.161803398874989), MM(30))

zDir = Direction.Create(0.809016994374947, 0.587785252292473, 0)

result = DatumPlaneCreator.Create(origin, zDir, False, Info10)

# EndBlock

# Create Datum Plane

origin = Point.Create(MM(0.0618033988749895), MM(-0.190211303259031), MM(30))

zDir = Direction.Create(0.951056516295154, 0.309016994374948, 0)

result = DatumPlaneCreator.Create(origin, zDir, False, Info11)

# EndBlock

# Create Datum Plane

origin = Point.Create(MM(1.22460635382238E-17), MM(-0.2), MM(30))

zDir = Direction.DirX

result = DatumPlaneCreator.Create(origin, zDir, False, Info12)

# EndBlock

# Create Datum Plane

origin = Point.Create(MM(-0.0618033988749895), MM(-0.190211303259031),  
MM(30))

zDir = Direction.Create(0.951056516295154, -0.309016994374947, 0)

```
result = DatumPlaneCreator.Create(origin, zDir, False, Info13)
# EndBlock
```

```
# Create Datum Plane
origin = Point.Create(MM(-0.117557050458495), MM(-0.16180339887499), MM(30))
zDir = Direction.Create(0.809016994374948, -0.587785252292473, 0)
result = DatumPlaneCreator.Create(origin, zDir, False, Info14)
# EndBlock
```

```
# Create Datum Plane
origin = Point.Create(MM(-0.161803398874989), MM(-0.117557050458495), MM(30))
zDir = Direction.Create(0.587785252292473, -0.809016994374947, 0)
result = DatumPlaneCreator.Create(origin, zDir, False, Info15)
# EndBlock
```

```
# Create Datum Plane
origin = Point.Create(MM(-0.190211303259031), MM(-0.0618033988749895),
MM(30))
zDir = Direction.Create(0.309016994374948, -0.951056516295154, 0)
result = DatumPlaneCreator.Create(origin, zDir, False, Info16)
# EndBlock
```

```
# Delete Objects
selection = Selection.Create(Body41)
result = Delete.Execute(selection)
# EndBlock
```

```
# Slice Bodies by Plane
selection = Selection.Create(Body42)
datum = Selection.Create(DatumPlane13)
result = SplitBody.Execute(selection, datum, Info27)
# EndBlock
```

```
# Slice Bodies by Plane
selection = Selection.Create(Body42, Body43)
datum = Selection.Create(DatumPlane14)
result = SplitBody.Execute(selection, datum, Info28)
# EndBlock
```

```
# Slice Bodies by Plane
selection = Selection.Create(Body42, Body43, Body44, Body45)
```

```
datum = Selection.Create(DatumPlane15)
result = SplitBody.Execute(selection, datum, Info29)
# EndBlock
```

```
# Slice Bodies by Plane
selection = Selection.Create(Body42, Body43, Body44, Body45, Body46, Body47)
datum = Selection.Create(DatumPlane16)
result = SplitBody.Execute(selection, datum, Info30)
# EndBlock
```

```
# Slice Bodies by Plane
selection = Selection.Create(Body42, Body43, Body44, Body45, Body46, Body47,
Body48, Body49)
datum = Selection.Create(DatumPlane17)
result = SplitBody.Execute(selection, datum, Info31)
# EndBlock
```

```
# Slice Bodies by Plane
selection = Selection.Create(Body42, Body43, Body44, Body45, Body46, Body47,
Body48, Body49, Body50, Body51)
datum = Selection.Create(DatumPlane18)
result = SplitBody.Execute(selection, datum, Info32)
# EndBlock
```

```
# Slice Bodies by Plane
selection = Selection.Create(Body42, Body43, Body44, Body45, Body46, Body47,
Body48, Body49, Body50, Body51, Body52, Body53)
datum = Selection.Create(DatumPlane19)
result = SplitBody.Execute(selection, datum, Info33)
# EndBlock
```

```
# Slice Bodies by Plane
selection = Selection.Create(Body42, Body43, Body44, Body45, Body46, Body47,
Body48, Body49, Body50, Body51, Body52, Body53, Body54, Body55)
datum = Selection.Create(DatumPlane20)
result = SplitBody.Execute(selection, datum, Info34)
# EndBlock
```

```
# Slice Bodies by Plane
selection = Selection.Create(Body42, Body43, Body44, Body45, Body46, Body47,
Body48, Body49, Body50, Body51, Body52, Body53, Body54, Body55, Body56,
Body57)
```



```
datum = Selection.Create(DatumPlane21)
result = SplitBody.Execute(selection, datum, Info35)
# EndBlock
```

```
# Slice Bodies by Plane
selection = Selection.Create(Body42, Body43, Body44, Body45, Body46, Body47,
Body48, Body49, Body50, Body51, Body52, Body53, Body54, Body55, Body56,
Body57, Body58, Body59)
datum = Selection.Create(DatumPlane22)
result = SplitBody.Execute(selection, datum, Info36)
# EndBlock
```

```
# Rename 'Solid11' to 'Solid2'
selection = Selection.Create(Body45)
result = RenameObject.Execute(selection,"Solid2")
# EndBlock
```

```
# Rename 'Solid111' to 'Solid3'
selection = Selection.Create(Body47)
result = RenameObject.Execute(selection,"Solid3")
# EndBlock
```

```
# Rename 'Solid1111' to 'Solid4'
selection = Selection.Create(Body49)
result = RenameObject.Execute(selection,"Solid4")
# EndBlock
```

```
# Rename 'Solid111111' to 'Solid5'
selection = Selection.Create(Body53)
result = RenameObject.Execute(selection,"Solid5")
# EndBlock
```

```
# Rename 'Solid111111' to 'Solid6'
selection = Selection.Create(Body54)
result = RenameObject.Execute(selection,"Solid6")
# EndBlock
```

```
# Rename 'Solid111111' to 'Solid7'
selection = Selection.Create(Body56)
result = RenameObject.Execute(selection,"Solid7")
# EndBlock
```

```

# Rename 'Solid111111' to 'Solid8'
selection = Selection.Create(Body60)
result = RenameObject.Execute(selection,"Solid8")
# EndBlock

# Rename 'Solid111111' to 'Solid9'
selection = Selection.Create(Body62)
result = RenameObject.Execute(selection,"Solid9")
# EndBlock

# Rename 'Solid11111' to 'Solid10'
selection = Selection.Create(Body63)
result = RenameObject.Execute(selection,"Solid10")
# EndBlock

# Rename 'Solid1' to 'Solid11'
selection = Selection.Create(Body64)
result = RenameObject.Execute(selection,"Solid11")
# EndBlock

# Rename 'Solid1' to 'Solid12'
selection = Selection.Create(Body65)
result = RenameObject.Execute(selection,"Solid12")
# EndBlock

# Rename 'Solid1' to 'Solid13'
selection = Selection.Create(Body66)
result = RenameObject.Execute(selection,"Solid13")
# EndBlock

# Rename 'Solid1' to 'Solid14'
selection = Selection.Create(Body67)
result = RenameObject.Execute(selection,"Solid14")
# EndBlock

# Rename 'Solid' to 'Solid15'
selection = Selection.Create(Body68)
result = RenameObject.Execute(selection,"Solid15")
# EndBlock

# Rename 'Solid1' to 'Solid16'
selection = Selection.Create(Body69)

```

```
result = RenameObject.Execute(selection,"Solid16")
# EndBlock
```

```
# Rename 'Solid16' to 'Solid17'
selection = Selection.Create(Body70)
result = RenameObject.Execute(selection,"Solid17")
# EndBlock
```

```
# Rename 'Solid111' to 'Solid18'
selection = Selection.Create(Body71)
result = RenameObject.Execute(selection,"Solid18")
# EndBlock
```

```
# Rename 'Solid9' to 'Solid19'
selection = Selection.Create(Body61)
result = RenameObject.Execute(selection,"Solid19")
# EndBlock
```

```
# Rename 'Solid11111' to 'Solid20'
selection = Selection.Create(Body72)
result = RenameObject.Execute(selection,"Solid20")
# EndBlock
```

```
# Create New Part
selection = Selection.Create(Part4)
result = ComponentHelper.CreateNewComponent(selection, Info52)
# EndBlock
```

```
# Move Solid1
selections = Selection.Create(Body26)
component = Selection.Create(Part5)
result = ComponentHelper.MoveBodiesToComponent(selections, component, False,
Info53)
# EndBlock
```

```
# Move Solid2
selections = Selection.Create(Body27)
component = Selection.Create(Part5)
result = ComponentHelper.MoveBodiesToComponent(selections, component, False,
Info54)
# EndBlock
```

```
# Move Solid3
selections = Selection.Create(Body28)
component = Selection.Create(Part5)
result = ComponentHelper.MoveBodiesToComponent(selections, component, False,
Info55)
# EndBlock
```

```
# Move Solid4
selections = Selection.Create(Body29)
component = Selection.Create(Part5)
result = ComponentHelper.MoveBodiesToComponent(selections, component, False,
Info56)
# EndBlock
```

```
# Move Solid5
selections = Selection.Create(Body30)
component = Selection.Create(Part5)
result = ComponentHelper.MoveBodiesToComponent(selections, component, False,
Info57)
# EndBlock
```

```
# Move Solid6
selections = Selection.Create(Body31)
component = Selection.Create(Part5)
result = ComponentHelper.MoveBodiesToComponent(selections, component, False,
Info58)
# EndBlock
```

```
# Move Solid7
selections = Selection.Create(Body32)
component = Selection.Create(Part5)
result = ComponentHelper.MoveBodiesToComponent(selections, component, False,
Info59)
# EndBlock
```

```
# Move Solid8
selections = Selection.Create(Body33)
component = Selection.Create(Part5)
result = ComponentHelper.MoveBodiesToComponent(selections, component, False,
Info60)
# EndBlock
```

```
# Move Solid9
selections = Selection.Create(Body34)
component = Selection.Create(Part5)
result = ComponentHelper.MoveBodiesToComponent(selections, component, False,
Info61)
# EndBlock
```

```
# Move Solid10
selections = Selection.Create(Body35)
component = Selection.Create(Part5)
result = ComponentHelper.MoveBodiesToComponent(selections, component, False,
Info62)
# EndBlock
```

```
# Move Solid11
selections = Selection.Create(Body36)
component = Selection.Create(Part5)
result = ComponentHelper.MoveBodiesToComponent(selections, component, False,
Info63)
# EndBlock
```

```
# Move Solid12
selections = Selection.Create(Body37)
component = Selection.Create(Part5)
result = ComponentHelper.MoveBodiesToComponent(selections, component, False,
Info64)
# EndBlock
```

```
# Move Solid13
selections = Selection.Create(Body38)
component = Selection.Create(Part5)
result = ComponentHelper.MoveBodiesToComponent(selections, component, False,
Info65)
# EndBlock
```

```
# Move Solid14
selections = Selection.Create(Body39)
component = Selection.Create(Part5)
result = ComponentHelper.MoveBodiesToComponent(selections, component, False,
Info66)
# EndBlock
```

```
# Move Solid15
selections = Selection.Create(Body40)
component = Selection.Create(Part5)
result = ComponentHelper.MoveBodiesToComponent(selections, component, False,
Info67)
# EndBlock
```

```
# Move Solid16
selections = Selection.Create(Body73)
component = Selection.Create(Part5)
result = ComponentHelper.MoveBodiesToComponent(selections, component, False,
Info68)
# EndBlock
```

```
# Move Solid17
selections = Selection.Create(Body74)
component = Selection.Create(Part5)
result = ComponentHelper.MoveBodiesToComponent(selections, component, False,
Info69)
# EndBlock
```

```
# Move Solid18
selections = Selection.Create(Body75)
component = Selection.Create(Part5)
result = ComponentHelper.MoveBodiesToComponent(selections, component, False,
Info70)
# EndBlock
```

```
# Move Solid19
selections = Selection.Create(Body76)
component = Selection.Create(Part5)
result = ComponentHelper.MoveBodiesToComponent(selections, component, False,
Info71)
# EndBlock
```

```
# Move Solid20
selections = Selection.Create(Body77)
component = Selection.Create(Part5)
result = ComponentHelper.MoveBodiesToComponent(selections, component, False,
Info72)
# EndBlock
```

**The code used to assign material properties to the appropriate section, generate named selections, mesh and refine, assign boundary conditions, and generate post-processing commands in ANSYS-WB Mechanical.**

NOTE - Some features could not be automated and are, thus, commented out. Any errors can be manually corrected in the ANSYS Mechanical GUI.

File name = 'dissertation\_workbench\_act\_assign\_mats\_loads\_post.py'

```
#region UI Action
with Transaction(True):
    body_40 = DataModel.GetObjectById(40)
    body_40.Material = "CNC_Alginat_0"
#endregion
```

```
#region UI Action
with Transaction(True):
    body_43 = DataModel.GetObjectById(43)
    body_43.Material = "CNC_Alginat_1"
#endregion
```

```
#region UI Action
with Transaction(True):
    body_46 = DataModel.GetObjectById(46)
    body_46.Material = "CNC_Alginat_2"
#endregion
```

```
#region UI Action
with Transaction(True):
    body_49 = DataModel.GetObjectById(49)
    body_49.Material = "CNC_Alginat_3"
#endregion
```

```
#region UI Action
with Transaction(True):
    body_52 = DataModel.GetObjectById(52)
    body_52.Material = "CNC_Alginat_4"
#endregion
```

```
#region UI Action
with Transaction(True):
    body_55 = DataModel.GetObjectById(55)
    body_55.Material = "CNC_Alginat_5"
```

#endregion

#region UI Action

with Transaction(True):

body\_58 = DataModel.GetObjectById(58)

body\_58.Material = "CNC\_Alginat\_6"

#endregion

#region UI Action

with Transaction(True):

body\_61 = DataModel.GetObjectById(61)

body\_61.Material = "CNC\_Alginat\_7"

#endregion

#region UI Action

with Transaction(True):

body\_64 = DataModel.GetObjectById(64)

body\_64.Material = "CNC\_Alginat\_8"

#endregion

#region UI Action

with Transaction(True):

body\_67 = DataModel.GetObjectById(67)

body\_67.Material = "CNC\_Alginat\_9"

#endregion

#region UI Action

with Transaction(True):

body\_70 = DataModel.GetObjectById(70)

body\_70.Material = "CNC\_Alginat\_10"

#endregion

#region UI Action

with Transaction(True):

body\_73 = DataModel.GetObjectById(73)

body\_73.Material = "CNC\_Alginat\_11"

#endregion

#region UI Action

with Transaction(True):

body\_76 = DataModel.GetObjectById(76)

body\_76.Material = "CNC\_Alginat\_12"



```
#endregion
```

```
#region UI Action  
with Transaction(True):  
    body_79 = DataModel.GetObjectById(79)  
    body_79.Material = "CNC_Alginat_13"  
#endregion
```

```
#region UI Action  
with Transaction(True):  
    body_82 = DataModel.GetObjectById(82)  
    body_82.Material = "CNC_Alginat_14"  
#endregion
```

```
#region UI Action  
with Transaction(True):  
    body_85 = DataModel.GetObjectById(85)  
    body_85.Material = "CNC_Alginat_15"  
#endregion
```

```
#region UI Action  
with Transaction(True):  
    body_88 = DataModel.GetObjectById(88)  
    body_88.Material = "CNC_Alginat_16"  
#endregion
```

```
#region UI Action  
with Transaction(True):  
    body_91 = DataModel.GetObjectById(91)  
    body_91.Material = "CNC_Alginat_17"  
#endregion
```

```
#region UI Action  
with Transaction(True):  
    body_94 = DataModel.GetObjectById(94)  
    body_94.Material = "CNC_Alginat_18"  
#endregion
```

```
#region UI Action  
with Transaction(True):  
    body_97 = DataModel.GetObjectById(97)  
    body_97.Material = "CNC_Alginat_19"
```

```
#endregion
```

```
NS1 = DataModel.Project.Model.AddNamedSelection()  
NS1.ScopingMethod = GeometryDefineByType.Worksheet  
GenerationCriteria = NS1.GenerationCriteria  
Criterion1 = Ansys.ACT.Automation.Mechanical.NamedSelectionCriterion()  
Criterion1.Action = SelectionActionType.Add  
Criterion1.EntityType = SelectionType.GeoFace  
Criterion1.Criterion = SelectionCriterionType.LocationZ  
Criterion1.Operator = SelectionOperatorType.Equal  
Criterion1.Value = Quantity("30 [mm]")  
GenerationCriteria.Add(Criterion1)  
NS1.Generate()
```

```
NS1 = DataModel.Project.Model.AddNamedSelection()  
NS1.ScopingMethod = GeometryDefineByType.Worksheet  
GenerationCriteria = NS1.GenerationCriteria  
Criterion1 = Ansys.ACT.Automation.Mechanical.NamedSelectionCriterion()  
Criterion1.Action = SelectionActionType.Add  
Criterion1.EntityType = SelectionType.GeoFace  
Criterion1.Criterion = SelectionCriterionType.LocationZ  
Criterion1.Operator = SelectionOperatorType.Equal  
Criterion1.Value = Quantity("0 [mm]")  
GenerationCriteria.Add(Criterion1)  
NS1.Generate()
```

```
#region Details View Action  
mesh_35 = Model.Mesh  
mesh_35.TransitionOption = 1  
#endregion
```

```
#region Details View Action  
mesh_35.SpanAngleCenter = 1  
#endregion
```

```
#region Details View Action  
mesh_35.InitialSizeSeed = 2  
#endregion  
'''
```

```
#region Context Menu Action  
Named_selections = DataModel.GetObjectsByName("Selection")
```

```

refinement_172 = mesh_35.AddRefinement()
refinement_172.ScopingMethod = DataModel.GetObjectsByName("Selection")

#endregion

#region Context Menu Action
refinement_174 = mesh_35.AddRefinement()
refinement_174.ScopingMethod = "Selection_2"
#endregion
'''

#region Context Menu Action
mesh_35.GenerateMesh()
#endregion

#region Context Menu Action
solution_164 = DataModel.GetObjectById(164)
equivalent_elastic_strain_rst181 = solution_164.AddEquivalentElasticStrainRST()
#endregion

#region Context Menu Action
equivalent_stress_182 = solution_164.AddEquivalentStress()
#endregion
'''

#region Context Menu Action
geometry_34 = Model.Geometry
element_orientation_183 = geometry_34.AddElementOrientation()
#endregion
'''

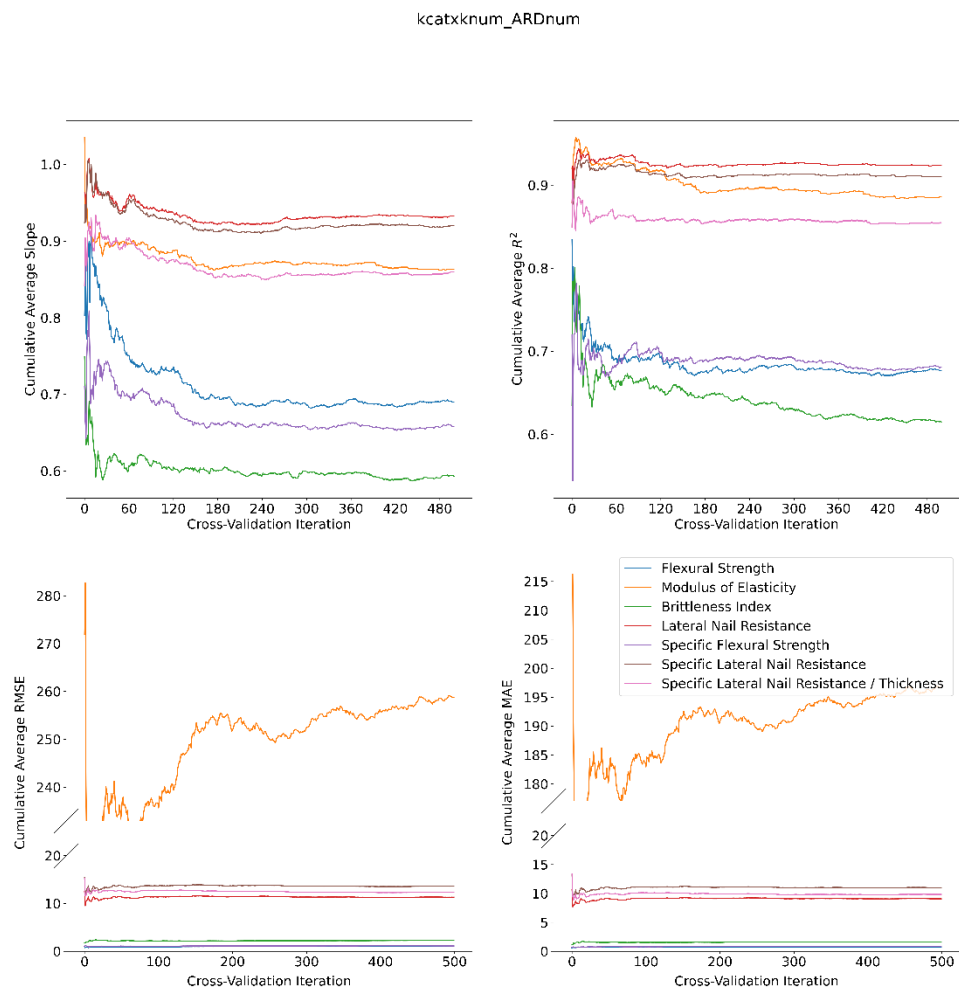
#region Context Menu Action
analysis_163 = DataModel.GetObjectById(163)
displacement_175 = analysis_163.AddDisplacement()
#endregion

#region Context Menu Action
fixed_support_177 = analysis_163.AddFixedSupport()
#endregion

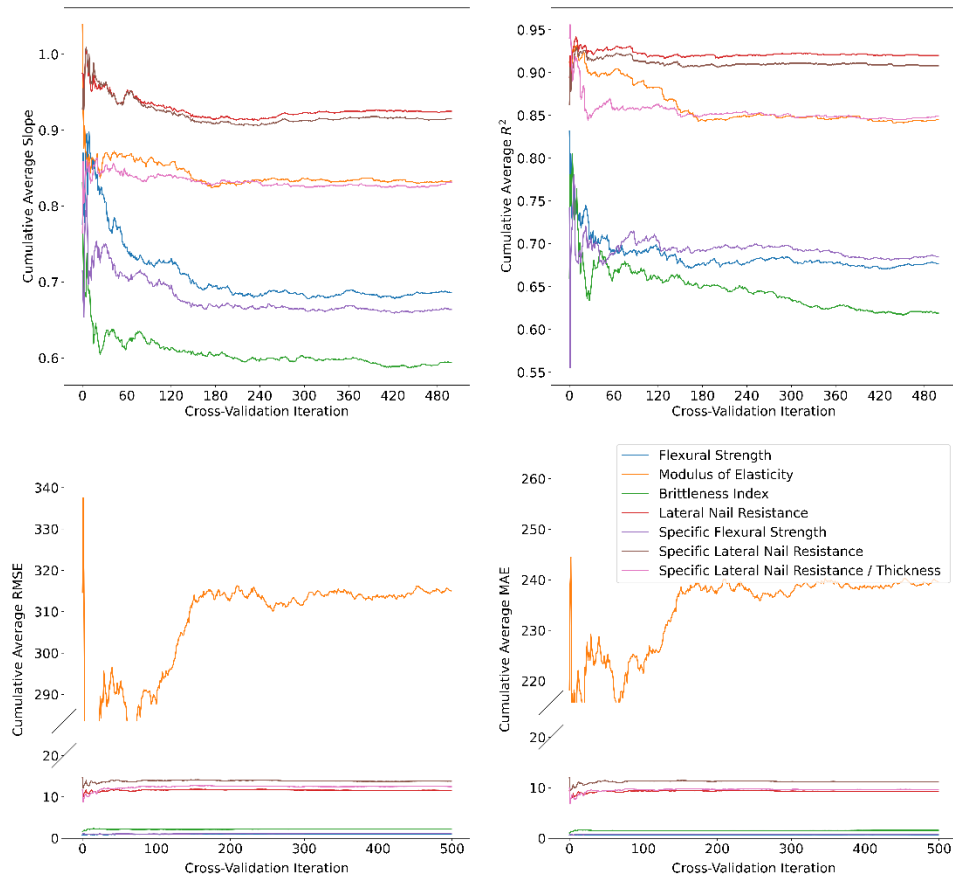
```

## APPENDIX C

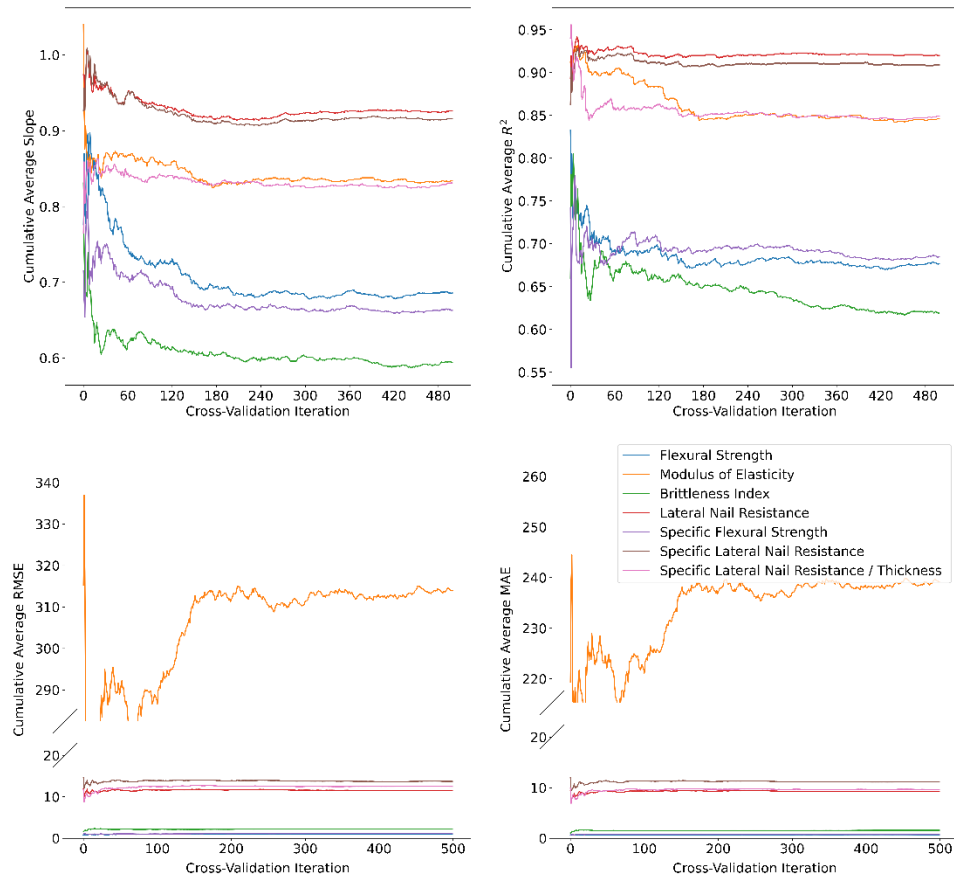
The cumulative cross-validation metrics were evaluated over the 500 shuffle-splits for the remaining kernel structures.



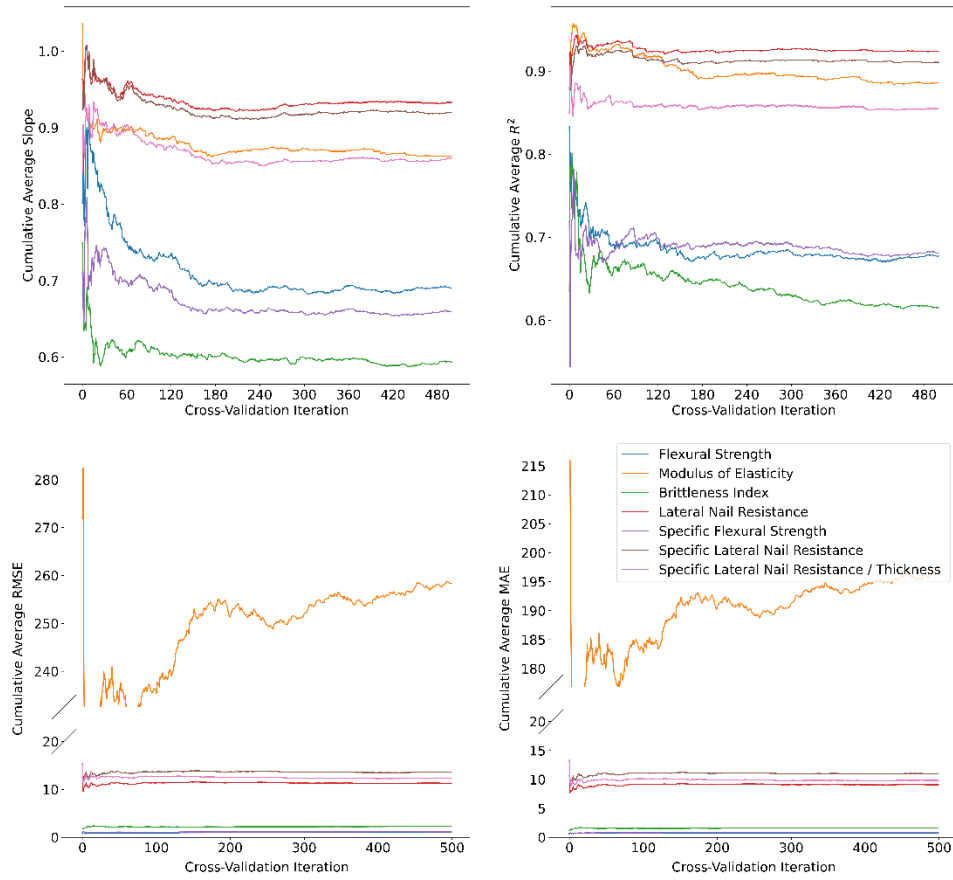
kcat+knum\_ARDcat\_ARDnum



kcat+knum\_ARDnum

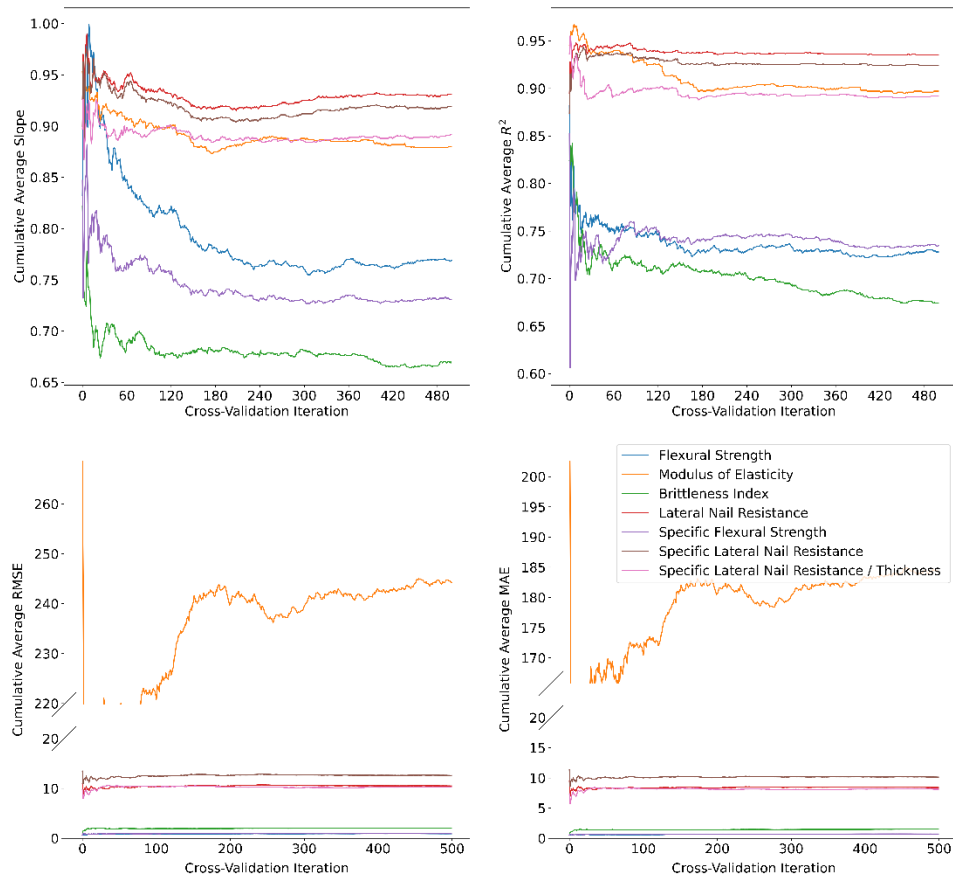


kcatxknum\_ARDcat\_ARDnum

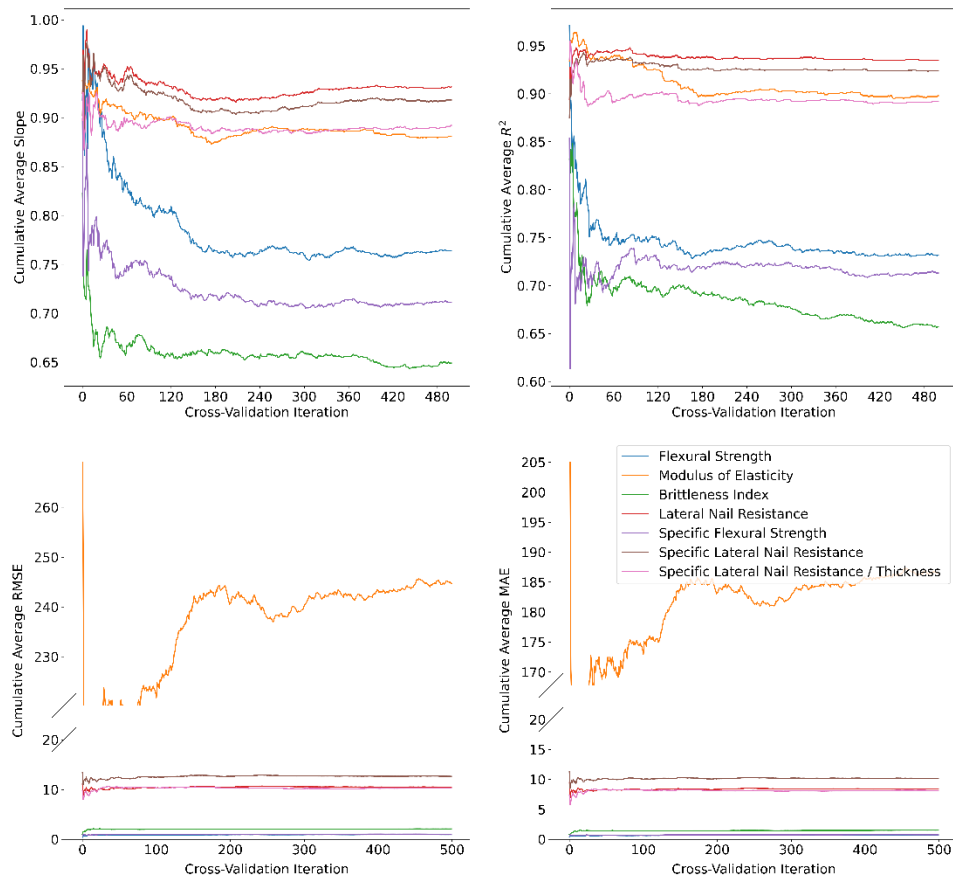




knum+kcat+kcatxknum\_ARDcat\_ARDnum\_repeat



knum+kcat+kcatxknum\_ARDnum



**Tables of the cross-validation performance for each kernel evaluated:**

Kernel	Slope	R <sup>2</sup>	RMSE	MAE	Y-Intercept
$k = k_{SE}^{cat} + k_{SE-ARD}^{num} + k_{SE}^{cat} \cdot k_{SE-ARD}^{num}$	0.764	0.732	0.933	0.671	2.38
$k = k_{SE-ARD}^{cat} + k_{SE-ARD}^{num} + k_{SE-ARD}^{cat} \cdot k_{SE-ARD}^{num}$	0.764	0.732	0.933	0.671	2.37
$k_{rpt} = k_{SE-ARD}^{cat} + k_{SE-ARD}^{num} + k_{SE-ARD}^{cat} \cdot k_{SE-ARD}^{num}$	0.769	0.728	0.922	0.649	2.29
$k = k_{SE-ARD}^{cat} \cdot k_{SE-ARD}^{num}$	0.69	0.678	0.987	0.739	3.06
$k = k_{SE}^{cat} + k_{SE-ARD}^{num}$	0.686	0.677	0.977	0.726	3.10
$k = k_{SE}^{cat} + k_{SE-ARD}^{num}$	0.686	0.677	0.977	0.726	3.10
$k = k_{SE}^{cat} \cdot k_{SE-ARD}^{num}$	0.69	0.677	0.988	0.739	3.06

Table 1: Cross-validation regression results for the sampled kernels averaged over 500 iterations, Flexural Strength (MPa).

Kernel	Slope	R <sup>2</sup>	RMSE	MAE	Y-Intercept
$k = k_{SE}^{cat} + k_{SE-ARD}^{num} + k_{SE}^{cat} \cdot k_{SE-ARD}^{num}$	0.881	0.898	245	186	252
$k = k_{SE-ARD}^{cat} + k_{SE-ARD}^{num} + k_{SE-ARD}^{cat} \cdot k_{SE-ARD}^{num}$	0.88	0.897	245	187	254
$k_{rpt} = k_{SE-ARD}^{cat} + k_{SE-ARD}^{num} + k_{SE-ARD}^{cat} \cdot k_{SE-ARD}^{num}$	0.88	0.897	244	184	256
$k = k_{SE-ARD}^{cat} \cdot k_{SE-ARD}^{num}$	0.863	0.886	258	196	295
$k = k_{SE}^{cat} \cdot k_{SE-ARD}^{num}$	0.863	0.886	259	197	296
$k = k_{SE}^{cat} + k_{SE-ARD}^{num}$	0.834	0.846	314	239	348
$k = k_{SE-ARD}^{cat} + k_{SE-ARD}^{num}$	0.833	0.845	315	240	350

Table 2: Cross-validation regression results for the sampled kernels averaged over 500 iterations, Modulus of Elasticity (MPa).

Kernel	Slope	R <sup>2</sup>	RMSE	MAE	Y-Intercept
$k = k_{SE-ARD}^{cat} + k_{SE-ARD}^{num} + k_{SE-ARD}^{cat} \cdot k_{SE-ARD}^{num}$	0.677	0.692	1.95	1.41	2.34
$k_{rpt} = k_{SE-ARD}^{cat} + k_{SE-ARD}^{num} + k_{SE-ARD}^{cat} \cdot k_{SE-ARD}^{num}$	0.669	0.674	2.05	1.50	2.41
$k = k_{SE}^{cat} + k_{SE-ARD}^{num} + k_{SE}^{cat} \cdot k_{SE-ARD}^{num}$	0.649	0.657	2.11	1.51	2.53
$k = k_{SE}^{cat} + k_{SE-ARD}^{num}$	0.594	0.619	2.24	1.57	2.94
$k = k_{SE-ARD}^{cat} + k_{SE-ARD}^{num}$	0.594	0.619	2.24	1.57	2.95
$k = k_{SE-ARD}^{cat} \cdot k_{SE-ARD}^{num}$	0.593	0.615	2.26	1.60	2.97
$k = k_{SE}^{cat} \cdot k_{SE-ARD}^{num}$	0.593	0.615	2.26	1.60	2.97

Table 3: Cross-validation regression results for the sampled kernels averaged over 500 iterations, Brittleness Index.

Kernel	Slope	R <sup>2</sup>	RMSE	MAE	Y-Intercept
$k = k_{SE-ARD}^{cat} + k_{SE-ARD}^{num} + k_{SE-ARD}^{cat} \cdot k_{SE-ARD}^{num}$	0.943	0.94	10.5	8.37	5.31
$k_{rpt} = k_{SE-ARD}^{cat} + k_{SE-ARD}^{num} + k_{SE-ARD}^{cat} \cdot k_{SE-ARD}^{num}$	0.931	0.935	10.5	8.41	6.98
$k = k_{SE}^{cat} + k_{SE-ARD}^{num} + k_{SE}^{cat} \cdot k_{SE-ARD}^{num}$	0.932	0.935	10.5	8.40	6.91
$k = k_{SE}^{cat} + k_{SE-ARD}^{num}$	0.933	0.924	11.3	9.08	7.05
$k = k_{SE-ARD}^{cat} \cdot k_{SE-ARD}^{num}$	0.933	0.924	11.3	9.09	7.08
$k = k_{SE}^{cat} + k_{SE-ARD}^{num}$	0.926	0.92	11.5	9.23	7.88
$k = k_{SE-ARD}^{cat} + k_{SE-ARD}^{num}$	0.925	0.92	11.6	9.27	7.96

Table 4: Cross-validation regression results for the sampled kernels averaged over 500 iterations, Lateral Nail Resistance (lb<sub>f</sub>).

Kernel	Slope	R <sup>2</sup>	RMSE	MAE	Y-Intercept
$k_{rpt} = k_{SE-ARD}^{cat} + k_{SE-ARD}^{num} + k_{SE-ARD}^{cat} \cdot k_{SE-ARD}^{num}$	0.731	0.735	1.01	0.722	3.30
$k = k_{SE-ARD}^{cat} + k_{SE-ARD}^{num} + k_{SE-ARD}^{cat} \cdot k_{SE-ARD}^{num}$	0.726	0.728	1.02	0.730	3.39
$k = k_{SE}^{cat} + k_{SE-ARD}^{num} + k_{SE}^{cat} \cdot k_{SE-ARD}^{num}$	0.711	0.713	1.05	0.767	3.54
$k = k_{SE}^{cat} + k_{SE-ARD}^{num}$	0.663	0.685	1.13	0.850	4.15
$k = k_{SE-ARD}^{cat} + k_{SE-ARD}^{num}$	0.664	0.685	1.13	0.850	4.14
$k = k_{SE-ARD}^{cat} \cdot k_{SE-ARD}^{num}$	0.659	0.681	1.14	0.849	4.22
$k = k_{SE}^{cat} \cdot k_{SE-ARD}^{num}$	0.658	0.681	1.14	0.850	4.22

Table 5: Cross-validation regression results for the sampled kernels averaged over 500 iterations, Specific Flexural Strength (MPa·cm<sup>3</sup>/g).

Kernel	Slope	R <sup>2</sup>	RMSE	MAE	Y-Intercept
$k = k_{SE-ARD}^{cat} + k_{SE-ARD}^{num} + k_{SE-ARD}^{cat} \cdot k_{SE-ARD}^{num}$	0.923	0.925	12.4	10.0	9.95
$k_{rpt} = k_{SE-ARD}^{cat} + k_{SE-ARD}^{num} + k_{SE-ARD}^{cat} \cdot k_{SE-ARD}^{num}$	0.919	0.924	12.6	10.1	10.4
$k = k_{SE}^{cat} + k_{SE-ARD}^{num} + k_{SE}^{cat} \cdot k_{SE-ARD}^{num}$	0.918	0.924	12.6	10.2	10.5
$k = k_{SE-ARD}^{cat} \cdot k_{SE-ARD}^{num}$	0.92	0.91	13.6	11.0	10.6
$k = k_{SE}^{cat} \cdot k_{SE-ARD}^{num}$	0.92	0.91	13.6	11.0	10.6
$k = k_{SE}^{cat} + k_{SE-ARD}^{num}$	0.916	0.909	13.7	11.1	11.2
$k = k_{SE-ARD}^{cat} + k_{SE-ARD}^{num}$	0.915	0.908	13.8	11.2	11.3

Table 6: Cross-validation regression results for the sampled kernels averaged over 500 iterations, Specific Lateral Nail Resistance (lb<sub>f</sub>·cm<sup>3</sup>/g).

Kernel	Slope	R <sup>2</sup>	RMSE	MAE	Y-Intercept
$k = k_{SE-ARD}^{cat} + k_{SE-ARD}^{num} + k_{SE-ARD}^{cat} \cdot k_{SE-ARD}^{num}$	0.892	0.892	10.3	8.12	13.3
$k_{rpt} = k_{SE-ARD}^{cat} + k_{SE-ARD}^{num} + k_{SE-ARD}^{cat} \cdot k_{SE-ARD}^{num}$	0.892	0.892	10.3	8.12	13.3
$k = k_{SE}^{cat} + k_{SE-ARD}^{num} + k_{SE}^{cat} \cdot k_{SE-ARD}^{num}$	0.892	0.892	10.3	8.12	13.3
$k = k_{SE-ARD}^{cat} \cdot k_{SE-ARD}^{num}$	0.86	0.855	12.3	9.82	17.2
$k = k_{SE}^{cat} \cdot k_{SE-ARD}^{num}$	0.86	0.854	12.4	9.83	17.3
$k = k_{SE}^{cat} + k_{SE-ARD}^{num}$	0.831	0.849	12.5	9.59	20.2
$k = k_{SE-ARD}^{cat} + k_{SE-ARD}^{num}$	0.831	0.849	12.5	9.59	20.2

Table 7: Cross-validation regression results for the sampled kernels averaged over 500 iterations, Specific Lateral Nail Resistance / Thickness (lb<sub>f</sub>·cm<sup>2</sup>/g).

### Tables of the validation performance for each kernel evaluated:

Kernel	Slope	R <sup>2</sup>	RMSE	MAE	Y-Intercept
$k_{rpt} = k_{SE-ARD}^{cat} + k_{SE-ARD}^{num} + k_{SE-ARD}^{cat} \cdot k_{SE-ARD}^{num}$	0.718	0.659	0.979	0.697	2.55
$k = k_{SE-ARD}^{cat} + k_{SE-ARD}^{num}$	0.594	0.650	1.130	0.855	4.03
$k = k_{SE-ARD}^{cat} \cdot k_{SE-ARD}^{num}$	0.706	0.636	1.180	0.842	2.91
$k = k_{SE-ARD}^{cat} + k_{SE-ARD}^{num} + k_{SE-ARD}^{cat} \cdot k_{SE-ARD}^{num}$	0.608	0.557	1.120	0.839	3.75
$k = k_{SE-ARD}^{cat} + k_{SE-ARD}^{num} + k_{SE-ARD}^{cat} \cdot k_{SE-ARD}^{num}$	0.627	0.529	1.300	1.020	3.37
$k = k_{SE-ARD}^{cat} \cdot k_{SE-ARD}^{num}$	0.698	0.529	1.320	0.944	3.09
$k = k_{SE-ARD}^{cat} + k_{SE-ARD}^{num}$	0.521	0.500	1.400	0.967	4.83

Table 1: Validation regression results for the sampled kernels averaged over ten iterations, Flexural Strength (MPa).

Kernel	Slope	R <sup>2</sup>	RMSE	MAE	Y-Intercept
$k = k_{SE-ARD}^{cat} + k_{SE-ARD}^{num} + k_{SE-ARD}^{cat} \cdot k_{SE-ARD}^{num}$	0.876	0.908	263.0	207.0	212.0
$k = k_{SE-ARD}^{cat} \cdot k_{SE-ARD}^{num}$	0.858	0.897	265.0	195.0	309.0
$k_{rpt} = k_{SE-ARD}^{cat} + k_{SE-ARD}^{num} + k_{SE-ARD}^{cat} \cdot k_{SE-ARD}^{num}$	0.890	0.884	247.0	180.0	266.0
$k = k_{SE-ARD}^{cat} + k_{SE-ARD}^{num} + k_{SE-ARD}^{cat} \cdot k_{SE-ARD}^{num}$	0.885	0.869	287.0	214.0	212.0
$k = k_{SE-ARD}^{cat} \cdot k_{SE-ARD}^{num}$	0.881	0.860	307.0	236.0	217.0
$k = k_{SE-ARD}^{cat} + k_{SE-ARD}^{num}$	0.736	0.762	438.0	319.0	589.0
$k = k_{SE-ARD}^{cat} + k_{SE-ARD}^{num}$	0.651	0.611	512.0	389.0	716.0

Table 2: Validation regression results for the sampled kernels averaged over ten iterations, Modulus of Elasticity (MPa).

Kernel	Slope	R <sup>2</sup>	RMSE	MAE	Y-Intercept
$k = k_{SE-ARD}^{cat} + k_{SE-ARD}^{num} + k_{SE-ARD}^{cat} \cdot k_{SE-ARD}^{num}$	0.589	0.535	2.69	2.03	2.99
$k = k_{SE-ARD}^{cat} + k_{SE-ARD}^{num} + k_{SE-ARD}^{cat} \cdot k_{SE-ARD}^{num}$	0.595	0.483	2.77	2.05	2.84
$k = k_{SE-ARD}^{cat} + k_{SE-ARD}^{num}$	0.472	0.475	2.51	1.73	3.81
$k_{rpt} = k_{SE-ARD}^{cat} + k_{SE-ARD}^{num} + k_{SE-ARD}^{cat} \cdot k_{SE-ARD}^{num}$	0.635	0.463	2.63	1.92	3.03
$k = k_{SE-ARD}^{cat} + k_{SE-ARD}^{num}$	0.422	0.419	2.81	1.92	4.20
$k = k_{SE-ARD}^{cat} \cdot k_{SE-ARD}^{num}$	0.398	0.379	3.08	2.33	4.48
$k = k_{SE-ARD}^{cat} \cdot k_{SE-ARD}^{num}$	0.450	0.378	2.92	2.08	4.03

Table 3: Validation regression results for the sampled kernels averaged over ten iterations, Brittleness Index.

Kernel	Slope	R <sup>2</sup>	RMSE	MAE	Y-Intercept
$k = k_{SE}^{cat} \cdot k_{SE-ARD}^{num}$	0.963	0.940	10.2	8.13	3.04
$k = k_{SE-ARD}^{cat} + k_{SE-ARD}^{num}$	0.894	0.930	14.6	11.10	8.19
$k_{rpt} = k_{SE-ARD}^{cat} + k_{SE-ARD}^{num} + k_{SE-ARD}^{cat} \cdot k_{SE-ARD}^{num}$	0.951	0.918	11.9	9.06	7.10
$k = k_{SE}^{cat} + k_{SE-ARD}^{num}$	0.828	0.903	14.5	11.00	18.30
$k = k_{SE}^{cat} \cdot k_{SE-ARD}^{num}$	0.951	0.901	12.0	9.44	5.25
$k = k_{SE}^{cat} + k_{SE-ARD}^{num} + k_{SE}^{cat} \cdot k_{SE-ARD}^{num}$	0.912	0.899	15.8	12.70	10.00
$k = k_{SE-ARD}^{cat} + k_{SE-ARD}^{num} + k_{SE-ARD}^{cat} \cdot k_{SE-ARD}^{num}$	0.891	0.888	15.6	12.90	11.50

Table 4: Validation regression results for the sampled kernels averaged over ten iterations, Lateral Nail Resistance ( $lb_f$ ).

Kernel	Slope	R <sup>2</sup>	RMSE	MAE	Y-Intercept
$k = k_{SE-ARD}^{cat} + k_{SE-ARD}^{num} + k_{SE-ARD}^{cat} \cdot k_{SE-ARD}^{num}$	0.684	0.691	1.15	0.843	3.82
$k_{rpt} = k_{SE-ARD}^{cat} + k_{SE-ARD}^{num} + k_{SE-ARD}^{cat} \cdot k_{SE-ARD}^{num}$	0.732	0.666	1.14	0.839	3.14
$k = k_{SE}^{cat} \cdot k_{SE-ARD}^{num}$	0.651	0.652	1.28	0.916	4.33
$k = k_{SE-ARD}^{cat} + k_{SE-ARD}^{num}$	0.608	0.615	1.29	0.993	4.89
$k = k_{SE}^{cat} + k_{SE-ARD}^{num} + k_{SE}^{cat} \cdot k_{SE-ARD}^{num}$	0.636	0.534	1.40	1.150	4.15
$k = k_{SE}^{cat} + k_{SE-ARD}^{num}$	0.497	0.520	1.50	1.060	6.28
$k = k_{SE}^{cat} \cdot k_{SE-ARD}^{num}$	0.592	0.477	1.41	1.040	4.86

Table 5: Validation regression results for the sampled kernels averaged over ten iterations, Specific Flexural Strength ( $MPa \cdot cm^3/g$ ).

Kernel	Slope	R <sup>2</sup>	RMSE	MAE	Y-Intercept
$k = k_{SE}^{cat} \cdot k_{SE-ARD}^{num}$	0.945	0.921	12.9	10.1	6.12
$k_{rpt} = k_{SE-ARD}^{cat} + k_{SE-ARD}^{num} + k_{SE-ARD}^{cat} \cdot k_{SE-ARD}^{num}$	0.985	0.896	15.0	11.3	3.87
$k = k_{SE-ARD}^{cat} + k_{SE-ARD}^{num}$	0.850	0.893	19.2	13.9	16.20
$k = k_{SE}^{cat} \cdot k_{SE-ARD}^{num}$	0.936	0.887	14.3	11.4	8.72
$k = k_{SE}^{cat} + k_{SE-ARD}^{num}$	0.793	0.878	18.9	14.1	27.40
$k = k_{SE}^{cat} + k_{SE-ARD}^{num} + k_{SE}^{cat} \cdot k_{SE-ARD}^{num}$	0.860	0.866	21.3	15.9	17.80
$k = k_{SE-ARD}^{cat} + k_{SE-ARD}^{num} + k_{SE-ARD}^{cat} \cdot k_{SE-ARD}^{num}$	0.838	0.853	19.7	15.7	20.70

Table 6: Validation regression results for the sampled kernels averaged over ten iterations, Specific Lateral Nail Resistance ( $lb_f \cdot cm^3/g$ ).

Kernel	Slope	R <sup>2</sup>	RMSE	MAE	Y-Intercept
$k = k_{SE}^{cat} \cdot k_{SE-ARD}^{num}$	0.867	0.860	11.1	8.77	15.70
$k_{rpt} = k_{SE-ARD}^{cat} + k_{SE-ARD}^{num} + k_{SE-ARD}^{cat} \cdot k_{SE-ARD}^{num}$	0.940	0.849	13.6	10.90	8.84
$k = k_{SE-ARD}^{cat} + k_{SE-ARD}^{num} + k_{SE-ARD}^{cat} \cdot k_{SE-ARD}^{num}$	0.831	0.838	14.8	12.10	17.10
$k = k_{SE-ARD}^{cat} \cdot k_{SE-ARD}^{num}$	0.876	0.801	13.7	10.60	14.50
$k = k_{SE}^{cat} + k_{SE-ARD}^{num} + k_{SE}^{cat} \cdot k_{SE-ARD}^{num}$	0.890	0.773	17.4	13.90	11.30
$k = k_{SE}^{cat} + k_{SE-ARD}^{num}$	0.708	0.768	16.6	13.20	37.60
$k = k_{SE-ARD}^{cat} + k_{SE-ARD}^{num}$	0.801	0.738	14.9	11.90	22.40

Table 7: Validation regression results for the sampled kernels averaged over ten iterations, Specific Lateral Nail Resistance / Thickness ( $lb_f \cdot cm^2/g$ ).

## REFERENCES

- (1) Committee on Integrated Computational Materials Engineering, N. R. C. *Integrated Computational Materials Engineering: A Transformational Discipline for Improved Competitiveness and National Security*; National Academies Press Washington, DC, 2008.
- (2) SUBCOMMITTEE ON THE MATERIALS GENOME INITIATIVE COMMITTEE ON TECHNOLOGY. MATERIALS GENOME INITIATIVE STRATEGIC PLAN, 2021.
- (3) Lupulescu, A.; Flowers, T.; Vermillion, L.; Henry, S. ASM Micrograph Database™. *Metallogr. Microstruct. Anal.* **2015**, 4 (4), 322–327. <https://doi.org/10.1007/s13632-015-0212-6>.
- (4) Ashby, M. F.; Cebon, D. Materials Selection in Mechanical Design. *J. Phys. IV France* **1993**, 03 (C7), C7-1-C7-9. <https://doi.org/10.1051/jp4:1993701>.
- (5) Jain, A.; Ong, S. P.; Hautier, G.; Chen, W.; Richards, W. D.; Dacek, S.; Cholia, S.; Gunter, D.; Skinner, D.; Ceder, G. Commentary: The Materials Project: A Materials Genome Approach to Accelerating Materials Innovation. *APL materials* **2013**, 1 (1).
- (6) Otsuka, S.; Kuwajima, I.; Hosoya, J.; Xu, Y.; Yamazaki, M. PoLyInfo: Polymer Database for Polymeric Materials Design. In *2011 International Conference on Emerging Intelligent Data and Web Technologies*; IEEE, 2011; pp 22–29.
- (7) Karger-Kocsis, J.; Mahmood, H.; Pegoretti, A. Recent Advances in Fiber/Matrix Interphase Engineering for Polymer Composites. *Progress in Materials Science* **2015**, 73, 1–43. <https://doi.org/10.1016/j.pmatsci.2015.02.003>.
- (8) Ghanbari, A.; Ndoro, T. V. M.; Leroy, F.; Rahimi, M.; Böhm, M. C.; Müller-Plathe, F. Interphase Structure in Silica–Polystyrene Nanocomposites: A Coarse-Grained Molecular Dynamics Study. *Macromolecules* **2012**, 45 (1), 572–584. <https://doi.org/10.1021/ma202044e>.
- (9) Thomason, J.; Rooyen, A. Transcrystallized Interphase in Thermoplastic Composites. *Journal of Materials Science* **1992**, 27, 897–907. <https://doi.org/10.1007/BF01197639>.
- (10) Hodzic, A.; Kalyanasundaram, S.; Kim, J. K.; Lowe, A. E.; Stachurski, Z. H. Application of Nano-Indentation, Nano-Scratch and Single Fibre Tests in Investigation of Interphases in Composite Materials. *Micron* **2001**, 32 (8), 765–775. [https://doi.org/10.1016/S0968-4328\(00\)00084-6](https://doi.org/10.1016/S0968-4328(00)00084-6).
- (11) Bedi, H. S.; Tiwari, M.; Agnihotri, P. K. Quantitative Determination of Size and Properties of Interphases in Carbon Nanotube-Based Multiscale Composites. *Carbon* **2018**, 132, 181–190. <https://doi.org/10.1016/j.carbon.2018.02.059>.
- (12) Kim, J.-K.; Sham, M.-L.; Wu, J. Nanoscale Characterisation of Interphase in Silane Treated Glass Fibre Composites. **2001**, 12.
- (13) Theocaris, P. S.; Papanicolaou, G. C. The Effect of the Boundary Interphase on the Thermomechanical Behaviour of Composites Reinforced with Short Fibres. *Fibre*

- Science and Technology* **1979**, 12 (6), 421–433. [https://doi.org/10.1016/0015-0568\(79\)90016-2](https://doi.org/10.1016/0015-0568(79)90016-2).
- (14) Wang, Y.; Zhang, Y.; Zhao, H.; Li, X.; Huang, Y.; Schadler, L. S.; Chen, W.; Brinson, L. C. Identifying Interphase Properties in Polymer Nanocomposites Using Adaptive Optimization. *Composites Science and Technology* **2018**, 162, 146–155. <https://doi.org/10.1016/j.compscitech.2018.04.017>.
  - (15) Williams, J. G.; Donnellan, M. E.; James, M. R.; Morris, W. L. Properties of the Interphase in Organic Matrix Composites. *Materials Science and Engineering: A* **1990**, 126 (1), 305–312. [https://doi.org/10.1016/0921-5093\(90\)90137-R](https://doi.org/10.1016/0921-5093(90)90137-R).
  - (16) Wilson, K. S.; Allen, A. J.; Washburn, N. R.; Antonucci, J. M. Interphase Effects in Dental Nanocomposites Investigated by Small-angle Neutron Scattering. *Journal of Biomedical Materials Research Part A* **2007**, 81 (1), 113–123.
  - (17) Eitan, A.; Fisher, F. T.; Andrews, R.; Brinson, L. C.; Schadler, L. S. Reinforcement Mechanisms in MWCNT-Filled Polycarbonate. *Composites Science and Technology* **2006**, 66 (9), 1162–1173. <https://doi.org/10.1016/j.compscitech.2005.10.004>.
  - (18) Korsunsky, A. M. Elastic Behavior of Materials: Continuum Aspects. *Encyclopedia of Materials: Science and Technology* **2001**, 2398–2404.
  - (19) Theory Reference for the Mechanical APDL and Mechanical Applications, Release 12.0, 2009.
  - (20) Ortolano González, J. M.; Hernández Ortega, J. A.; Oliver Olivella, X. *A Comparative Study on Homogenization Strategies for Multi-Scale Analysis of Materials*; Centre Internacional de Mètodes Numèrics en Enginyeria (CIMNE), 2013.
  - (21) Nemat-Nasser, S.; Hori, M. *Micromechanics: Overall Properties of Heterogeneous Materials*; Elsevier, 2013.
  - (22) Voigt, W. Ueber Die Beziehung Zwischen Den Beiden Elasticitätsconstanten Isotroper Körper. *Annalen der physik* **1889**, 274 (12), 573–587.
  - (23) Reuß, A. Berechnung Der Fließgrenze von Mischkristallen Auf Grund Der Plastizitätsbedingung Für Einkristalle. *ZAMM-Journal of Applied Mathematics and Mechanics/Zeitschrift für Angewandte Mathematik und Mechanik* **1929**, 9 (1), 49–58.
  - (24) Eshelby, J. D.; Peierls, R. E. The Determination of the Elastic Field of an Ellipsoidal Inclusion, and Related Problems. *Proceedings of the Royal Society of London. Series A. Mathematical and Physical Sciences* **1957**, 241 (1226), 376–396. <https://doi.org/10.1098/rspa.1957.0133>.
  - (25) Mura, T. *Micromechanics of Defects in Solids*; Springer Science & Business Media, 2013.
  - (26) Benveniste, Y. A New Approach to the Application of Mori-Tanaka's Theory in Composite Materials. *Mechanics of materials* **1987**, 6 (2), 147–157.
  - (27) Mori, T.; Tanaka, K. Average Stress in Matrix and Average Elastic Energy of Materials with Misfitting Inclusions. *Acta Metallurgica* **1973**, 21 (5), 571–574. [https://doi.org/10.1016/0001-6160\(73\)90064-3](https://doi.org/10.1016/0001-6160(73)90064-3).
  - (28) Budarapu, P. R.; Zhuang, X.; Rabczuk, T.; Bordas, S. P. A. Chapter One - Multiscale Modeling of Material Failure: Theory and Computational Methods. In *Advances in*



- Applied Mechanics*; Hussein, M. I., Ed.; Advances in Crystals and Elastic Metamaterials, Part 2; Elsevier, 2019; Vol. 52, pp 1–103. <https://doi.org/10.1016/bs.aams.2019.04.002>.
- (29) Kerner, E. H. The Elastic and Thermo-Elastic Properties of Composite Media. *Proceedings of the physical society. Section B* **1956**, 69 (8), 808.
  - (30) Ahmed, S.; Jones, F. R. A Review of Particulate Reinforcement Theories for Polymer Composites. *Journal of Materials Science* **1990**, 25, 4933–4942. <https://doi.org/10.1007/BF00580110>.
  - (31) Cox, H. L. The Elasticity and Strength of Paper and Other Fibrous Materials. *British journal of applied physics* **1952**, 3 (3), 72.
  - (32) Yan, J.; Demirci, E.; Gleadall, A. Are Classical Fibre Composite Models Appropriate for Material Extrusion Additive Manufacturing? A Thorough Evaluation of Analytical Models. *Additive Manufacturing* **2023**, 62, 103371. <https://doi.org/10.1016/j.addma.2022.103371>.
  - (33) Barbero, E. J. *Finite Element Analysis of Composite Materials Using ANSYS®*, 2nd edition.; CRC Press: Boca Raton, 2013.
  - (34) David Müzel, S.; Bonhin, E. P.; Guimarães, N. M.; Guidi, E. S. Application of the Finite Element Method in the Analysis of Composite Materials: A Review. *Polymers (Basel)* **2020**, 12 (4), 818. <https://doi.org/10.3390/polym12040818>.
  - (35) Guedes, J.; Kikuchi, N. Preprocessing and Postprocessing for Materials Based on the Homogenization Method with Adaptive Finite Element Methods. *Computer Methods in Applied Mechanics and Engineering* **1990**, 83 (2), 143–198. [https://doi.org/10.1016/0045-7825\(90\)90148-F](https://doi.org/10.1016/0045-7825(90)90148-F).
  - (36) Alfano, G.; Crisfield, M. A. Finite Element Interface Models for the Delamination Analysis of Laminated Composites: Mechanical and Computational Issues. *Int. J. Numer. Meth. Engng.* **2001**, 50 (7), 1701–1736. <https://doi.org/10.1002/nme.93>.
  - (37) Carniel, T. A.; Klahr, B.; Fancello, E. A. A Multiscale Numerical Approach for the Finite Strains Analysis of Materials Reinforced with Helical Fibers. *Mechanics of Materials* **2018**, 126, 75–85. <https://doi.org/10.1016/j.mechmat.2018.07.014>.
  - (38) Hassani, B.; Hinton, E. A Review of Homogenization and Topology Optimization IDhomogenization Theory for Media with Periodic Structure. *Computers and Structures* **1998**, 11.
  - (39) Charalambakis, N. Homogenization Techniques and Micromechanics. A Survey and Perspectives. *Applied Mechanics Reviews* **2010**, 63 (3), 030803. <https://doi.org/10.1115/1.4001911>.
  - (40) Kanouté, P.; Boso, D. P.; Chaboche, J. L.; Schrefler, B. A. Multiscale Methods for Composites: A Review. *Arch Computat Methods Eng* **2009**, 16 (1), 31–75. <https://doi.org/10.1007/s11831-008-9028-8>.
  - (41) Turner, M. J.; Clough, R. W.; Martin, H. C.; Topp, L. J. Stiffness and Deflection Analysis of Complex Structures. *journal of the Aeronautical Sciences* **1956**, 23 (9), 805–823.

- (42) Sabat, L.; Kundu, C. K. History of Finite Element Method: A Review. *Recent Developments in Sustainable Infrastructure: Select Proceedings of ICRDSI 2019* **2020**, 395–404.
- (43) Nguetseng, G. A General Convergence Result for a Functional Related to the Theory of Homogenization. *SIAM J. Math. Anal.* **1989**, *20* (3), 608–623. <https://doi.org/10.1137/0520043>.
- (44) Allaire, G.; El Ganaoui, K. Homogenization of a Conductive and Radiative Heat Transfer Problem. *Multiscale Model. Simul.* **2009**, *7* (3), 1148–1170. <https://doi.org/10.1137/080714737>.
- (45) DeLyser, R. R.; Kuester, E. F. Homogenization Analysis of Electromagnetic Strip Gratings. *Journal of electromagnetic waves and applications* **1991**, *5* (11), 1217–1236.
- (46) Song, Y. S.; Youn, J. R. Asymptotic Expansion Homogenization of Permeability Tensor for Plain Woven Fabrics. *Composites Part A: Applied Science and Manufacturing* **2006**, *37* (11), 2080–2087. <https://doi.org/10.1016/j.compositesa.2005.12.002>.
- (47) Hollister, S. J.; Kikuchi, N. A Comparison of Homogenization and Standard Mechanics Analyses for Periodic Porous Composites. *Computational Mechanics* **1992**, *10* (2), 73–95.
- (48) Hassani, B.; Hinton, E. A Review of Homogenization and Topology Optimization II—Analytical and Numerical Solution of Homogenization Equations. *Computers & structures* **1998**, *69* (6), 719–738.
- (49) Digimat 2019-FE.
- (50) Ansys® Academic Research Mechanical, Release 19.0.
- (51) Kanit, T.; Forest, S.; Galliet, I.; Mounoury, V.; Jeulin, D. Determination of the Size of the Representative Volume Element for Random Composites: Statistical and Numerical Approach. *International Journal of Solids and Structures* **2003**, *40* (13), 3647–3679. [https://doi.org/10.1016/S0020-7683\(03\)00143-4](https://doi.org/10.1016/S0020-7683(03)00143-4).
- (52) Hill, R. Elastic Properties of Reinforced Solids: Some Theoretical Principles. *Journal of the Mechanics and Physics of Solids* **1963**, *11* (5), 357–372.
- (53) El Moumen, A.; Kanit, T.; Imad, A. Numerical Evaluation of the Representative Volume Element for Random Composites. *European Journal of Mechanics - A/Solids* **2021**, *86*, 104181. <https://doi.org/10.1016/j.euromechsol.2020.104181>.
- (54) Wang, H.; Bai, Y.; Liu, S.; Wu, J.; Wong, C. Combined Effects of Silica Filler and Its Interface in Epoxy Resin. *Acta Materialia* **2002**, *50* (17), 4369–4377.
- (55) Suquet, P. M. Elements of Homogenization for Inelastic Solid Mechanics, Homogenization Techniques for Composite Media. *Lecture notes in physics* **1985**, 272, 193.
- (56) Sun, C. T.; Vaidya, R. S. Prediction of Composite Properties from a Representative Volume Element. *Composites Science and Technology* **1996**, *56* (2), 171–179. [https://doi.org/10.1016/0266-3538\(95\)00141-7](https://doi.org/10.1016/0266-3538(95)00141-7).

- (57) Kennedy, M. C.; O'Hagan, A. Bayesian Calibration of Computer Models. *Journal of the Royal Statistical Society: Series B (Statistical Methodology)* **2001**, 63 (3), 425–464. <https://doi.org/10.1111/1467-9868.00294>.
- (58) Rajaram, D.; Puranik, T. G.; Ashwin Renganathan, S.; Sung, W.; Fischer, O. P.; Mavris, D. N.; Ramamurthy, A. Empirical Assessment of Deep Gaussian Process Surrogate Models for Engineering Problems. *Journal of Aircraft* **2021**, 58 (1), 182–196.
- (59) Zhou, Z.; Ong, Y. S.; Nguyen, M. H.; Lim, D. A Study on Polynomial Regression and Gaussian Process Global Surrogate Model in Hierarchical Surrogate-Assisted Evolutionary Algorithm. In *2005 IEEE congress on evolutionary computation*; IEEE, 2005; Vol. 3, pp 2832–2839.
- (60) Radaideh, M. I.; Kozłowski, T. Surrogate Modeling of Advanced Computer Simulations Using Deep Gaussian Processes. *Reliability Engineering & System Safety* **2020**, 195, 106731.
- (61) Box, G. E.; Tiao, G. C. *Bayesian Inference in Statistical Analysis*; John Wiley & Sons, 2011.
- (62) Vigneshwaran, S.; Sundarakannan, R.; John, K. M.; Joel Johnson, R. D.; Prasath, K. A.; Ajith, S.; Arumugaprabu, V.; Uthayakumar, M. Recent Advancement in the Natural Fiber Polymer Composites: A Comprehensive Review. *Journal of Cleaner Production* **2020**, 277, 124109. <https://doi.org/10.1016/j.jclepro.2020.124109>.
- (63) Venkatesan, J.; Bhatnagar, I.; Manivasagan, P.; Kang, K.-H.; Kim, S.-K. Alginate Composites for Bone Tissue Engineering: A Review. *International journal of biological macromolecules* **2015**, 72, 269–281.
- (64) Hollaway, L. *Polymer Composites for Civil and Structural Engineering*; Springer Science & Business Media, 2012.
- (65) Olusegun, D. S.; Stephen, A.; Adekanye, T. A. Assessing Mechanical Properties of Natural Fibre Reinforced Composites for Engineering Applications. *Journal of Minerals and Materials Characterization and Engineering* **2012**, 11 (1), 780–784.
- (66) Jancar, J.; Douglas, J. F.; Starr, F. W.; Kumar, S. K.; Cassagnau, P.; Lesser, A. J.; Sternstein, S. S.; Buehler, M. J. Current Issues in Research on Structure–Property Relationships in Polymer Nanocomposites. *Polymer* **2010**, 51 (15), 3321–3343. <https://doi.org/10.1016/j.polymer.2010.04.074>.
- (67) Khan, I.; Saeed, K.; Khan, I. Nanoparticles: Properties, Applications and Toxicities. *Arabian Journal of Chemistry* **2019**, 12 (7), 908–931. <https://doi.org/10.1016/j.arabjc.2017.05.011>.
- (68) Vaia, R. A.; Giannelis, E. P. Polymer Nanocomposites: Status and Opportunities. *MRS Bull.* **2001**, 26 (5), 394–401. <https://doi.org/10.1557/mrs2001.93>.
- (69) Jiang, Y.; Zhang, D.; He, L.; Zhang, L. Entropic Interactions in Semiflexible Polymer Nanocomposite Melts. *J. Phys. Chem. B* **2016**, 120 (3), 572–582. <https://doi.org/10.1021/acs.jpcb.5b09551>.

- (70) Picu, R. C.; Ozmusul, M. S. Structure of Linear Polymeric Chains Confined between Impenetrable Spherical Walls. *The Journal of Chemical Physics* **2003**, *118* (24), 11239–11248. <https://doi.org/10.1063/1.1576216>.
- (71) Quan, H.; Zhong, G.; Yang, M.-B.; Huang, R. On Transcrystallinity in Semi-Crystalline Polymer Composites. *Composites Science and Technology* **2005**, *65*, 999–1021. <https://doi.org/10.1016/j.compscitech.2004.11.015>.
- (72) Odegard, G. M.; Clancy, T. C.; Gates, T. S. Modeling of the Mechanical Properties of Nanoparticle/Polymer Composites. *Polymer* **2005**, *46* (2), 553–562. <https://doi.org/10.1016/j.polymer.2004.11.022>.
- (73) Llorca, J.; Elices, M.; Termonia, Y. Elastic Properties of Sphere-Reinforced Composites with a Mesophase. *Acta Materialia* **2000**, *48* (18), 4589–4597. [https://doi.org/10.1016/S1359-6454\(00\)00245-7](https://doi.org/10.1016/S1359-6454(00)00245-7).
- (74) Yu, S.; Yang, S.; Cho, M. Multi-Scale Modeling of Cross-Linked Epoxy Nanocomposites. *Polymer* **2009**, *50* (3), 945–952. <https://doi.org/10.1016/j.polymer.2008.11.054>.
- (75) Papanicolaou, G. C.; Paipetis, S. A.; Theocaris, P. S. The Concept of Boundary Interphase in Composite Mechanics. *Colloid & Polymer Sci* **1978**, *256* (7), 625–630. <https://doi.org/10.1007/BF01784402>.
- (76) Reynaud, E.; Jouen, T.; Gauthier, C.; Vigier, G.; Varlet, J. Nanofillers in Polymeric Matrix: A Study on Silica Reinforced PA6. *Polymer* **2001**, *42* (21), 8759–8768. [https://doi.org/10.1016/S0032-3861\(01\)00446-3](https://doi.org/10.1016/S0032-3861(01)00446-3).
- (77) Khodadadi, A.; Golestanian, H.; Aghadavoudi, F. Two Modified Multiscale Modeling Approaches for Determination of Two-Phase and Hybrid Nanocomposite Properties. *Proceedings of the Institution of Mechanical Engineers, Part C: Journal of Mechanical Engineering Science* **2022**, *236* (1), 496–510.
- (78) Munz, M.; Sturm, H.; Schulz, E.; Hinrichsen, G. The Scanning Force Microscope as a Tool for the Detection of Local Mechanical Properties within the Interphase of Fibre Reinforced Polymers. *Composites Part A: Applied Science and Manufacturing* **1998**, *29* (9), 1251–1259. [https://doi.org/10.1016/S1359-835X\(98\)00077-3](https://doi.org/10.1016/S1359-835X(98)00077-3).
- (79) Vollenberg, P.; Heikens, D. Particle Size Dependence of the Young's Modulus of Filled Polymers: 1. Preliminary Experiments. *Polymer* **1989**, *30* (9), 1656–1662.
- (80) Benveniste, Y.; Dvorak, G. J.; Chen, T. On Diagonal and Elastic Symmetry of the Approximate Effective Stiffness Tensor of Heterogeneous Media. *Journal of the Mechanics and Physics of Solids* **1991**, *39* (7), 927–946. [https://doi.org/10.1016/0022-5096\(91\)90012-D](https://doi.org/10.1016/0022-5096(91)90012-D).
- (81) Kari, S.; Berger, H.; Rodriguez-Ramos, R.; Gabbert, U. Computational Evaluation of Effective Material Properties of Composites Reinforced by Randomly Distributed Spherical Particles. *Composite Structures* **2007**, *77* (2), 223–231. <https://doi.org/10.1016/j.compstruct.2005.07.003>.
- (82) Shen, L.; Li, J. Homogenization of a Fibre/Sphere with an Inhomogeneous Interphase for the Effective Elastic Moduli of Composites. *Proc. R. Soc. A* **2005**, *461* (2057), 1475–1504. <https://doi.org/10.1098/rspa.2005.1447>.

- (83) Shojaie, M.; Golestanian, H. Effects of Interface Characteristics on Mechanical Properties of Carbon Nanotube Reinforced Polymer Composites. *Materials Science and Technology* **2011**, 27 (5), 916–922.
- (84) Santner, T. J.; Williams, B. J.; Notz, W. I.; Williams, B. J. *The Design and Analysis of Computer Experiments*; Springer, 2003; Vol. 1.
- (85) McKay, M. D.; Beckman, R. J.; Conover, W. J. A Comparison of Three Methods for Selecting Values of Input Variables in the Analysis of Output from a Computer Code. *Technometrics* **1979**, 21 (2), 239–245. <https://doi.org/10.2307/1268522>.
- (86) Loeppky, J. L.; Moore, L. M.; Williams, B. J. Batch Sequential Designs for Computer Experiments. *Journal of Statistical Planning and Inference* **2010**, 140 (6), 1452–1464. <https://doi.org/10.1016/j.jspi.2009.12.004>.
- (87) Omairey, S. L.; Dunning, P. D.; Sriramula, S. Development of an ABAQUS Plugin Tool for Periodic RVE Homogenisation. *Engineering with Computers* **2019**, 35 (2), 567–577. <https://doi.org/10.1007/s00366-018-0616-4>.
- (88) Okereke, M. I.; Akpoyomare, A. I. A Virtual Framework for Prediction of Full-Field Elastic Response of Unidirectional Composites. *Computational Materials Science* **2013**, 70, 82–99. <https://doi.org/10.1016/j.commatsci.2012.12.036>.
- (89) ANSYS Meshing User's Guide, Release 13.0, 2010.
- (90) Roache, P. J. *Fundamentals of Verification and Validation*; Hermosa Publishers: Socorro, New Mexico, 2009.
- (91) Jones, D. R.; Schonlau, M.; Welch, W. J. Efficient Global Optimization of Expensive Black-Box Functions. *Journal of Global Optimization* **1998**, 13 (4), 455–492. <https://doi.org/10.1023/A:1008306431147>.
- (92) Gelman, A.; Carlin, J. B.; Stern, H. S.; Dunson, D. B.; Vehtari, A.; Rubin, D. B. *Bayesian Data Analysis*; CRC press, 2013.
- (93) Van Krevelen, D. W.; Te Nijenhuis, K. *Properties of Polymers: Their Correlation with Chemical Structure; Their Numerical Estimation and Prediction from Additive Group Contributions*; Elsevier, 2009.
- (94) Brown, D.; Mele, P.; Marceau, S.; Alberola, N. D. A Molecular Dynamics Study of a Model Nanoparticle Embedded in a Polymer Matrix. *Macromolecules* **2003**, 36 (4), 1395–1406.
- (95) Munz, M. Evidence for a Three-Zone Interphase with Complex Elastic–Plastic Behaviour: Nanoindentation Study of an Epoxy/Thermoplastic Composite. *J. Phys. D: Appl. Phys.* **2006**, 39 (18), 4044–4058. <https://doi.org/10.1088/0022-3727/39/18/016>.
- (96) Ureña-Benavides, E. E.; Brown, P. J.; Kitchens, C. L. Effect of Jet Stretch and Particle Load on Cellulose Nanocrystal–Alginate Nanocomposite Fibers. *Langmuir* **2010**, 26 (17), 14263–14270. <https://doi.org/10.1021/la102216v>.
- (97) Aderibigbe, B. A.; Buyana, B. Alginate in Wound Dressings. *Pharmaceutics* **2018**, 10 (2), 42.

- (98) Barbu, A.; Neamtu, B.; Zăhan, M.; Iancu, G. M.; Bacila, C.; Mireșan, V. Current Trends in Advanced Alginate-Based Wound Dressings for Chronic Wounds. *Journal of Personalized Medicine* **2021**, *11* (9), 890.
- (99) Varaprasad, K.; Jayaramudu, T.; Kanikireddy, V.; Toro, C.; Sadiku, E. R. Alginate-Based Composite Materials for Wound Dressing Application: A Mini Review. *Carbohydrate polymers* **2020**, *236*, 116025.
- (100) Dhivya, S.; Padma, V. V.; Santhini, E. Wound Dressings—a Review. *BioMedicine* **2015**, *5* (4), 22.
- (101) Taskin, A.; Yasar, M.; Ozaydin, I.; Kaya, B.; Bat, O.; Ankarali, S.; Yildirim, U.; Aydin, M. The Hemostatic Effect of Calcium Alginate in Experimental Splenic Injury Model. *ULUSAL TRAVMA VE ACIL CERRAHI DERGISI-TURKISH JOURNAL OF TRAUMA & EMERGENCY SURGERY* **2013**, *19* (3).
- (102) Ureña-Benavides, E. E.; Kitchens, C. L. Wide-Angle X-Ray Diffraction of Cellulose Nanocrystal–Alginate Nanocomposite Fibers. *Macromolecules* **2011**, *44* (9), 3478–3484. <https://doi.org/10.1021/ma102731m>.
- (103) N’Gatta, K. M.; Belaid, H.; El Hayek, J.; Assanvo, E. F.; Kajdan, M.; Masquelez, N.; Boa, D.; Cavaillès, V.; Bechelany, M.; Salameh, C. 3D Printing of Cellulose Nanocrystals Based Composites to Build Robust Biomimetic Scaffolds for Bone Tissue Engineering. *Sci Rep* **2022**, *12* (1), 21244. <https://doi.org/10.1038/s41598-022-25652-x>.
- (104) Wang, B.; Torres-Rendon, J. G.; Yu, J.; Zhang, Y.; Walther, A. Aligned Bioinspired Cellulose Nanocrystal-Based Nanocomposites with Synergetic Mechanical Properties and Improved Hygromechanical Performance. *ACS Appl. Mater. Interfaces* **2015**, *7* (8), 4595–4607. <https://doi.org/10.1021/am507726t>.
- (105) Dri, F. L.; Hector, L. G.; Moon, R. J.; Zavattieri, P. D. Anisotropy of the Elastic Properties of Crystalline Cellulose Iβ from First Principles Density Functional Theory with Van Der Waals Interactions. *Cellulose* **2013**, *20* (6), 2703–2718. <https://doi.org/10.1007/s10570-013-0071-8>.
- (106) Moon, R. J.; Martini, A.; Nairn, J.; Simonsen, J.; Youngblood, J. Cellulose Nanomaterials Review: Structure, Properties and Nanocomposites. *Chem. Soc. Rev.* **2011**, *40* (7), 3941. <https://doi.org/10.1039/c0cs00108b>.
- (107) Šturcová, A.; Davies, G. R.; Eichhorn, S. J. Elastic Modulus and Stress-Transfer Properties of Tunicate Cellulose Whiskers. *Biomacromolecules* **2005**, *6* (2), 1055–1061. <https://doi.org/10.1021/bm049291k>.
- (108) Kumar, A.; Negi, Y. S.; Choudhary, V.; Bhardwaj, N. K. Characterization of Cellulose Nanocrystals Produced by Acid-Hydrolysis from Sugarcane Bagasse as Agro-Waste. *Journal of materials physics and chemistry* **2014**, *2* (1), 1–8.
- (109) Pandi, Narsimha.; Sonawane, S. H.; Anand Kishore, K. Synthesis of Cellulose Nanocrystals (CNCs) from Cotton Using Ultrasound-Assisted Acid Hydrolysis. *Ultrasonics Sonochemistry* **2021**, *70*, 105353. <https://doi.org/10.1016/j.ultsonch.2020.105353>.

- (110) Chen, S.; Schueneman, G.; Pipes, R. B.; Youngblood, J.; Moon, R. J. Effects of Crystal Orientation on Cellulose Nanocrystals–Cellulose Acetate Nanocomposite Fibers Prepared by Dry Spinning. *Biomacromolecules* **2014**, *15* (10), 3827–3835.
- (111) Park, S.; Baker, J. O.; Himmel, M. E.; Parilla, P. A.; Johnson, D. K. Cellulose Crystallinity Index: Measurement Techniques and Their Impact on Interpreting Cellulase Performance. *Biotechnology for biofuels* **2010**, *3*, 1–10.
- (112) Hermans, J. J.; Hermans, P. H.; Vermaas, D.; Weidinger, A. Quantitative Evaluation of Orientation in Cellulose Fibres from the X-ray Fibre Diagram. *Recueil des Travaux Chimiques des Pays-Bas* **1946**, *65* (6), 427–447.
- (113) Nakamura, K.; Wada, M.; Kuga, S.; Okano, T. Poisson's ratio of cellulose I $\beta$  and cellulose II. *Journal of Polymer Science Part B: Polymer Physics* **2004**, *42* (7), 1206–1211. <https://doi.org/10.1002/polb.10771>.
- (114) Ting, T. T. C. *Anisotropic Elasticity: Theory and Applications*; Oxford Engineering Science Series; Oxford University Press: New York, 1996. <https://doi.org/10.1093/oso/9780195074475.001.0001>.
- (115) Bond, W. L. The Mathematics of the Physical Properties of Crystals. *The Bell System Technical Journal* **1943**, *22* (1), 1–72. <https://doi.org/10.1002/j.1538-7305.1943.tb01304.x>.
- (116) Rivero, L. Transformation of the Mechanical Properties of Fiber-Reinforced Plastic Tubes from the Cartesian Coordinate Syst...
- (117) Kopp, R. A. Multi-Fidelity Modeling of Interfacial Micromechanics for Off-Aligned Polymer/Carbon Nanotube Nanocomposites. **2016**.
- (118) Sorel, S. On a New Magnesium Cement. *CR Acad. Sci* **1867**, *65*, 102–104.
- (119) Aiken, T. A.; Russell, M.; McPolin, D.; Bagnall, L. Magnesium Oxychloride Boards: Understanding a Novel Building Material. *Mater Struct* **2020**, *53* (5), 118. <https://doi.org/10.1617/s11527-020-01547-z>.
- (120) Záleská, M.; Pavlíková, M.; Jankovský, O.; Lojka, M.; Pivák, A.; Pavlík, Z. Experimental Analysis of MOC Composite with a Waste-Expanded Polypropylene-Based Aggregate. *Materials (Basel)* **2018**, *11* (6), 931. <https://doi.org/10.3390/ma11060931>.
- (121) Li, K.; Wang, Y.; Yao, N.; Zhang, A. Recent Progress of Magnesium Oxychloride Cement: Manufacture, Curing, Structure and Performance. *Construction and Building Materials* **2020**, *255*, 119381. <https://doi.org/10.1016/j.conbuildmat.2020.119381>.
- (122) Walling, S. A.; Provis, J. L. Magnesia-Based Cements: A Journey of 150 Years, and Cements for the Future? *Chem. Rev.* **2016**, *116* (7), 4170–4204. <https://doi.org/10.1021/acs.chemrev.5b00463>.
- (123) Matkovic, B.; Young, J. F. Microstructure of Magnesium Oxychloride Cements. *Nature Physical Science* **1973**, *246* (153), 79–80. <https://doi.org/10.1038/physci246079a0>.

- (124) Gomes, C. M.; de Oliveira, A. D. S. Chemical Phases and Microstructural Analysis of Pastes Based on Magnesia Cement. *Construction and Building Materials* **2018**, *188*, 615–620. <https://doi.org/10.1016/j.conbuildmat.2018.08.083>.
- (125) Siddique, R.; Naik, T. R. Properties of Concrete Containing Scrap-Tire Rubber – an Overview. *Waste Management* **2004**, *24* (6), 563–569. <https://doi.org/10.1016/j.wasman.2004.01.006>.
- (126) Biel, T. D.; Lee, H. Magnesium Oxychloride Cement Concrete with Recycled Tire Rubber. *Transportation Research Record* **1996**, *1561* (1), 6–12. <https://doi.org/10.1177/0361198196156100102>.
- (127) Lowther, M.; Robinson, T. E.; Villapun, V. M.; Stark, C. P.; Grover, L. M.; Cox, S. C. Formulation of Inherently Antimicrobial Magnesium Oxychloride Cement and the Effect of Supplementation with Silver Phosphate. *Materials Science and Engineering: C* **2021**, *126*, 112158. <https://doi.org/10.1016/j.msec.2021.112158>.
- (128) Tan, Y.; Liu, Y.; Grover, L. Effect of Phosphoric Acid on the Properties of Magnesium Oxychloride Cement as a Biomaterial. *Cement and concrete research* **2014**, *56*, 69–74.
- (129) Guan, X.; Zhou, G.; Cui, Y.; Fei, J.; Fan, Y. Effect of Different-Sizes of Hydroxyapatite on the Water Resistance of Magnesium Oxychloride Cement for Bone Repair. *RSC advances* **2019**, *9* (66), 38619–38628.
- (130) Li, H.; Liao, J.; Zhang, Y.; Yang, Y.; Wen, J.; Ma, T.; Guan, Y. Strontium Hydroxyapatite/Magnesium Oxychloride Cement with High Strength and High Osteogenic Activity for Bone Defect Repair. *Biomedical Materials* **2023**, *18* (2), 025023.
- (131) Guo, Y.; Zhang, Y.; Soe, K.; Pulham, M. Recent Development in Magnesium Oxychloride Cement. *Structural Concrete* **2018**, *19* (5), 1290–1300. <https://doi.org/10.1002/suco.201800077>.
- (132) Tooper, B.; Cartz, L. Structure and Formation of Magnesium Oxychloride Sorel Cements. *Nature* **1966**, *211* (5044), 64–66. <https://doi.org/10.1038/211064a0>.
- (133) Ye, Q.; Wang, W.; Zhang, W.; Li, J.; Chen, H. Tuning the Phase Structure and Mechanical Performance of Magnesium Oxychloride Cements by Curing Temperature and H<sub>2</sub>O/MgCl<sub>2</sub> Ratio. *Construction and Building Materials* **2018**, *179*, 413–419. <https://doi.org/10.1016/j.conbuildmat.2018.05.257>.
- (134) Li, K.; Wang, Y.; Zhang, X.; Wang, X.; Zhang, A. Raw Material Ratio Optimisation of Magnesium Oxychloride Cement Using Response Surface Method. *Construction and Building Materials* **2021**, *272*, 121648. <https://doi.org/10.1016/j.conbuildmat.2020.121648>.
- (135) Li, Z.; Chau, C. K. Influence of Molar Ratios on Properties of Magnesium Oxychloride Cement. *Cement and Concrete Research* **2007**, *37* (6), 866–870. <https://doi.org/10.1016/j.cemconres.2007.03.015>.
- (136) Jankovský, O.; Lojka, M.; Lauermannová, A.-M.; Antončík, F.; Pavlíková, M.; Pavlík, Z.; Sedmidubský, D. Carbon Dioxide Uptake by MOC-Based Materials. *Applied Sciences* **2020**, *10* (7), 2254.



- (137) Power, I. M.; Dipple, G. M.; Francis, P. S. Assessing the Carbon Sequestration Potential of Magnesium Oxychloride Cement Building Materials. *Cement and Concrete Composites* **2017**, *78*, 97–107. <https://doi.org/10.1016/j.cemconcomp.2017.01.003>.
- (138) Góchez, R.; Vreeland, T.; Wambaugh, J.; Kitchens, C. L. Conversion of Magnesium Oxychloride to Chlorartinite and Resulting Increased Water Resistance. *Materials Letters* **2017**, *207*, 1–3. <https://doi.org/10.1016/j.matlet.2017.06.124>.
- (139) Prymelski, F. *Building Materials in the Form of Woodstone Panels or Sheets and Processes for Their Production*; Google Patents, 1979.
- (140) Feigin, M. E.; Jr, J. W. W.; Wambaugh, J. A. Construction Board with Carbonate. US7867597B2, January 11, 2011. <https://patents.google.com/patent/US7867597B2/en?q=US7867597B2> (accessed 2023-06-08).
- (141) Rossiter, W. J.; Mathey, R. G. *Magnesium Oxychloride Cement-Based Foam Insulation: A Review of Available Information and Identification of Research Needs*; National Bureau of Standards, 1986.
- (142) Pavlíková, M.; Pivák, A.; Záleská, M.; Jankovský, O.; Reiterman, P.; Pavlík, Z. Magnesium Oxychloride Cement Composites Lightened with Granulated Scrap Tires and Expanded Glass. *Materials* **2020**, *13* (21), 4828. <https://doi.org/10.3390/ma13214828>.
- (143) Deng, D. The Mechanism for Soluble Phosphates to Improve the Water Resistance of Magnesium Oxychloride Cement. *Cement and Concrete Research* **2003**, *33* (9), 1311–1317. [https://doi.org/10.1016/S0008-8846\(03\)00043-7](https://doi.org/10.1016/S0008-8846(03)00043-7).
- (144) Affdl, J. H.; Kardos, J. L. The Halpin-Tsai Equations: A Review. *Polymer Engineering & Science* **1976**, *16* (5), 344–352.
- (145) Elmasry, A.; Azoti, W.; El-Safty, S. A.; Elmarakbi, A. A Comparative Review of Multiscale Models for Effective Properties of Nano- and Micro-Composites. *Progress in Materials Science* **2023**, *132*, 101022. <https://doi.org/10.1016/j.pmatsci.2022.101022>.
- (146) Martínez-Ayuso, G.; Friswell, M. I.; Adhikari, S.; Khodaparast, H. H.; Berger, H. Homogenization of Porous Piezoelectric Materials. *International Journal of Solids and Structures* **2017**, *113–114*, 218–229. <https://doi.org/10.1016/j.ijsolstr.2017.03.003>.
- (147) Pivovarov, D.; Zabihiyan, R.; Mergheim, J.; Willner, K.; Steinmann, P. On Periodic Boundary Conditions and Ergodicity in Computational Homogenization of Heterogeneous Materials with Random Microstructure. *Computer Methods in Applied Mechanics and Engineering* **2019**, *357*, 112563. <https://doi.org/10.1016/j.cma.2019.07.032>.
- (148) Andreassen, E.; Andreassen, C. S. How to Determine Composite Material Properties Using Numerical Homogenization. *Computational Materials Science* **2014**, *83*, 488–495. <https://doi.org/10.1016/j.commatsci.2013.09.006>.

- (149) Hansbo, A.; Hansbo, P. A Finite Element Method for the Simulation of Strong and Weak Discontinuities in Solid Mechanics. *Computer Methods in Applied Mechanics and Engineering* **2004**, *193* (33), 3523–3540. <https://doi.org/10.1016/j.cma.2003.12.041>.
- (150) Gooneie, A.; Schuschnigg, S.; Holzer, C. A Review of Multiscale Computational Methods in Polymeric Materials. *Polymers (Basel)* **2017**, *9* (1), 16. <https://doi.org/10.3390/polym9010016>.
- (151) MacKrell, A. Multiscale Composite Analysis in Abaqus: Theory and Motivations. *Reinforced Plastics* **2017**, *61* (3), 153–156. <https://doi.org/10.1016/j.repl.2016.01.003>.
- (152) Radermacher, A.; Bednarczyk, B. A.; Stier, B.; Simon, J.; Zhou, L.; Reese, S. Displacement-Based Multiscale Modeling of Fiber-Reinforced Composites by Means of Proper Orthogonal Decomposition. *Advanced Modeling and Simulation in Engineering Sciences* **2016**, *3* (1), 29. <https://doi.org/10.1186/s40323-016-0082-8>.
- (153) Teixeira, J.; Kim, Y.-R.; Souza, F.; Allen, D.; Little, D. Multiscale Model for Asphalt Mixtures Subjected to Cracking and Viscoelastic Deformation. *Transportation Research Record: Journal of the Transportation Research Board* **2014**, *2447*, 136–145. <https://doi.org/10.3141/2447-15>.
- (154) Zeng, Q. H.; Yu, A. B.; Lu, G. Q. Multiscale Modeling and Simulation of Polymer Nanocomposites. *Progress in Polymer Science* **2008**, *33* (2), 191–269. <https://doi.org/10.1016/j.progpolymsci.2007.09.002>.
- (155) Hultquist, C.; Chen, G.; Zhao, K. A Comparison of Gaussian Process Regression, Random Forests and Support Vector Regression for Burn Severity Assessment in Diseased Forests. *Remote sensing letters* **2014**, *5* (8), 723–732.
- (156) Kan, M. S.; Tan, A. C.; Mathew, J. A Review on Prognostic Techniques for Non-Stationary and Non-Linear Rotating Systems. *Mechanical Systems and Signal Processing* **2015**, *62*, 1–20.
- (157) Heo, Y.; Zavala, V. M. Gaussian Process Modeling for Measurement and Verification of Building Energy Savings. *Energy and Buildings* **2012**, *53*, 7–18.
- (158) Duvenaud, D. K.; Nickisch, H.; Rasmussen, C. Additive Gaussian Processes. *Advances in neural information processing systems* **2011**, *24*.
- (159) Kim, H.; Teh, Y. W. Scaling up the Automatic Statistician: Scalable Structure Discovery Using Gaussian Processes. In *International Conference on Artificial Intelligence and Statistics*; PMLR, 2018; pp 575–584.
- (160) Plate, T. A. Accuracy versus Interpretability in Flexible Modeling: Implementing a Tradeoff Using Gaussian Process Models. *Behaviormetrika* **1999**, *26*, 29–50.
- (161) Duvenaud, D. Automatic Model Construction with Gaussian Processes, University of Cambridge, 2014.
- (162) Wambaugh, J. A.; Rochner, B. Ultra Stable Cementitious Material Formulation, Process for Its Making, and Ultra Stable Tile Backer Board Formulation and Processes for Its Making. US10696595B2, June 30, 2020.

<https://patents.google.com/patent/US10696595B2/en?q=us10696595b2> (accessed 2023-06-08).

- (163) C1185-08, A. *Standard Test Methods for Sampling and Testing Non-Asbestos Fiber-Cement Flat Sheet, Roofing and Siding Shingles, and Clapboards*; ASTM-American Society for Testing and Materials Pennsylvania, 2016; pp 1–9.
- (164) C1218/C1218M–20, A. *Standard Test Method for Water-Soluble Chloride in Mortar and Concrete*; ASTM-American Society for Testing and Materials Pennsylvania, 2020.
- (165) Coelho, A. A. TOPAS and TOPAS-Academic: An Optimization Program Integrating Computer Algebra and Crystallographic Objects Written in C++. *J Appl Cryst* **2018**, 51 (1), 210–218. <https://doi.org/10.1107/S1600576718000183>.
- (166) Rietveld, H. M. A Profile Refinement Method for Nuclear and Magnetic Structures. *J Appl Cryst* **1969**, 2 (2), 65–71. <https://doi.org/10.1107/S0021889869006558>.
- (167) D1037-12, A. *Standard Test Methods for Evaluating Properties of Wood-Base Fiber and Particle Panel Materials*; ASTM-American Society for Testing and Materials Pennsylvania, 2020.
- (168) Chaurasia, P.; Younis, K.; Qadri, O. S.; Srivastava, G.; Osama, K. Comparison of Gaussian Process Regression, Artificial Neural Network, and Response Surface Methodology Modeling Approaches for Predicting Drying Time of Mosambi (Citrus Limetta) Peel. *Journal of Food Process Engineering* **2019**, 42 (2), e12966.
- (169) Bishnoi, S.; Ravinder, R.; Singh, H.; Kodamana, H.; Krishnan, N. M. Scalable Gaussian Processes for Predicting the Properties of Inorganic Glasses with Large Datasets. *arXiv preprint arXiv:2007.02795* **2020**.
- (170) Williams, C. K.; Rasmussen, C. E. *Gaussian Processes for Machine Learning*; MIT press Cambridge, MA, 2006; Vol. 2.
- (171) GPy, Gp. *A Gaussian Process Framework in Python*; University of Sheffield, Sheffield, England, UK, 2012.
- (172) Neal, R. M. *Bayesian Learning for Neural Networks*; Springer Science & Business Media, 2012; Vol. 118.
- (173) Roustant, O.; Padonou, E.; Deville, Y.; Clément, A.; Perrin, G.; Giorla, J.; Wynn, H. Group Kernels for Gaussian Process Metamodels with Categorical Inputs. *SIAM/ASA Journal on Uncertainty Quantification* **2020**, 8 (2), 775–806.
- (174) Abdalla, A.; Salih Mohammed, A. Surrogate Models to Predict the Long-Term Compressive Strength of Cement-Based Mortar Modified with Fly Ash. *Arch Computat Methods Eng* **2022**, 29 (6), 4187–4212. <https://doi.org/10.1007/s11831-022-09734-7>.
- (175) Stevens, R. J.; Poppe, K. K. Validation of Clinical Prediction Models: What Does the “Calibration Slope” Really Measure? *Journal of Clinical Epidemiology* **2020**, 118, 93–99. <https://doi.org/10.1016/j.jclinepi.2019.09.016>.
- (176) Legates, D. R.; McCabe Jr., G. J. Evaluating the Use of “Goodness-of-Fit” Measures in Hydrologic and Hydroclimatic Model Validation. *Water Resources Research* **1999**, 35 (1), 233–241. <https://doi.org/10.1029/1998WR900018>.

- (177) Willmott, C. J.; Matsuura, K. Advantages of the Mean Absolute Error (MAE) over the Root Mean Square Error (RMSE) in Assessing Average Model Performance. *Climate Research* **2005**, *30* (1), 79–82.
- (178) Hendrycks, D.; Lee, K.; Mazeika, M. Using Pre-Training Can Improve Model Robustness and Uncertainty. In *International Conference on Machine Learning*; PMLR, 2019; pp 2712–2721.
- (179) Fan, Z.; Han, X.; Wang, Z. HyperBO+: Pre-Training a Universal Prior for Bayesian Optimization with Hierarchical Gaussian Processes. *arXiv preprint arXiv:2212.10538* **2022**.
- (180) Paananen, T.; Piironen, J.; Andersen, M. R.; Vehtari, A. Variable Selection for Gaussian Processes via Sensitivity Analysis of the Posterior Predictive Distribution. In *The 22nd International Conference on Artificial Intelligence and Statistics*; PMLR, 2019; pp 1743–1752.
- (181) Wang, T.; Huang, H.; Tian, S.; Xu, J. Feature Selection for SVM via Optimization of Kernel Polarization with Gaussian ARD Kernels. *Expert Systems with Applications* **2010**, *37* (9), 6663–6668.
- (182) Leray, P.; Gallinari, P. Feature Selection with Neural Networks. *Behaviormetrika* **1999**, *26*, 145–166.
- (183) Gold, C.; Holub, A.; Sollich, P. Bayesian Approach to Feature Selection and Parameter Tuning for Support Vector Machine Classifiers. *Neural Networks* **2005**, *18* (5–6), 693–701.
- (184) Ngatchou, P.; Zarei, A.; El-Sharkawi, A. Pareto Multi Objective Optimization. In *Proceedings of the 13th international conference on, intelligent systems application to power systems*; IEEE, 2005; pp 84–91.
- (185) Konak, A.; Coit, D. W.; Smith, A. E. Multi-Objective Optimization Using Genetic Algorithms: A Tutorial. *Reliability engineering & system safety* **2006**, *91* (9), 992–1007.
- (186) Gunantara, N. A Review of Multi-Objective Optimization: Methods and Its Applications. *Cogent Engineering* **2018**, *5* (1), 1502242.
- (187) Marler, R. T.; Arora, J. S. Survey of Multi-Objective Optimization Methods for Engineering. *Structural and multidisciplinary optimization* **2004**, *26*, 369–395.
- (188) Janga Reddy, M.; Nagesh Kumar, D. An Efficient Multi-Objective Optimization Algorithm Based on Swarm Intelligence for Engineering Design. *Engineering Optimization* **2007**, *39* (1), 49–68.
- (189) Voigt, W. *Lehrbuch Der Kristallphysik*; Teubner Leipzig, 1928; Vol. 962.